Technische Universität München

Fakultät für Chemie

Professur für Anorganische Chemie

The Nature of Active Copper Species in Ethynylation Reactions and Methanol Synthesis

Tobias Bruhm

Vollständiger Abdruck der von der Fakultät für Chemie der Technischen Universität München zur Erlangung des akademischen Grades eines

Doktors der Naturwissenschaften (Dr. rer. nat.)

genehmigten Dissertation.

Vorsitzender: **Priv.-Doz. Dr. Friedrich Esch**

Prüfende der Dissertation:

1. **Prof. Dr. Klaus Köhler**
2. **Prof. Dr. Ulrich K. Heiz**

Die Dissertation wurde am **17.05.2021** bei der Technischen Universität München eingereicht und durch die Fakultät für Chemie am **21.06.2021** angenommen.

Die vorliegende Arbeit entstand im Zeitraum vom Oktober 2017 bis Mai 2021 an der Fakultät für Chemie und am Zentralinstitut für Katalyseforschung (CRC) der Technischen Universität München.

Mein besonderer Dank gilt meinen akademischen Lehrern

Prof. Dr. Klaus Köhler

und Prof. Dr. Ulrich Heiz

für die freundliche Aufnahme in ihre Arbeitskreise,

ihre uneingeschränkte Unterstützung,

ihr Vertrauen und die damit verbundenen Freiräume in der

Gestaltung und Bearbeitung der Aufgabenstellung

sowie ihr großes Interesse am Gelingen der Arbeit

ACKNOWLEDGEMENT

First and foremost, I wish to thank **Prof. Dr. Klaus Köhler** for giving me the opportunity to work in his research group. Without his support, patience, and understanding I would not have been able to accomplish the work presented here.

I want to thank **Prof. Dr. Ulrich Heiz** for supporting me and especially for coordinating the collaboration with King Abdullah University of Science and Technology (KAUST) in Saudi Arabia.

Prof. Dr. Jean-Marie Basset is thanked for the specialist advice and for the great research stay, I had in Saudi Arabia. I also want to thank the whole research group there for the warm welcome and great scientific support (**Dr. Manoja Kumar Samantary**, **Dr. Walid Al Maksoud, Dr. Dalaver H. Anjum**). **Dr. Dalaver H. Anjum** measured TEM and STEM-EELS and helped me to evaluate the data.

I would especially like to thank my former and present colleagues for welcoming me into the research group and for the help, advice, and fun we had. Namely, they are: **Andrea Abram**, **Hannah Augenstein**, **Dr. Florian Boch**, **Dr. Patrick Bretzler**, **Dr. Christoph Dörfelt**, **Dr. Christoph Gnad**, **Dr. Carmen Haeßner**, **Max Hiller**, **Lingdi Kong**, **Lea Kopietz**, **Patrick Schlachta**, **Dr. Oliver Thomys**, **Dr. Chengyang Wang,** and **Dr. Xiaoqiao Zhang**.

Special thanks to **Hannah Augenstein** for helping to build up the catalytic testing setup and for her advices regarding the synthesis of the catalysts. **Dr. Oliver Thomys** for guiding me how to use the parallel testing unit, introducing me to statistical methods and all the nice discussions about science and about anything else. **Andrea Abram** for Raman and ICP-OES measurements.

The students who worked with me in lab also deserve my gratitude. They are **Fiona Cole**, **Janina Förtsch**, **Karina Hemmer**, **Christoph Gross**, **Felix Kinzner**, **Matthias Krinninger**, **Dan-Ioan Mehelean**, **Samuel Merk**, **Matthias Rehner**, **Sebastian Stiegler,** and **Chong Zu Teng**. The work performed during the master theses of **Johannes Häusler**, **Manuel Botta** and **Lion Maier** also played a role in the success of this project. It was a pleasure to work together with all of you.

Prof. Dr. Sebastian Günther and **Tim Kratky** are thanked for measuring XPS and for helping to evaluate the data.

Prof. Dr. Kai-Olaf Hinrichsen and **Tabea Gros** have my gratitude for giving me the opportunity to perform H_2-TPD experiment using the FAST-setup.

I want to thank all the people from the central analytics laboratory of the CRC. **Dr. Eliza Gemel** for maintenance of the analytical devices and **Ulrike Ammari**, **Petra Ankenbauer**, and **Bircan Dilki** for performing elemental analysis.

In addition, I would like to thank Dr. Oksana Storcheva and Richard Wetzel for organizing the lab course for chemical engineering students. It was a pleasure to work in the perfectly planned lab course.
Furthermore, financial support for the catalytic testing unit for the ethynylation by **Clariant AG** is acknowledged.
It would not have been possible to finish this work without my parents **Irmgard** and **Rainer Bruhm**. They supported me before and during the PhD program. I want to thank my sister **Alexandra Bruhm** for the time we spent together (e.g. skiing) and the jokes how short it takes to do a PhD in medicine. A special thanks to all my friends from school and from university to support me during difficult periods and for all the trips, evenings, parties and nice moments, we spent together.
I would especially like to thank my wife **Lisa Bruhm** for her continuous support before and during this work. I enjoyed the time we spent together and I am excited to experience many more moments with you in future.

ABSTRACT

Due to the specific chemical and physical properties and reasonable costs, Cu based catalysts are applied in various reactions. The present thesis reports new insights in the ethynylation of formaldehyde and the CO_2 hydrogenation to methanol by supported Cu catalysts

The active species of the ethynylation of formaldehyde is still not clear despite the reaction is established since the fifties of the 20th century. With catalytic tests as well as different characterization and analytical methods using $CuO/Bi_2O_3/SiO_2$ and copper(I) acetylide , Cu_2C_2, catalysts it is proven that copper(I) acetylide , Cu_2C_2, is the active species in ethynylation reactions based on acetylene. Cu_2C_2 is formed by dissolution/re-precipitation processes during the activation of the catalyst precursor meaning that Cu(II) leaches from the CuO catalyst, reacts with dissolved C_2H_2 and precipitates as Cu_2C_2. Cu(II) is reduced to Cu(I) and C_2H_2 acts as reducing agent. Furthermore, it turned out that the nature of the formed Cu_2C_2 influences the catalytic performance of different CuO/Bi_2O_3 catalysts.

Similar to the ethynylation reaction, the active species and especially the role of Zn in industrial like $Cu/ZnO/Al_2O_3$ catalysts is still discussed for the CO_2 hydrogenation to methanol. A new synthesis approach via surface organometallic chemistry was applied to deposit Zn targeted onto Cu nanoparticles supported on Al_2O_3. By reductive pre-treatment of the catalysts, it is possible to adjust the Zn/Cu ratio at the surface and hence the extent of Zn/Cu surface alloy formation. It turned out that the formation of Cu/Zn surface alloy after reductive pretreatment leads to the formation of highly dispersed $Cu/Zn^{\delta+}$ sites during the catalytic reaction. In addition, the Zn coverage is crucial depending on the Cu particle size and consequently on the level of Zn/Cu alloy formation. Catalysts are prepared where Zn or rather ZnO was first deposited on Al_2O_3 and Cu was precipitated afterwards onto the support to simulate an industrial like catalyst. It turned out that these catalysts are more resistant towards sintering.

Furthermore, a parallel testing unit was put in operation successfully for methanol synthesis based on CO_2 at 10 bar. The catalytic results are reliable and reproducible using different Cu/ZrO_2 catalysts. Promotor screening shows that the addition of Zn, Al, Sm, Ga and the earth alkaline metals enhance the CO_2 conversion and Ag and Cd the MeOH selectivity of Cu/ZrO_2 catalysts.

KURZZUSAMMENFASSUNG

Wegen seiner besonderen chemischen und physikalischen Eigenschaften sowie der vertretbaren Kosten werden kupferbasierte Katalysatoren in verschiedensten Reaktionen eingesetzt. Durch diese Arbeit werden neue Einblicke in die Ethinylierung von Formaldehyd sowie der CO_2 Hydrierung zu Methanol mit Kupfer-Trägerkatalysatoren gewonnen.

Obwohl die Ethinylierung von Formaldehyd seit Mitte des zwanzigsten Jahrhunderts industriell durchgeführt wird, ist die aktive Spezies dieser Reaktion noch nicht erforscht worden. Mit Hilfe von Katalysetests sowie verschiedensten Charakterisierungs- und Analysemethoden durch Verwendung von $CuO/Bi_2O_3/SiO_2$ und Kupfer(I)acetylid (Cu_2C_2) Katalysatoren konnte gezeigt werden, dass Kupfer(I)acetylid, Cu_2C_2, die aktive Spezies in Ethinylierungen auf Basis von Acetylen ist. Cu_2C_2 wird in Lösung durch Auflösungs- und Wiederabscheidungsprozesse während der Aktivierung des Katalysatorvorläufers gebildet. Das heißt, dass Cu(II) von CuO in Lösung geht, dort mit C_2H_2 reagiert und als Cu_2C_2 wieder ausfällt. Cu(II) wird dabei zu Cu(I) mittels Acetylen reduziert. Zudem stellte sich heraus, dass die Eigenschaften des gebildeten Cu_2C_2 einen Einfluss auf die katalytische Aktivität von unterschiedlichen CuO/Bi_2O_3 Katalysatoren haben.

Ähnlich wie bei der Ethinylierung, wird über die aktive Spezies und insbesondere die Rolle von Zink in der Methanolsynthese ausgehend von CO_2 in industriellen $Cu/ZnO/Al_2O_3$ Katalysatoren immer noch diskutiert. Ein neuer Syntheseansatz mittels metallorganischer Koordinationschemie (SOMC) wurde entwickelt, um Zn gezielt auf Kupfernanopartikel, welche auf Al_2O_3 geträgert sind, abzuscheiden. Durch reduktive Vorbehandlung der Katalysatoren kann das Zn/Cu Verhältnis auf der Oberfläche und somit das Ausmaß der Bildung einer Zn/Cu-Oberflächenlegierung eingestellt werden. Es stellte sich heraus, dass die Cu/Zn-Oberflächenlegierung zur Bildung von fein verteilten $Cu/Zn^{\delta+}$-Zentren während der Katalyse führt. Zusätzlich spielt die Zinkbeladung in Abhängigkeit von der Größe der Kupfernanopartikel eine Rolle bei Bildung und Ausmaß der Zn/Cu-Oberflächenlegierung. Katalysatoren, bei denen Zn beziehungsweise ZnO zuerst auf den Al_2O_3-Träger aufgebracht und danach Cu abgeschieden wurde, um einen industriellen $Cu/ZnO/Al_2O_3$ Katalysator nachzubilden, wurden ebenfalls präpariert. Diese Katalysatoren verhindern stärker das Sintern der Kupfernanopartikel verglichen mit den Katalysatoren, bei denen Zn gezielt auf die Kupfernanopartikel abgeschieden wurde.

Außerdem wurde eine Paralleltestanlage mit zwölf Reaktoren erfolgreich für die Methanolsynthese aus CO_2 bei 10 bar in Betrieb genommen. Die Katalyseergebnisse sind zuverlässig und reproduzierbar, was mittels verschiedener Cu/ZrO_2-Katalysatoren getestet wurde. Zusätzliches Promotorscreening zeigte, dass die Zugabe von Zn, Al, Sm, Ga und von Erdalkalimetallen den CO_2-Umsatz und Ag und Cd die Methanol-Selektivität von Cu/ZrO_2 Katalysatoren erhöhen.

LIST OF ABBREVIATIONS

2 θ	Bragg angle
a.u.	Arbitrary unit
BET	Brunauer-Emmett-Teller
BJH	Barrett-Joyner-Halenda
CNG	Compressed natural gas
E_a	Activation energy
EELS	Electron energy loss spectroscopy
EPR	Electron paramagnetic resonance spectroscopy
FT-IR	Fourier-transform – infrared spectroscopy
GC	Gas chromatography
GHSV	Gas hourly space velocity
H_2-TA	H_2-Transient adsorption
H_2-TPD	H_2-Temperature programmed desorption
H_2-TPR	H_2-Temperature programmed reduction
HRTEM	High-resolution transmission electron microscopy
ICP-OES	Inductively coupled plasma – optical emission spectrometry
LNG	Liquefied natural gas
LPG	Liquefied petroleum gas
m/z	Mass to charge ratio
MS	Mass spectroscopy
MTG	Methanol-to-gasoline
MTO	Methanol-to-olefins
N_2O-RFC	N_2O-Reactive frontal chromatography
NMR	Nuclear magnetic resonance
RDS	Rate-determining step
RWGS	Reverse water-gas shift
SRK	Soave-Redlich-Kwong
STEM	Scanning transmission electron microscopy
TEM	Transmission electron microscopy
TG	Thermogravimetric analysis
TOF	Turnover frequency
TPD	Temperature programmed decomposition
vol.%	Volume percentage
WGS	Water-gas shift

wt.%	Weight percentage
XPS	X-Ray photoelectron spectroscopy
XRD	X-Ray diffraction
θ_{Zn}	Zinc coverage

TABLE OF CONTENTS

1

Introduction and Objectives

Copper is widely used for the synthesis of different catalyst materials in industry due to the specific chemical and physical properties, its low costs and the high availability.[1]

Cu catalysts are applied in many catalytic reactions like electrocatalysis, photocatalysis, coupling reactions, oxidation catalysis and hydrogenation catalysis. Even in industrially large-scale processes like the ethynylation of formaldehyde or methanol synthesis Cu based catalysts are employed.[1-7]

In this work, these two Cu catalyzed reactions are investigated, on the one hand the ethynylation of formaldehyde which is carried out in solution and on the other hand the CO_2 hydrogenation to methanol which is a gas phase reaction.[6, 8, 9]

For the ethynylation reaction, CuO based catalysts are used which are activated by acetylene forming copper(I) acetylide, Cu_2C_2. Copper(I) acetylide, Cu_2C_2, is supposed to be the active species in ethynylation reactions based on acetylene. The identification as well as its formation during the activation of CuO/Bi_2O_3 catalysts have not been done so far in detail. The characterization of copper(I) acetylide, Cu_2C_2, is very challenging due to its instability as well as the limitations concerning the analytical tools, which can be applied. The catalytic reaction is carried out in a water-formaldehyde solution with a solid catalyst and gaseous C_2H_2. In addition, pure Cu_2C_2 is only stable under wet conditions. Hence, characterization methods are necessary, which work with suspensions or wet samples. However, aim of this work is to get new insights regarding the identification of Cu_2C_2 and its formation during the activation of supported CuO/Bi_2O_3 catalysts.[9-13]

Similar to ethynylation reactions, the active site and especially the role of Zn in industrially $Cu/ZnO/Al_2O_3$ catalysts for methanol synthesis is still not clear and is discussed controversially in literature. It is known that somehow strong Cu/Zn interactions are important for highly active and efficient $Cu/ZnO/Al_2O_3$ methanol synthesis catalysts. Nowadays, methanol synthesis from pure CO_2 feeds is of great interest because of environmental reasons. Compared to the ethynylation, methanol synthesis is a gas phase reaction, which takes place in a reactor tube filled with the catalyst. For this work, a surface organometallic chemistry (SOMC) approach is applied to synthesize $Cu/Zn/Al_2O_3$ catalysts with defined Cu/Zn particles as well as strong Cu/Zn interactions. The preparation method for Al_2O_3 supported Cu nanoparticles is varied to form different Cu particle sizes and different Cu/Al_2O_3 support interactions. In addition, differently Cu and Zn loaded catalysts are prepared.[7, 14, 15]

For both reactions, the catalysts are characterized in detail with various analytical tools. It allows getting deep insights into the catalytic reactions as well as the structures and properties of the catalysts.

2

Reppe Revival – Ethynylation of Formaldehyde with Acetylene to 1,4-Butynediol

2.1 Introduction

Crude oil and its derivatives serve as main feedstock for many petrochemicals. This makes access to reasonably priced and constantly available crude oil crucial for the industrial production thereof. In recent years, large price fluctuations and a generally high price of crude oil have made coal as an alternative feedstock more and more interesting for the chemical industry. This is especially true for countries that have large coal but few oil reserves. Therefore, these countries are trying to be more independent of oil imports and to use coal as a raw material for chemicals. An approach is the production of acetylene which is further converted to 1,4-butynediol and 1,4-butanediol whereas the first reaction is of interest for this work.[16-20] *Walter Reppe* and *Julius Nieuwald* were the first who managed to carry out ethynylation reactions based on acetylene on industrial scale. They solved the problem to work with acetylene under higher pressures by improving the reactor setup (e.g., smaller reactor diameter or filling the reactor with steel spheres). *Walter Reppe* also developed processes for carbonylation, oligomerization and vinylization. He also studied the ethynylation and proposed some mechanistic aspects. According to *Reppe*, propargyl alcohol acts as intermediate meaning that first acetylene reacts with one formaldehyde molecule. Then a second formaldehyde molecule can either react again with acetylene to propargyl alcohol or in a concurrent reaction with the formed propargyl alcohol to 1,4-butynediol (see Figure 1).[8-10, 21-31]

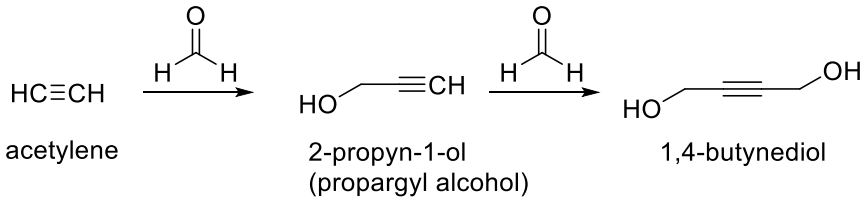

Figure 1: Reaction mechanism proposed by *Walter Reppe* for the ethynylation of formaldehyde forming 1,4-butynediol.[9]

There are no analytical proofs for the reaction mechanism, the nature of the active species, Cu(I) acetylide (Cu_2C_2) and how the active species is formed. Therefore, leaching experiments, Raman spectroscopy, X-Ray diffraction (XRD) and other methods are applied to get a clear idea how the activation of the catalyst occurs in detail using industrial like $CuO/Bi_2O_3/SiO_2$ and pure Cu_2C_2 catalysts. Before the results are discussed, the ethynylation reaction itself and previous studies from other groups are presented.

2.2 Theoretical background

In this chapter, the ethynylation reaction itself is presented. In addition, a closer look is taken on Cu acetylides because Cu acetylides play a crucial role in this reaction based on acetylene. Finally, recent developments are discussed based on a literature review.

2.2.1 Ethynylation reaction

Acetylene is produced in two steps. First CaO is converted to CaC_2 with coke in an electric arc at 2000 to 2300 °C. Second, CaC_2 is transformed to C_2H_2 by addition of H_2O. The reaction equations are shown in Figure 2. There are also efforts to synthesize acetylene by a direct route from coal via arc plasma reactions. In this case, the electric arc has a temperature between 10 000 and 15 000 °C.[19]

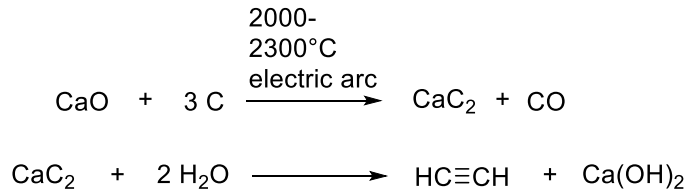

Figure 2: Reaction equations for the two step synthesis of C_2H_2 based on coal.[19]

Acetylene can be further converted to many chemicals for example 2-butyne-1,4-diol (1,4-butynediol), which can be hydrogenated to either 2-butene-1,4-diol or butane-1,4-diol. Latter can be used as monomer in polymer production.[10, 32, 33]

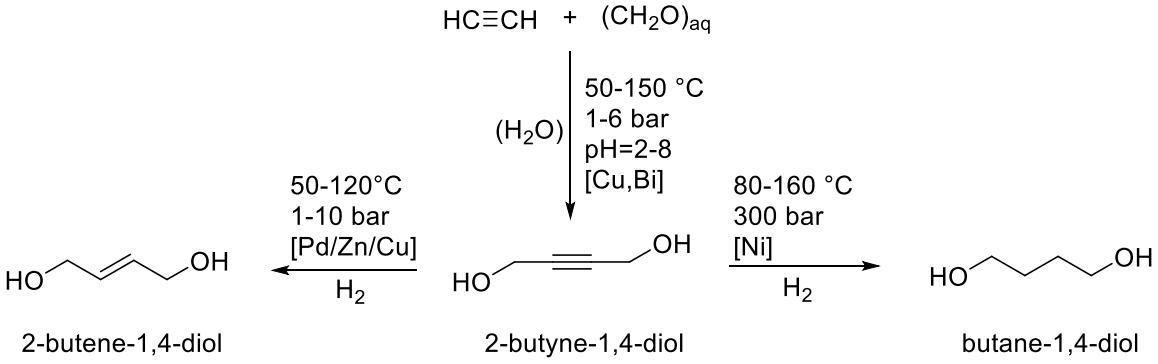

Figure 3: Reaction scheme based on formaldehyde and acetylene for the production of 2-butyne-1,4-diol and the subsequent hydrogenation to 2-butene-1,4 diol and butane-1,4-diol.[10, 32, 33]

The reaction scheme based on acetylene and formaldehyde is depicted in Figure 3. The ethynylation reaction forming 1,4-butynediol is industrially carried out at 50-150°C and 1-6 bar with Cu catalysts. Ag, Au and Hg catalysts can be applied as well. Mostly supported catalysts were used whereas magnesium silicate or pure silica acts as support. In the case of Cu catalysts, loadings up to 50 wt.% are applied. In addition, the catalysts consist of promotors primary Bi (also: iodine compounds, Hg, Ce, Se,) mainly for preventing the formation of cuprene. The

reaction is a three-phase reaction containing gaseous acetylene, liquid formaldehyde solution and a solid catalyst. A 20 to 50% formaldehyde solution in water is used and acetylene is often diluted with nitrogen due to safety hazards. The pH-value is adjusted between 2 and 8 either by addition of a buffer (e.g. NaH_2PO_4/NaOH) or by continuous adding of a base (e.g. NaOH). A very low pH-value leads to the decomposition of copper acetylide, which is formed during the reaction and crucial for the catalytic reaction. A high pH-value is also not desired because of polymerization of formaldehyde, which can stick the reactor or pipes. The process is carried in several batch reactors, which are connected in series. This has the advantage that the reaction can be applied at low pressures and additionally a better heat distribution is achieved. A disadvantage of this system is the high mechanic stress of the catalysts, which leads to heavy abrasion. Consequently, the separation of the solid catalyst from the liquid is made difficult. Usually two products are formed, 2-propyn-1-ol (propargyl alcohol) and 1,4-butynediol with yields of 20-60 % (1,4-butynediol) and 1-5 % (propargyl alcohol) (see Figure 4). The selectivity can be influenced by changing the reaction conditions. At low pressures and in aqueous media 1,4-butynediol is formed nearly quantitatively. Higher acetylene pressures and organic solvents such as tetrahydrofuran increase the acetylene concentration, which favors the formation of propargyl alcohol.[8, 9, 11-13, 27, 33-65]

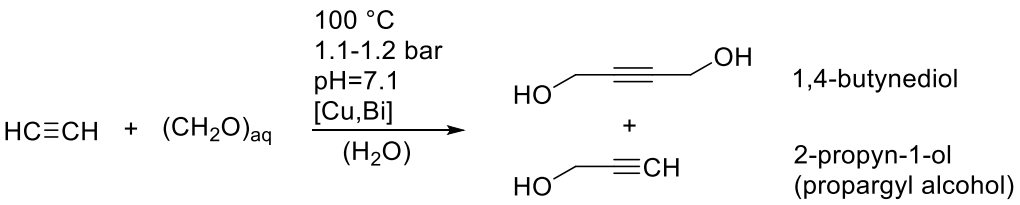

Figure 4: Ethynylation reaction of acetylene and formaldehyde to 1,4-butynediol and 2-propyn-1-ol including the parameter applied for this work.

In addition, Walter Reppe assumed that Cu(I) acetylide (Cu_2C_2) is the active species in the ethynylation reaction. Cu(I) acetylide is formed by the reaction between CuO of the catalyst and acetylene. He proposed that this active species consists of three acetylene molecules coordinated to one Cu(I) acetylide molecule ($Cu_2C_2 \cdot 3\ C_2H_2$).

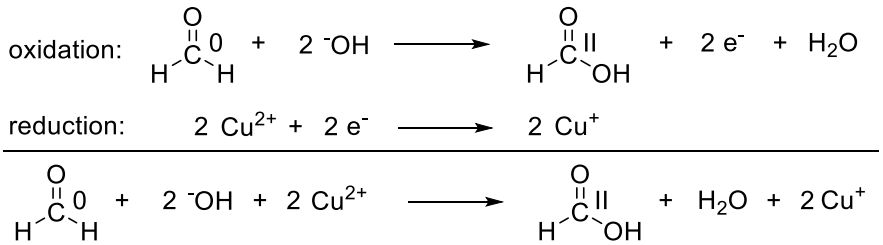

Figure 5: Redox equation for the oxidation of formaldehyde to formic acid and the simultaneous reduction of Cu(II) to Cu(I).[9, 10, 66]

For the formation of Cu(I) acetylide Cu(II) has to be reduced to Cu(I). It is widely accepted in literature that formaldehyde acts as reducing agent forming formic acid (see Figure 5).[9, 10, 66] There are no analytical proofs for all his proposals and assumptions.

2.2.2 Cu acetylides

Because Cu acetylides play an important role in the ethynylation of formaldehyde, they will be described in more detail in this chapter. Metal acetylides are compounds formed when replacing one or both hydrogen atoms of terminal acetylenes by a metal atom. They can be described by the coordination of a $[C{\equiv}C\text{-}R]^{2-}$ or a $[C{\equiv}C]^{2-}$ ligand to a metal or another cationic group (see Figure 6). R hereby represents either an H atom or an organic rest. Depending on both the metal and the rest R, metal acetylides show varying stabilities and chemical properties.[67-69]

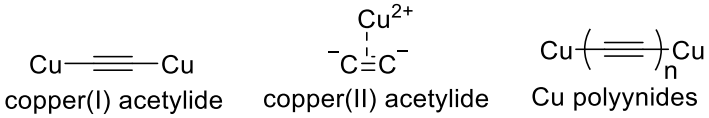

Figure 6: Possible chemical structures of a copper(I) acetylide molecule (left), a copper(II) acetylide molecule (middle) and Cu polyynides (right).

In heavy metal acetylides of acetylene, the acetylide compound acts nucleophilic. This enables the transfer of the acetylene structure to a carbonyl group, making them good catalysts for ethynylation reactions. Compared to their alkali- and earth alkali metal counterparts, heavy metal acetylides are also relatively stable in air when moistened. When dried however, they exhibit explosive behavior. The characterization of their crystalline structure therefore is challenging.[67, 69, 70]

Cu(I) aceteylide (Cu_2C_2), which is present during the ethynylation reaction, is a red to brownish substance. It can be formed as monohydrate by reaction of acetylene either with an ammoniacal solution of a cuprous salt or with a basic solution of cupric salt in presence of a reducing agent.

Passing acetylene gas through aqueous suspensions of Cu metal or insoluble cupric salts yields also to Cu_2C_2 as adducts with acetylene molecules. This would be the case for the catalytic ethynylation of formaldehyde.[8, 17, 67]

As it was mentioned before, the characterization of Cu(I) acetylide remains challenging due to the explosiveness and the insolubility in common solvents. A crystal structure of Cu_2C_2 was not published to date. For example, *Brameld et al.* studied Cu acetylides very detailed especially their formation under different reaction conditions. However, there are no analytical proofs for their experiments like spectra or diffractograms.[71] *Blake et al.* managed to dissolve Cu acetylides based on phenyl acetylene and propinyl derivate in toluene mixed with a strong

π-donor triethylphosphane because they assumed a structure containing coordination polymers.[72] Especially for Ag acetylides this is well known.[73] *Lang et al.* published a crystal structure for (*tert*-butynyl)copper(I) (see Figure 7). This structure also consists of oligomers with different side-on and end-on bounded alkynyl compounds.[74]

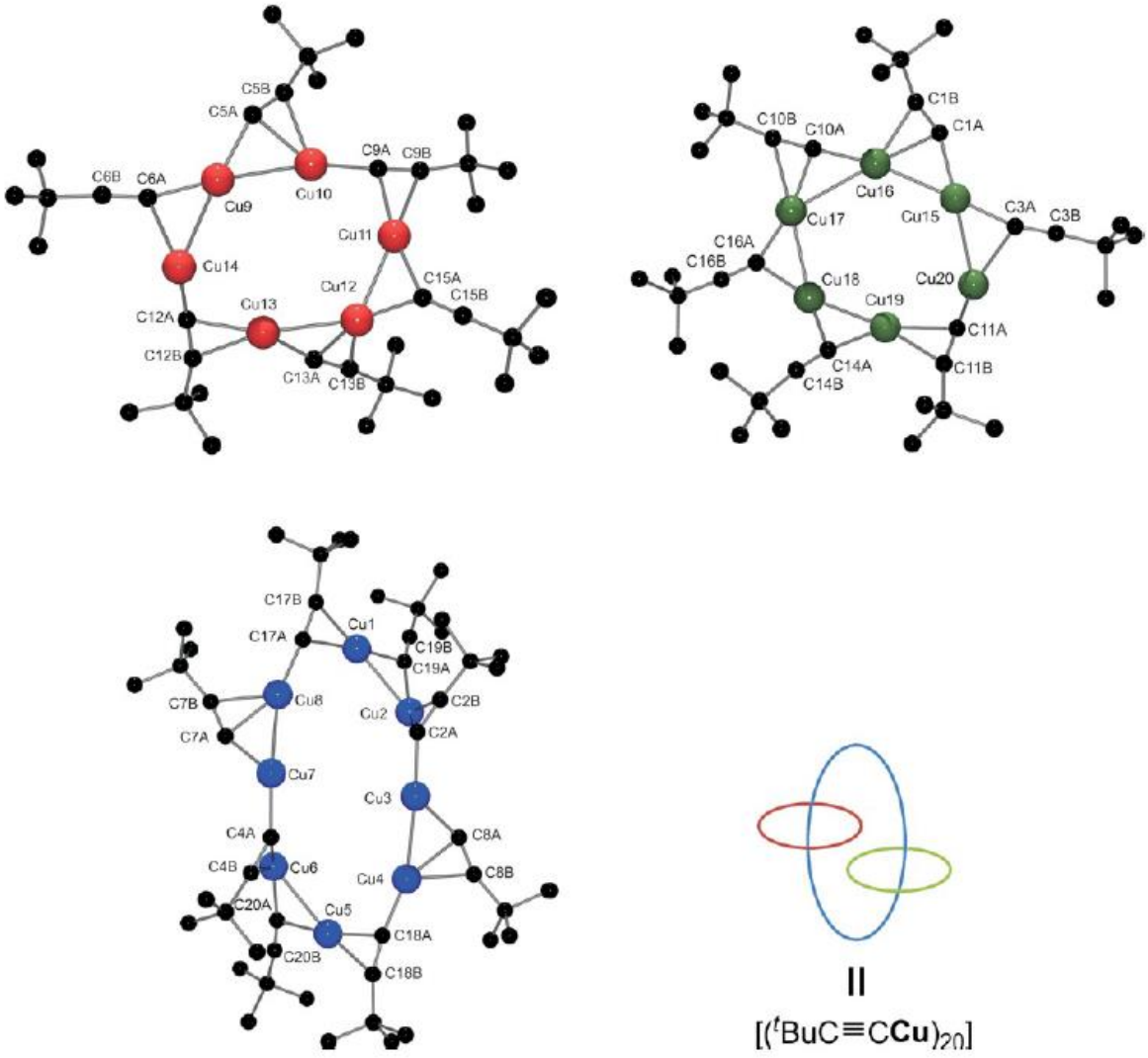

Figure 7: Crystal structure of (*tert*-butinyl)copper(I) published by *Lang et al.*.[74] The three different rings are coordinated as it is shown at the right bottom. Cu is represented by blue, green and red dots. Carbon atoms are black dots.

A structure for (phenylethynyl)copper(I) (PEC, $(CuC{\equiv}CPh)_x$) assumed by *Garbuzova et al* consists of an infinite rectangular tube of Cu atoms. The PhC≡C-groups are located outside the tube and are σ-bonded to one Cu atom. Additionally, they form π-bonds to Cu atoms surrounding them (see Figure 8a).[75] *Chui et al*. published a very similar structure of the same compound.[76] A general structure for Cu(I) acetylide was proposed by *Sladkov et al.* containing coordination polymers in which each copper atom is π-bounded to two acetylene unites, decreasing the order of the C≡C bond (see Figure 8b).[69]

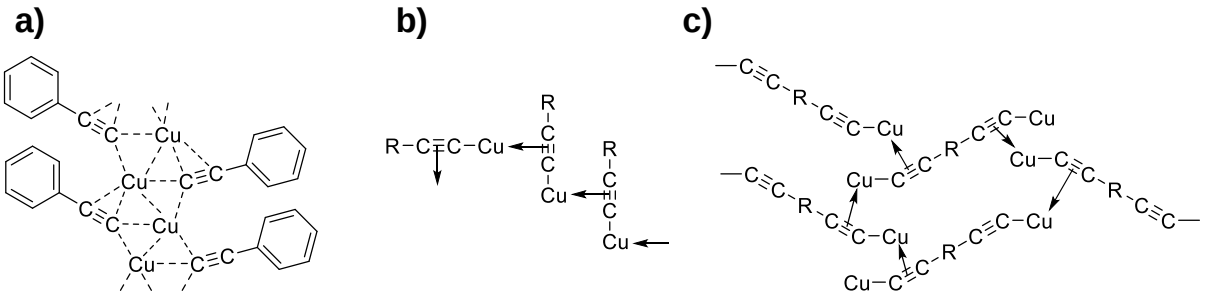

Figure 8: Proposed structures of different Cu acetylides or polyynides: a) structure of (phenylethynyl)copper(I) (PEC, $(CuC{\equiv}CPh)_x$), b) general structure of Cu acetylides, R = Cu, H, organic group[69], c) Cu polyynide, R = polyene segment of any length[77].

Furthermore, investigations by *Cataldo et al.* showed that transitions in the electronic spectrum of Cu_2C_2 are similar to the transitions obtained for Cu aryl or alkyl acetylides (e.g. PEC). Hence, they proposed that the structure of Cu_2C_2 is very similar to them and it is a polymeric coordination compound like the structures depicted in Figure 8a and b.[78]

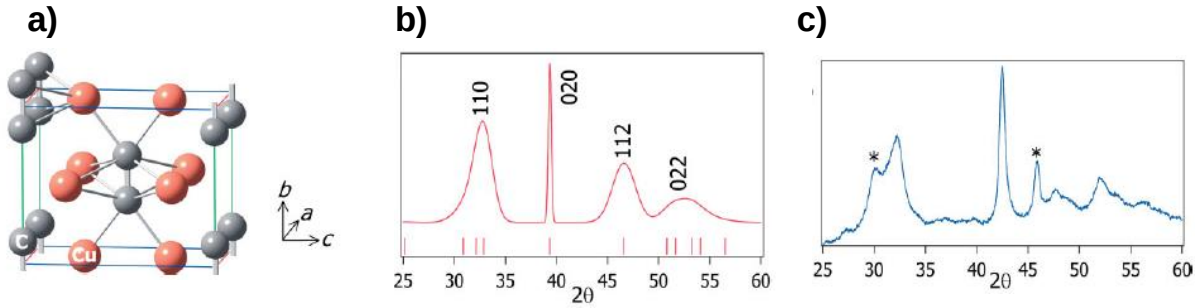

Figure 9: a) Structure of lowest energy of Cu_2C_2 via DFT based on crystal structures of alkali metal acetylide compounds, b) calculated powder diffractogram, c) measured powder diffractogram. All figures were published by *Judai et al*.[79]

Additionally, *Judai et al.* calculated the structure of lowest energy of Cu_2C_2 via DFT based on crystal structures reported for alkaline metal acetylide compounds (see Figure 9a). They also determined the theoretical powder diffractogram of their calculated Cu_2C_2 structure and compared it to the measured one (see Figure 9b and c). Their supposed structure consists of a C_2-unit with a bond distance between 1.29 Å, which lies between a triple and a double bond. Four end-on coordinated Cu atoms and four side-on coordinated Cu atoms surround the C_2-unit. The Cu atoms itself are enclosed equivalently by C atoms.[79] This structure is similar to the structure of Li_2C_2.[80]

In presence of oxidants, Cu_2C_2 reacts in *Glaser* coupling reactions to Cu polyynides. Polyynides can be described as chains of *sp*-hybridised carbon atoms with metals replacing the terminal hydrogen atom (see Figure 6). *Cataldo et al.* proposed a structure of these polyynides (see Figure 8c). The structure is very similar to the structure suggested from *Sladkov et al.* (see Figure 8b).[69, 77, 81]

In conclusion, the structure of Cu_2C_2 is very complex and most likely consists of different coordination polymers, which are connected mainly by π-bonds.

2.2.3 Recent developments

The ethynylation of formaldehyde with acetylene has been applied on industrial scale since the middle of the 20th century.[9, 10, 27-30] Therefore, it is of great interest to study the reaction in more detail to improve the process and for the development of new catalysts. Hence, many scientists have investigated the reaction since then. In this part, the most important outcomes are presented. At the beginning of the investigations, mainly kinetic aspects were examined. It changed a little in recent years and the role of the catalyst components were studied more detailed.

In the fifties of the 20th century *Kiyama et al.* published several works concerning the ethynylation. They used Cu/Bi catalysts and a stationary reactor system. Their main focus was to study the influence of several reaction parameters like pH value, temperature, pressure, formaldehyde concentration and methanol content (methanol is added to prevent formaldehyde polymerization[82, 83]). They found out that with increasing temperature the formaldehyde conversion rises linearly and consequently the yields of 1,4-butynediol and propargyl alcohol increase as well. Higher pressures lead to higher selectivity to propargyl alcohol. The formaldehyde conversion is independent on the pressure. A higher formaldehyde concentration at the beginning of the reaction leads to higher 1,4-butynediol and propargyl alcohol yield. However, the methanol content influences this effect and hence the higher product yields do not increase linearly. If the methanol concentration is increased, the formaldehyde conversion is lowered. According to the authors, the influence of the pH value is not trivial. However, with decreasing pH value the propargyl alcohol formation increases. They determined the order of reaction as zero order based on formaldehyde. The activation energy for formaldehyde adsorption is 50.21 kJ, for 1,4-butynediol formation 20.92 kJ and for propargyl alcohol formation 33.47 kJ. The high activation energy of formaldehyde is caused by depolymerization of formaldehyde agglomerates or even paraformaldehyde and hence this step is rate determining. With the kinetic data, *Kiyama et al.* postulated a reaction mechanism. Acetylene and Cu form copper(I) acetylide which can be converted to propargyl alcohol by the reaction with adsorbed formaldehyde. Propargyl alcohol desorbs and adsorbs at free and active copper centers again where it reacts with another formaldehyde molecule to 1,4-butynediol. The propargyl alcohol concentration increase and hence more propargyl alcohol molecules are adsorbed because the adsorptions constant of propargyl alcohol is smaller than of acetylene. The concentration of propargyl alcohol increases until the formation of propargyl alcohol and the further reaction to 1,4-butynediol are in equilibrium. To support the assumption that propargyl alcohol is an intermediate they carried out successfully the reaction of propargyl alcohol without the addition of acetylene. The order of reaction based on propargyl alcohol can be zero or first order depending on its concentration and hence the coverage of the active Cu centres.[84-86]

Suzuki et al. also investigated mainly the kinetics of the reaction but in the continuous process. They propose an order of reaction of one after 70 to 80 min reaction time and argue that compared to the stationary process a longer reaction period was observed. However, during the time before the order of reaction is zero. Additionally, they found out that the activation energy of formaldehyde is lower and that the formaldehyde conversion depends on the pressure. The group concludes that the diffusion of formaldehyde to the catalyst surface is the rate-limiting step. In another work, they investigated the solvent dependency of the stationary and the continuous process. The solvent has a great influence on the selectivity. A formaldehyde/tetrahydrofuran 1:2 ratio leads to the highest propargyl alcohol selectivity in both processes. Due to the fact that in the continuous process lower pressures and temperature are applied the selectivity to 1,4-butynediol is very high.[87, 88]

Later in the eighties of the 20th century, *Kale et al.* investigated the ethynylation of formaldehyde using pure copper acetylide as catalyst and a batch reactor (stationary system). Like *Kiyama et al.* they propose that the order of reaction is zero based on acetylene and 0.4 based on formaldehyde applying a Langmuir-Hinshelwood-model at pressures smaller 0.3 bar. In addition, they found out that a high 1,4-butynediol concentration lead to blocking of some active sites and the formaldehyde conversion is hindered.[89]

Gupte et al. was one of the first who investigated the influence of the catalysts itself by applying different Cu catalysts. It turned out that the Cu(II)oxide catalysts exhibit the highest activity. The calculated order of reactions are not integer (based on formaldehyde: 0.58, based on acetylene: 0.41) which is similar to the results obtained by *Kale et al..*[90]

Chang et al. also investigated the kinetics of the ethynylation of formaldehyde. They used an impregnated Cu/Bi catalyst which is supported on magnesium silicate. The catalyst system is like the systems that are applied nowadays. To avoid limitations concerning the gas entry they carried out experiments with different stirring rates. Only at stirrer rotations higher than 400 rpm the stirring rate do not influence the reaction anymore. For their kinetic models, they used a Langmuir-Hinshelwood-model like *Kale et al.* As well as *Kiyama et al.* they calculated the activation energy and the value of 51.88 kJ/mol is in good agreement.[91]

Chu et al. investigated the same catalysts as *Chang et al* did but they used a continuous reactor system. They confirmed the results concerning the stirring rates. They also applied a Langmuir-Hinshelwood-model for their kinetic examinations. It turned out that the rate-determining step is the reaction of an adsorbed formaldehyde molecule with an adsorbed acetylene molecule. The activation energy is 105 kJ/mol and the adsorptions heats are -57.4 kJ/mol for acetylene and -82.3 kJ/mol for formaldehyde respectively.[92]

Nowadays the focus of the research changed and some works were published regarding the role of the catalyst components. Especially groups from China are active in this field because the main industrial application of the ethynylation of formaldehyde is located there. *Gao et al.*

investigated the influence of chloride on the ethynylation with chloride doped Cu_2O nanoparticles. It turned out that Cl^- decreases the amount of adsorbed oxygen and hence strengthens the Cu-O bond. Compared to undoped Cu_2O nanoparticles less Cu metal was formed during reduction. Cu metal leads to the creation of polyacetylene and consequently to a decrease of active Cu(I) centres and lower catalytic performance.[66]

Li et al. examined the structure-activity relationship between the Cu species and its catalytic performance in the ethynylation of formaldehyde by applying different catalyst preparation methods. They found out that CuO particles with less support interactions are transformed rapidly into Cu(I) acetylide, which reflects in the performances of the catalysts. In addition they also stated that the catalysts deactivate over time caused by loss of catalyst.[93]

Because in industrial Cu/Bi catalysts often magnesium silicate is used as support *Wang et al.* investigated the influence of different Mg species on the ethynylation. Strong Si-O-Mg interactions are formed out of the SiO_2-MgO support. The Si-O-Mg species modifies the Cu dispersion as well as the reduction behavior of the Cu species. The addition of Mg leads to a change of the basicity of the surface of the catalysts. The group found out that basic sites improve the ≡C-H activation because of their enhanced deprotonation ability. The synergistic effect of Cu dispersion and ≡C-H activation leads to a significant increase of the catalyst performances. The incorporation of Al_2O_3 to get a more acidic support results in the formation of polyacetylene, which causes deactivation of the catalyst.[94, 95]

In another work, *Wang et al.* examined the interaction of Cu and Bi at different calcination temperatures. Higher calcination temperatures lead to the formation strong Bi_2O_3 and CuO interactions which enhance the stability of the Cu(I) oxidation state and to stabilization of the Cu dispersion. Besides strong Bi_2O_3-CuO interactions a $CuBi_2O_4$ spinel is formed at higher calcination temperatures (>600°C) as well. It results in maintaining the catalytic stability by continuous release of Cu to form the active cuprous species over multiple reaction cycles. In addition, the group found a linear dependency of the catalytic performance on the Cu(I) surface area. They conclude that Cu(I) is the active species in the ethynylation reaction.[96]

Yang et al. investigated the promotion effect of Bi by applying different Cu/Bi/MCM-41 catalysts. They stated that the addition of Bi reduces the CuO particle sizes and enhances the CuO dispersion. In addition, Bi weakens the interaction between CuO and the support which leads to a better reducibility of Cu(II) to Cu(I).[97, 98]

In summary, many studies were carried out to investigate the kinetics of the ethynylation reaction of formaldehyde and which parameters affect the reaction. In addition, the role of different catalyst components of Cu/Bi catalysts is well investigated. However, in most studies the catalysts were characterized before or after the catalytic reaction. Hence, there is a lack of information about what happens during the catalytic reaction and especially during the activation of the catalyst and about how the catalytic active species is formed.

2.3 . Motivation

The investigation of copper(I) acetylide, Cu_2C_2, which is supposed to be the active species in ethynylation reactions based on acetylene and its formation during the activation of CuO/Bi_2O_3 catalysts is very challenging due to the instability of this compound as well as the limitations concerning the analytical tools, which can be applied. The catalytic reaction is carried out in a water-formaldehyde solution with a solid catalyst and gaseous C_2H_2. In addition, pure Cu_2C_2 is only stable under wet conditions. Hence, characterization methods are necessary, which work with suspensions or wet samples. Nevertheless, aim of this work is to get new insights regarding the Cu_2C_2 formation during the activation of supported CuO/Bi_2O_3 catalysts.

For all measurements pure or SiO_2 supported Cu_2C_2 or industrial like SiO_2 or Al_2O_3 supported Cu/Bi catalysts are used. With these catalysts the reduction behavior of Cu(II) to Cu(I) is investigated and what compound acts as reducing agent. In addition, the formation of Cu_2C_2 is investigated by Raman spectroscopy and X-Ray diffraction during the activation. Furthermore, leaching experiments are carried out to investigate if Cu_2C_2 is formed on the catalyst surface or in solution via a leaching mechanism. TGA is performed to quantify the formed amount of Cu_2C_2. The standard activation/catalytic test is carried out in three-neck-vessels with 100 mL formaldehyde solution stabilized by methanol and 5 g catalyst. The reaction conditions are depicted in Figure 4 and the products are analyzed by gas chromatography.

2.4 Results and Discussion

First, the results concerning the investigation of the active species Cu_2C_2 are presented and discussed which are obtained by using SiO_2 supported or pure Cu_2C_2 and SiO_2 supported Cu/Bi catalysts. The results obtained by applying Al_2O_3 supported Cu/Bi catalysts are shown and discussed afterwards.

2.4.1 Investigations concerning the active species using Cu_2C_2 based and SiO_2 supported Cu/Bi catalysts

In this part the synthesis and characterization of the catalysts is presented. The catalysts are characterized before, during and after the catalytic reaction by different analytical tools like Raman spectroscopy, X-Ray diffraction (XRD) or thermo gravimetric analysis (TGA). The Cu content in solution and of the catalysts itself is determined by elemental analysis via ICP-OES.

2.4.1.1 Synthesis and characterization of the catalysts

SiO_2 supported Cu/Bi catalysts

SiO_2 supported Cu/Bi catalysts are prepared by a co-precipitation procedure with $Cu(NO_3)_2 \cdot 3\ H_2O$, Bi_2O_3 (dissolved in concentrated HNO_3) and Na_2SiO_3 as raw materials.[99] Catalysts with different Cu and Bi loadings between 5 to 35 wt.% Cu and 0.6 to 4 wt.% Bi are prepared. The Cu to Bi ratio is constant. The standard loading of industrial like catalysts is 30-60 wt.% Cu and 2-4 wt.% Bi catalysts.[11-13] The standard loading of catalysts used for this work are 35 wt.% for Cu and 4 wt.% for Bi. After the precipitation, the catalysts are washed and dried at 80°C. Afterwards the catalysts with standard loadings are calcined at different temperatures (450°C, 600°C, 700°C). For simplification, the catalysts are labelled as follows: CuxBiy-z (x = Cu loading in wt.%, y = Bi loading in wt.%, z = calcination temperature, see Table 1). The standard calcination temperature is 450°C if the calcination temperature is not noted.

The powder diffractograms of Cu35Bi4-80, Cu35Bi4-450, Cu35Bi4-600 and Cu35Bi4-700 are shown in Figure 10A. The sample, that is just dried at 80 °C (Cu35Bi4-80), consists of basic copper nitrate ($Cu_2NO_3(OH)_3$) which is the main product of the co-precipitation. The calcined samples contain CuO whereby (Cu35Bi4-700) shows the narrowest reflexes. In Table 2, the crystallite sizes are summarized calculated with the Scherrer equation.[100-104] The reflexes at 12.8 2θ and 25.7 2θ of Cu35Bi4-80 and the reflexes at 35.4 2θ and 38.7 2θ of the calcined samples (Cu35Bi4-450, Cu35Bi4-600, Cu35Bi4-700) serve for the determination of the crystallite sizes. After drying, the crystallite size is around 43 nm (Cu35Bi4-80). During the calcination at 450°C and 600°C the crystallite size decreases to around 15 nm (Cu35Bi4-450, Cu35Bi4-600). Calcination at 700°C leads to larger crystallites of around 20 nm (Cu35Bi4-700) which is most likely caused by sintering of the CuO particles.

The powder diffractograms for the catalysts with different Cu and Bi loadings (Cu35Bi4, Cu25Bi2.9, Cu15Bi1.7 and Cu5Bi0.6) are shown in Figure 10B.

Table 1: Abbreviations of the different SiO_2 supported catalysts and the declaration of the different numbers CuxBiy-z (x = desired Cu loading in wt.%, y = desired Bi loading in wt.%, z = calcination temperature). Cu^a = Cu loading in wt.% and Bi^b = Bi loading in wt.%. T_{calc} = calcination temperature in °C.

Abbreviation	Cu^a	Bi^b	T_{calc}
Cu5Bi0.6	5	0.6	450
Cu15Bi1.7	15	1.7	450
Cu25Bi2.9	25	2.9	450
Cu35Bi4/Cu35Bi4-450	35	4.0	450
Cu35Bi4-80	35	4.0	only dried
Cu35Bi4-600	35	4.0	600
Cu35Bi4-700	35	4.0	700

Because all the catalysts are calcined at 450°C, the calcination temperature is not noted in the catalyst labels. Cu25Bi2.9, Cu15Bi1.7 and Cu5Bi0.6 nearly solely consist of amorphous structures except very broad reflexes of the SiO_2 support. The sample containing 25 wt.% Cu shows a very broad reflex at around 35 to 40 2θ which refers to CuO. Only at Cu loading of 35 wt.%, narrow CuO reflexes are observable (Cu35Bi4). Due to the amorphous structure of the samples with lower Cu loadings, it is not possible to determine the CuO crystallite sizes of these catalysts.

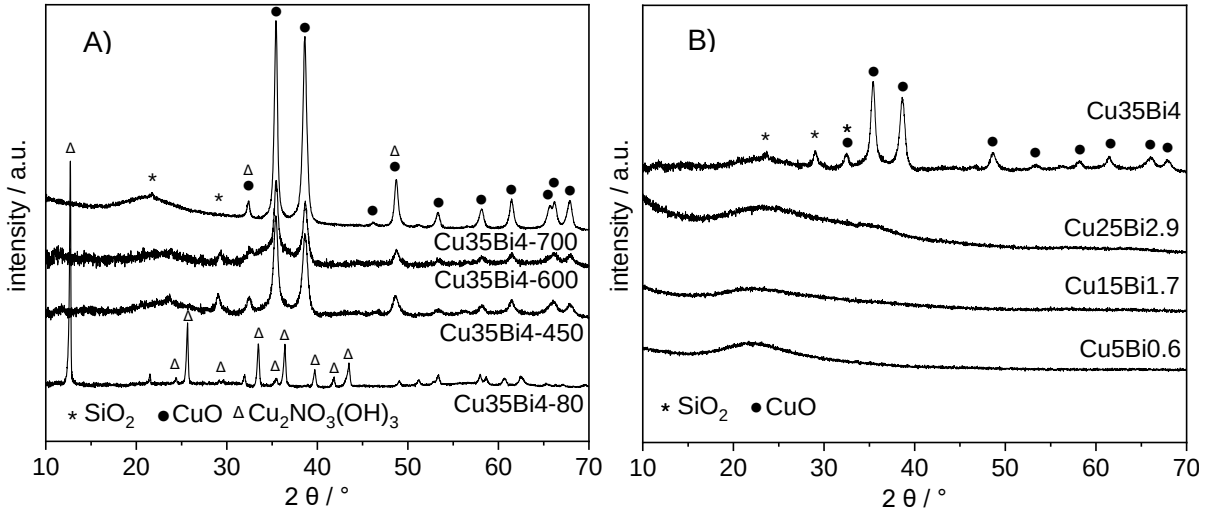

Figure 10: (A) Powder diffractograms of Cu35Bi4-80, Cu35Bi4-450, Cu35Bi4-600 and Cu35Bi4-700. (B) Powder diffractograms of Cu35Bi4, Cu25Bi2.9, Cu15Bi1.7 and Cu5Bi0.6. $Cu_2NO_3(OH)_3$ (triangles)[105], CuO (black dots)[106] and SiO_2 (stars)[107] serve as reference. The samples are calcined for 4 h with a heating rate of 2.5 K/min in air. Diffractograms are recorded in an angle range between 5° and 70° in steps of 0.013°.

In addition to X-Ray diffraction, the catalysts calcined at different temperatures are characterized by Raman spectroscopy due to the surface sensitivity of this method. This is important

especially for measurements, which are performed later of catalysts separated during the catalytic reaction. In Figure 11, the Raman spectra of Cu35Bi4-80, Cu35Bi4-450 and Cu35Bi4-700 are shown.

Table 2: BET surface area (SA_{BET}) in m_2/g, pore volume (V_{pore}) in cc/g and pore radius (r_{pore}) in nm of the catalysts. The error is estimated to be between 5-10%.[108-110] Cu (Cu^a) and Bi (Bi^b) loadings in wt.% determined by ICP-OES. The error is determined to be around 5% including the preparation and the ICP-OES measurement itself. Crystallite sizes ($Size_{crys}$) calculated with the Scherrer equation of Cu35Bi4-80, Cu35Bi4-450, Cu35Bi4-600 and Cu35Bi4-700. The reflexes at 12.8 2θ and 25.7 2θ of Cu35Bi4-80 and the reflexes at 35.4 2θ and 38.7 2θ of the calcined samples (Cu35Bi4-450, Cu35Bi4-600, Cu35Bi4-700) serve for the determination of the crystallite sizes (see Figure 10A).

Sample	SA_{BET}	V_{pore}	r_{pore}	Cu^a	Bi^b	$Size_{crys}$
Cu5Bi0.6	140	0.52	1.69	5.9	0.6	-
Cu15Bi1.7	190	0.69	1.79	15.5	1.5	-
Cu25Bi2.9	132	0.45	1.69	24.4	2.9	-
Cu35Bi4/Cu35Bi4-450	115	0.24	1.88	35.3	4.1	14.1 ± 1.3
Cu35Bi4-80	171	0.49	1.69	33.3	4.4	43.2 ± 3.1
Cu35Bi4-600	75	0.25	1.90	33.4	4.2	15.4 ± 1.3
Cu35Bi4-700	25	0.12	1.69	35.3	4.6	20.2 ± 2.0

The spectra of the calcined (Cu35Bi4-450, Cu35Bi4-700) samples fit well with the CuO reference spectrum, especially the signals at 298 cm^{-1} and 607 cm^{-1}. Also, the signals of Cu35Bi4-80 match to the signals of the $Cu_2NO_3(OH)_3$ reference. Particularly the three signals between 415 and 513 cm^{-1} and the signal at 1051 cm^{-1} are in good accordance with the reference signals. Both reference spectra are taken from the RRUFF database.[111] The mineral tenorite serves as CuO reference and the mineral rouaite as $Cu_2NO_3(OH)_3$ reference.

The surface area as well as the mean pore size and the mean pore volume are determined by N_2 physisorption (BJH/BET method). All values are summarized in Table 2. The BET surface area increases with increasing Cu content to a maximum of 190 m^2/g for 15 wt.% Cu. Higher Cu loadings lead to a decrease of the BET surface area (see Cu35Bi4, Cu25Bi2.9). In addition, higher calcination temperatures reduce the BET surface area (171 m^2/g for Cu35Bi4-80 to 25 m^2/g for Cu35Bi4-700). It is caused by pore blocking through larger CuO particles and by disruption of the porous SiO_2 structure. The pore volume increases or decreases in the same course as the surface area while the pore radii remain more or less constant.

The Cu and Bi loadings are determined by elemental analysis via ICP-OES. The results are summarized in Table 2. The Cu and Bi loadings fit well with the aimed loadings meaning that the co-precipitation method is reliable. The Cu loading is partly lower than the desired value. This could be the consequence of the sample preparation for the ICP-OES measurements. The SiO_2 support does not dissolve by the addition of phosphoric acid (dissolution of CuO and Bi_2O_3) and heating at 90°C. CuO and Bi_2O_3 are dissolved out of the support. Hence, some

strongly incorporated CuO could remain in the SiO_2 support and the Cu value obtained by ICP-OES seems to be slightly lower.

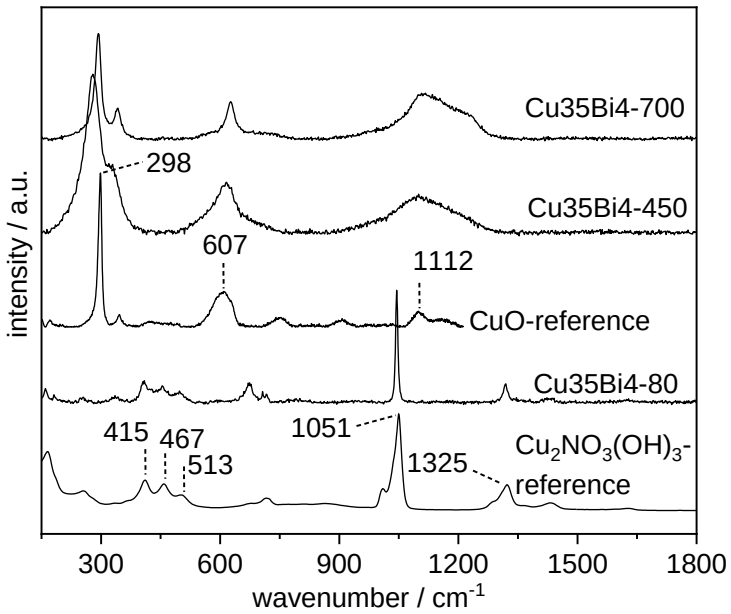

Figure 11: Raman spectra of Cu35Bi4-80, Cu35Bi4-450, Cu35Bi4-600 and Cu35Bi4-700 in the range from 150 cm^{-1} to 1800 cm^{-1}. The reference spectra are taken from the RRUFF database.[111] The laser intensity is 0.015 mW and the wavelength of the laser is 532 nm. An objective with 50x magnification is used. The standard scanning time is 5 sec with 10 repetitions. The samples are calcined for 4 h with a heating rate of 2.5 K/min in air.

Copper(I) acetylide based catalysts

Besides industrial like Cu/Bi catalysts, pure Cu(I) acetylide (Cu_2C_2) is synthesized and characterized to get information about its structure. The synthesis is carried out under inert conditions by purging the flask with nitrogen before introducing acetylene. It should prevent that acetylene can mix with oxygen from air to form an explosive atmosphere. An ammoniacal Cu(I) solution is used as Cu source. Acetylene is passed over the solution, so it can dissolve in the Cu(I) solution. Red to brownish solid is formed directly. After purging with nitrogen again, the solid is washed with water to get rid of the ammoniacal solution. The wet solid is directly transferred into the flask where the catalysis is carried out or is used for further analysis. In the case of SiO_2 supported Cu_2C_2 SiO_2 support is added to the ammoniacal Cu(I) solution.

Cu_2C_2 was not characterized extensively so far. However, the characterization would help to understand how the active species is formed during the activation of solid CuO based catalysts. It must be considered that characterization of Cu_2C_2 is challenging due to its explosive properties when it is dry. That is the reason why characterization techniques are necessary by which it is possible to work under moist conditions for example Cu_2C_2 suspended in H_2O. Raman spectroscopy is a technique that fulfills all the demands. In addition, it has the advantage compared to IR spectroscopy that the main signals of H_2O arise between 3000 and 3500 cm^{-1}. Hence, the signals of C-C- and C-H-bonds are not influenced or overlapped by the H_2O signals.

Furthermore, we found out that SiO_2 supported Cu_2C_2 as well as spent catalysts are more stable at dry conditions and it is possible to characterize them in powdered form. For powdered samples, Raman spectroscopy is a suitable characterization technique as well.

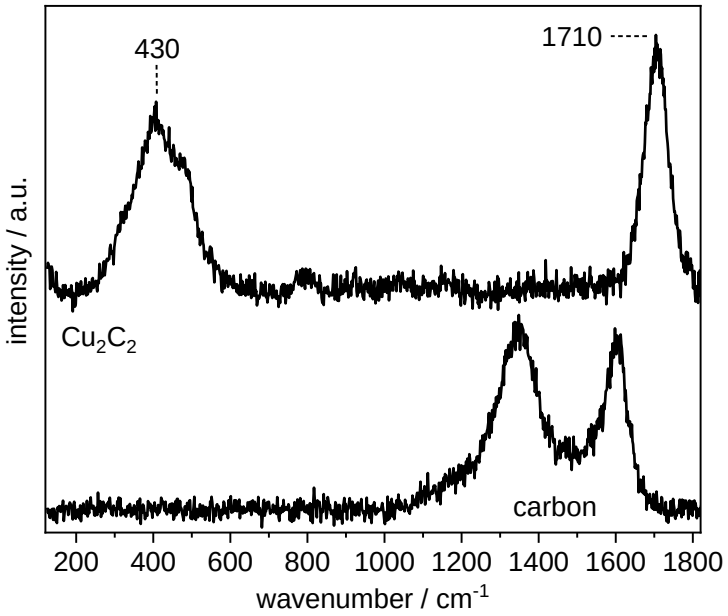

Figure 12: Raman spectrum of freshly prepared Cu_2C_2 in the range from 115 cm^{-1} to 1880 cm^{-1}. For illustration, a carbon reference (activated charcoal from FLUKA) spectrum is shown with the typical G-peak (1350 cm^{-1}) and D-peak (1600 cm^{-1}).[112] Cu_2C_2 is measured in wet state due to safety issues. The laser intensity is 0.015 mW and the wavelength of the laser 532 nm. An objective with 50x magnification is used. The standard scanning time is 5 sec with 10 repetitions.

In Figure 12, the Raman spectrum of freshly prepared Cu_2C_2 is shown to get information about the character of the Cu-C bond and the C≡C bond. The Raman spectrum of carbon is also depicted for illustration. The carbon spectrum shows the typical peak at 1350cm^{-1} (D-peak) and at 1600 cm^{-1} (G-peak).[112] The D-peak is referred to ordered graphite like structures whereas the G-peak is assigned to disordered structures.[112] The Cu_2C_2 spectrum was recorded of Cu_2C_2 suspended in H_2O. Signals arise at 430 cm^{-1} including a shoulder at higher wavenumbers and at 1710 cm^{-1}. The signal at 430 cm^{-1} corresponds to the Cu-C bond. *Garbuzova et al.* and *Aleksanyan et al*. indicate the same wavenumber for the Cu-C σ-bond in other copper(I) acetylide compounds for example (phenylethynyl)copper(I) (PEC, $(CuC{\equiv}CPh)_x$).[75, 113] The signal at 1710 cm^{-1} corresponds to the C≡C bond. It is unusual that a triple bond appears at such small wavenumbers because the C≡C bond is normally located at 2100 cm^{-1}. But *Aleksanyan et al.* found out during the investigation of other copper(I) acetylide compounds that the frequencies of C≡C bonds are lower on average by 180 – 200 cm^{-1} compared to the corresponding alkyne precursor molecules.[113] *Sladkov et al.* propose that the C≡C bond in copper(I) acetylide compounds can be shifted towards lower frequencies by 300 cm^{-1} because of the decreasing order of the C≡C bond.[69]

The difference of the copper (I) acetylide compounds investigated by *Aleksanyan et al.* and *Sladkov et al.* to Cu_2C_2 is that only one side of the triple bond is substituted by copper. If the other carbon atom of the triple bond also bonds to copper, it is expected that the frequency of the C≡C bond further decreases, which fits well with the measured signal at 1710 cm^{-1}. It is important to measure Raman spectra at very low laser intensities because Cu_2C_2 is a very unstable compound towards radiation and it is decomposed easily forming carbon. It will be discussed later in more detail.

Besides the characterization of Cu_2C_2 by Raman spectroscopy, it is possible to measure X-Ray powder diffraction because Cu_2C_2 contains crystalline phases.[79, 114, 115] In Figure 13 the powder diffractogram of pure Cu_2C_2 is depicted. The powder diffractogram was measured of moist Cu_2C_2 directly after preparation. The pattern obtained for the freshly prepared Cu_2C_2 matches well with the pattern published by *Judai et al*. (see chapter 2.2.2).[79]

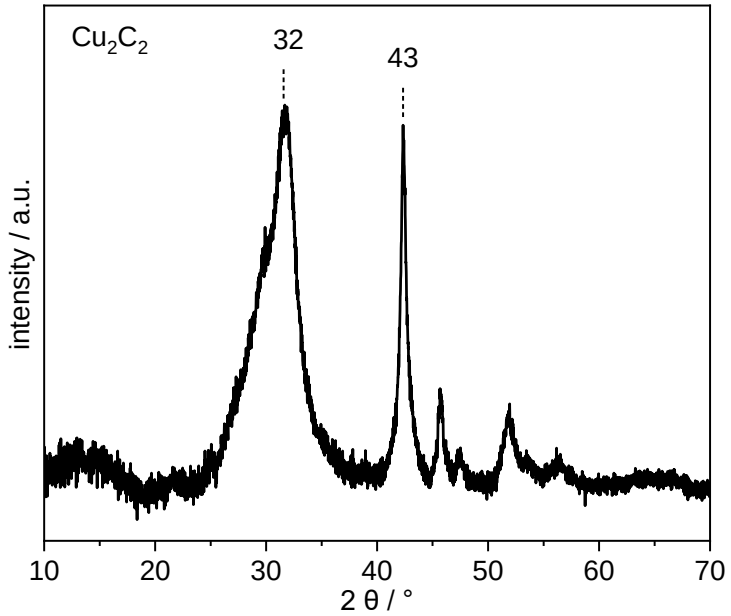

Figure 13: Powder diffractogram of freshly prepared Cu_2C_2. The diffractogram is recorded in an angle range between 5° and 70° in steps of 0.013°. Cu_2C_2 is moistened with H_2O.

They proposed a polymeric coordination compound consisting of C_2-units with end-on and side-on bounded Cu atoms.[79] Other groups published similar structures (see chapter 2.2.2).

The proposed structures of Cu_2C_2 in literature match well with the results obtained by Raman and by X-Ray diffraction in this work. The signal at 1710 cm^{-1} corresponds to the C_2-building block representing the triple bond with decreased order caused by the π-bonded Cu atoms and by the σ-Cu-C≡-bond. The very broad signal at 430 cm^{-1} corresponds to the σ-Cu-C-bond. Furthermore, the broadness of the signal including the shoulder is caused by the variation of differently weak π-bonds between Cu and the triple bonds or just by coordination between both.

Besides the characterization, the amount of formed Cu_2C_2 is analyzed, too. Thermogravimetric analysis (TG) is used to quantify the formation of Cu_2C_2 because the decomposition of Cu_2C_2 in an oxygen containing atmosphere leads to different decomposition reactions (see Scheme 1) and consequently to mass changes of the sample.[116, 117] The initial Cu_2C_2 amount can be calculated based on the mass change.

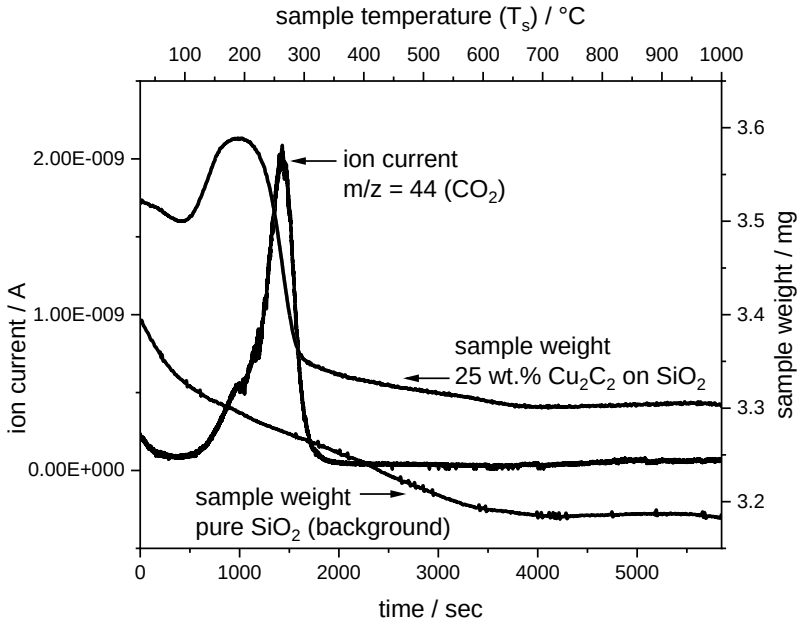

Figure 14: Quantification of formed Cu_2C_2 by TG. The dependency of the sample weight on the sample temperature of freshly prepared SiO_2 supported Cu_2C_2 (25 wt.%) and of a pure SiO_2 reference sample (background) are shown. The sample is heated to 1000°C under synthetic air at a rate of 10 K/min. Additionally, the measured ion current for m/z = 44 (CO_2) obtained by MS is depicted.

Three SiO_2 supported Cu_2C_2 samples with different loadings (5 wt.%, 15 wt.%, 25wt.%) are synthesized to evaluate the reliability of the method. The samples are heated to 1000°C with 5 K/min in synthetic air. The gas phase is analyzed using a mass spectrometer. The sample temperature, the sample weight, the ion current for m/z = 44 (CO_2) and the reaction time for the 25 wt.% Cu_2C_2 on SiO_2 as well as for a pure SiO_2 reference sample (background) is depicted in Figure 14.

$$Cu_2C_2 \longrightarrow Cu + C \xrightarrow{O_2} CuO + C \xrightarrow{O_2} CO_2$$

Scheme 1: Proposed reactions occurring during the thermal decomposition in air of Cu_2C_2 supported on SiO_2.[116]

At around 100°C the sample mass increases. It is related to the decomposition of Cu_2C_2 into Cu and C and the simultaneous oxidation of Cu(I) to Cu(II)O. The decomposition temperature of Cu_2C_2 into Cu and C is indicated at 127°C under inert conditions by *Cataldo et al.* and at 131 to 183°C in air by *Klement et al.*.[115, 116] The decomposition of Cu_2C_2 into CuO and C is

also described by *Cataldo et al.*[116] After the formation of CuO, C is oxidized to CO_2. Consequently, the sample weight decreases. The formation of CO_2 is confirmed using a mass spectrometer (m/z = 44, black line in Figure 14). The formation of CO_2 takes place at the same time as the sample weight decreases. A slight decrease of the sample weight over the whole temperature treatment is caused by desorption of surface species like water from the SiO_2 surface because the reference SiO_2 reference sample shows the same trend.

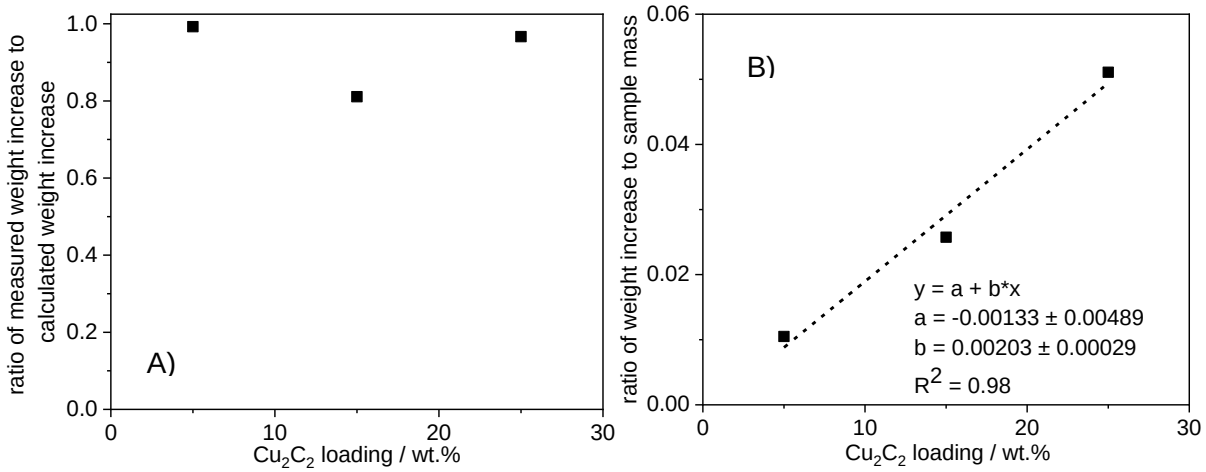

Figure 15: (A) Ratio of measured weight increase to calculated weight increase obtained by TGA for freshly prepared supported Cu_2C_2 on SiO_2 with different Cu_2C_2 loadings. (B) Ratio of weight increase to sample mass used for TGA for freshly prepared supported Cu_2C_2 on SiO_2 with different Cu_2C_2 loadings. The samples are heated to 1000°C under synthetic air at a rate of 10 K/min.

The mass increase or rather the oxidation of Cu(I) to Cu(II)O is used to calculate the amount of Cu_2C_2 of the prepared sample. In Figure 15A the ratio of the measured weight increase to the calculated weight increase are shown. For the 5 wt.% and the 25 wt.% Cu_2C_2 samples the ratio is almost 1. Only the 15 wt.% sample differs slightly with a value of 0.85.

In Figure 15B the ratio of the weight increases to the amount of sample used for the TG is depicted. The linearly dependency of the ratio to the Cu_2C_2 loading can be clearly figured out. Hence, the TG method is a suitable and reliable technique to determine the amount of formed Cu_2C_2. The TG measurements are carried out with supported Cu_2C_2 because of the explosive character of dry, pure Cu_2C_2 and to compare the results with supported Cu/Bi catalysts, which are described later.

2.4.1.2 Application of the catalysts in the ethynylation reaction

In industry, the catalytic reaction is carried out below 2 bar acetylene pressure and at temperatures between 85 to 120°C in batch reactors that are connected in series. The pH-value is adjusted to 4.5 to 7 either by the addition of a base or buffer solutions. The typical formaldehyde concentration is around 30 to 40 % of aqueous solution. The formalin solution is stabilized by methanol to prevent polymerization.[11-13] First, the CuO precursor must be activated with acetylene. It is industrially carried out either separately before the reaction or in situ during the

reaction by adding new catalyst precursor to the reaction slurry. In the case of separate activation, a typical activation time is 5 h. Then, the catalyst is filtered and added to a fresh formaldehyde solution.[11-13, 39]

Generally, the activation is not separated from the catalytic reaction because even during the activation both reactants are present and the same conditions are applied. Hence, 1,4-butynediol is formed during the activation of the catalyst as well. In principle, the activation can also be described as the first use of the catalyst.

For this work, the activation and reaction conditions are selected to be as equal as compared to the industrial process. Therefore, the activation and catalytic reaction of formaldehyde and acetylene to 1,4-butynediol is carried out at 100°C under slight pressure of acetylene (0.1 bar). Two catalysts can be tested simultaneously. The reaction setup is shown in Figure 108 in the experimental section (chapter 7). A $NaOH/NaH_2PO_4$ buffer was used to keep a constant pH-value of 7. The formaldehyde concentration is 37% at the beginning of the reaction. Methanol is added to simulate an industrial like formalin feed. Methanol is not converted during the reaction (see Figure 109A in section 0). The flask is purged with N_2 prior the addition of acetylene for avoiding contact with air. Different SiO_2 supported Cu/Bi catalysts as well as pure Cu_2C_2 are used as catalyst. In addition, some experiments are exemplarily carried out with Cu(I)-1-hydroxypropinid (acetylide based on propargyl alcohol, CuC_2CH_2OH) as catalyst.

Copper(I) acetylide, Cu_2C_2 – The active species in the ethynylation of formaldehyde

If copper(I) acetylide, Cu_2C_2, is just an reaction intermediate and therefore not the active species on which the catalytic reaction takes place it should be converted (stoichiometrically) with formaldehyde to 1,4-butynediol. In Figure 16, the yields of propargyl alcohol and 1,4-butynediol in the ethynylation reaction with formaldehyde in presence of Cu_2C_2 are shown.

Formaldehyde and Cu_2C_2 are not converted to either propargyl alcohol or 1,4-butynediol in the absence of acetylene (left part in Figure 16A). That means that Cu_2C_2 cannot be converted (stoichiometrically) to 1,4-butynediol. After the addition of acetylene 1,4-butynediol and propargyl alcohol are formed. Consequently, Cu_2C_2 is not an reaction intermediate but it acts as catalyst to catalyze the reaction of formaldehyde and acetylene to 1,4-butynediol (see Figure 17).

Furthermore, the addition of propargyl alcohol leads also to the formation of 1,4-butynediol using Cu_2C_2 as catalyst (see Figure 16B) confirming the proposal that Cu_2C_2 is the active species and that propargyl alcohol is an intermediate.[86-88] The 1,4-butynediol yield increase faster if acetylene is present. It is difficult to compare the different reaction rates (acetylene or propargyl alcohol as reactant) because acetylene is continuously available and whereas certain amounts of propargyl alcohol are added with syringe. Nevertheless, there are kinetic studies

regarding the ethynylation reaction. *Kiyama et al.* determined the order of reaction as zero order based on formaldehyde also studying a batch reaction.[84-86]

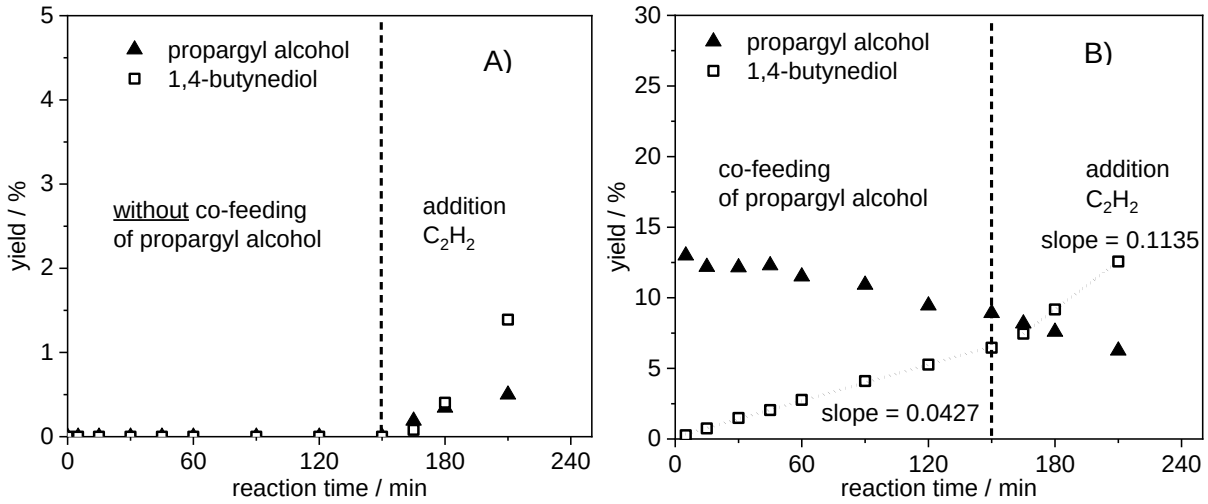

Figure 16: (A) Reaction of formaldehyde with pure Cu_2C_2 as catalysts and (B) reaction of formaldehyde and propargyl alcohol with pure Cu_2C_2 as catalyst. The reaction temperature is 100°C and the product analysis is done by GC. Acetylene pressure is 1.1 bar.

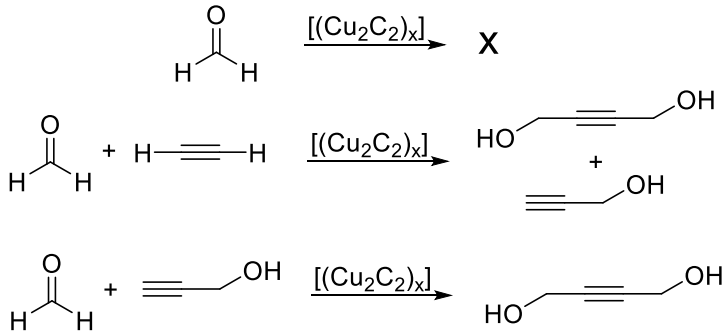

Figure 17: Reactions taking place during the catalytic ethynylation of formaldehyde. The reaction temperature is 100°C and the product analysis is done by GC. Acetylene pressure is 1.1 bar.

Another Cu(I) acetylide compound that could be formed during the reaction is Cu(I)-1-hydroxypropinid (acetylide based on propargyl alcohol, CuC_2CH_2OH). Hence, this acetylide compound could theoretically be the active species as well. From an experiment in which Cu(I)-1-hydroxypropinid is used as catalyst with propargyl alcohol and formaldehyde as reactants (without acetylene) can be concluded that this acetylide is also active as catalysts because 1,4-butynediol is formed (see Figure 18A). The same experiment is carried out without the addition of propargyl alcohol to check if CuC_2CH_2OH can be converted (stoichiometrically) to 1,4-butynediol (see Figure 18B). Interestingly instead of 1,4-butynediol propargyl alcohol is formed. It means that Cu(I)-1-hydroxypropinid is not stable if propargyl alcohol is not present. It decomposes and propargyl alcohol is released.

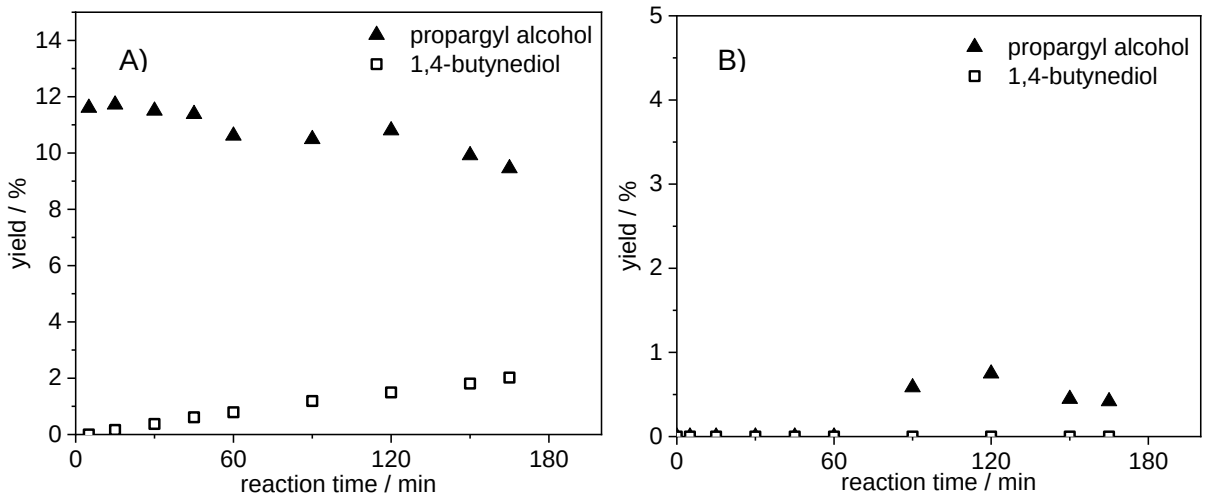

Figure 18: (A) Reaction of formaldehyde and propargyl alcohol with pure Cu(I)-1-hydroxypropinid as catalysts and (B) reaction of formaldehyde with Cu(I)-1-hydroxypropinid as catalyst as well. The reaction temperature is 100°C and the product analysis is done by GC. Acetylene pressure is 1.1 bar.

However, this is not a proof that propargyl alcohol is not the active species. Therefore, another experiment is carried out with Cu(I)-1-hydroxypropinid as catalyst and with formaldehyde and acetylene as reactants. Besides the product analysis via GC the catalyst itself is investigated by Raman spectroscopy (see Figure 19A and B). At the beginning during the N_2 purging period 1,4-butynediol is not formed, which is not surprising. After the addition of acetylene 1,4-butynediol arises and the yield increases linearly. The Raman spectrum of the catalysts before the addition of acetylene shows only signals for Cu(I)-1-hydroxypropinid comparing to the reference spectra (e.g., at 1916 cm^{-1}). However, already after 5 min after the addition of acetylene the signals decrease a lot and signals assigning to Cu_2C_2 appear (at 1710 cm^{-1}). It means that CuC_2CH_2OH is converted with acetylene to Cu_2C_2 under reaction conditions. Hence, CuC_2CH_2OH cannot be the catalytic active species that catalyzes the formation of 1,4-butynediol shown in Figure 19A but it is Cu_2C_2. It proves that under ethynylation reaction conditions Cu_2C_2 must be the active species.

To strengthen the findings an industrial like catalyst (Cu35Bi4-450) is investigated by doing a co-feeding experiment as well. The yields of propargyl alcohol and 1,4-butynediol are shown in Figure 20. During the N_2 purging period (getting rid of oxygen) any products are not formed because acetylene is not present. After the addition of acetylene, the catalyst is activated forming Cu_2C_2 and consequently propargyl alcohol and 1,4-butynediol are formed.

The propargyl alcohol yield is very low because it is an intermediate to form 1,4-butynediol. The selectivity is strongly shifted to the formation of 1,4-butynediol under these reaction conditions as mentioned before (see chapter 2.2.1).

Acetylene is replaced by nitrogen after 180 min again. The yields do not increase anymore. Although formaldehyde is still present Cu_2C_2 does not further react with formaldehyde to 1,4-butynediol or propargyl alcohol. This agrees with the results obtained with pure Cu_2C_2 as catalyst (see Figure 16). Cu_2C_2 cannot be converted (stoichiometrically) but acts as active species.

The addition of propargyl alcohol after 300 min leads to the formation of 1,4-butyndiol again and strengthens the finding that Cu_2C_2 is the active species in the ethynylation of formaldehyde.

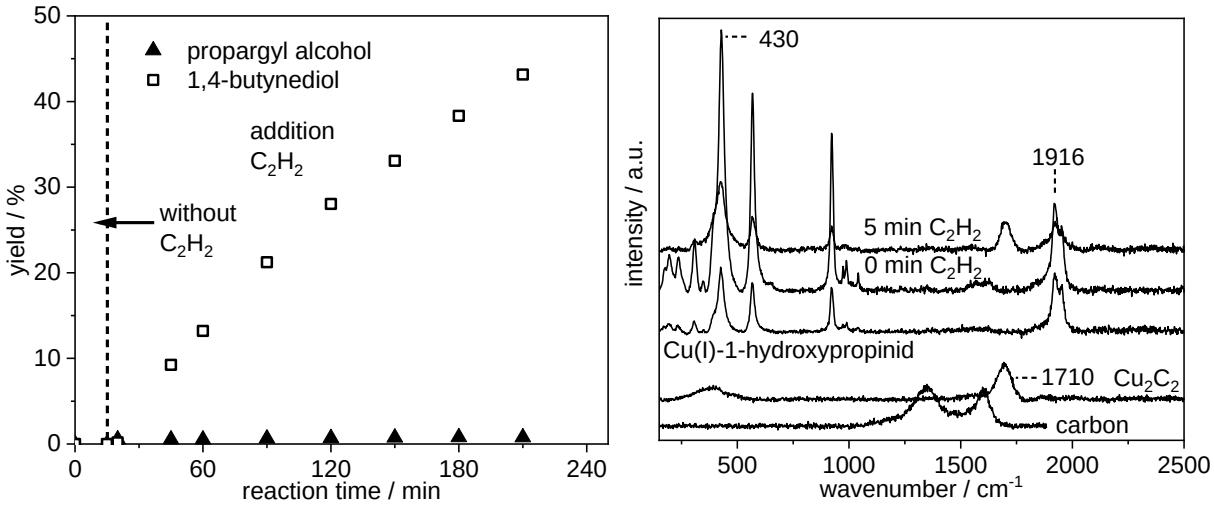

Figure 19: (A) Reaction of formaldehyde and acetylene with pure Cu(I)-1-hydroxypropinid as catalysts and (B) Raman spectra of the catalyst during the reaction. Carbon (activated charcoal from FLUKA with the typical G-peak (1350 cm^{-1}) and D-peak (1600 cm^{-1})[112], Cu_2C_2 and Cu(I)-1-hydroxypropinid serve as reference. The reaction temperature is 100°C and the product analysis is done by GC. Acetylene pressure is 1.1 bar. The laser intensity of the laser of the Raman spectrometer is 0.015 mW and the wavelength of the laser 532 nm. An objective with 50x magnification is used. The standard scanning time is 5 sec with 10 repetitions.

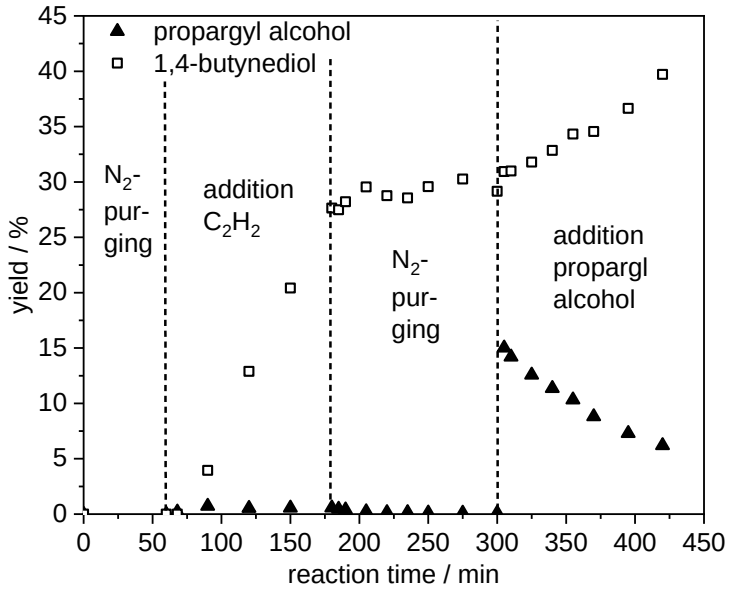

Figure 20: Ethynylation of formaldehyde with Cu35Bi4-450 as catalysts. The reaction temperature is 100°C and the product analysis is done by GC. Acetylene pressure is 1.1 bar.

Pre-reduction of Cu(II) – Formation of Cu_2C_2

In the pre-catalysts ($CuO/Bi_2O_3/SiO_2$) which are applied in the ethynylation of formaldehyde to 1,4-butynediol copper is present as CuO or $Cu_2NO_3(OH)_3$ depending on whether the pre-catalysts are just dried or calcined (see Figure 10). Therefore, it is necessary to reduce Cu(II) to

Cu(I) to form the Cu_2C_2 species (activation of the catalyst). According to literature, formaldehyde that is oxidized to formic acid acts as reducing agent (see Figure 5 in chapter 2.2.1). Simultaneously Cu(II) is reduced to Cu(I).[66]

In fact, there are no studies in which the reducing step is investigated in detail. Therefore, the reduction of Cu(II) to Cu(I) is investigated by EPR spectroscopy for this work. EPR spectroscopy has the advantage, that it is possible to determine the oxidation states of components in solutions, solids or even slurries. All samples that are measured are either aqueous solutions or slurries. Hence, all samples are recorded in frozen state at -120°C.

In first experiments, $CuCl_2$ is added to a formaldehyde solution at 25°C and 100°C (standard reaction temperature during catalysis) and the reaction is followed by EPR spectroscopy. Samples of the solution are taken after certain times and quenched in an ice bath. The same experiment is carried out with the difference that additionally acetylene is added.

In Figure 21, the EPR spectra of the reaction of $CuCl_2$ with formaldehyde are depicted. Cu(II) has a nuclear spin of I=3/2. Therefore, four signals should appear for the parallel and the vertical portion. If Cu(II) is reduced to Cu(I) the Cu(II) signals should disappear. Since Cu(I) is EPR inactive, no further signals should appear. It can be clearly seen in Figure 21A and B that in all spectra Cu(II) is present. The g-values of $g_{\parallel}$ (g_p) = 2.40823 and $g_{\perp}$ (g_v) = 2.07525 are in accordance with literature.[118, 119] The intensity of the signals do not decrease during the reaction either at 25°C nor at 100°C. Therefore, the reduction of Cu(II) to Cu (I) does not take place under these conditions and it cannot be confirmed that formaldehyde acts as reducing reagent.

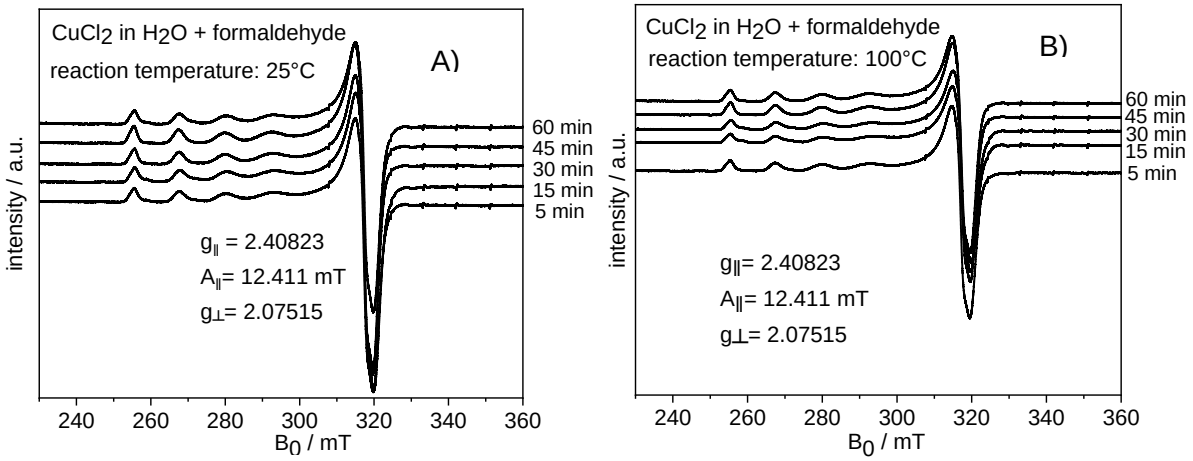

Figure 21: Anisotropic EPR spectra ($T_{recorded}$ = -120°C) of $CuCl_2$ in formaldehyde solution at 25 °C (A) and 100°C (B) for different reaction times. Samples are taken after different reaction times with a syringe and are transferred into capillaries that are placed in EPR tubes.

In Figure 22, the EPR spectra of the reaction of $CuCl_2$ with formaldehyde and additional acetylene are shown. Reduction of Cu(II) does not take place at 25°C during the first 15 min (Figure 22A). After that (between 15 min and 30 min) Cu(II) is reduced. It is indicated by the decrease of the Cu(II) signals. Cu(II) is completely converted to Cu(I) after 45 min. Simultaneously a new

species is formed with a g-value of 2.00259 which corresponds to a carbon based radical. Compared to that, the reduction at 100°C takes place substantially faster (Figure 22B). Already after 2 min a complete reduction of Cu(II) to Cu(I) is achieved and the new species is formed.

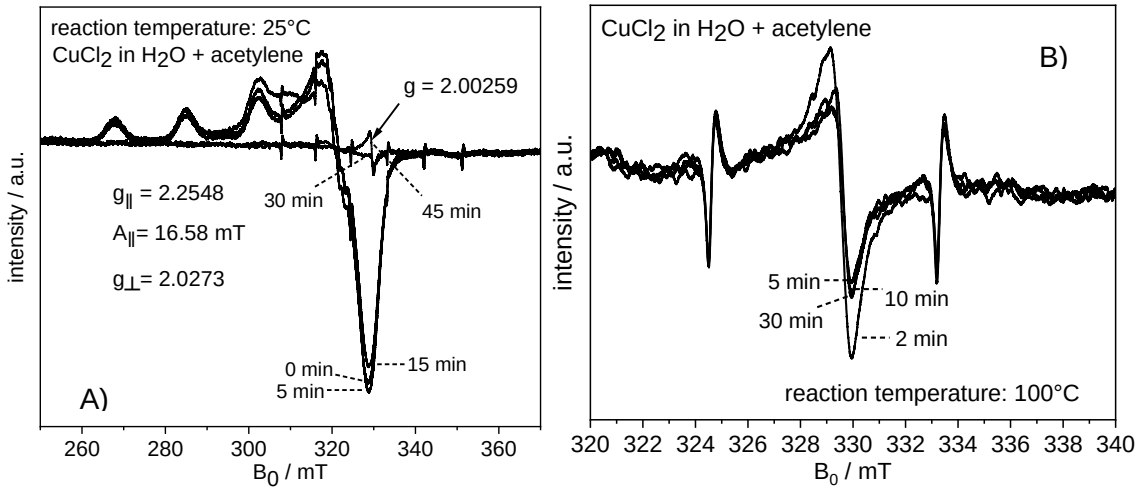

Figure 22: Anisotropic EPR spectra ($T_{recorded}$ = -120°C) of $CuCl_2$ in formaldehyde solution and acetylene at 25 °C (A) and 100°C (B) for different reaction times. Samples are taken after different reaction times with a syringe and are transferred into capillaries that were placed in EPR tubes.

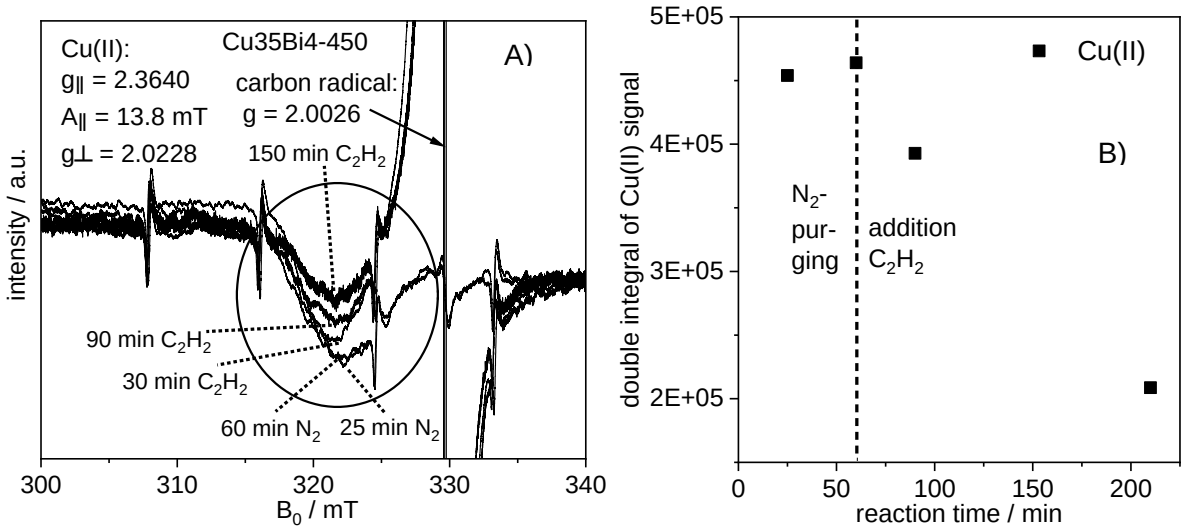

Figure 23: A) Anisotropic EPR spectra ($T_{recorded}$ = -120°C) of separated Cu35Bi4-450 catalyst after different reaction times. In the first 60 min the set-up is purged with N_2 before switching to acetylene. The activation is carried out at 100°C with 1.1 bar acetylene. B) Intensities of the Cu(II) signals obtained by double integration from the spectra of Figure 23A. The dashed line separates the N_2-purging period (60 min) from the activation with acetylene. Samples are taken after different reaction times with a syringe and are transferred into capillaries that were placed in EPR tubes.

To strengthen the obtained results the reduction behavior of a solid Cu/Bi catalyst (Cu35Bi4-450) is investigated doing the same experiments at 100°C. The results are depicted in Figure 23.

During the purging period with N_2 only formaldehyde and no acetylene is present. Hence, the reduction from Cu(II) to Cu(I) does not take place (see 25 min N_2 and 60 min N_2 in Figure 23A).

After the addition of acetylene the intensity of the Cu(II) signals decreases and Cu(II) is reduced to Cu(I). The new species with a g-value = 2.00259 is formed as soon as the reduction occurs. This is in accordance with the results obtained with $CuCl_2$ solution. However the decrease of the Cu(II) signals is hardly visible in these EPR spectra because of the high metal loading (35 wt.% Cu Therefore, the double integrals of the Cu(II) signals calculated from the spectra shown in Figure 23A at different reaction times are depicted in Figure 23B. The decrease of Cu(II) and consequently the reduction of Cu(II) to Cu(I) induced by acetylene can clearly be figured out by the decline of the double integrals of the Cu(II) signals after the addition of acetylene (right part in Figure 23B). With ongoing activation time Cu(II) is further converted into Cu(I) which is discussed later.

The same experiment is carried out with a Cu5Bi0.6 catalyst to avoid the influence of the high metal loading on the EPR measurement. The results are depicted in Figure 24 and confirm the results obtained with the higher loaded Cu35Bi4-450 catalyst.

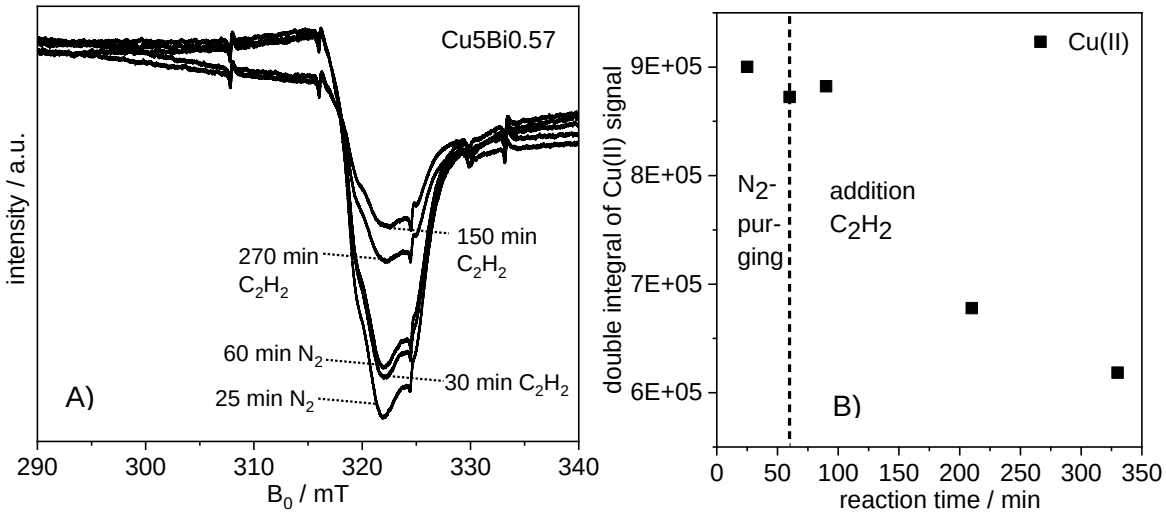

Figure 24: A) Anisotropic EPR spectra ($T_{recorded}$ = -120°C) of Cu5Bi0.57-450 catalyst in formaldehyde at different reaction times. B) Intensities of the Cu(II) signals obtained from the spectra of Figure 24A. The dashed line separates the N_2-purging period (60 min) from the reaction with acetylene. The activation is carried out at 100°C with 1.1 bar acetylene. Samples are taken after different reaction times with a syringe and are transferred into capillaries that are placed in EPR tubes.

In addition, the reduction behavior of Cu35Bi4-450 is investigated only with acetylene as reducing agent (without formaldehyde) to exclude that a combination of formaldehyde and acetylene is necessary for the reduction of Cu(II). The EPR spectra are depicted in Figure 25. It turns out that acetylene itself is capable of reducing Cu(II) to Cu(I). It agrees with *Brameld et al.* who reported that Cu_2C_2 can be synthesized from Cu(II) solutions without formaldehyde.[71] From the EPR results obtained from a $CuCl_2$ solution and real solid Cu/Bi catalysts it can be concluded that the reduction of Cu(II) to Cu(I) under ethynylation reaction conditions (100°C) is induced by acetylene not by formaldehyde in contrast to literature.

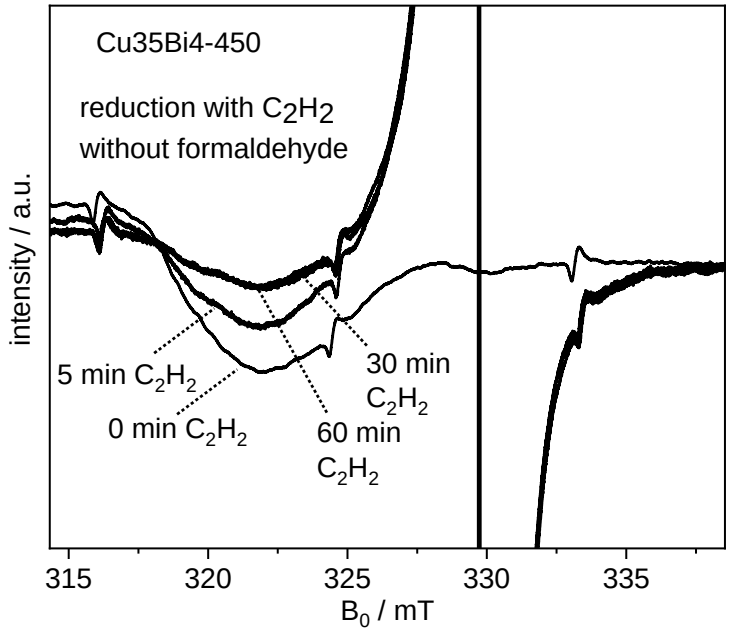

Figure 25: Anisotropic EPR spectra ($T_{recorded}$ = -120°C) investigating the reduction behavior of Cu(II) to Cu(I) of the Cu35Bi4-450 catalyst in water and acetylene atmosphere (without formaldehyde). In the first 60 min the set-up is purged with N_2 before switching to acetylene. The reduction is carried out at 100°C with 1.1 bar acetylene.

Raman spectroscopy – Characterization of Cu_2C_2 during the catalytic reaction

With the knowledge that Cu_2C_2 is the active species and the opportunity to characterize it via Raman spectroscopy, the formation of Cu_2C_2 is investigated during the activation of the catalyst. In Figure 26 the Raman spectra of activated Cu35Bi4-80 catalyst after certain reaction times are shown. The freshly prepared Cu_2C_2 and carbon (activated charcoal from FLUKA) serve as reference.

Signals corresponding to Cu_2C_2 do not appear during the purging period under N_2 because acetylene is not present. Only the signals for $Cu_2NO_3(OH)_3$ are present but they decrease in intensity during the N_2 purging period which indicates a structural change of the surface of the catalyst. After the addition of acetylene, two new signals arise (at 430 cm^{-1} and 1710 cm^{-1}). Between 15 min and 60 min under acetylene gas the signals get more pronounced and a third signal is visible at 580 cm^{-1}. The signals remain constant with increasing reaction time. The signals match very well with the signals appearing at the reference Cu_2C_2 and correspond to the Cu-C bond and the C≡C bond respectively as discussed before. The intensity of the signal of the reference Cu_2C_2 at 1710 cm^{-1} is very similar to the signals of the activated catalysts that indicates that C≡C bond has the same order. In contrast to that the signal at 430 cm^{-1} in the spectrum of the spent catalyst is much more intense than the signal of the Cu_2C_2 reference. It indicates that the Cu_2C_2 is more structured or rather more crystalline.

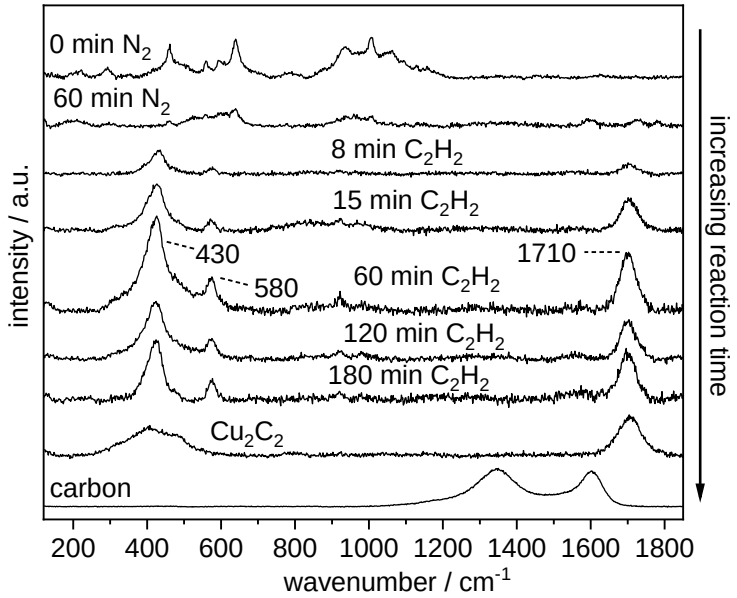

Figure 26: Raman spectra of spent Cu35Bi4-80 catalyst in the range from 115 cm^{-1} to 1880 cm^{-1}. Freshly prepared Cu_2C_2 and carbon (activated charcoal from FLUKA with the typical G-peak (1350 cm^{-1}) and D-peak (1600 cm^{-1})[112] serve as reference. Samples are taken by a syringe and they are measured in dry state. The laser intensity is 0.015 mW, the wavelength of the laser 532 nm. An objective with 50x magnification is used. The standard scanning time is 5 sec with 10 repetitions.

The signal at 580 cm^{-1} which can only be observed at the spent catalyst corresponds to a ≡C-C-bond[75]. It indicates that small amounts of coupling products like Cu polyynides are formed. The more crystalline structure of Cu_2C_2 formed during the ethynylation reaction is probably caused by the controlled long-term formation of Cu_2C_2 which takes place during the first hours in the activation. The precipitation of pure Cu_2C_2, as it was done for the synthesis of the reference, is carried out with a Cu(I) solution. In this case, the Cu_2C_2 formation is much faster because of precipitation of solid and poorly soluble Cu_2C_2 out of a supersaturated solution. Hence, the formation of numerous crystallization seeds leads to small and less crystalline Cu_2C_2 agglomerates.

The range of the measurement is selected between 115 cm^{-1} to 1880 cm^{-1} because further signals are not detected at higher wavenumbers. A spectrum of the activated catalyst in the range between 115 cm^{-1} to 2830 cm^{-1} is shown for illustration in Figure 27.

Cu_2C_2 is very sensitive towards irradiation, heat and impacts. Therefore, Raman spectra of an activated catalyst (Cu35Bi4-80) are measured with different Raman laser intensities (see Figure 28) to exclude that the samples are destroyed during the measurement and hence the results are not reliable. The signals for Cu_2C_2 are visible with laser intensities of 0.015 and 0.030 mW. Increasing the laser intensity up to 0.300 mW leads to the decomposition of Cu_2C_2 to carbon that corresponds well to the reference carbon spectrum. Normally the Raman spectra in this work are recorded at Raman laser intensities of 0.015 mW.

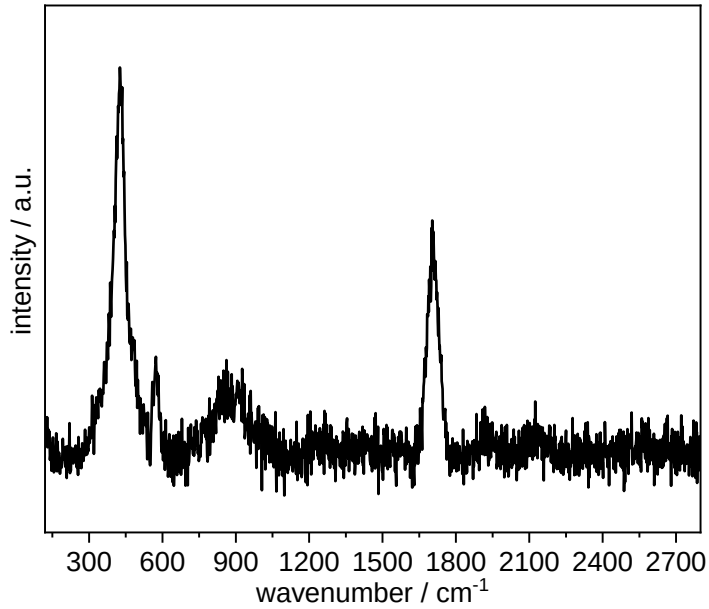

Figure 27: Raman spectra of activated Cu35Bi4-80 catalyst in the range from 115 cm^{-1} to 2830 cm^{-1}. The sample is taken with a syringe and it is measured in dry state. The laser intensity is 0.015 mW, the wavelength of the laser 532 nm. An objective with 50x magnification is used. The standard scanning time is 5 sec with 10 repetitions.

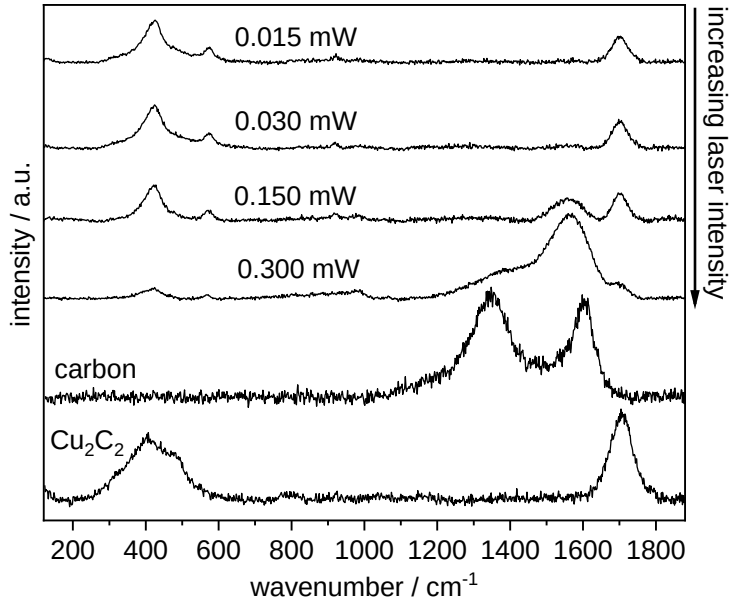

Figure 28: Raman spectra of activated Cu35Bi4-80 catalyst. Freshly prepared Cu_2C_2 and carbon (activated charcoal from FLUKA with the typical G-peak (1350 cm^{-1}) and D-peak (1600 cm^{-1})[112] serve as reference. The sample are taken by a syringe and it is measured in dry state. The wavelength of the laser 532 nm. An objective with 50x magnification is used. The standard scanning time is 5 sec with 10 repetitions.

To get information about the formation of Cu_2C_2 during the activation and the influence on the 1,4-butynediol formation Raman spectra of different loaded Cu/Bi/SiO_2 (Cu5Bi0.6, Cu15Bi1.7, Cu25Bi2.9, Cu35Bi4) catalysts are measured. As it was mentioned above the activation is not separated from ethynylation because even during the activation 1,4-butynediol is formed. The

catalysts performances regarding the 1,4-butynediol yield are depicted in Figure 29A and the 1,4-butynediol yield after 180 min reaction time regarding the Cu loading in Figure 29B.

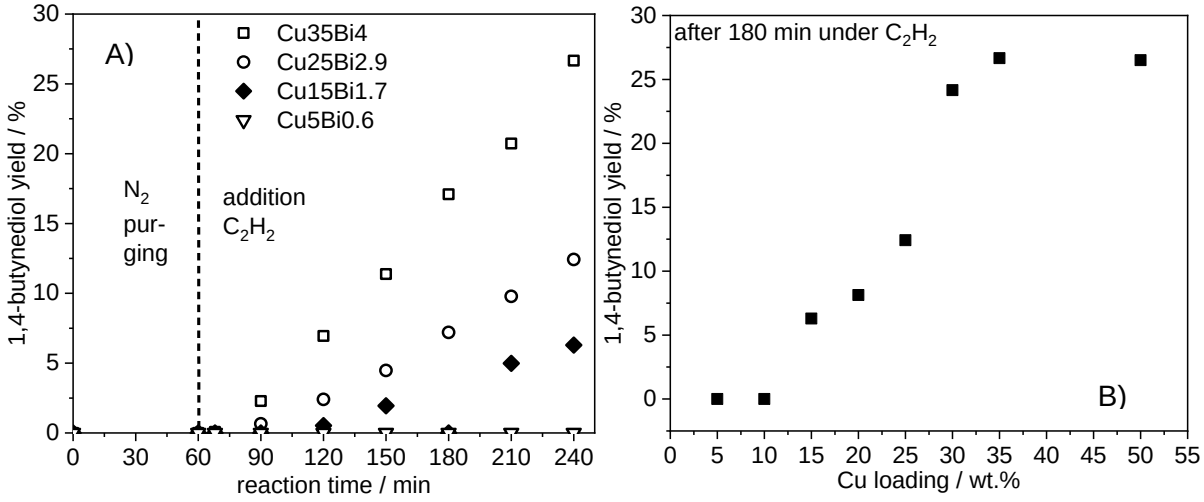

Figure 29: (A) 1,4-butynediol yields obtained with four different loaded Cu/Bi/SiO_2 catalysts. The dashed line separates the N_2-purging period (60 min) from the activation with acetylene (180 min). (B) 1,4-butynediol yield after 180 min activation time depending on the Cu loading in wt.% The reaction is carried out at 100°C with 1.1 bar acetylene. The product analysis is done by GC.

The reaction is divided into two parts. In the first 60 min the system is purged with N_2 to get rid of oxygen. After that, N_2 is replaced by acetylene and the activation period starts. During the initializing/activation period (first 30 min depending on the catalyst loading), a minimum amount of Cu_2C_2 must be formed so that the ethynylation reaction can start. After that, a linear increase of the 1,4-butynediol yield is obtained which indicate an order of reaction of 1.[84-86]

The highest yield (38.5 % after 3 hours acetylene) is obtained with the Cu35Bi4 catalyst. Consequently, higher copper loadings lead to higher 1,4-butynediol yields (see Figure 29B). 35 wt.% Cu is the ideal Cu loading for these catalysts and their application in the ethynylation.[12, 13] Higher Cu loadings (50 wt.%) do not increase the 1,4-butynediol yield. Very low Cu amounts (5 and 10 wt.% Cu) exhibit low catalytic performance. In this case, most likely the CuO particles are strongly embedded into the SiO_2 support and hence the conversion of CuO into Cu_2C_2 is hindered.

Table 3: 1,4-Butynediol (BD) formation rates of different Cu and Bi loaded catalysts in $g_{BD}g_{Cu}^{-1}h^{-1}$.

Sample	$g_{BD}g_{Cu}^{-1}h^{-1}$
Cu5Bi0.6	0.2
Cu15Bi1.7	0.6
Cu25Bi2.9	1.6
Cu35Bi4	3.1

To strengthen that the Cu loading is crucial for the efficiency of the catalysts, the formation rates of 1,4-butynediol ($g_{BD}g_{Cu}^{-1}h^{-1}$) concerning the amount of Cu of the different catalysts are summarized in Table 3.

In Figure 30 the Raman spectra of the separated catalysts after different activation times are shown. During the purging period no signals for Cu_2C_2 in the Raman spectra are visible (Figure 30A) because acetylene is not present. Just weak signals assigning to the pre-catalyst (CuO) are observable at Cu35Bi4. 8 min after switching to acetylene the two characteristic Raman signals for Cu_2C_2 appear except in the spectrum of Cu5Bi0.6 catalyst (Figure 30B). The signals with highest intensity are obtained with the Cu35Bi4 catalyst. After 60 and 120 min under reaction conditions, the order of the signal intensities remains unchanged. The signal intensities of Cu25Bi2.9 and Cu15Bi1.7 lie between the intensities of Cu35Bi4 and Cu5Bi0.6 (see Figure 30C and D).

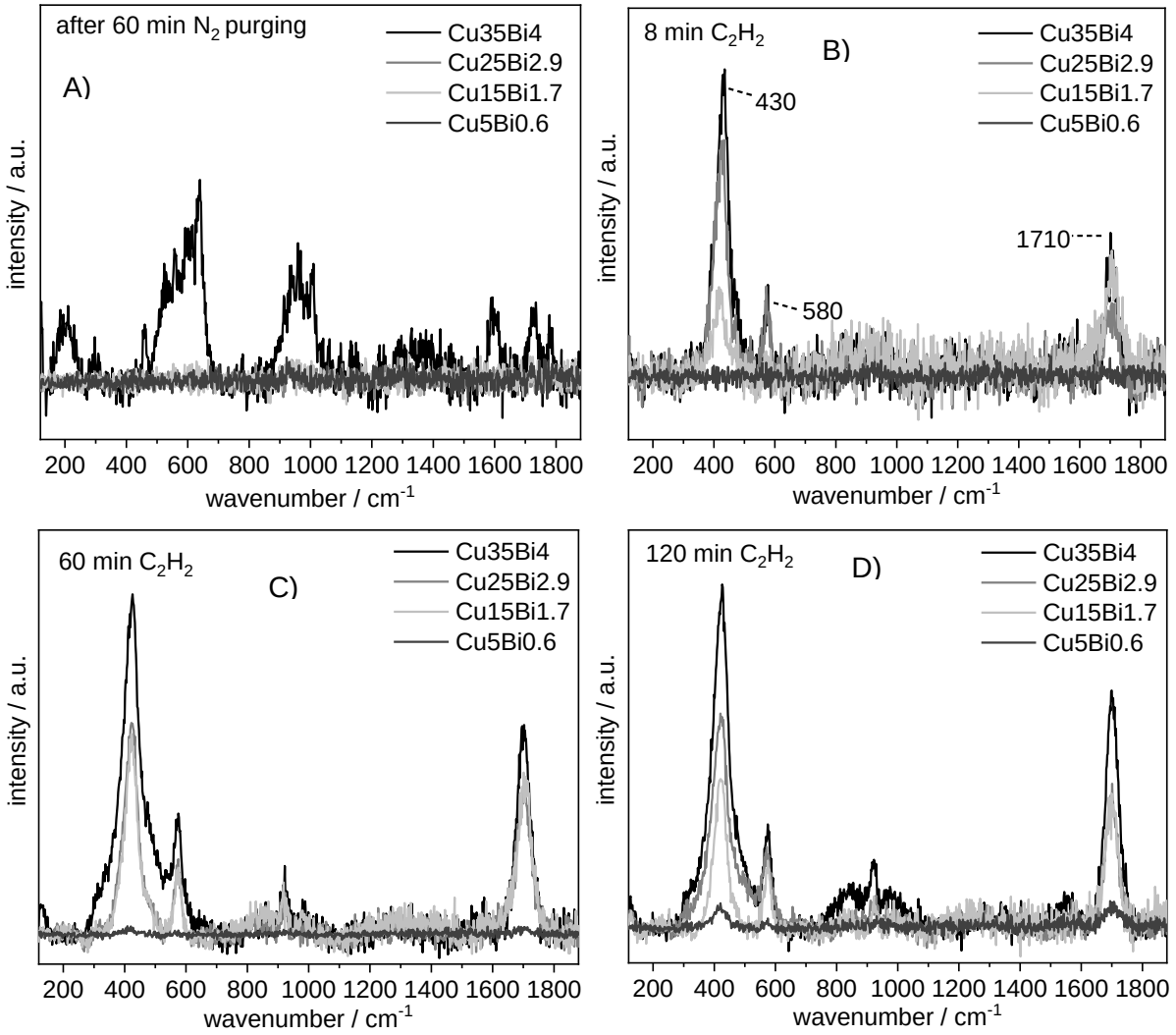

Figure 30: Raman spectra of separated Cu/Bi/SiO_2 catalysts with different loadings. The samples are taken with a syringe during the purging phase and during the activation period with acetylene. They are measured in dry state. The laser intensity is 0.015 mW, the wavelength of the laser 532 nm. An objective with 50x magnification is used. The standard scanning time is 5 sec with 10 repetitions.

That agrees with the catalytic activity because the higher the 1,4-butynediol yield the higher are the signal intensities of Cu_2C_2 in Raman spectroscopy. A good example is the Cu5Bi0.6 catalyst. Even after 120 min activation time, the Cu_2C_2 signals are very week. Simultaneously 1,4-butynediol is hardly formed.

To illustrate, the area of the Raman peaks at 430 cm^{-1} obtained by integration of the peaks of the Raman spectra depicted in Figure 30 are shown in Figure 31 after different times as well as the corresponding 1,4-butynediol yield. It clearly shows the dependency of the 1,4-butynediol yield on the Cu_2C_2 formation. It is important to note, that the area of the Raman peaks act only for qualitative claims because the Raman peaks are influenced by the crystallinity as well as the configuration of the compound.

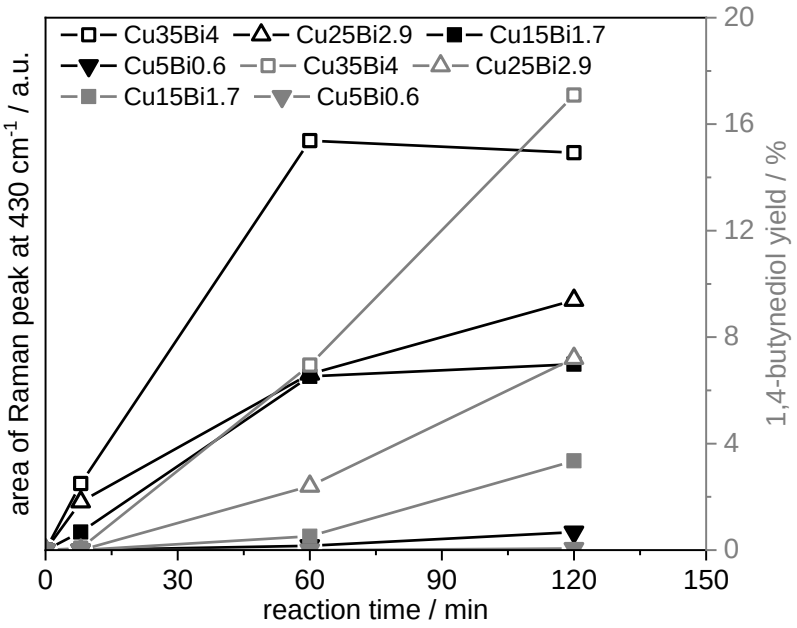

Figure 31: Areas of the Raman peaks at 430 cm-1 obtained from integration of the peaks of the Raman spectra depicted in Figure 30 as well as the corresponding 1,4-butynediol yield at different activation times. The samples were taken with a syringe. They are measured in dry state. The laser intensity is 0.015 mW, the wavelength of the laser 532 nm. An objective with 50x magnification is used. The standard scanning time is 5 sec with 10 repetitions.

To strengthen the assumption that the formation of Cu_2C_2 defines the 1,4-butynediol formation rate of the Cu/Bi/SiO_2 catalysts four different calcined catalysts with the same copper loading (Cu35Bi4-80 (just dried), Cu35Bi4-450, Cu35Bi4-600, Cu35Bi4-700) are investigated. The 1,4-butynediol yield as well as the Raman spectra of the separated catalysts after different activation times are depicted in Figure 32. The Raman spectra of Cu35Bi4-600 are not shown because it follows the same trend as the other samples.

Cu35Bi4-80 produces the highest 1,4-butynediol yield. The yields of the catalysts calcined at different temperatures are similar (ca. 40 %) after 5 h activation time (see Figure 32D). After 15 min activation time, Raman signals of Cu_2C_2 are visible for Cu35Bi4-450 and Cu35Bi4-80. The signals of Cu35Bi4-80 are more intense (see Figure 32A). The course continues during

the whole activation (see Figure 32B and C). Compared to that, the Raman signals concerning Cu_2C_2 appear only after 60 min activation time for Cu35Bi4-700. They quickly increase until 300 min activation time (see Figure 32B and C).

The appearance of the Raman signals of Cu_2C_2 correlates with the beginning of 1,4-butynediol formation. The 1,4-butynediol formation begins just after adding acetylene regarding Cu35Bi4-80. Using Cu35Bi4-450 and Cu35Bi4-700 as catalyst 1,4-butynediol is formed only after 30 min and 60 min which agrees with the appearance of the Cu_2C_2 Raman signals or rather of their increasing intensity (see Figure 33). Interestingly, despite the similar 1,4-butynediol yield, the 1,4-butynediol (BD) formation rates differ. They are summarized in Table 4. Cu35Bi4-80 and Cu35Bi4-700 as well as Cu35Bi4-450 and Cu35Bi4-600 have almost the same formation rate.

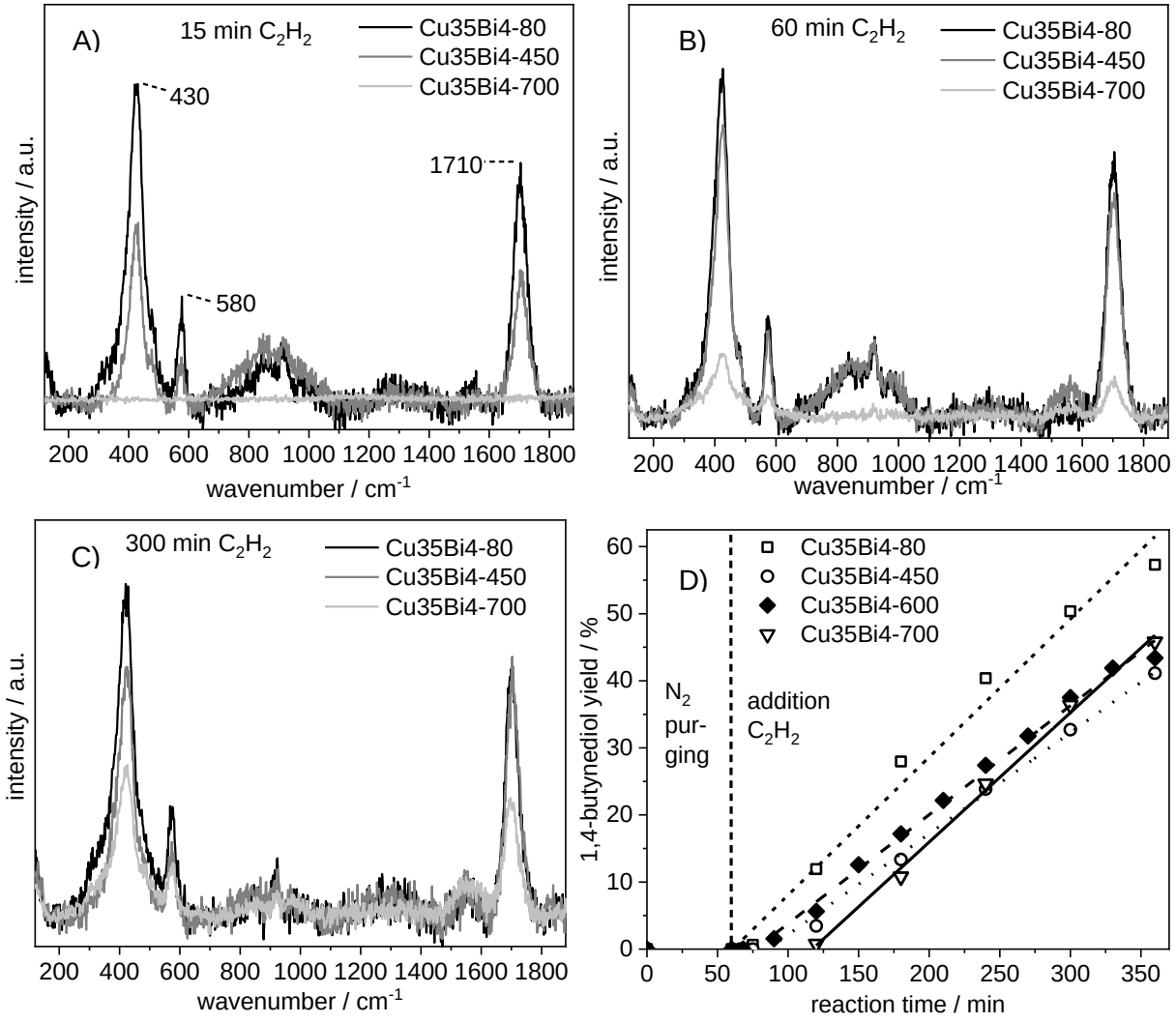

Figure 32: Raman spectra of separated Cu/Bi/SiO_2 catalysts (A, B, C) calcined at different temperatures (80°C, 450°C, 600°C, 700°C) as well as the 1,4-butynediol yield they achieved in the ethynylation reaction (D). The samples are taken with a syringe during the purging phase and during the activation period with acetylene. They are measured in dry state. The laser intensity is 0.015 mW, the wavelength of the laser 532 nm. An objective with 50x magnification is used. The standard scanning time is 5 sec with 10 repetitions.

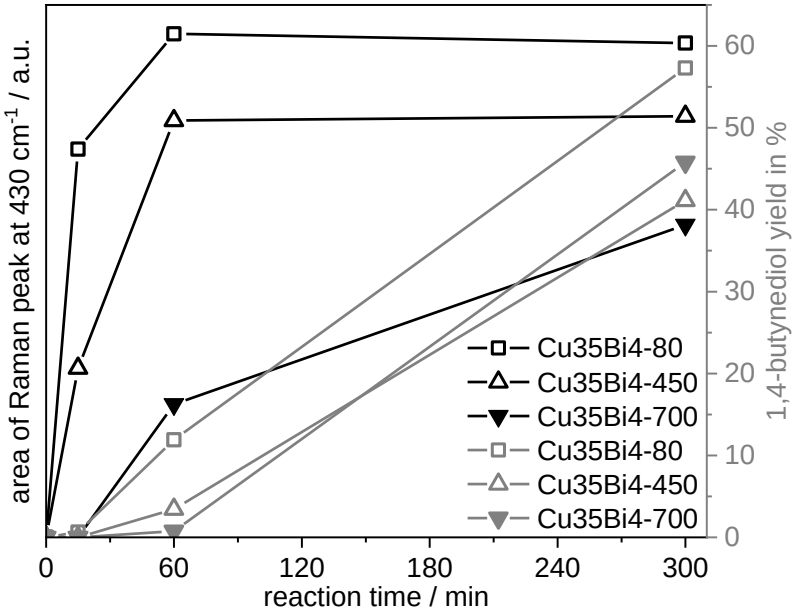

Figure 33: Areas of the Raman peaks at 430 cm^{-1} obtained from integration of the peaks of the Raman spectra depicted in Figure 32 as well as the corresponding 1,4-butynediol yield at different activation times. The samples were taken with a syringe. They are measured in dry state. The laser intensity is 0.015 mW, the wavelength of the laser 532 nm. An objective with 50x magnification is used. The standard scanning time is 5 sec with 10 repetitions.

The reasons for the differences of the formation rates of the catalysts are more complex. Therefore, the crystallite sizes obtained with the Scherrer equation from the powder diffractograms shown in Figure 10 and the Raman peak full width at half maximum (FWHM) after 300 min for the peak at 430 cm^{-1} are summarized in Table 4. The crystallite sizes of Cu35Bi4-80 and Cu35Bi4-700 are the largest which correlates with largest 1,4-butynediol formation rates. It means that highly active Cu_2C_2 is favorably formed from larger crystals.[93] In addition, the Raman peak FWHM after 300 min for the peak at 430 cm^{-1} is the largest for these two catalysts. The broader Raman signals indicate a less crystalline (ordered) Cu_2C_2 phase as it was discussed before. Less crystalline Cu_2C_2 is favorably formed from bigger crystallites and is probably more active in the ethynylation reaction.

Table 4: Formation rates of 1,4-butynediol (BD) concerning the amount of Cu in $g_{BD}g_{Cu}^{-1}h^{-1}$, the crystallite size ($Size_{crys}$) in nm of CuO or rather $Cu_2NO_3(OH)_3$ of the calcined catalysts determined by the Scherrer equation and the Raman peak full width at half maximum ($FWHM_{Raman}$) in cm^{-1} after 300 min for the peak at 430 cm^{-1}.

catalyst	$g_{BD}g_{Cu}^{-1}h^{-1}$	$Size_{crys}$	$FWHM_{Raman}$
Cu35Bi4-80	3.8	43.2	64
Cu35Bi4-450	3.1	14.1	56
Cu35Bi4-600	3.1	15.4	-
Cu35Bi4-700	3.7	20.2	66

The difference of the 1,4-butynediol formation of $Cu_{35}Bi_4$-80 and $Cu_{35}Bi_4$-700 at the beginning of the activation is most likely caused by the different Cu precursor. In contrast to the calcined

catalysts $Cu_{35}Bi_4$-80 consists of $Cu_2NO_3(OH)_3$ instead of CuO. It indicates that $Cu_2NO_3(OH)_3$ could favor the formation of Cu_2C_2 and consequently the early formation of 1,4-butynediol.
In conclusion, the dependency of the catalytic activity on the formation of Cu_2C_2 is influenced by the Cu_2C_2 formation rate as well as by the structure (crystallinity) of the formed Cu_2C_2.

X-Ray diffraction – Characterization of Cu_2C_2 during the ethynylation

Since we know that XRD is a possible characterization method for the investigation of crystalline Cu_2C_2 we measured powder diffractograms of the catalysts separated after different activation times with same Cu loading but different calcination temperatures.

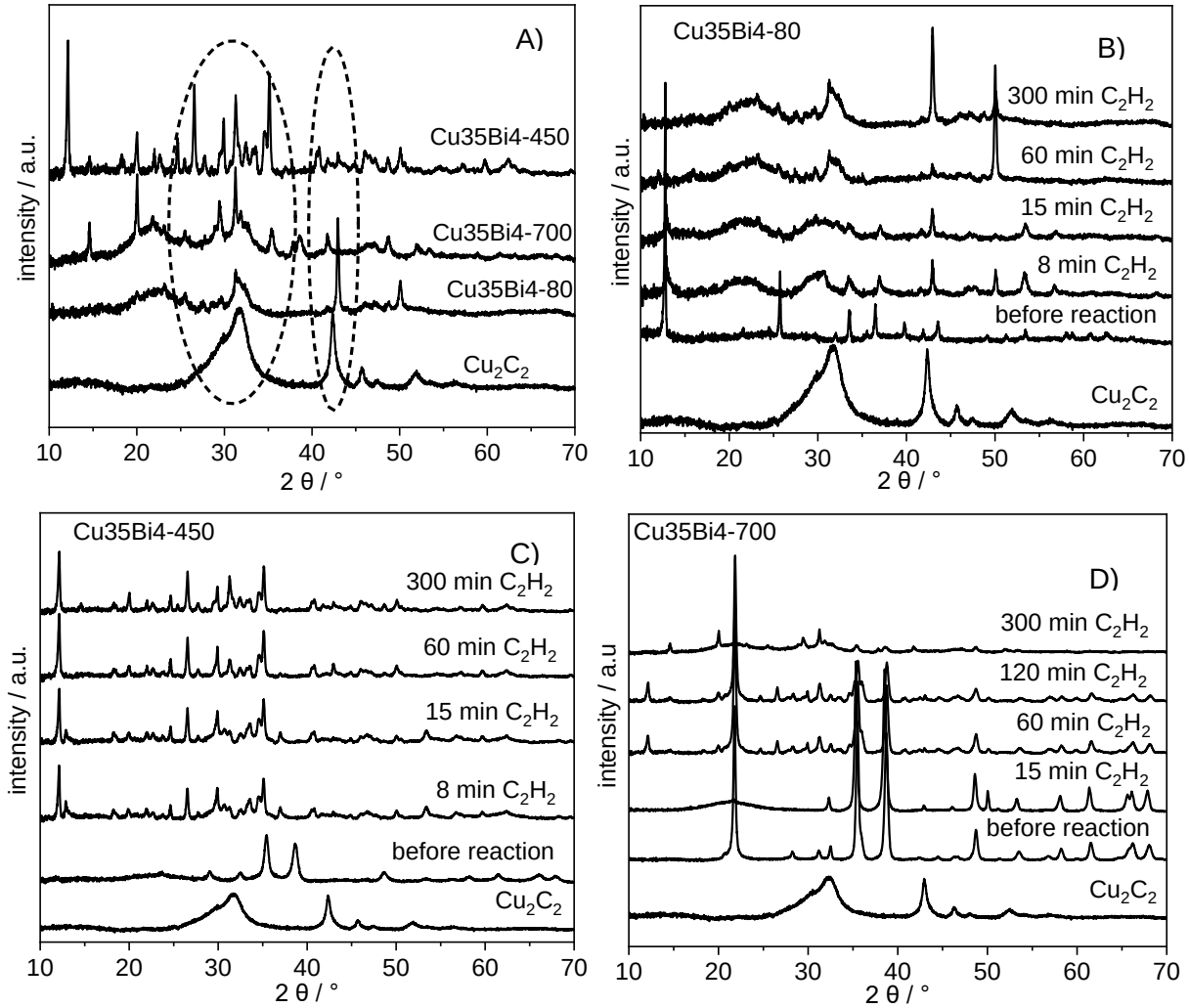

Figure 34: (A) Powder diffractograms of separated Cu35Bi4-450, Cu35Bi4-700 and Cu35Bi4-80 after 300 min reaction time and of freshly prepared Cu_2C_2. (B-D) Powder diffractograms of separated Cu35Bi4-80 (B), Cu35Bi4-450 (C) and Cu35Bi4-700 (D) after different activation time. The samples are taken during or after the activation with a syringe and they are measured in dry state. The powder diffractogram of freshly prepared Cu_2C_2 and the powder diffractograms of the pre-catalysts before the catalytic reaction serve as reference. Diffractograms are recorded in an angle range between 5° and 70° in steps of 0.013°.

The powder diffractograms obtained after 300 min activation time are depicted in Figure 34A.

Besides the powder diffractograms of the catalysts after the activation, powder diffractograms of samples taken during the activation are measured as well. These powder diffractograms are shown in Figure 34B to Figure 34D.

The powder diffractograms of Cu35Bi4-700 and Cu35Bi4-80 differs compared to the powder diffractogram of Cu35Bi4-450 (Figure 34A). The reflexes assigned to Cu_2C_2 fit well but are broad compared to the pure Cu_2C_2 reference, especially for Cu35Bi4-80. It indicates the formation of small and less crystalline Cu_2C_2 particles during the activation. The diffractogram of separated Cu35Bi4-700 is very similar except some narrower reflexes, especially the reflex at 32 2θ (Figure 34A). In contrast to that, the crystallinity of Cu_2C_2 in spent Cu35Bi4-450 is more pronounced mainly in the region of the 32 2θ reflex and 43 2θ reflex (Figure 34A). It confirms the results obtained by Raman spectroscopy that a more crystalline Cu_2C_2 or rather larger Cu_2C_2 particles are less active in the ethynylation. In addition, the time course of the formation of Cu_2C_2 can also be observed via X-Ray diffraction. The CuO reflexes of the Cu35Bi4-700 catalyst decrease during the ethynylation reaction because of the formation of Cu_2C_2, which leads to the consumption of CuO (Figure 34D). The effect that Cu_2C_2 is formed directly at the beginning of the reaction and that the formation takes place much faster for Cu35Bi4-80 compared to Cu35Bi4-700 can be observed via powder diffraction as well as it was found out via Raman spectroscopy (Figure 34B).

Leaching experiments – Cu_2C_2 formation via a leaching mechanism

EPR experiments indicate that the reduction of Cu(II) to Cu(I) is induced by acetylene. In addition, the formation of Cu_2C_2 can be studied using Raman spectroscopy and X-Ray powder diffraction. However, it is still unclear how Cu_2C_2 is formed: in solution via a leaching mechanism or directly on the catalyst surface.

At first, we investigated a possible leaching mechanism. During the activation samples are taken of the liquid phase containing water, formaldehyde, methanol (acts as stabilizing agent for formaldehyde) and the catalyst (Cu35Bi4-80 or Cu35Bi4-700). The copper content of the reaction medium is determined via ICP-OES after different reaction times. The volume of the suspension is 100 mL. In Figure 35 the amount of leached copper as well as the Cu leaching percentage are shown for Cu35Bi4-80. Additionally the Cu(II) concentration in solution is measured by a specific Cu(II) electrode (Figure 36).

During the purging period copper from the Cu/Bi catalyst leaches and dissolves in the reaction medium. The copper content in percentage that leaches is around 0.07 % (12.3 ppm) regarding the overall copper amount. The leaching of Cu(II) leads to structural changes of the catalyst which was already observed by Raman spectroscopy (Figure 26).

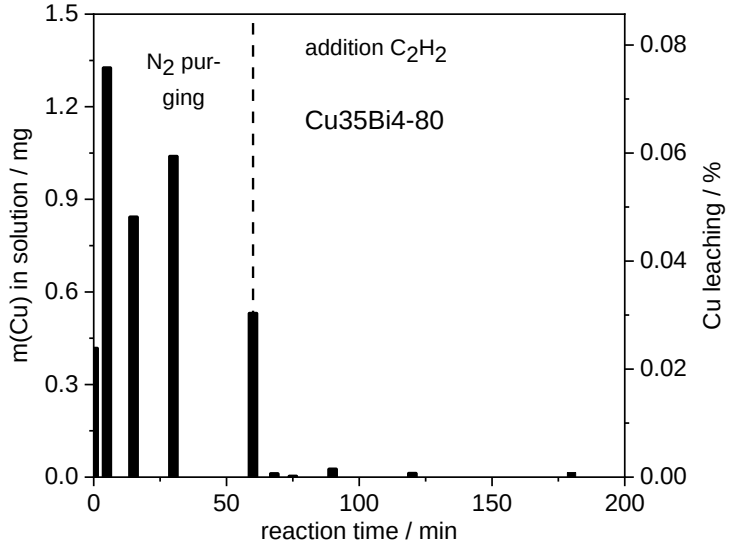

Figure 35: Determination of Cu content in solution by ICP-OES using Cu35Bi4-80 catalyst during the actication. The activation is carried out at 100°C with 1.1 bar acetylene.

The copper leaching can be confirmed by the conductivity measurement (Figure 36). After the addition of the catalysts the conductivity increases (after 10 minutes in Figure 36). After 30 min the increase drops because a maximum amount of leached copper in solution is reached. The maximum amount of dissolved Cu is most likely defined by the ratio between dissolved Cu(II) and Cu(II) which precipitates as $Cu(OH)_2$ under these conditions (pH = 7). The leached copper must have an oxidation state of II because the electrode used for this experiment is only sensitive for Cu(II) ions. After starting the activation by switching to C_2H_2 gas the Cu(II) concentration drops almost to zero indicating that Cu_2C_2 is formed. Probably, Cu_2C_2 forms small clusters, which are sparingly soluble, and they precipitate. Cu_2C_2 is almost insoluble in the reaction medium meaning that the copper content in solution is very low. Results obtained by Raman spectroscopy and X-Ray diffraction prove that the formation of Cu_2C_2 still takes place during the whole activation (around 5 h). Therefore, copper continuously leaches from the solid catalyst into the solution. Due to the insolubility of the precipitated Cu_2C_2 under activation conditions the measured Cu(II) concentration in solution (0.03 mg in 100 mL, 0.3 ppm) remains at a very low level during the whole activation time. The same course of leached Cu exhibits the Cu35Bi4-700 catalyst (Figure 37) but less Cu leaches during the purging period. In addition, the leached Cu amount decreases not as fast as it was observed at Cu35Bi4-80 after the addition of C_2H_2. Both confirms the result obtained by Raman and X-Ray diffraction that Cu_2C_2 is formed more slowly using Cu35Bi4-700 as catalyst. Cu leaching originating from CuO is hindered compared to Cu leaching from $Cu_2NO_3(OH)_3$ which explains the lower copper amount in solution during the purging period. Interestingly, the conductivity increases as soon as acetylene is replaced by nitrogen again (N_2-purging on the right side in Figure 36). It means that

Cu_2C_2 is partially decomposed, which was already observed for the acetylide of propargyl alcohol (see Figure 19). Hence the Cu(II) content in solution rises and an excess of acetylene is needed to stabilize Cu_2C_2.

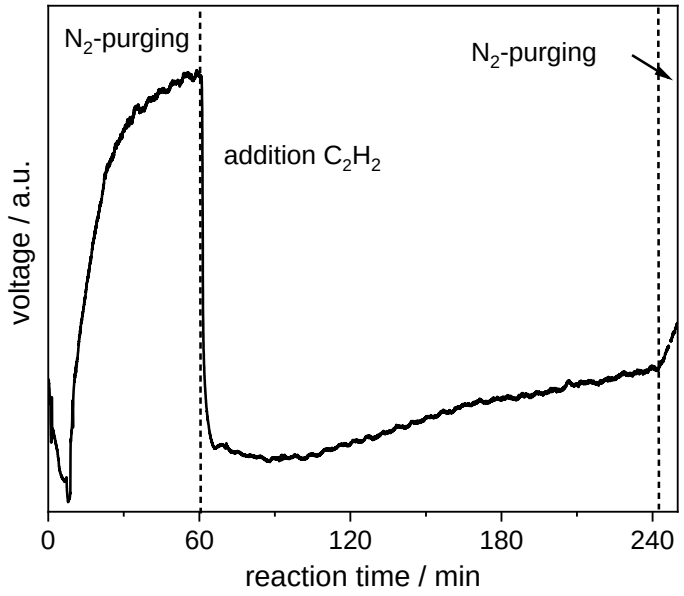

Figure 36: Conductivity measurement with a Cu(II) selective electrode (Ag/AgCl(aq) (3 M KCl reference electrode) using Cu35Bi4-80 as catalyst. The activation is carried out at 100°C with 1.1 bar acetylene.

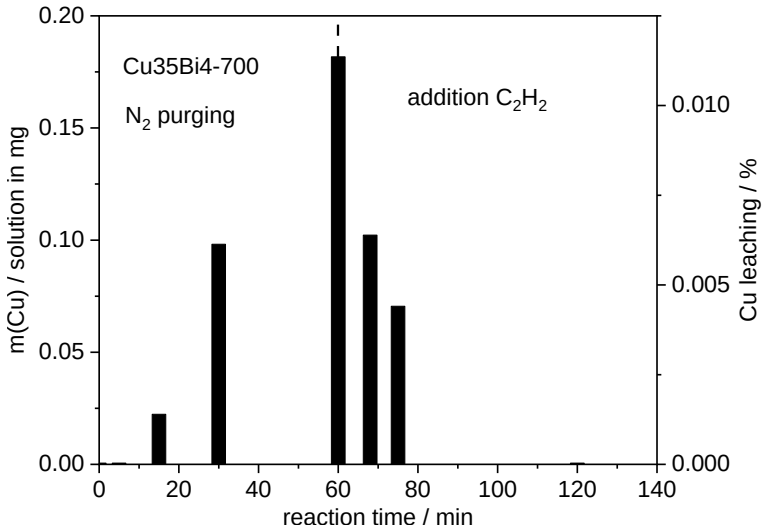

Figure 37: Determination of Cu content in solution by ICP-OES using Cu35Bi4-700 catalyst. The activation is carried out at 100°C with 1.1 bar acetylene.

In further experiments, we investigated the direct formation of Cu_2C_2 from acetylene and the solid catalyst without any solvent at 100°C. It would give a hint that Cu_2C_2 is formed directly on the catalyst surface and not via a leaching mechanism. A Cu35Bi4-80 catalyst without any solvents or reactants is purged with N_2 and after 60 min acetylene is introduced. After 4 h a sample of the catalysts is analyzed by Raman spectroscopy. In Figure 38 the Raman spectrum

of the catalysts after the treatment as well as the reference spectrum of Cu_2C_2 and carbon (activated charcoal from FLUKA) are shown.

The characteristic signals for Cu_2C_2 are visible at 430 and 1710 cm^{-1}. The intensities of the peaks are very low. Additionally, a carbon species is formed represented by the signal at 1580 cm^{-1}. Regarding the peak intensities the amount of formed Cu_2C_2 is very low and rather carbon is formed instead of Cu_2C_2. Therefore, Cu_2C_2 is preferably formed by a leaching mechanism.

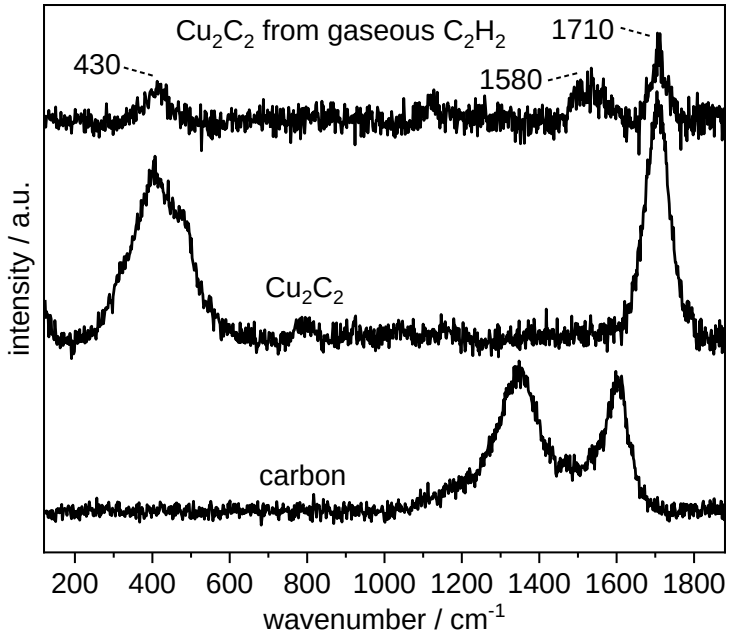

Figure 38: Raman spectrum of separated Cu35Bi4-80 catalyst treated with acetylene. Spectra of carbon (activated charcoal from FLUKA with the typical G-peak (1350 cm^{-1}) and D-peak (1600 cm^{-1})[112] and freshly prepared Cu_2C_2 serve as reference. The sample is taken after 4 h treatment and is measured in dry state. The laser intensity is 0.015 mW, the wavelength of the laser 532 nm. An objective with 50x magnification is used. The standard scanning time is 5 sec with 10 repetitions.

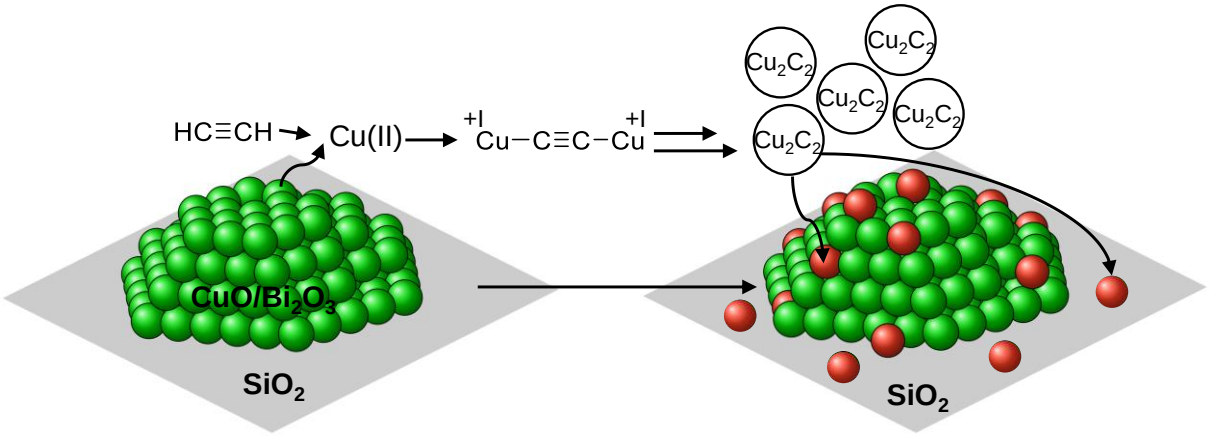

Figure 39: Proposed leaching mechanism for the formation Cu_2C_2 during the activation of a Cu/Bi/SiO_2 catalyst under typical activation conditions (100°C, 1.1 bar acetylene).

A possible leaching mechanism is depicted in Figure 39. Cu(II) leaches from the solid catalyst into the reaction medium containing water, formaldehyde and methanol. Cu immediately precipitates as Cu_2C_2 due to the poor solubility after reacting with acetylene and deposit onto the support as well as onto the CuO particles. The Cu_2C_2 formation is long-term controlled, meaning that the Cu leaching as well as Cu_2C_2 precipitation is continuously repeated during the whole reaction time.

Thermogravimetric analysis – Quantification of Cu_2C_2

The TG method is a suitable and reliable technique to determine the amount of formed Cu_2C_2 as discussed before. Therefore, the amount of formed Cu_2C_2 in the catalytic reaction is determined using Cu/Bi catalysts with different Cu loadings and calcination temperatures.

In Figure 40 the conversion of the overall Cu(II) amount in the catalyst into Cu_2C_2 for Cu35Bi4-80, Cu35Bi4-700, Cu25Bi2.9 and Cu5Bi0.6 catalysts are shown.

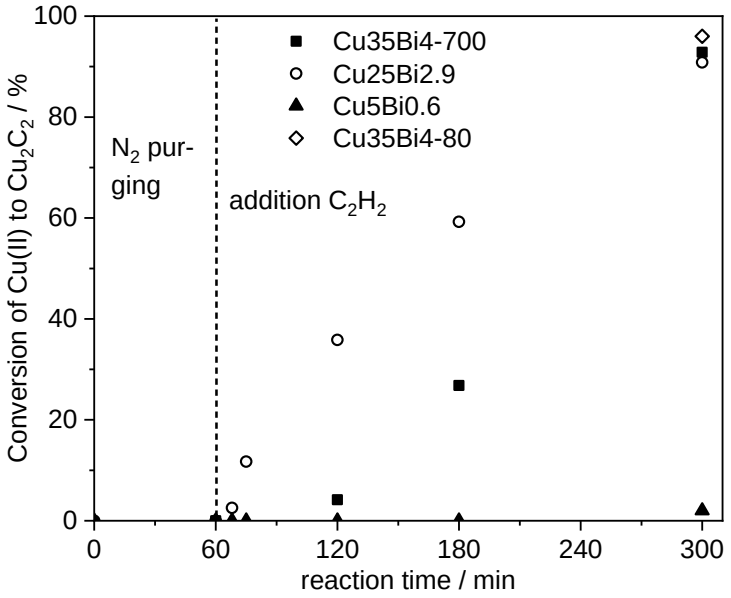

Figure 40: Conversion of Cu(II) into Cu_2C_2 of the initial $CuO/Bi_2O_3/SiO_2$ catalysts with different loadings and calcination temperatures measured by TGA. The samples are heated to 1000°C under synthetic air at a rate of 10 K/min during the TGA. The activation of the catalysts are carried out at 100°C with 1.1 bar acetylene. Samples are taken during the activation to separate the catalyst.

Cu(II) is not converted into Cu_2C_2 during the purging period for all catalysts because acetylene is not present. Cu_2C_2 is formed as soon as acetylene is introduced especially using Cu25Bi2.9 and consequently Cu(II) from the catalyst precursor is consumed. The formation of Cu_2C_2 increases nearly linearly after a short initializing period. This is in accordance to the Raman results. The decrease of Cu(II) in the catalyst precursor and consequently the continuously formation of Cu_2C_2 during the catalytic reaction is in agreement with the obtained X-Ray diffraction results. 91 % of the overall Cu(II) amount is converted into Cu_2C_2 after 4 h reaction time. The same amount or even more is achieved using Cu35Bi4-80 and Cu35Bi4-700. Only

the course of the curve differs regarding Cu35Bi4-700. The initialization period is more pronounced. After that, the Cu_2C_2 formation rate increases linearly as well. The conversion of Cu(II) into Cu_2C_2 is up to 90 % for these three catalysts which confirms Raman und X-Ray diffraction results.

In contrast to that, the amount of formed Cu_2C_2 using Cu5Bi0.6 is too low to be quantifed. It agrees with Raman spectroscopy where the characteristic Cu_2C_2 peaks appear only after 120 min with weak signal intensities and with the 1,4-butynediol formation rate as well because this catalyst is not active in the ethynylation.

Investigations regarding the ethynylation reaction itself

In summary, it can be concluded that the Cu_2C_2 formation takes place via a leaching mechanism. But it is not clear where the catalytic reaction itself proceeds. It could be possible that small agglomerates of Cu_2C_2 which are in solution before they precipitate or that the Cu_2C_2 which is already precipitated onto the support act as active phase. Therefore, the same $Cu_{35}Bi_4$-700 catalyst was first activated for 5 h (as it was done for the other measurements) and then applied in a fresh formalin batch (ethynylation reaction). The yields of 1,4-butynediol and propargyl alcohol as well as the 1,4-butynediol (BD) formation rates are shown in Figure 41.

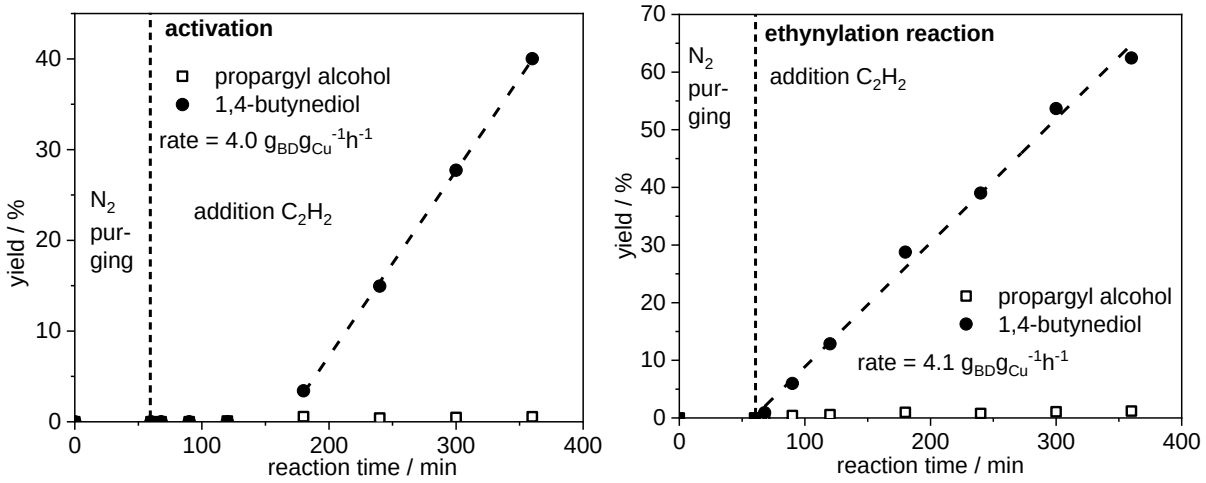

Figure 41: Yields of 1,4-butynediol and propargyl alcohol including the 1,4-butynediol formation rate using Cu35Bi4-700 as catalysts during activation and after addition to a new batch of formalin (ethynylation reaction). Both, the activation and the ethynylation are carried out at 100°C with 1.1 bar acetylene. The product analysis is done by GC.

During the activation of the catalyst the 1,4-butynediol yield increases linearly after the initializing period. If the catalytic reaction takes place on the surface of Cu_2C_2 agglomerates which are in solution either the reaction rate must decrease when the whole CuO of the calcined catalyst is converted into Cu_2C_2 or Cu_2C_2 dissolves after its precipitation again. The latter remains very unlikely because Cu_2C_2 is practically insoluble in all common solvents. After the activation, the catalyst is separated from the liquid phase and is added to a freshly prepared

formaldehyde solution. The initializing period is not observable anymore which means that the active species must be already formed. The 1,4-butynediol yield increases linearly as well. The 1,4-butynediol (BD) formation rate remains constant (4.0 for activation and 4.1 $g_{BD}g_{Cu}^{-1}h^{-1}$for ethynylation reaction) which indicates that the same active species is present and the same reaction pathway is conducted. As we know from Raman spectroscopy, X-Ray diffraction and TG the entire CuO of the calcined catalyst is most likely completely converted into Cu_2C_2 which precipitates onto the catalyst support after the activation. It means that Cu_2C_2 is present as SiO_2 supported precipitate at the beginning of the second use of the catalyst. The lacking initializing period as well as the same formation rate indicates that the catalytic reaction takes place on the surface of the precipitated Cu_2C_2. In contrast to that, one would expect if the reaction takes place on the surface of soluble Cu_2C_2 agglomerates that the formation rate decreases dramatically at the second use because Cu_2C_2 already precipitated and the CuO of the initial catalyst is consumed. The propargyl alcohol yield stays constant during both reactions (around 0.2 %) which means that the selectivity does not change and supports the conclusion that the same active phase is present comparing the activation and the ethynylation. A reaction pathway via soluble Cu_2C_2 agglomerates cannot be excluded completely but the rate of this pathway is too slow or the pathway is hindered so that the effect is not visible regarding the 1,4-butynediol formation rate.

In addition, experiments are carried out at which the activation of a Cu35Bi4-80 catalyst was carried out without formaldehyde. After the activation the catalysts was applied in the ethynylation reaction.

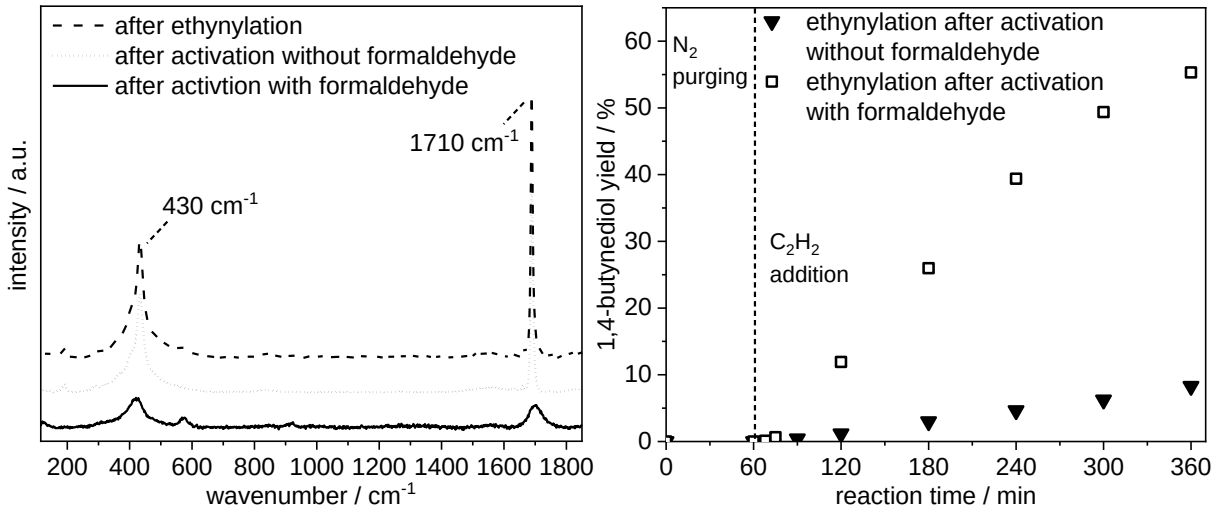

Figure 42: Raman spectra of separated Cu35Bi4-80 catalysts activated with and without formaldehyde as well as of the catalyst after the ethynylation (activated without formaldehyde) and the 1,4-butynediol yield they achieved in the ethynylation. The samples are taken with a syringe. They are measured in dry state. The laser intensity is 0.015 mW, the wavelength of the laser 532 nm. An objective with 50x magnification is used. The standard scanning time is 5 sec with 10 repetitions. The activation and ethynylation is carried out at 100°C at 1.1 bar acetylene.

The Raman spectra of the separated catalyst after activation or rather ethynylation as well as the Raman spectrum of the same catalysts activated with formaldehyde are shown in Figure 42. In addition, the catalytic performance regarding the 1,4-butynediol yield is shown as well. It can clearly be figured out that the activation without formaldehyde leads to the formation of highly crystalline Cu_2C_2, which is assigned to the narrow Raman peaks at 430 cm^{-1} and 1710 cm^{-1} compared to the broad peaks of the catalysts activated with formaldehyde. The 1,4-butynediol yield is much higher for the catalyst activated with formaldehyde. It underlines the importance of less crystalline and highly dispersed Cu_2C_2 for a high active ethynylation catalyst. In another experiment a precipitated CuO/Bi_2O_3 (CuO/Bi_2O_3-450) catalyst without SiO_2 support but the same Cu amount is applied to investigate if the SiO_2 support is essential for a high formation rate of 1,4-butynediol. The performance of the catalyst is compared to a SiO_2 supported catalysts calcined at the same temperature (Cu35Bi4-450). The 1,4-butynediol yields are shown in Figure 43 and the formation rates of 1,4-butynediol (BD) are summarized in Table 5.

It can clearly be figured out that the unsupported catalyst produces by far less 1,4-butynediol. In addition, the formation rate is much lower. It means that the SiO_2 support is very important, most likely to gain a high distribution of Cu_2C_2, which is precipitated during the ethynylation. Catalysts containing Cu, which is precipitated onto mesoporous SiO_2 with high BET surface area, are also very efficient (around 60 % 1,4-butynediol yield after 5 h). It supports the assumption that the SiO_2 support is very important in this type of catalysts by creation and stabilization of highly distributed Cu_2C_2.

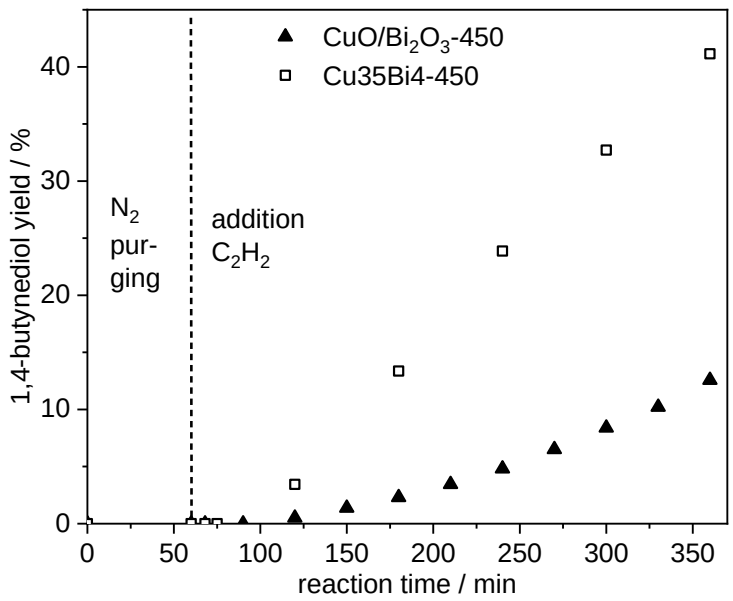

Figure 43: Yields of 1,4-butynediol using Cu35Bi4-450 and an unsupported CuO/Bi_2O_3-450 catalyst. The reaction is carried out at 100°C with 1.1 bar acetylene. The product analysis is done by GC.

Table 5: Formation rates of 1,4-butynediol of unsupported CuO/Bi_2O_3 catalyst and Cu35Bi4-450.

catalyst	$g_{BD}g_{Cu}^{-1}h^{-1}$
Cu35Bi4-450	3.1
CuO/Bi_2O_3-450	1.0

Furthermore, an experiment is carried out using a Cu salt (Cu acetate) dissolved in the formaldehyde solution and additional SiO_2 support. Dissolved Cu should form Cu_2C_2 instantly after the addition of acetylene. Hence, 1,4-butynediol should be formed simultaneously with high yields. The 1,4-butyediol and propargyl alcohol yields are shown in Figure 44 and are compared to Cu35Bi4-80, which is the most efficient catalyst. The formation rates of 1,4-butynediol (BD) are depicted in Table 6.

Interestingly, the 1,4-butynediol and the formation rate using Cu acetate is very low. If a leaching mechanism for Cu_2C_2 formation is considered one would expect that starting with already dissolved Cu leads to fast Cu_2C_2 formation and hence a high formation rate of 1,4-butynediol. But the opposite case can be observed.

However, the propargyl alcohol yield is two times higher using Cu acetate instead of Cu35Bi4-80 (Figure 44B). It means that probably the acetate anion decreases the overall conversion and it changes the selectivity towards propargyl alcohol. The same experiment is carried out with other Cu(II) salts like $CuCl_2$ and $Cu(NO_3)_2$. However, these anions also influence the reaction itself. The nitrate, for example, oxidizes the internal standard (1,3-propanediol) and formaldehyde. Hence, both compounds disappeared in the chromatograms after a while and the experiment could not be evaluated.

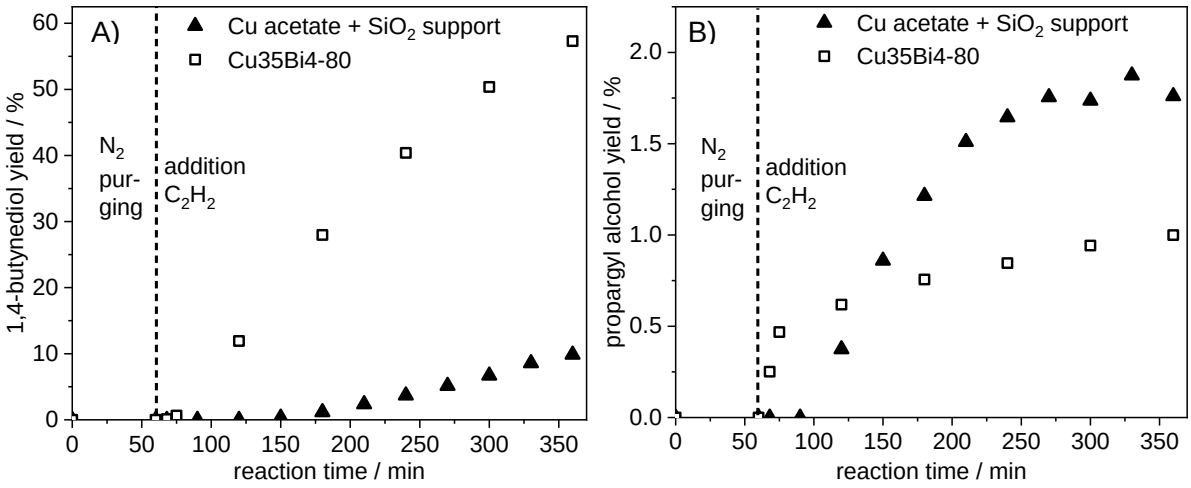

Figure 44: (A) Yields of 1,4-butynediol and (B) propargyl alcohol using Cu35Bi4-450 and Cu acetate with additional SiO_2 support. The reaction is carried out at 100°C with 1.1 bar acetylene. The product analysis is done by GC.

Table 6: Formation rates of 1,4-butynediol of Cu acetate and additional SiO_2 support as catalyst and Cu35Bi4-80.

catalyst	$g_{BD}g_{Cu}^{-1}h^{-1}$
Cu35Bi4-80	3.8
Cu acetate/SiO_2	1.0

2.4.2 Investigations using Al_2O_3 supported Cu/Bi catalysts

To strengthen the finding that Cu_2C_2 is formed via leaching mechanism the activation/ethynylation is carried out with Al_2O_3 supported Cu/Bi catalysts. The stronger support interactions between Cu and Al_2O_3 compared to Cu and SiO_2 should hinder the leaching of Cu especially after the catalyst is calcined at high temperatures forming $CuAl_2O_4$ spinel.

2.4.2.1 Synthesis of Al_2O_3 supported Cu/Bi catalysts

Al_2O_3 supported Cu/Bi catalysts are prepared by co-precipitation procedure with $Cu(NO_3)_2 \cdot 3\ H_2O$, Bi_2O_3 (dissolved in concentrated HNO_3) and $Al(NO_3)_3 \cdot 9\ H_2O$ as raw materials. The catalysts are dried at 80°C and calcined at different temperatures (450°C, 600°C, 700°C) to create different Cu/Al_2O_3 interactions. For simplification, the catalysts are labelled as follows: CuxBiyAl-z (x = Cu loading in wt.%, y = Bi loading in wt.%, z = calcination temperature, see Table 7)

Table 7: Abbreviations of the different Al_2O_3 supported catalysts and the declaration of the different numbers CuxBiyAl-z (x = Cu loading (Cu^a) in wt.%, y = Bi loading (Bi^b) in wt.%, z = calcination temperature (T_{calc}) in °C).

Abbreviation	Cu^a	Bi^b	T_{calc}
Cu35Bi5Al-80	35	4	only dried
Cu35Bi5Al-450	35	4	450
Cu35Bi5Al-600	35	4	600
Cu35Bi5Al-700	35	4	700

The Cu and Bi loadings are determined by ICP-OES (Table 8). For all catalysts, a Cu loading of almost 35 wt.% is achieved.

Besides the determination of the Cu loading, the catalysts are investigated by X-Ray diffraction to get information about the crystalline phases and crystallite sizes. The powder diffractograms are shown in Figure 45. The Cu35Bi4Al-80 catalyst, which is just dried after co-precipitation, exhibits $Al(OH)_3$ and $Cu_2NO_3(OH)_3$. It is not surprising because NaOH is used as precipitation agent. The reflexes are low in intensity, most likely caused by amorphous parts of the sample. This is why the ratio between $Cu_2NO_3(OH)_3$ and $Al(OH)_3$ could not be determined by Rietveld refinement. The samples calcined at 450°C and 600°C (Cu35Bi4Al-450, Cu35Bi4Al-600), only consist of CuO. In contrast to that, calcination at 700°C (Cu35Bi4Al-700) leads to the formation

of $CuAl_2O_4$ spinel (74.8 %) as well as CuO (25.2 %). The phase composition of the sample is determined by Rietveld refinement with a goodness of fit of 3.4.

Table 8: Cu (Cu^a) and Bi (Bi^b) loadings of the Al_2O_3 supported catalysts in wt.% determined by ICP-OES. The error is determined to be around 5% including the preparation and the ICP-OES measurement itself. BET surface area SA_{BET} in m^2/g, pore volume (V_{pore}) in cc/g, pore radius (r_{pore}) in nm as well as the crystallite sizes ($Size_{crys}$) in nm calculated with the Scherrer equation of Cu35Bi4Al-80, Cu35Bi4Al-450, Cu35Bi4Al-600 and Cu35Bi4Al-700. The error of the BET measurements is estimated to be between 5-10%.[108-110] The reflexes at 12.7 2θ and 63.6 2θ of Cu35Bi4Al-80 and the reflexes at 35.4 2θ and 38.7 2θ of the calcined samples (Cu35Bi4Al-450, Cu35Bi4Al-600, Cu35Bi4Al-700) are used for calculation of the crystallite sizes (Figure 45).

catalyst	Cu^a	Bi^b	SA_{BET}	V_{pore}	r_{pore}	$Size_{crys}$
Cu35Bi5Al-80	34.9	3.8	126	0.20	1.69	12.7 ± 4.9
Cu35Bi5Al-450	34.5	4.1	157	0.38	2.73	14.0 ± 1.3
Cu35Bi5Al-600	35.2	4.1	117	0.34	3.19	15.6 ± 0.9
Cu35Bi5Al-700	34.4	4.0	103	0.35	5.78	19.7 ± 1.2

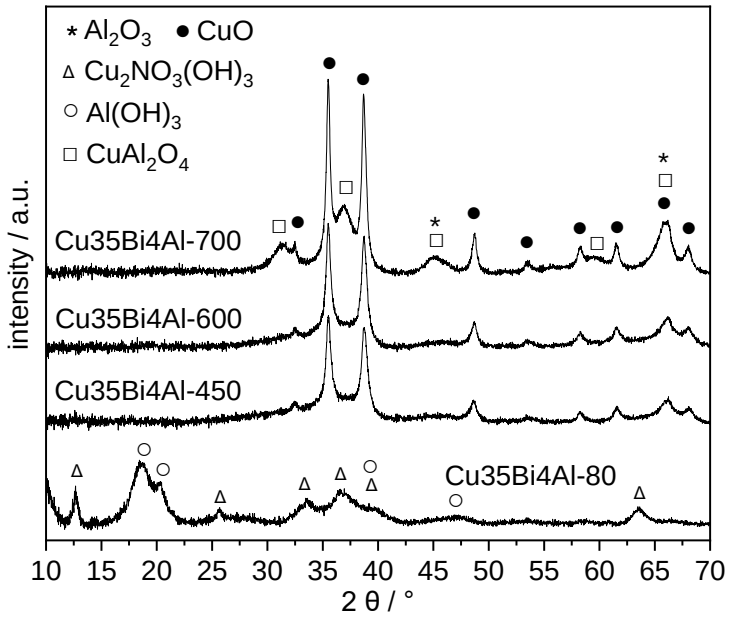

Figure 45: Powder diffractograms of Cu35Bi4Al-80, Cu35Bi4Al-450, Cu35Bi4Al-600 and Cu35Bi4Al-700. $Cu_2NO_3(OH)_3$ (triangles)[105], CuO (black dots)[106], Al_2O_3 (stars)[120, 121], $Al(OH)_3$ (circles)[122] and $CuAl_2O_4$ (quads)[123] serve as reference. The samples are calcined for 4 h with a heating rate of 2.5 K/min in air. Diffractograms are recorded in an angle range between 5° and 70° in steps of 0.013°.

The crystallite sizes are determined with the Scherrer equation and are summarized in Table 8.[100-104] Cu35Bi4Al-80 contains small $Cu_2NO_3(OH)_3$ crystallites with 12.7 nm. The value must be treated carefully because the amorphous character of the sample influences the crystallite size determination. The reflexes at 12.7 2θ and 63.6 2θ are used for determination. The CuO crystallites of Cu35Bi4Al-450 and Cu35Bi4Al-600 have almost the same size with 14.0 nm for Cu35Bi4Al-450 and 15.6 nm for Cu35Bi4Al-600. For CuO the reflexes at 35.4 2θ and 38.7 2θ serve for the crystallite size calculation. The CuO crystallites of Cu35Bi4Al-700 are the largest

with 19.7 nm. The crystallite size of $CuAl_2O_4$ could not be determined because all reflexes regarding the spinel are overlapped by reflexes either of CuO or of Al_2O_3.
The BET surface area as well as the mean pore volume and the mean pore size are determined by N_2 physisorption. The values are depicted in Table 8.
Cu35Bi4Al-450 exhibits the largest BET surface area with 157 m^2/g. Increasing calcination temperature leads to a decrease of the BET surface area. It is caused by extended blocking of pores due to larger CuO particles, disruption of the Al_2O_3 structure as well as by $CuAl_2O_4$ formation. The pore radii increase with increasing calcination temperature whereby the pore volume remains nearly constant.

2.4.2.2 Al_2O_3 supported Cu/Bi catalysts in the ethynylation of formaldehyde

The prepared catalysts are applied in the ethynylation of formaldehyde. The activation/catalytic reaction is carried out at 1.1 bar acetylene at 100°C like it was done for testing the SiO_2 supported Cu/Bi catalysts. The catalyst is used as a powder and it is suspended in 100 mL formaldehyde solution. The 1,4-butynediol yields of the different catalysts are shown in Figure 46. The N_2-purging period is separated from the activation/catalytic reaction period with a dashed line. The initialization period is by far longer for Al_2O_3 supported catalysts compared to the SiO_2 supported ones. The initializing period for Cu35Bi4Al-80 is around 30 min whereby the SiO_2 supported Cu35Bi4-80 catalyst produces 1,4-butynediol as soon as acetylene is present (Figure 32). Also, the highest yield is obtained using Cu35Bi4Al-80 with around 45 % 1,4-butynediol after 5 h. It agrees with the result achieved with the SiO_2 supported catalyst (Cu35Bi4-80; around 60 % 1,4-butynediol yield after 5 h; Figure 32) but the absolute 1,4-butynediol yield is much lower. The catalysts calcined at 450°C (Cu35Bi4Al-450) and 600°C (Cu35Bi4Al-600) follow the same trend as their SiO_2 supported counterpart but also the absolute yield is lower as well as their initializing period is more pronounced.
Dissolution of Cu from the surface of Al_2O_3 supported Cu/Bi catalysts seems to be hindered due to stronger support interactions compared to SiO_2 supported Cu/Bi catalysts. It agrees well with the results obtained with SiO_2 supported catalysts if a leaching mechanism is assumed for Cu_2C_2 formation. The Cu_2C_2 formation is hindered and consequently active Cu_2C_2 is formed slower. It becomes particularly clear by comparing the Al_2O_3 and SiO_2 supported catalysts calcined at 700°C. Whereas Cu35Bi4-700 is a very efficient catalysts (around 45 % 1,4-butynediol yield after 5 h, Figure 32) the Al_2O_3 supported counterpart (Cu35Bi4Al-700) is very inefficient (below 10 % 1,4-butynediol yield after 5 h). The formation of Cu_2C_2 originating from $CuAl_2O_4$ is extremely impeded and hence the catalytic performance of the catalyst is poor.
The formation rates of 1,4-butynediol (BD) confirm the conclusions obtained from the absolute 1,4-butynediol yields. The values are summarized in Table 9. All catalysts exhibit lower 1,4-

butynediol yields compared to their SiO_2 supported counterparts (Table 4) supporting the obtained results.

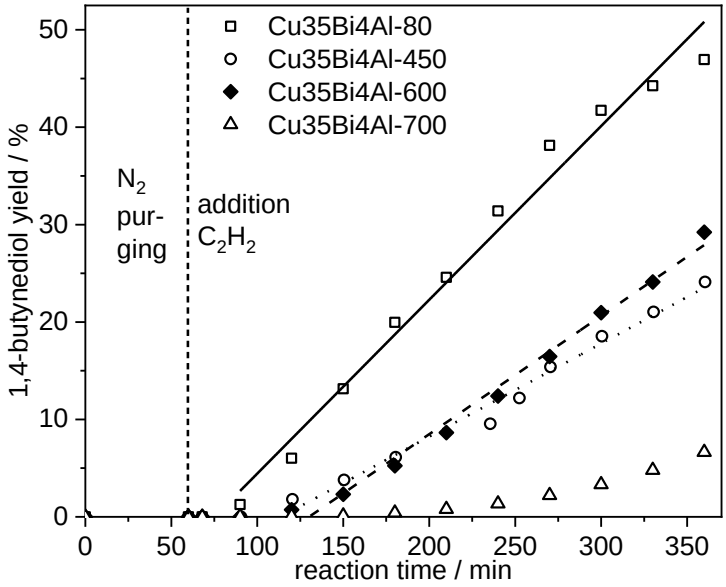

Figure 46: 1,4-butynediol yield of Al_2O_3 supported catalysts in the ethynylation reaction. The activation/catalytic reaction is carried out at 100°C with 1.1 bar acetylene. The product analysis is done by GC.

Table 9: Formation rates of 1,4-butynediol concerning the amount of Cu in $g_{BD}g_{Cu}^{-1}h^{-1}$.

Sample	$g_{BD}g_{Cu}^{-1}h^{-1}$
Cu35Bi4Al-80	3.4
Cu35Bi4Al-450	1.8
Cu35Bi4Al-600	2.4
Cu35Bi4Al-700	0.7

2.5 Conclusion

Copper(I) acetylide, Cu_2C_2, and its formation is characterized and investigated during the activation of industrial like $CuO/Bi_2O_3/SiO_2$ catalysts for the first time. New insights regarding the Cu_2C_2 formation and the catalytic reaction itself could be generated. It could be confirmed by using pure Cu_2C_2 as well as $CuO/Bi_2O_3/SiO_2$ catalysts that Cu_2C_2 is the active species in the ethynylation reaction of formaldehyde to 1,4-butynediol.

EPR studies show that the reduction of Cu(II) to Cu(I) is induced by acetylene not by formaldehyde in contrast to literature reports. Additionally, a new species is formed with a g-value of 2.00259 and corresponds to a carbon based radical.

Furthermore, Cu_2C_2 can be detected by Raman spectroscopy and X-ray diffraction. In Raman spectra it shows characteristic signals at 430 cm^{-1} and 1710 cm^{-1}. The first signal corresponds to the Cu-C σ-bonds and the second signal to the C≡C bond. The shift of the C≡C bond to lower frequencies is induced by the substitution of H^+ at both ends of the C≡C bond by Cu(I) atoms and by π-interactions to other copper atoms that decrease the order of the C≡C bond. Additionally, a clear relationship between the Cu_2C_2 formation and the catalytic activity of catalysts with different Cu loadings and different temperature treatments is proven based on the signal intensities obtained by Raman spectroscopy and based on the crystallinity obtained by X-Ray diffraction. The smaller and less crystalline the Cu_2C_2 particles are the higher is the 1,4-butynediol formation rate in the ethynylation reaction.

Determination of soluble Cu(II) via ICP-OES and conductivity measurements showed that the formation of Cu_2C_2 most likely takes place in liquid phase via dissolution/precipitation processes. Investigations with Al_2O_3 supported catalysts in which the Cu/support interactions are more pronounced underline these results.

The amount of formed Cu_2C_2 is quantified by TGA. After 4 h activation time almost 100% of the initial Cu(II) of the catalysts is converted into Cu_2C_2. The result is consistent with X-ray diffraction where the reflex intensities of CuO decrease with progressing activation time induced by the conversion of CuO into Cu_2C_2.

The lacking initializing period as well as the same 1,4-butynediol formation rate by comparing the activation and the ethynylation itself indicates that the ethynylation reaction itself takes place at the surface of precipitated Cu_2C_2.

The combination of all results leads to the following formation mechanism of Cu_2C_2 (Figure 47). Cu(II) leaches from the catalyst and dissolve in the reaction media. Dissolved C_2H_2 reacts with Cu(II) forming Cu_2C_2 like it takes place during the synthesis of pure Cu_2C_2.[71, 79, 117] Simultaneously Cu(II) is reduced to Cu(I) and C_2H_2 acts as reducing agent. Cu_2C_2 clusters are formed by agglomeration of Cu_2C_2. Due to the insolubility in the reaction medium, Cu_2C_2 clusters precipitate onto the silica support, where the catalytic reaction itself takes place on the Cu_2C_2 surface. Acetylene can coordinate to Cu_2C_2 and the triple bond is activated.

Formaldehyde is predominantly present as methanediol in aqueous solution under these reaction conditions.[28, 124] Hence, the diol coordinated to Cu(I) of Cu_2C_2 reacts with acetylene. Water is released and propargyl alcohol is formed. The same reaction takes place with another formaldehyde forming 1,4-butynediol. After desorption of 1,4-butynediol Cu_2C_2 is able to activate a new acetylene molecule to close the catalytic cycle. The reaction mechanism would correlate to a Langmuir-Hinshelwood mechanism.[89, 91, 92]

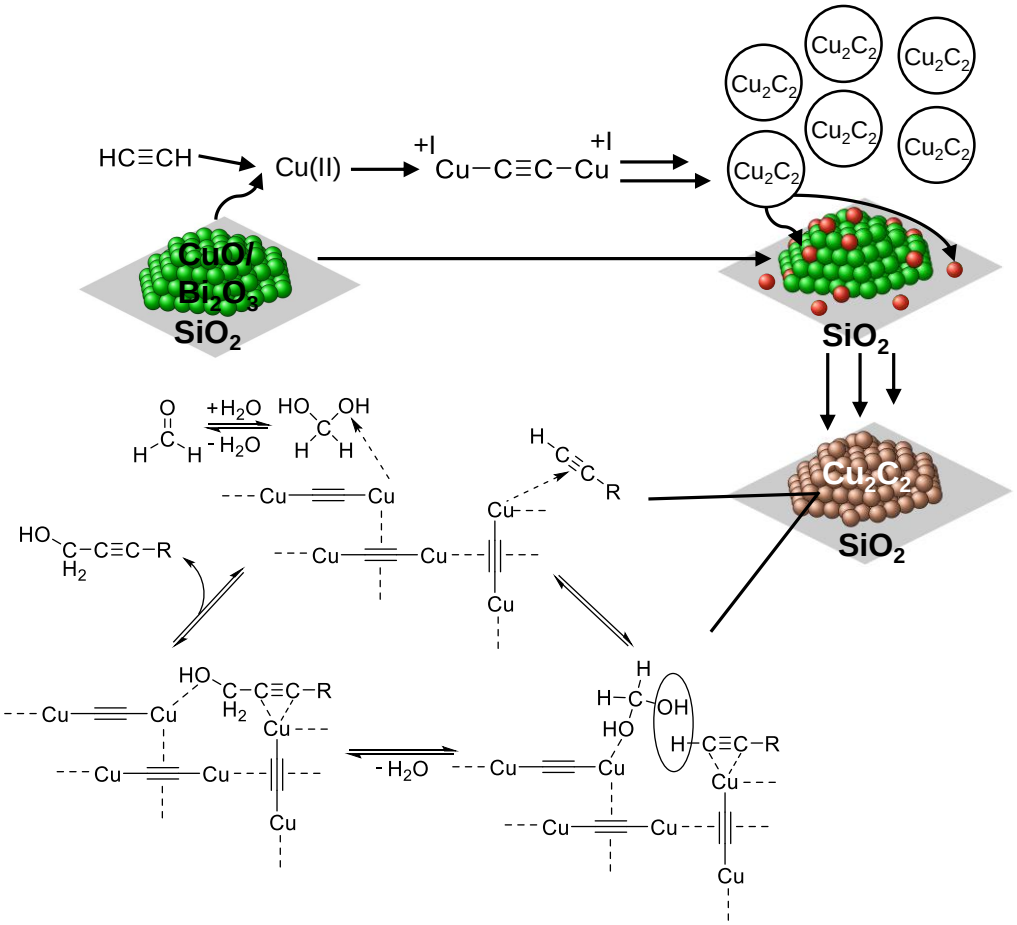

Figure 47: Proposal for the formation mechanism of Cu_2C_2 and the ethynylation mechanism on the Cu_2C_2 surface.

3

MeOH Synthesis – Synthesis of Methanol Catalysts via Diethyl Zinc Grafting on Alumina Supported Copper Nanoparticles

3.1 Introduction

Methanol is produced from syngas (see Figure 48) and is one of the most important C_1 building blocks for industrial chemicals. It is used as solvent itself or it acts as feedstock to produce base chemicals such as formaldehyde, acetic acid or methyl methacrylate.[125, 126] In addition, MeOH has the potential to use it as fuel via MTG (methanol to gasoline) especially when it is converted to dimethyl ether (DME) which is a clean burning high cetane fuel, capable of replacing Diesel fuel. DME can also act as a substitute for liquefied petroleum gas (LPG), compressed natural gas (CNG) and liquefied natural gas (LNG). Even ethylene and propylene can be produced from methanol via MTO (methanol to olefins) which could replace oil as raw material.[126, 127]

$$CO_2 + 3\,H_2 \rightleftharpoons CH_3OH + H_2O \qquad \Delta H = -49.5\ kJ/mol \qquad (1)$$

$$CO + 2\,H_2 \rightleftharpoons CH_3OH \qquad \Delta H = -90.6\ kJ/mol \qquad (2)$$

$$CO_2 + H_2 \rightleftharpoons CO + H_2O \qquad \Delta H = 41.2\ kJ/mol \qquad (3)$$

Figure 48: Reaction equations of the reactions occurring by the synthesis of MeOH based on syngas.[125, 126]

Because CO_2 is a greenhouse gas and its contribution to global warming methanol synthesis from pure CO_2 feed is of great interest.[6, 127, 128]

Despite methanol synthesis is established for many years the reaction mechanism and the active site of $Cu/ZnO/Al_2O_3$ catalysts are still discussed controversially in literature. Especially the role of ZnO is still not sure.[7, 15, 129-140] It could act as structural promotor as well as a stabilizer for the Cu particles and consequently maintaining the Cu surface area.[141] Another proposal is the so-called spillover model that ZnO acts as a reservoir for H_2.[142] In addition to that, ZnO could be important for bond activation especially for oxygen containing intermediates.[15, 138] *Martin et al.* found out that CO adsorbs preferably on Cu sites that are near to ZnO.[138] Besides ZnO acting as promotor itself Zn can interact with Cu to form Zn-Cu sites. *Lunkenbein et al.* showed that even during the reductive activation, ZnO overlayers can be formed due to strong metal-support interactions with Cu. Furthermore, it is possible that Zn(II) is partially reduced at the interfaces between Cu and ZnO. It is conceivable that a Zn-Cu, a ZnO-Cu or a ZnCu-alloy species act as active site.[15, 129, 135]

Hence, the interaction between Cu and Zn plays an important role. In this work, Al_2O_3 supported bimetallic Zn/Cu nanoparticles are synthesized in which Zn is exclusively deposited onto the Cu surface by surface organometallic chemistry (SOMC). The catalysts are characterized by multiple methods including TEM-EELS, XPS or IR spectroscopy. MeOH synthesis is carried out at 28 bar with pure H_2/CO_2 = 3/1 feed.

3.2 Theoretical background

In this chapter the MeOH synthesis is described in general, how the reaction is applied on industrial scale and which challenges appear by using a pure CO_2 feed. In addition, the reaction mechanism and the catalytic active site, which is still discussed controversially in literature, are presented. It includes especially the role of Zn in $Cu/ZnO/Al_2O_3$ catalysts, which are the commonly used catalyst in the industrial process.

3.2.1 MeOH synthesis

Global methanol production in 2016 was around 85 million metric tons. A standard methanol plant produces up to 5000 metric tons methanol per day. Even larger plants with capacities of around 10 000 metric tons methanol per day are planned.[126] On industrial scale the low pressure methanol process (LPM) is established. The reaction conditions vary between 200 and 300°C at 50 to 100 bar. Most of the new methanol plants are constructed to work between 80 to 100 bar. The gas feed consists of syngas containing $CO/CO_2/H_2$ (10:10:80). The CO_2 content amounts up to 30% in some plants.[7, 125, 126]

Adiabatic or quasi-isothermal reactors are commonly used in industry. In the first reactor type, several catalyst beds are arranged axially in series and the heat of reaction is removed by intermediate coolers. In these reactors, syngas flows axial, radial or axial/radial. In the second reactor type, the catalyst is located in tubes that are surrounded by boiling water for heat of reaction removal. Syngas flows axially through the tubes.[143]

The reaction equation for methanol formation from CO and CO_2 as well as the reverse water-gas shift reaction (RWGS) are shown in Figure 48.[125, 126]

Methanol formation is favored by low temperatures and high pressures according to Le Chatelier's principle. All three equilibrium reactions occur simultaneously. The equilibrium conversions can be calculated using a suitable equation of state mode, e.g., the Soave Redlich-Kwong model (SRK). For a standard synthesis gas containing CO, CO_2, and inerts (15 vol.% CO, 8 vol.% CO_2, 74 vol.% H_2, and 3 vol.% CH_4) the equilibrium conversions at different conditions are shown in Figure 49. With increasing temperature, the RWGS reaction is dominant whereas the reaction pathway towards methanol is not favored.[143]

Commonly used catalysts are based on $Cu/ZnO/Al_2O_3$ containing 60% CuO, around 30% ZnO and 10% Al_2O_3. The active catalyst contains metallic Cu, which is generated by reductive pretreatment. Selectivity up to 99.5 % can be achieved. Despite high methanol selectivity the product gas stream consists of impurities, mainly water. The crude methanol must be purified by several distillation steps.[7, 125, 126]

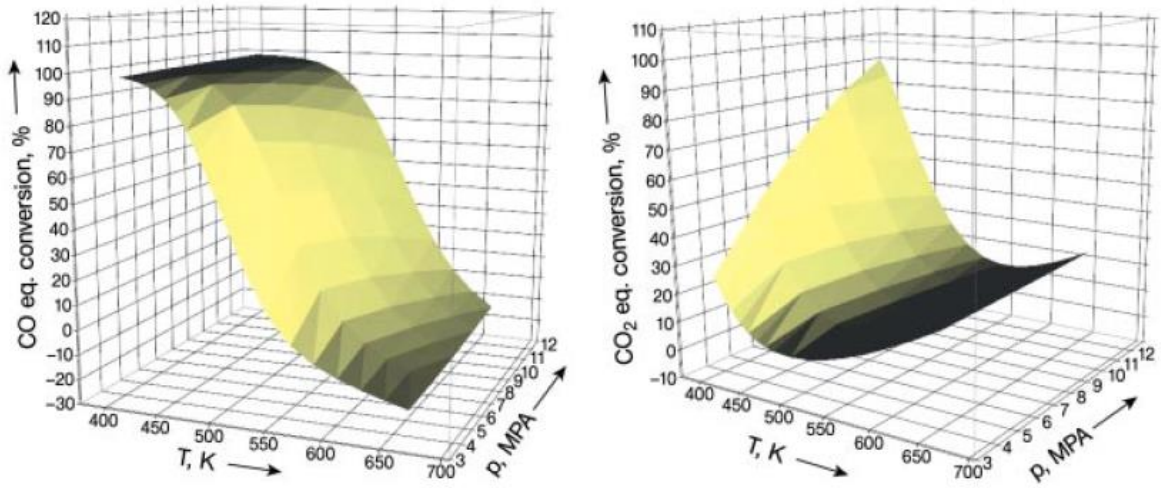

Figure 49: Dependence of reaction equilibrium on pressure and temperature regarding CO and CO_2 conversion published in *Ullmann's Encyclopedia of Industrial Chemistry*.[143]

Due to the environmental debate and consequently the role of CO_2 as greenhouse gas leads to the task to use CO_2 as C_1 building block. Therefore, methanol synthesis from pure CO_2 feed is of great interest. Around 35 000 million tons of CO_2 were released in 2018. The CO_2 concentration in the atmosphere reached 407.65 ppm in September 2019, which is an increase of around 20% over the last 40 years. Therefore, it is indispensable that CO_2 must be captured and reused. CO_2 itself is thermodynamically and chemically stable. Hence, much energy is needed to use it as single reactant. By introducing another reactant with higher Gibbs free energy such as H_2, the conversion of CO_2 becomes thermodynamically much easier. That is the reason why CO_2 hydrogenation for example to methanol is very promising.[6, 125-128]

The required CO_2 can be captured from different sources like from the combustion of natural gas, high-concentration exhausts of power plants, various chemical plants, cement plants, fermentation plants (breweries) or many more. H_2, nowadays, is mainly produced from fossil fuels by steam reforming, partial oxidation of methane or coal gasification. However, with the help of renewable energy such as solar/wind power, photovoltaic cells, or geothermal power H_2 could be produced via water electrolysis. In Iceland (at the *Svartsengi* geothermal power station) the first *CO_2-to-Renewable Methanol Plant* was built by *Carbon Recycling International (CRI)*. At this plant, more than 4 million liters of methanol are produced, and 5 500 tons of CO_2 are recycled per year. In this case, H_2 has already been supplied via water electrolysis. The use of the renewable methanol plant release 90% less CO_2 in comparison to the use of a comparable amount of energy from fossil fuels.[6, 126]

3.2.2 Reaction mechanism on Cu/ZnO/Al_2O_3 catalysts

Despite the methanol synthesis is established since many years the reaction mechanism is still discussed controversially in literature. Because in this work methanol synthesis is exclusively based on pure CO_2 feed, this part focusses mainly on the reaction mechanism originating from CO_2.

Grabow et al. investigated the reaction by density functional theory (DFT) and developed a microkinetic model based on elementary steps. They mainly studied CO_2 hydrogenation as the main reaction, but they also include different CO and CO_2 hydrogenation pathways, the water-gas shift (WGS) reaction, and the formation of possible byproducts and intermediates, such as formic acid and formaldehyde. Due to extensive DFT calculation they made no assumptions regarding the rate limiting step or the reaction mechanism itself. They used the Cu(111) surface as basis of their calculations. In Figure 50 the potential energy surface of methanol synthesis via CO_2 hydrogenation is shown.[130]

After the adsorption of CO_2 and hydrogen a formate species (HCOO*) is formed which is the most prominent intermediate at the start of the mechanism of methanol synthesis and many studies were published investigating it.[144-150] Despite the HCOO* species could be formed via a carbonate species (CO_3*) or the decomposition of formic acid (HCOOH) the direct CO_2* hydrogenation is the preferred pathway due to the barrier of only 0.87 eV and an exothermicity of -0.25 eV. On the basis that breaking the C-O bond of the HCOO* species is very unlikely a stepwise hydrogenation takes place forming dioxymethylene (H_2CO_2*, red line) or formic acid (HCOOH*, black line). It turned out that the HCOOCH* is more stable and that the formation is less endothermic that the formation of H_2CO_2*. Further hydrogenation leads to the formation of CH_3O_2*. C-O bond breaking and the release of OH* forms the CH_2O* species. For the formation of methanol two hydrogenation pathways would be possible, either via a methoxy (CH_3O*) intermediate or its isomer hydroxymethyl (CH_2OH*). The hydrogenation step of CH_3O* to CH_3OH* has the highest individual energy barrier (E_a = 1.17 eV), but the whole energy trace lies permanently lower than the energy trace for the CH_2OH* pathway. The higher stability and consequently the higher surface coverage of CH_3O* compensates the high activation barrier for the last hydrogenation step. The RWGS reaction that occurs simultaneously as the methanol formation takes place via a COOH* species which reacts to CO* and OH*. Another possibility is the direct dissociation of CO_2.[130] The RWGS and methanol synthesis pathways are independent on Cu/ZnO/Al_2O_3 catalysts, which means both reactions do not share an intermediate in the rate-determining step (RDS).[151] In addition, *Yang et al.* indicate that methanol production from CO formed by the RWGS is hindered because the first hydrogenation to formyl is suppressed. Formyl is not a stable intermediate and dissociate into CO* and H*.[150]

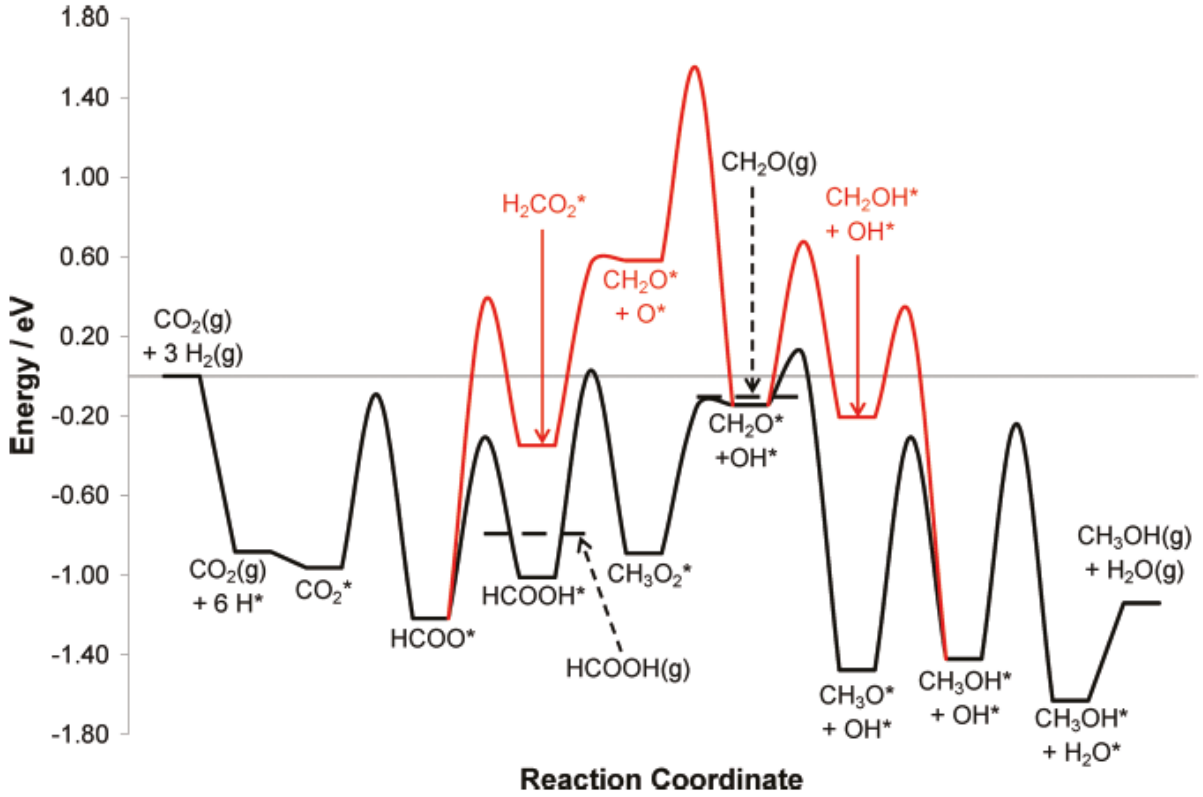

Figure 50: Potential energy surface of methanol synthesis via CO_2 hydrogenation concerning two possible reaction pathways calculated by *Grabow et al.*[130]

The reaction pathway based on CO is a bit different. Two different pathways are possible, either the direct hydrogenation via HCO*, H_2CO* and H_3CO* or the formation of a formate species and a similar pathway than that based on CO_2.[14, 15, 130, 152, 153] The mechanism via the formate species would require additional oxygen atoms which are not present in a pure CO/H_2 feed. In this case, it is assumed that oxygen atoms of the support, especially basic supports, could play a role. If the oxygen atoms of the support are not available and no CO_2 is present, it is very likely that the direct hydrogenation pathway is the main methanol formation route.[152, 153]

As noted in the section before (3.2.1), a typical syngas feed in industry consists of CO and CO_2. It is still not clear in which extent both reactants contribute to the different hydrogenation pathways. *Grabow et al.* found out that methanol is primarily produced via the CO_2 pathway and less via the CO pathway (direct hydrogenation). One would assume that the CO pathway is preferred because it is more exothermic and there exists a high barrier to form H_2O* from OH* in the pathway of CO_2 (see Figure 50). But the competitive pathway of CO* + 2OH* → COOH* + OH* and finally to CO_2* + H_2O (WGS reaction) has only a small barrier. This reaction does not only consume CO, but it also bypasses the highly activated OH* + H* → H_2O +* step. That is why CO contributes to the hydrogenation of CO_2.[130]

The hydrogenation of CH_3O* is slow and consequently the product of CH_3O* and H* describes the behavior of overall methanol synthesis rates for a large range of conditions and CO_2-rich

reed compositions. *Kunkes et al.* propose that analogically to hydrogenation of aldehydes the formate hydrogenation is the rate-determining step for CO_2 hydrogenation.[151, 154, 155]
For CO-rich feeds, the formation of CH_3O* could become rate limiting which leads to a volcano-shaped curve for methanol production as a function of the CO_2 / (CO + CO_2) feed ratio.[130]
Behrens et al., *Studt et al.* and *Kattel et al.* also calculated the reaction mechanism via DFT, mainly for CO_2 hydrogenation to methanol. It turned out that the reaction intermediates and the barriers are very similar to that calculated by *Grabow et al.*.[14, 15, 135, 156]
Another approach for CO and CO_2 hydrogenation and to combine both pathways was published by *Yang et al.* in which the carboxyl species (COOH*) that is formed during the WGS/RWGS reaction serves as starting intermediate (see Figure 51). Hydrogenation to a carbene diol species (HOCOH*), release of OH* (forming methynol, COH*) and stepwise hydrogenation leads to methanol. This pathway can be followed by both CO and CO_2.[157]

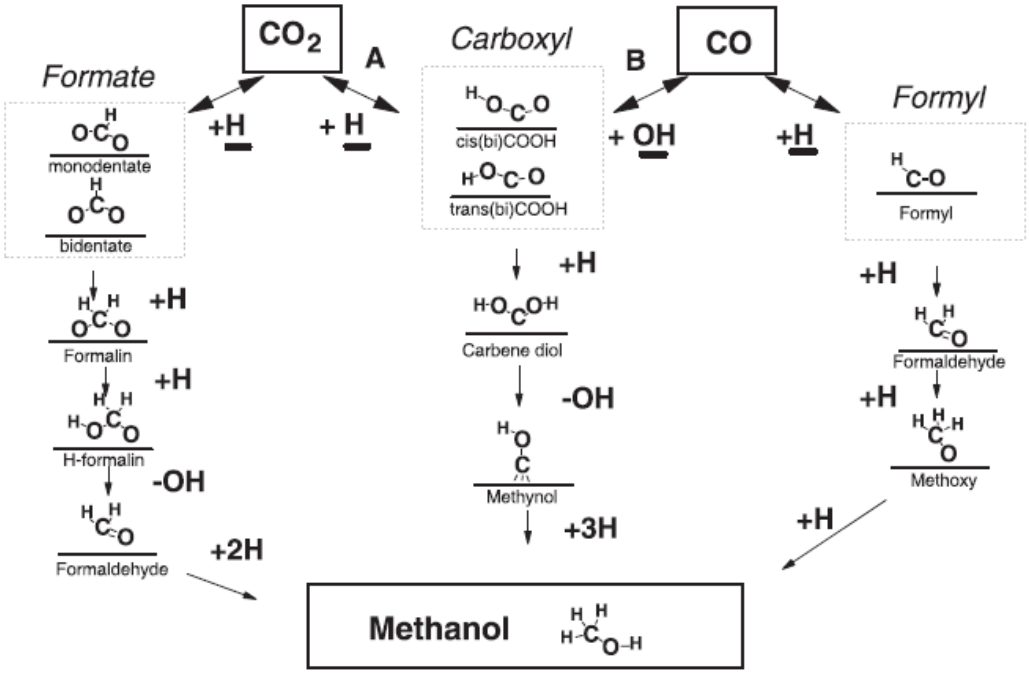

Figure 51: Reaction mechanism and the different intermediates for methanol synthesis via CO and CO_2 hydrogenation concerning three possible reaction pathways published by *Grabow et al.*[157]

Industrial catalysts contain not only Cu but also Zn. Zn has also an impact on the methanol formation mechanism and its influence will be discussed in the next chapter (3.2.3).
Besides the reaction mechanism it was discussed controversially in literature what is the main carbon source in methanol synthesis.
Chinchen et al. carried out isotope labeling experiments using ^{14}C-labelled reactants. It clearly turned out that CO_2 serves as main carbon source in all common CO_2/CO/H_2 feeds using Cu/ZnO/Al_2O_3 catalysts. However, methanol formation from CO is possible but only at very low levels of CO_2 and adsorbed oxygen on the Cu surface.[158] *Yang et al.* confirmed the result but

at low temperatures (< 443 K) the carbon source switches from CO_2 to CO. They assume that in their alternative reaction mechanism, which was described above, at lower temperatures the formation of the carboxyl species (COOH*) from CO gets easier due to the lower effective activation energy of CO compared to CO_2.[157] Nowadays, it is widely accepted in literature that CO_2 is the main carbon source in methanol synthesis in $CO/CO_2/H_2$ feeds.[7, 159, 160]

3.2.3 The role of Zn and the active site in $Cu/ZnO/Al_2O_3$ methanol synthesis catalysts

There are many proposals about the active site of $Cu/ZnO/Al_2O_3$ catalysts. Especially the role of Zn is still not sure, and many approaches exist to clarify it. In this section, the different active site concepts of $Cu/ZnO/Al_2O_3$ catalysts are presented especially regarding the interplay between Cu and Zn. The publications that are introduced mainly focus on applying $CO/CO_2/H_2$ or pure CO_2/H_2 feed compositions.

Cu alone can catalyze the methanol synthesis from syngas. Previous studies showed that the reaction is structure sensitive by applying foils or single crystals with different defined Cu surfaces like Cu(100), Cu(110), Cu(111), Cu(211), Cu surfaces with high index planes and many more.[129, 135, 161-167]

However, despite Cu itself acts as methanol synthesis catalyst it is widely accepted that Zn has a great influence on the activity and selectivity of methanol synthesis catalysts and there are many approaches that try to explain the synergy between Cu and Zn.[15, 129, 135, 168]

Cu-Zn alloy concept

Nakamura et al., *Fujitani et al.* and others published a series of studies using Zn deposited defined Cu surfaces in the form of foils or single crystals as catalyst.[145, 146, 164, 169-173] *Nakamura et al.* assume a Cu-Zn surface alloy as active species for CO_2 hydrogenation to methanol.[129] *Choi et al.* confirms it by applying a physical mixture of Cu/SiO_2 + ZnO/SiO_2 as catalyst.[174] Both metals are metallic during the catalytic reaction because no oxygen was found on Zn/Cu(111) which they used as model catalyst by post-reaction surface analysis via XPS. They propose that Zn facilitate the hydrogenation of the formate species to the methoxy species. The formate species is bound to Zn and Cu forming a bridging bidentate species that is also reported by other groups.[129, 171, 173, 175-177] A Zn coverage of θ_{Zn} = 0.19 leads to a maximum TOF for methanol synthesis. Lower or higher Zn coverages decrease the TOF.[129, 155] The group could also show that Zn has no promotional effect on the RWGS which means that for RWGS only the pure metallic surface acts as active site. Both sites, the metallic Cu as well as the Cu-Zn site, work cooperatively to catalyze the methanol synthesis reaction because metallic Cu is necessary for the hydrogenation reactions during the catalytic cycle. It also turned out that the Cu-Zn surface alloy is more stable than bulk alloy under reaction conditions.[129, 172]

The Cu/Zn surface alloy has already been formed during reductive pretreatment at 523 K in a co-precipitated catalyst, which disagrees with the results obtained by *Poels et al.* (catalyst: $Cu/ZnO/SiO_2$ by deposition precipitation), *Viitanen et al.* (catalyst: $^{63}Cu/^{68}ZnO/SiO_2$ by deposition precipitation) and *Grunwaldt et al.* (catalyst: Cu/ZnO by co-precipitation) where alloy formation takes place only at high reduction temperatures (>700°C).[129, 178-181] The alloy formation is induced by migration of Zn into the Cu lattice. The alloy formation starts at the steps on the surface of Cu nanoparticles. When Zn migration proceeds it is distributed homogeneously over the whole Cu particle. The activation energy for Zn migration was estimated to be 24.7 ± 9.0 kJ/mol.[182] The Zn content in the Cu particles was found to be around 13-17 %.[129, 183, 184] Cu-Zn alloy formation even below 600 K was reported *Herwijnen et al.* and *Spencer et al*..[142, 182, 185-189] Both groups observed α-brass formation and especially *Spencer et al.* investigated the thermodynamic and kinetic aspects of the formation of it. *Spencer et al.* also claimed that the high specific activity of Cu/ZnO catalysts derived from α-brass formation.[142, 186-190] *Kuld et al.* investigated the Zn coverage (θ_{Zn}) in the Cu surface during methanol synthesis using $Cu/ZnO/Al_2O_3$ catalyst in more detail. It turned out that small ZnO nanoparticles in the catalyst precursor enhance the migration of Zn and consequently the θ_{Zn}. In contrast to *Nakamura et al.* they propose that a θ_{Zn}= 0.47 is most beneficial towards the relative methanol activity. Their explanation for the difference is the coverage of ZnO of the Cu nanoparticles under reaction conditions applied by *Nakamura et al.*.[134] To quantify the Zn atoms on the surface *Kuld et al.* combined XPS, H_2-TPD (temperature programmed desorption), N_2O-RFC (reactive frontal chromatography) and H_2-TA (transient adsorption) measurements.[131, 134] With N_2O-RFC the metallic Cu surface area and the oxygen defects which are present at the Cu/Zn interface can be detected. H_2-TPD serves exclusively for the determination of the metallic Cu surface area. Both methods combined, quantitative measurements of oxygen vacancies in methanol synthesis catalysts become feasible.[191] *Kuld et al.* clearly showed the incorporation of metallic Zn into the Cu surface under reductive conditions at around 500 K in H_2. Cu is needed to promote the reduction of ZnO and does not change its surface geometry during the pretreatment. Under reaction conditions, they claim that Zn is most likely in its metallic state like *Nakamura et al*. but they do not exclude that Zn could be oxidized by oxygen containing intermediates.[131, 134]

Cu-$Zn^{\delta+}$ concept

Laudenschleger et al. and *Behrens et al* propose that under reaction conditions (CO_2 hydrogenation to methanol) Zn exists in an oxidized form originating by oxidation of Cu-Zn surface alloy or by reduction of ZnO forming Cu^0-$Zn^{\delta+}$ interface sites.[15, 192] *Behrens et al.* investigated several $Cu/ZnO/Al_2O_3$ catalysts concerning their Cu metal surface areas and their catalytic performances. It turned out that no linear fit between both properties could be found, which

confirmed the results obtained by *Lunkenbein et al.* and *Zander et al.*.[15, 132, 193] Hence, *Behrens et al.* examined the structure of the Cu nanoparticles and they could show that a high stacking fault concentration leads to a high catalytic performance. In addition, they did DFT calculation to confirm the result and to determine the effect of Zn using a Cu(111), a Cu(211) and a CuZn(211) surface. It turned out that the CuZn(211) increases the adsorption strength of oxygen bounded intermediates and decreases the energy barriers. They conclude that due to the higher oxophilicity of Zn compared to Cu, Zn exists partially oxidized during steady-state reaction conditions. Due to the fact that Cu(111) surface is quite inactive according to the DFT calculations they could confirm that steps and consequently defect sites are required at the Cu surface to give a high catalytic performance. In addition, $Zn^{\delta+}$ is needed at these defect sites (Cu(211)) which strengthen the binding of the oxygen bound intermediates and form Cu-$Zn^{\delta+}$ sites.[15] The importance of defect sites was reported by *Kasatkin et al.* as well.[133] *Laudenschleger et al.* also reported a Cu-$Zn^{\delta+}$ site to be the active site. Their results base on partially poisoning of the active sites with NH_3 and different types of methylamines using a new developed high-pressure pulse method.[192] In addition, *Zander et al.* also showed that Zn is needed directly on the Cu by replacing ZnO with MgO, which has similar properties as ZnO. MgO does not form an overlayer on the Cu particles and hence the catalytic performance in CO_2 hydrogenation decreased a lot.[193] *Naumann d'Alnoncourt et al.* confirm the presence of Zn in an oxidized state even without CO_2 in the gas feed (strongly reducing conditions). They also completely rule out that Cu is oxidized meaning Cu exists in its metallic state.[194, 195]

Kattel et al. synthesized different well defined model systems based among other things on Cu(111) (Cu(111), ZnCu(111), ZnO/Cu(111)) which was previous studied by other groups as active Cu surface.[135, 196] They compared the experimental results (mainly catalytic performance and XPS-spectra) to DFT calculations and kinetic Monte Carlo (KMC) simulations. ZnCu(111) represents Cu-Zn alloy and ZnO/Cu(111) simulates the inverse ZnO/Cu motif. XPS measurements showed that no Cu-Zn alloy formation takes place with H_2 rich CO_2/H_2-feed as well as under typical reductive pretreatment with pure H_2 using ZnO/Cu(111). The Zn of ZnCu(111) is oxidized to ZnO under reaction conditions. After low catalytic performance at the beginning the amount of methanol increases using ZnCu(111) and achieves the values of ZnO/Cu(111) after certain time. Hence, they conclude that ZnO/Cu(111) must be the active surface. In further experiments they compared a Cu/ZnO and ZnO/Cu/ZnO catalyst concerning their catalytic performance. A large increase in activity was observed using ZnO/Cu/ZnO as catalyst which underlines the importance of inverse ZnO-Cu interface for methanol synthesis on Cu/ZnO catalysts. They did also not find any hints of ZnO reduction. The DFT calculations confirm the presence of an oxidized Zn species during the catalytic reaction because of direct dissociation of CO_2* to CO* and O* which competes with the hydrogenation to HCOO* (see

chapter 3.2.2). The reaction pathways are very similar for ZnO/Cu(111) and ZnCu(111). For both catalysts, the addition of Zn or ZnO helps to stabilize the HCOOH* intermediates and activating HCOO* which agrees with the results of *Behrens et al.*.[15, 135] In summary, *Kattel et al.* indicate that Cu-Zn surface alloy is not the active catalysts itself but the well dispersion of Zn sites leads to well dispersed ZnO on the top of the Cu particles under reaction conditions which results in an increase of active Zn-O-Cu sites.[135] *Zabilskiy et al.* come to similar conclusions doing high-pressure operando measurements using different Cu based catalysts.[197]

ZnO overlayer

Lunkenbein et al. indicate that during the reductive pretreatment a graphitic like ZnO overlayer is formed onto the Cu nanoparticles by investigating industrial like $Cu/ZnO/Al_2O_3$ catalysts.[132] *Schott et al.* confirm that by DFT calculations, FT-IR measurements and XPS.[198] The results of *Lunkenbein et al.* mainly base on TEM-EELS, HRTEM, N_2O-RFC and H_2-TA. In long-term experiments (148 days) they could show that the overlayer is transformed into a dense and nanocrystalline ZnO surface with around 5 nm thickness located on the Cu nanoparticles. They propose that Cu-ZnO or even $Cu^{\delta+}$-O-ZnO serves as active site. Despite the Cu nanoparticles are covered by ZnO, the catalysts activity remains high and, furthermore, they assume that the Cu surface is part of the active site. In addition, they note that even when the Cu surface is fully covered by nanocrystalline ZnO a Cu surface area can be measured by H_2-TA meaning that some Cu must be still accessible. They explain the discrepancy that by TEM imaging only 2D images are observed and consequently the accessibility of the Cu surface cannot be detected. Furthermore, they assume that this contradicting observation could be caused by certain penetration pathways in the polycrystalline ZnO overlayer.[132, 199] *Jansen et al.* also reported of ZnO layer on top of the Cu nanoparticles after reductive pretreatment.[200]

Role of Zn as structural promoter

In addition, ZnO can act as a structural promoter in the form of a spacer to prevent sintering of the Cu particles.[201, 202] *Fujitani et al.* found out that the addition of Zn leads to a nine-fold larger surface area by measuring the Cu metal surface area via N_2O-RFC. The addition of Zn leads to a high dispersion of the Cu nanoparticles, which is definitely needed despite no linear relationship between the Cu metal surface area of the catalyst and activity in methanol synthesis can be found.[15, 166, 183, 203-209] It also turned out that co-precipitation is the most suitable preparation method to create a very active methanol synthesis catalyst with high Cu dispersion and strong Cu/Zn interactions.[183, 206] Aurichalcite $(Cu,Zn)_5(CO_3)_2(OH)_6$ is an excellent precursor for Cu/ZnO catalysts.[193] Furthermore, *Zander et al.* indicate that zincian malachite $(Cu,Zn)_2(OH)_2CO_3$ precursor leads to crystallization of distorted Cu crystallite which are known

to be favorable for a high catalytic activity in methanol synthesis.[186, 193] *Behrens et al.* confirm it. They indicate that the zincian malachite which is formed during the co-precipitation and subsequent ageing thin needles crystallize which determines the porous structure of the final catalyst. Subsequent calcination leads to small CuO and ZnO nanoparticles.[210]

Besides acting as spacer itself, Zn influences the structure of the Cu particles.[203] *Naumann d'Alnoncourt et al.* propose that the wetting of the Cu nanoparticles with Zn leads to a shape change of the particles. The particles change from spherical structure without Zn to flatter particles after wetting with Zn.[194, 195] Water causes a similar effect on the shape of the Cu nanoparticles. *Grunwaldt et al.* investigated the influence of water on the active site by applying alternating "dry" syngas and "wet" syngas (addition of water) conditions. It turned out that under reducing conditions ("dry" syngas) the activity of the catalyst increases. Like *Naumann d'Alnoncourt et al.* they propose that the morphology of the Cu particles changes but, in this case, induced by water. It means under reducing conditions flat particles are present that have a higher surface area and Cu atoms with low coordination numbers than the particles during "wet" syngas conditions. The activity increase drops after several alternations between both syngas conditions. According to the authors, it is caused by sintering which is induced by the addition of water.[178] *Hansen et al.* and *Vesborg et al.* found out that even an oxidizing gas feed leads to more spherical Cu particles whereas reducing gas feed leads to flatter Cu particles.[211-213] *Hadden et al.* propose that also without Zn the Cu particle morphology changes only by applying alternating CO/H_2 and CO_2/H_2 feed gas. However, reduction with H_2 leads to the initial Cu particle morphology indicating that Cu surface is continuously reconstructed during methanol synthesis.[214]

Importance of the morphology of ZnO

On top of the role of Zn forming strong interactions or acting as structural promoter, there are also approaches that the morphology of the ZnO itself in $Cu/ZnO/Al_2O_3$ catalysts could be important. In contrast to *Hansen et al.*, *Grunwaldt et al.* and *Naumann d'Alnoncourt et al.*, *Martin et al.* indicate that the Cu nanoparticles morphology (cuboctahedral) does not change during methanol synthesis no matter which feed gas compositions are applied. They explain the discrepancy by the 10 times higher Cu loading of their catalyst system. Slight sintering of Cu particles is induced by segregation of Cu from ZnO under CO/H_2 feed gas and is further supported by H_2O during CO_2/H_2 feed gas conditions. Unlike the consistent morphology and slight sintering of the Cu nanoparticles, the ZnO particles grow a lot under CO_2/H_2 feed gas and platelet-like particles are formed. This structure leads to a higher methanol selectivity because of improved electronic interactions between Cu and Zn.[138, 209, 215]

H_2 spillover

Besides the role as electronic promotor by forming strong Cu/Zn interactions and as structural promotor studies were published in which Zn acts as hydrogen reservoir by spillover from ZnO to Cu.[142, 216, 217] *Burch et al.* indicate that H_2 spillover takes place even if ZnO and Cu are not in direct contact. Due to the H_2 spillover, ZnO becomes hydrated or hydroxyl groups are formed. Mobile hydroxyl groups could migrate to the Cu surface forming active adsorption sites.[216] In another study they verified their results by applying different support materials for methanol synthesis catalysts. They found out that the promotional effect of the support increases in the order: $SiO_2 < Al_2O_3 < ZrO_2 < Ga_2O_3 < ZnO$. According to *Burch et al.* ZnO is the most beneficial support because of the most distinguished H_2 spillover.[208]

Junction effects

Another concept that is not very popular is the formation of junction effects. Junction effects occur when the support is partially reducible. Reducing conditions lead to ionized oxygen vacancies.[218] *Frost et al.* state that the concentration of ionized oxygen vacancies $[V_0^{++}]$ in ZnO is in the region of 5×10^{16} cm^{-3} under 0.1 CO_2/CO gas ratio at 523 K. The surface concentration (if it is assumed that the gas-solid interface is around 1 nm) is around 10^9-10^{10} cm^{-2}. If a metal is present (in this case Cu) the electrons produced by ionizing the oxygen vacancies are distributed between the oxide conduction band states and the states available at the metal Fermi level (E_f). The conduction band edge (E_c) for these oxides is much higher than E_f. Hence, a net transfer of charge from the oxide to the metal takes place. Normally the energy needed for the formation of an oxygen vacancy is high. But the allowance that the electrons can move to the metal Fermi levels lowers the energy. The promotional effect of these oxygen vacancies is explained as follows. At these sites, H_2 can dissociate forming a hydride by using an electron from the support. It leads to an imbalance between E_c and E_f and consequently H_2 is incorporated into the support. The carbon species (CO) can insert and further hydrogenation leads to the formation of MeOH. The final desorption of methanol is difficult because the electrons associated with the ions must remain at the solid. Either the lower energy metal Fermi level is available or concerted chemisorption of reactants at another vacancy site provides an even more willing acceptor state. Both could be accountable that the desorption of uncharged methanol can occur.[218] *Waugh et al.* stated that according to their studies no junction effects arise in methanol synthesis catalysts.[219]

Cu^+ as active Cu species

In all the presented concepts up to here, Cu is in its metallic state during the CO_2 hydrogenation to methanol. But there also publications in which it is proposed that Cu exists in an oxidized

form.[163, 167, 186, 200, 220-225] *Kanai et al.* determined the oxygen coverage of Cu by N_2O adsorption and subsequent reduction. It turned out that an oxygen coverage of θ = 0.15 to 0.18 leads to an optimal activity in methanol synthesis indicating that besides metallic Cu also Cu^+ is active.[163, 184, 226] *Chinchen et al.* state that Cu is partially oxidized under $CO/CO_2/H_2$ syngas conditions. The adsorbed oxygen species is identical wich the adsorbed oxygen formed by purging with N_2O. The surface oxygen species takes part as reactant and supports the adsorption of CO_2, H_2O and H_2.[227] *Chu et al.* also indicate that besides metallic Cu Cu^+ is present at the catalyst surface measured by ^{65}Cu NMR.[228]

In summary, there are many approaches to explain the important role of Zn as well as the strong synergy between Cu and Zn for highly active methanol synthesis catalysts. Most likely it is an interplay between all presented features of Zn depending on the catalyst composition, the gas feed composition, the pretreatment/reaction conditions and many more. *Laudenschleger et al.*[192] proposed that the catalysts structure alter over time: "At the beginning, highly reduced ZnO_x species migrate onto the metallic Cu^0 nanoparticles during reduction forming a finely dispersed Cu^0–Zn^0 alloy according to *Nakamura et al.*.[129] The change to a CO_2-containing syngas mixture initializes the formation of different oxygen-containing adsorbates as well as the oxidation of the metallic Zn species to $Zn^{\delta+}$ species at the defective Cu^0 surface according to *Behrens et al.*.[15] The migration of further Zn species results in the formation first of a graphitic-like ZnO_x layer on Cu^0 according to *Lunkenbein et al.* and then a more crystalline and stable thick ZnO layer or particles according to *Kattel et al.*.[132, 135] The formation of thick ZnO layers due to segregation from the metallic Cu^0 phase were observed in recent long-term studies[199]."[192]

3.2.4 Deactivation of $Cu/ZnO/Al_2O_3$ methanol synthesis catalysts

Fichtl et al. reported that the active site does not change under typical reaction conditions. Hence, the deactivation of the catalysts derives from the reduction of active sites. Cu particle sintering occurs which lowers the dispersion of Cu. Hence, the Cu metal surface area decrease. Because the specific activity per m^2 active surface area is not constant over time, additional deactivation processes must proceed.[229] The addition of water increases Cu particle sintering and it lowers the specific catalyst activity possibly caused by segregating Cu and ZnO which leads to weakening of Cu/Zn interactions that is needed for high active catalysts. *Grunwaldt et al.* reported the same effect of water as mentioned in the section before (3.2.3).[178, 229]

Twigg et al. stated that carbon and polymeric deposits deactivate the surface of the catalyst. Especially high ratios of CO/CO_2 in the feed gas can lead to extended deposits due to the *Boudouard* reaction.[230]

Like *Fichtl et al.*, *Kurtz et al.* also reported that particle sintering occurs particularly in catalysts without Al_2O_3. They concluded that Al_2O_3 acts as stabilizer for the Cu dispersion and consequently inhibits Cu particle sintering.[231]

Rasmussen et al. reported that certain reaction intermediates lead to a high Cu mobility on the surface (e.g. Cu-CO and Cu_2H-COO). This mobile Cu species can cause metal migration through displacements over the support and sintering by particle migration and coalescence. The extent of the Cu migration depends on the concentration, on the mobility of the Cu species and on the Cu particle size. When the particles are large enough Ostwald ripening is the main sintering mechanism.[232]

Lunkenbein et al. stated that the main deactivation is not induced by changes of the Cu dispersion but in alterations of the ZnO by performing long-term experiments (148 days). In the first 50 days ZnO is partially converted to Zn,Al-spinel by consuming ZnO and Al_2O_3. ZnO particle sintering takes place including overgrowth of the Cu particles by ZnO layers. After 50 days the ZnO particle sintering almost stops and ZnO domains are structurally stabilized. Zn,Al-spinel and ZnO overlayer formation are irreversible processes. During the first 50 days the rate of MeOH production decreases whereas it stays constant for the reaming time on stream. Hence, the recrystallization of ZnO as well as Zn,Al-spinel formation decrease the interface between ZnO and Cu and consequently the rate of MeOH production.[199]

3.3 Motivation

CO_2 hydrogenation to methanol is of great interest because of environmental reasons. As it was summarized in the section before (3.2.3) the nature of the active as well as the promotional role of Zn for the hydrogenation of CO_2 to methanol is still discussed controversially in literature. Somehow, strong Cu/Zn interactions are important for highly active and efficient $Cu/ZnO/Al_2O_3$ methanol synthesis catalysts.

Hence, a surface organometallic chemistry (SOMC) approach is applied to synthesize $Cu/Zn/Al_2O_3$ catalysts with defined Cu/Zn particles as well as strong Cu/Zn interactions. The preparation method for Al_2O_3 supported Cu nanoparticles is varied to form different Cu particle sizes and different Cu/Al_2O_3 support interactions. In addition, differently Cu and Zn loaded catalysts are prepared to study how the metal loading influences the CO_2 hydrogenation to methanol. Furthermore, $Cu/ZnO/Al_2O_3$ catalysts are synthesized in which Zn and Cu are deliberately separated from each other to compare them to the other catalysts.

The catalysts are characterized by X-ray powder diffraction (XRD), IR spectroscopy and transmission electron microscopy (TEM). The overall surface area (BET/BJH-method) and the Cu surface area (N_2O-RFC, H_2-TPD) are determined. In addition, techniques like scanning transmission electron microscopy – electron energy loss spectroscopy (STEM-EELS) and X-ray photoelectron spectroscopy (XPS) are applied to get information about the location of Zn and the oxidation states. The Zn and Cu loadings as well as the C content are determined by elemental analysis.

The different catalysts are applied in MeOH synthesis from pure CO_2 and H_2. Different pretreatment conditions as well as different reaction temperatures are adjusted to get information about the activity of the catalysts and to get insights into the role of Zn.

3.4 Results and discussion

First, the preparation method of the catalysts is presented including the differences of $Cu/Zn/Al_2O_3$ catalysts with different Cu nanoparticles. In the following section, the influence of different Cu and Zn loadings on the CO_2 hydrogenation to methanol is stated. In the third and last section, a comparative study is demonstrated using a $Cu/ZnO/Al_2O_3$ catalyst in which ZnO and CuO is deposited separately.

3.4.1 $Zn/Cu/Al_2O_3$ catalysts by $ZnEt_2$ grafting on supported Cu nanoparticles

As mentioned before, strong Cu/Zn interactions are essential for a highly active and efficient methanol synthesis catalysts.[15] Therefore, a synthesis method for model catalysts is required to prepare catalysts in which Cu and Zn are in maximum vicinity. In addition, for investigation of the role of Zn regarding the Cu/Zn interactions it is important that Zn is only located on the Cu nanoparticles and not on the Al_2O_3 support to exclude any unintended effects. A method to synthesize bimetallic systems is grafting or deposition of organometallic complexes on metal particles via surface organometallic chemistry (SOMC).[233-240] The advantage of this synthesis method is the systematic deposition of a metal onto metal particles and to avoid the deposition onto the catalyst support.[240] The method is well known for the grafting of Sn compounds onto Ni and Pt particles.[233-240] But also Cr or Ge compounds can be used as grafting agents.[238, 240] The general principle behind the method is the activation of H_2 on metal particles and the subsequent reaction of the organometallic compound with it to deposit the metal precursor onto the metal particles. The most commonly used organometallic complexes are alkyl complexes because an easily removable or volatile leaving group is needed to accelerate the reaction. An example is $Sn(n\text{-}C_4H_9)_4$ whereby butyl groups react with activated H_2 forming butane.[233, 240]

In the case of Cu and Zn, Cu nanoparticles are the metal particles that are doped with a Zn alkyl compound. Diethyl zinc ($ZnEt_2$) seems to be a suitable grafting agent because ethyl groups are easily removable and the compound itself is reactive enough to react with the activated H_2. Due to its volatility and high reactivity, $ZnEt_2$ is often used as reactant in chemical vapor deposition (CVD) procedures even for the deposition of highly dispersed Zn for methanol synthesis catalysts.[241, 242] In addition it acts as reactant for the synthesis of brass particles by thermolysis or as precursor for colloidal catalysts.[243, 244]

For the synthesis of the catalysts used for this work, the Cu nanoparticles are supported on Al_2O_3 to synthesize a model catalyst that is as similar as possible to the systems used in industry.[245] After the activation of H_2, $ZnEt_2$ is added in order to deposit Zn directly onto the Cu nanoparticles. This procedure should help to gain strong interactions between Cu and Zn, which is supposed to be promising for MeOH synthesis.[15]

The preparation of the catalysts is divided into two steps. First Cu nanoparticles supported on Al_2O_3 are prepared by four different methods and second Zn is deposited onto them. For simplification, the different Al_2O_3 supported Cu nanoparticles are abbreviated as follows: Cu_{DP} (deposition precipitation with urea), Cu_{LR} (deposition precipitation via ligand removal), Cu_{RP} (reductive precipitation) and Cu_{CoPr} (co-precipitation) before Zn deposition and $ZnCu_{DP}$, $ZnCu_{LR}$, $ZnCu_{RP}$ and $ZnCu_{CoPr}$ after Zn deposition. The abbreviations and descriptions of the catalysts are summarized in Table 10.

The desired Cu and Zn loadings are 10 wt.% and 2 wt.% respectively. The Al_2O_3 supported Cu nanoparticles are designated as pre-catalysts in this chapter.

Table 10: Abbreviations of the different $ZnCu_x$ catalysts, the declaration of the catalyst labels and the desired Cu ($Cu^{a)}$ and Zn (Zn^b) loadings in wt.%.

Abbreviation	Cu^a	Zn^b	Description
Cu_{DP}	10	-	deposition precip. with urea without Zn
Cu_{LR}	10	-	deposition precip. via ligand removal without Zn
Cu_{RP}	10	-	reductive precip. without Zn
Cu_{CoPr}	10	-	co-precipitation without Zn
$ZnCu_{DP}$	10	2	deposition precip. with urea with Zn
$ZnCu_{LR}$	10	2	deposition precip. via ligand removal with Zn
$ZnCu_{RP}$	10	2	reductive precip. with Zn
$ZnCu_{CoPr}$	10	2	co-precipitation with Zn

3.4.1.1 Preparation and characterization of the pre-catalysts

The Al_2O_3 supported Cu nanoparticles are prepared either by deposition precipitation via urea, by deposition precipitation via ligand removal, by reductive precipitation or by co-precipitation, which is the standard procedure for methanol synthesis catalysts. In the following, the preparation methods are briefly described.

Deposition precipitation with urea

Al_2O_3 support, Cu nitrate and urea are added to a flask. The suspension is heated to decompose urea. Hence, the suspension becomes alkaline and Cu is precipitated as a Cu hydroxide species onto the Al_2O_3 support.[246, 247]

Deposition precipitation via ligand removal

Aqueous ammonia, Al_2O_3 support and Cu nitrate are added to an Erlenmeyer flask. $[Cu(NH_3)_4]^{2+}$ forms. Ammonia evaporates over time, which means that the ammonia content of

the solution decreases. When the ammonia content is not sufficient to complex the Cu^{2+} ions, Cu^{2+} precipitates as $Cu(OH)_2$ onto Al_2O_3 support.[246, 248]

Reductive precipitation

The addition of hydrazine to a suspension of Cu acetate and Al_2O_3 support leads to reduction of Cu^{2+} to Cu^0. Consequently, hydrazine is oxidized to nitrogen. Metallic Cu particles precipitate and deposit onto the Al_2O_3 support.[246, 249]

Co-precipitation

A solution containing Al and Cu nitrate is continuously mixed with a NaOH solution. Al^{3+} and Cu^{2+} precipitate simultaneously yielding in a homogenous precipitate. The support and active metal precursor is formed simultaneously.[250]

Deposition precipitation as well as co-precipitation leads to high metal surface areas and small nanoparticles in a narrow range. However, deposition precipitation has the advantage compared to co-precipitation that the complete Cu amount is located on the Al_2O_3 surface and the particles are not incorporated into the support. Especially for model catalysts, it plays an important role to exclude unintended effects as much as possible. In contrast, co-precipitation has the benefit that strong metal support interactions can be generated due to the simultaneous precipitation of the support and the catalytic active phase.[246, 250]

In addition, the different precipitation methods should lead to the preparation of different Cu particles sizes. Small particles are beneficial for the catalytic performance[183] whereas large particles facilitate particular analytical measurements. Especially for STEM-EELS to get high resolved images and for some XPS measurements Al_2O_3 supported Cu nanoparticles are prepared by reductive precipitation to gain larger nanoparticles between 50 and 100 nm.

Table 11: Cu (Cu^a) and Zn (Zn^b) loadings in wt.% determined by ICP-OES. The error is determined to be around 5% including the preparation and the ICP-OES measurement itself.

Sample	Cu^a	Zn^b
$ZnCu_{DP}$	9.8	1.8
$ZnCu_{LR}$	10.0	2.0
$ZnCu_{RP}$	9.1	1.8
$ZnCu_{CoPr}$	9.8	1.8

The Cu loading of all catalyst precursors is determined by elemental analysis via ICP-OES. The Cu loading of the samples is in a narrow range of 9-10 wt.% (Table 11). Only the value of $ZnCu_{RP}$ deviates a little. It was observed during the reductive precipitation procedure that to

some extent Cu precipitates on the glass wall of the flask, which most likely causes the lower Cu loading.

X-Ray powder diffraction of the pre-catalyst

All samples except Cu_{RP} are dried, calcined at 450°C and reduced at 300°C in H_2 after precipitation. The powder diffractograms of the calcined samples (Cu_{DP}, Cu_{LR}, Cu_{CoPr}) and of Cu_{RP} are shown in Figure 52. The particles of Cu_{RP} already consist of metallic Cu. Hence, post-treatment is no longer necessary.

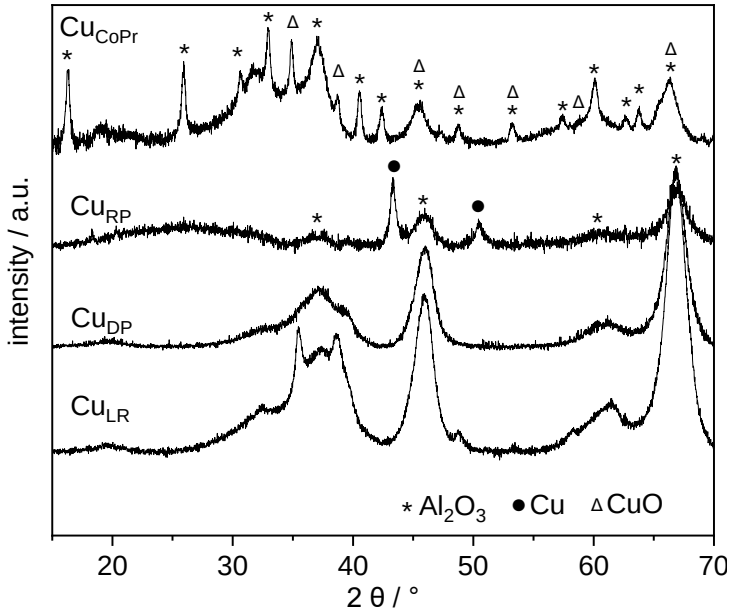

Figure 52: Powder diffractograms of Cu_{CoPr}, Cu_{DP} and Cu_{LR} after calcination at 450°C for 4 h (2.5 K/min) and of Cu_{RP} directly after reductive precipitation. The stars mark γ-Al_2O_3-reflexes[120, 121], the triangles represent CuO[106] and the dots metallic Cu[251]. Diffractograms are recorded in an angle range between 5° and 70° in steps of 0.013°.

The Al_2O_3 support in Cu_{CoPr} gives multiple reflexes and it can be figured out that they originate of *γ*-Al_2O_3. In addition, CuO reflexes are visible which is not surprising because during the calcination precipitated $Cu(OH)_2$ is transformed into CuO. In contrast to the multiple reflexes of the support in the powder diffractogram of Cu_{CoPr} the reflexes of the commercial *γ*-Al_2O_3 support used for Cu_{LR}, Cu_{DP} and Cu_{RP} are broader and less pronounced. It means that by co-precipitation more crystalline Al_2O_3 is formed compared to the commercial one.

Similar to the diffractogram of Cu_{CoPr}, CuO is present in the pre-catalysts Cu_{DP} and Cu_{LR}. The CuO reflexes are broader or rather less distinguished in Cu_{DP}. It hints that very small CuO particles are formed in Cu_{DP} and they are smaller than the Cu particles of Cu_{LR}. To make a statement concerning the CuO particle size from the powder diffractogram of Cu_{CoPr} is not possible because the reflexes of the Al_2O_3 support strongly overlap the CuO reflexes. Since

Cu(0) is directly obtained after reductive precipitation only reflexes for Cu(0) are visible in the powder diffractogram of Cu_{RP}. The sharp Cu(0) reflexes of Cu_{RP} indicate large particles.

Temperature programmed reduction (TPR) of the pre-catalysts

TPR experiments for each CuO precursor are carried out to determine the reduction behavior of CuO to Cu and to get more information about the CuO species. The TPR profiles are depicted in Figure 53. The reduction takes place in the temperature range of around 100°C to 375°C. The reduction of Cu_{DP} starts already at 150°C and three peaks can be observed (dashed line in Figure 2). The low reduction temperature indicates weak CuO-Al_2O_3 interactions and a high CuO dispersion.[252, 253] In addition, two of the signals could be assigned to consecutive reduction of Cu(II) → Cu(I) → Cu(0).

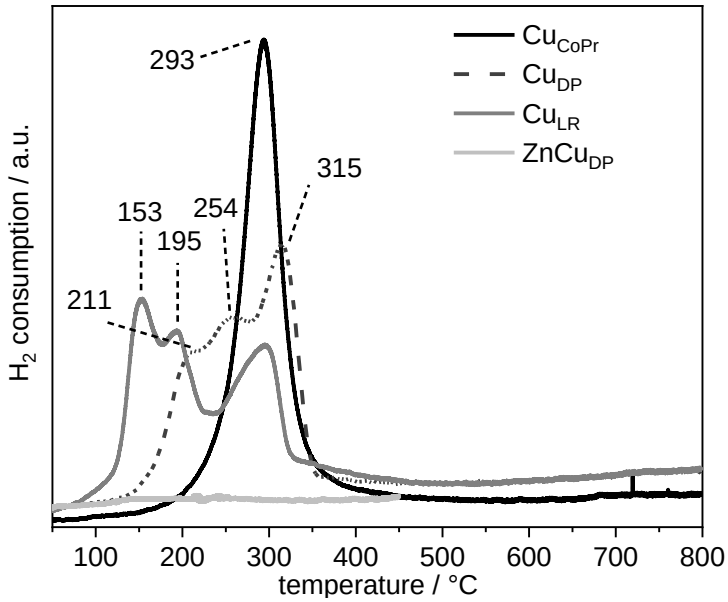

Figure 53: TPR profiles of Cu_{CoPr}, Cu_{DP} and Cu_{LR} after calcination in air at 450°C (2.5 K/min) for 4h and the TPR profile of $ZnCu_{DP}$ after Zn deposition. The TPR profiles are carried out in a temperature range of 50°C to 800°C (5 K/min) in 2.5 % H_2 in He.

A similar course of the TPR profile is obtained for Cu_{LR} containing three peaks with a shift to lower temperatures. As we know from XRD the particles of Cu_{DP} are seemingly smaller than that of Cu_{LR}. Consequently, the shifted TPR profile to lower temperatures is not caused by a smaller CuO particle size it is probably caused by weaker CuO-support interactions.

In contrast to the TPR profile of Cu_{DP} and Cu_{LR} the TPR profile of Cu_{CoPr} shows one peak with a maximum at 300 °C, beginning at 150°C to 200°C. The comparably high reduction temperature is typical for strongly distinct CuO-Al_2O_3 interactions. The existence of just one peak indicates a small particle size distribution.

N_2-physisorption of the pre-catalyst

All prepared samples feature type IV N_2 adsorption isotherms with H1 hysteresis loops. The BET surface area of Cu_{CoPr} is 185 m^2/g, of Cu_{DP} 208 m^2/g and of Cu_{LR} 192 m^2/g. The pure Al_2O_3 support has a BET surface area of 220 m^2/g. The lower BET surface area of Cu_{DP} and of Cu_{LR} compared to pure Al_2O_3 support is caused by CuO particles that block the pores. The BET surface area of Cu_{RP} is not determined because the Cu(0) particles are prone to oxidize and consequently this would distort the obtained BET surface area. Since the same support is used for the preparation of Cu_{RP} like for Cu_{DP} and Cu_{LR} the BET surface area is supposed to be in the same order. The pore volume of the catalysts varies from 0.51 to 0.57 mL/g_{cat} and the pore radius from 3.74 nm to 3.76 nm. The exact values for each pre-catalyst are summarized in Table 12.

Table 12: BET surface area (SA_{BET} in m^2/g), pore volume (V_{pore} in mL/g_{cat}) and pore radius (r_{pore} in nm) of the pre-catalysts and the pure Al_2O_3 support.

Sample	SA_{BET}	V_{pore}	r_{pore}
Cu_{DP}	208	0.54	3.74
Cu_{LR}	192	0.57	3.76
Cu_{RP}	-	-	-
Cu_{CoPr}	185	0.51	3.74
Al_2O_3	220	0.58	3.74

N_2O reactive frontal chromatography (N_2O-RFC) of the pre-catalysts

N_2O-RFC is a suitable method to determine the Cu metal surface area. N_2O reacts with Cu to N_2 and Cu is oxidized to Cu_2O. Measuring the formed N_2 amount allows calculating the Cu metal surface area.[254, 255] Before the N_2O flow experiments the pre-catalysts (except Cu_{RP}) are reduced at 300°C for 1 h in pure H_2 to get Cu metal nanoparticles. Cu_{RP} contains already Cu metal particles but even during storage in a glovebox, an oxide layer can form. Consequently, this sample is treated at 40°C for 1 h to get rid of it. The reduction conditions are selected after evaluating the TPR experiment results. In Figure 54 the N_2O flow experiment profile of Cu_{DP} is shown as an example and in Table 13 the Cu metal surface areas of all four samples are summarized.

The Cu metal surface area of Cu_{DP} (10.1. m^2/g) is the largest compared to the other three samples. It confirms the results obtained by XRD and H_2-TPR that Cu_{DP} contain the smallest Cu nanoparticles.

The Cu metal surface area of Cu_{CoPr} is slightly smaller which indicates that the Cu nanoparticles are slightly larger, but they are still in the same range as the particles of Cu_{DP}. The Cu metal surface area of Cu_{LR} is 6.0 m^2/g. It is accordance with the more distinguished reflexes of

Cu_{LR} compared to Cu_{DP} obtained by XRD. As expected Cu_{RP} has the lowest Cu metal surface area with around 1.0 m^2/g.

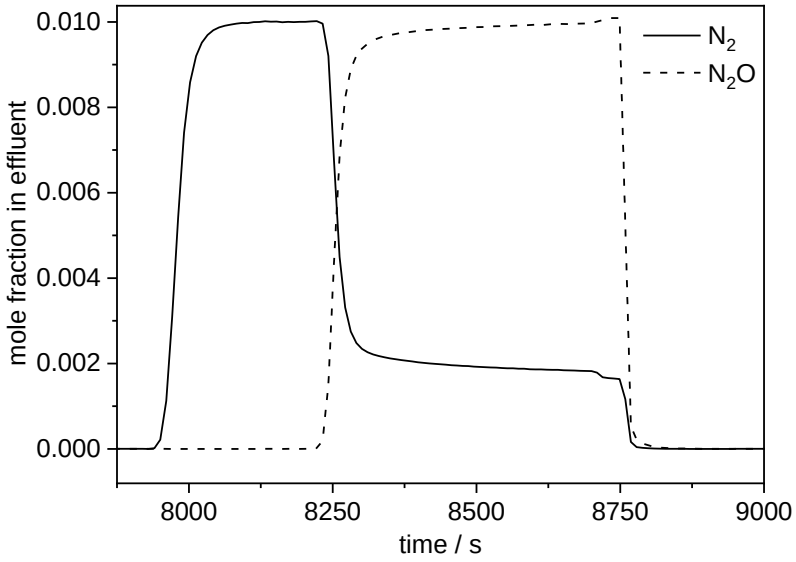

Figure 54: N_2O flow experiment with Cu_{DP} pre-catalyst. The N_2O-RFC is carried out in 1 % N_2O in He at ambient conditions. Before the measurement Cu_{CoPr} is reduced in pure H_2 at 300°C (1 K/min) for 1 h.

Table 13: Cu metal surface area determined by N_2O-RFC ($Cu\text{-}SA_{N2O\text{-}RFC}$ in m^2/g) and H_2-TPD ($Cu\text{-}SA_{H2\text{-}TPD}$ in m^2/g). The N_2O-RFC is carried out in 1 % N_2O in He at ambient conditions. The H_2 adsorption for H_2-TPD is carried out at 24 bar and 235 K for 30 min. Desorption is carried out from 77 K to 523 K at atmospheric pressure with a heating rate of 6 K/min in He. Before the measurement Cu_{DP}, Cu_{LR} and Cu_{CoPr} are reduced in pure H_2 at 300°C (1 K/min) for 1 h. Cu_{RP} is pretreated in pure H_2 at 40°C (1 K/min) for 1 h.

Sample	$Cu\text{-}SA_{N2O\text{-}RFC}$	$Cu\text{-}SA_{H2\text{-}TPD}$
Cu_{DP}	10.1	9.4
Cu_{LR}	6.0	5.2
Cu_{RP}	1.0	0.5
Cu_{CoPr}	8.5	8.0

H_2 temperature programmed desorption (H_2-TPD) of the pre-catalysts

H_2-TPD can be used as well as N_2O-RFC to determine the metallic Cu surface area but it also suggest the nature of the Cu surface. In contrast to N_2O-RFC where N_2O can react also with defect sites (e.g., of Al_2O_3) or with bulk Cu atoms H_2-TPD has the advantage that H_2 adsorbs only on the surface of Cu nanoparticles. This is the reason why higher Cu metal surface areas are obtained by the determination with N_2O-RFC.[255-258]

The H_2-TPD profiles of Cu_{DP}, Cu_{CoPr}, Cu_{RP} and Cu_{LR} are shown in Figure 55. The corresponding metal surface areas are summarized in Table 13. One TPD peak is obtained for each catalyst

precursor and the narrow symmetric shape indicates a second-order desorption without readsorption.[256]

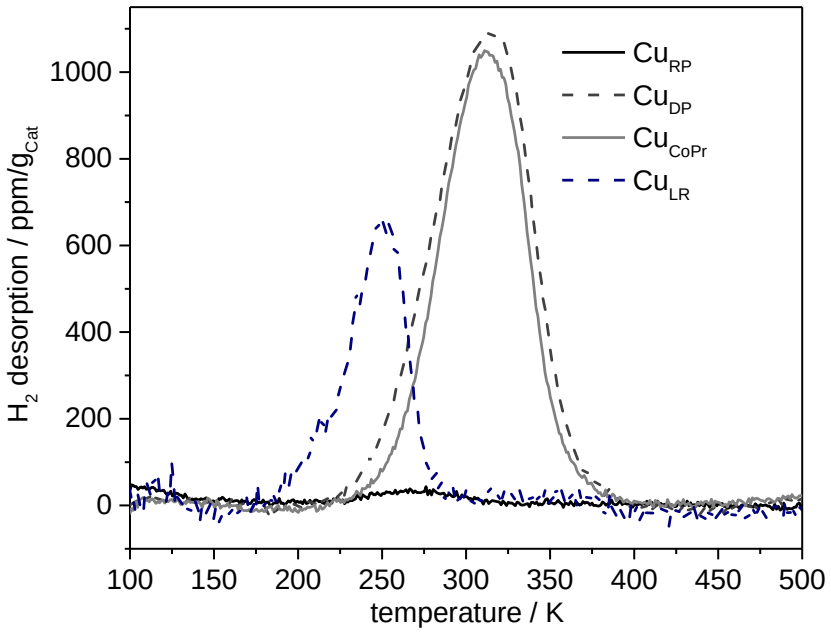

Figure 55: H_2-TPD experiment of Cu_{RP}, Cu_{DP}, Cu_{LR} and Cu_{CoPr}. The H_2 adsorption is carried out at 24 bar and 235 K for 30 min. Desorption is carried out from 77 K to 523 K at atmospheric pressure with a heating rate of 6 K/min in He. Before the measurement Cu_{DP}, Cu_{LR} and Cu_{CoPr} are reduced in pure H_2 at 300°C (1 K/min) for 1 h. Cu_{RP} is pretreated in pure H_2 at 40°C (1 K/min) for 1 h.

The only difference that can be figured out is that the H_2 desorption temperature for Cu_{RP} (285 K) and Cu_{LR} (250 K) are much lower than that of Cu_{DP} and Cu_{CoPr} (310 K). *Anger et al.* state that the desorption at around 280 K could derive from the Cu(100) surface whereby a desorption at around 310 K or higher corresponds to a Cu(111) or a Cu(110) surface.[257] *Fichtl* states that the desorption peaks of the different Cu surfaces overlap forming only one desorption peak by investigating polycrystalline Cu. He developed a model to clarify how the different Cu surfaces contributes to the desorption peak. It turned out that the desorption at lower temperatures is assigned to desorption from Cu(100) whereas desorption from Cu(111) occurs at around 300 K. The desorption from Cu(110) appears at even higher temperatures (around 325 K).[259] It means that Cu_{LR} most likely consists of Cu(100). Cu_{RP} contains mainly both Cu(100) and Cu(111) whereas Cu_{CoPr} and Cu_{DP} exhibit a mixture of Cu(111) and Cu(110). In these considerations only low index planes (Cu(100), Cu(110), Cu(111)) can be regarded because the existence of higher index planes like Cu(211), Cu(311) cannot be proven by H_2-TPD.[254-257] Commonly used $CuO/ZnO/Al_2O_3$ catalysts expose largely Cu(111) surfaces.[256]

By means of integration of the TPD peaks the Cu metal surface area can be calculated. The Cu metal surface areas are the largest for Cu_{DP} and Cu_{CoPr}, which confirms the results obtained by N_2O-RFC but the values itself are smaller as discussed at the beginning of this section. The larger difference between both Cu metal surface areas for Cu_{DP} is caused either by larger

accessibility of bulk Cu that can react with N_2O or by the existence of more defect sites in the commercial Al_2O_3. Latter is very unlikely because the Al_2O_3 support is also used for the preparation of Cu_{LR} and Cu_{RP}. Compared to Cu_{Copr} and Cu_{DP} the Cu metal surface area of Cu_{RP} is very low again and indicates larger Cu nanoparticles.

Transmission electron microscopy (TEM) of the pre-catalysts

TEM images are conducted to get information about the sizes of the Cu nanoparticles. In Figure 56 the TEM image and the particle size distribution of the pre-catalysts are shown.

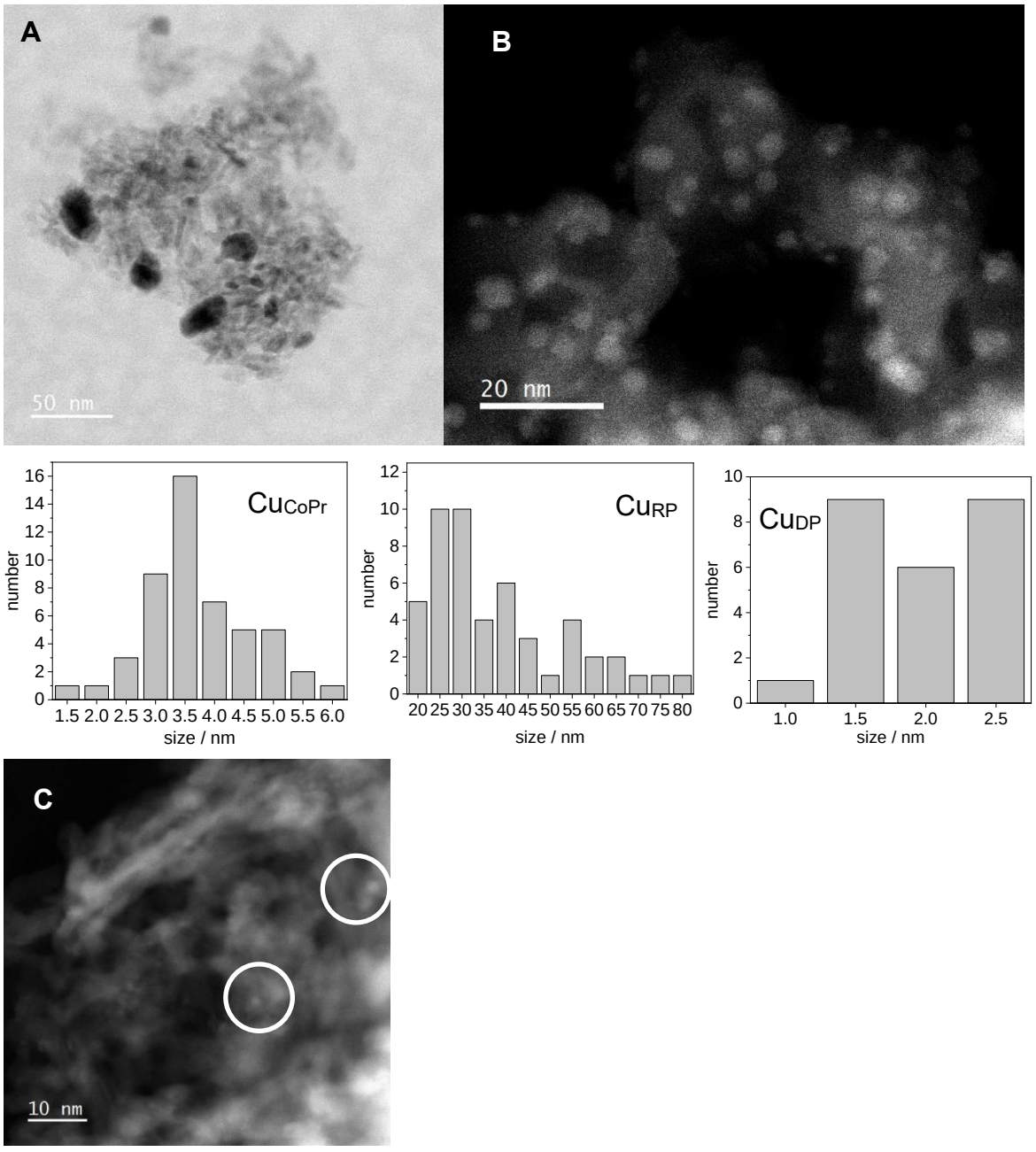

Figure 56: TEM-images of Cu_{RP} (A), Cu_{CoPr} (B) and Cu_{DP} (C) and the particle size distributions of Cu_{CoPr}, Cu_{RP} and Cu_{DP}. 50 particles are counted for each sample except for C_{UDP} due to the small particle sizes and thus the lack of useable images.

The Cu nanoparticles of Cu_{RP} are the largest in a range of 20 to 80 nm with an average size of 38 ± 16 nm (A). In contrast to that the Cu nanoparticles of Cu_{CoPr} are much smaller from 2 to 6 nm (3.7 ± 0.9 nm) (Figure 4B). The Cu nanoparticles of Cu_{DP} are even smaller (1 to 3 nm with an average of 2.0 ± 0.5 nm) and it is difficult to image them (Figure 4C). The results confirm the results obtained by X-Ray powder diffraction, H_2-TPR and chemisorption methods. Cu_{RP} with the largest nanoparticles, for example, shows the most distinct Cu reflexes and exhibits the lowest Cu metal surface area. TEM images of Cu_{LR} are not recorded.

3.4.1.2 Zn deposition via surface organometallic chemistry

Aim of the Zn deposition is to graft a Zn organometallic compound, in this case $ZnEt_2$, well defined and solely onto the Cu nanoparticles creating exclusively Cu/Zn sites. The SOMC synthesis route should avoid Zn deposition onto the Al_2O_3 support for studying just the interaction between Cu and Zn during the MeOH synthesis from CO_2. In Figure 57, the Zn deposition is presented graphically.

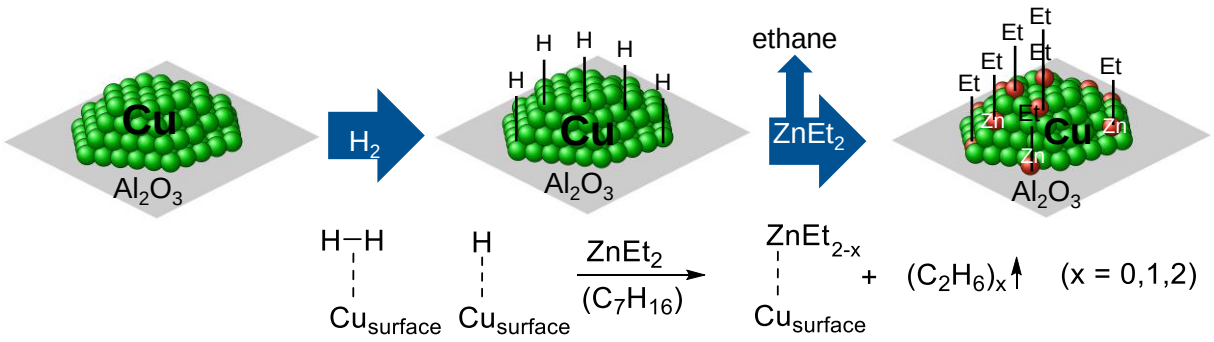

Figure 57: Graphic presentation including a reaction equation of the $ZnEt_2$ deposition procedure including the activation of H_2 and the reaction with $ZnEt_2$ forming ethane.

First, H_2 is activated on the surface of the Cu nanoparticles. After adding a $ZnEt_2$/heptane solution, $ZnEt_2$ reacts with activated hydrogen and ethane is released. Simultaneously Zn is deposited onto the Cu nanoparticles. The desired Zn content should be 2 wt.% for each of the samples. Prior the Zn grafting procedure all samples except Cu_{RP} are reduced in H_2 at 300 °C to get Al_2O_3 supported Cu metal nanoparticles. The grafting reaction is monitored using a mass spectrometer to characterize fragments of ethane especially (Figure 58).

It can clearly be figured out that after the addition of $ZnEt_2$ ethane is formed. After around 45 min the reaction is finished displayed by the decrease of ethane formation. Besides fragments of ethane, fragments of heptane can also be found. Heptane is used as solvent and evaporates slightly during the reaction time. After the grafting procedure, the Zn loading is determined by ICP-OES. The Zn loadings of all samples ($ZnCu_{DP}$, $ZnCu_{CoPr}$, $ZnCu_{RP}$) including the reference catalysts ($ZnCu_{ref1}$, $ZnCu_{ref2}$) are summarized in Table 11.

The targeted Zn loading of 2 wt.% is almost achieved for all samples. The formation of ethane and the results obtained by ICP-OES indicate the validity of the grafting procedure.

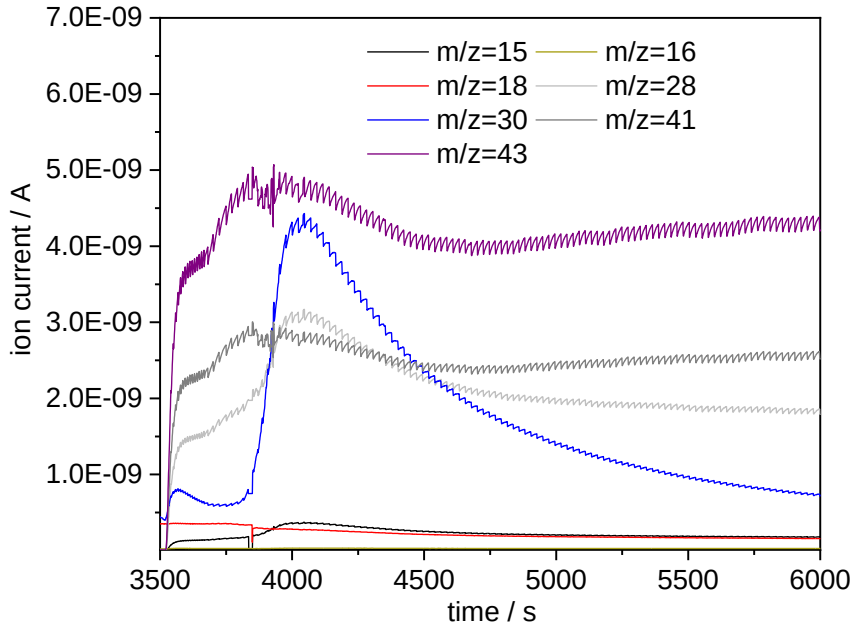

Figure 58: Monitoring the deposition procedure with $ZnEt_2$ via mass spectrometry. The gas phase of the reaction flask is continuously piped to the MS. m/z values: 15 → methyl, 16 → methane, 18 → water, 28 → ethylene/N_2, 30 → ethane, 41 → heptane, 43 → heptane.

X-Ray powder diffraction of the samples after Zn grafting

X-ray powder diffraction is measured to get information in which form Zn is deposited onto the Al_2O_3 supported Cu nanoparticles.

The diffractograms of $ZnCu_{DP}$, $ZnCu_{CoPr}$, $ZnCu_{LR}$ and $ZnCu_{RP}$ are shown in Figure 59. All samples contain Cu(0) indicated by the typical reflexes at 43, 50 and 73 2θ which confirms the presence of metallic Cu. The Zn deposition procedure does not lead to the oxidation of Cu to CuO. The H_2-TPR profile of $ZnCu_{DP}$ (see Figure 53) confirms it because no hydrogen is consumed and hence no signal can be observed. Additionally, reflexes corresponding to either Cu/Zn-alloy (brass) or ZnO do not appear. It indicates that Zn is deposited in thin layers that are not detectable via XRD onto the Cu nanoparticles. Due to the narrow width of the Cu reflexes $ZnCu_{RP}$ contains larger nanoparticles. The broad Cu reflexes for Zn_{CuDP} and $ZnCu_{CoPr}$ are assigned to smaller nanoparticles that agrees with the TEM images. The Cu nanoparticle size of $ZnCu_{LR}$ lies in between. The determination of the crystallite sizes ($ZnCu_{DP}$ ~5 ±3nm, $ZnCu_{RP}$ ~18 ±4nm, $ZnCu_{CoPr}$ not possible, $ZnCu_{LR}$ ~12 ±3nm) of Cu by the Scherrer equation is not particularly accurate because the reflexes of the Al_2O_3 support shade into the reflexes of metallic Cu and the equation itself gives no exact values for very small nanoparticles.[100-104]

Compared to the powder diffractograms obtained after calcination (see Figure 52) the Al_2O_3 support is not influenced by the reduction or the Zn deposition.

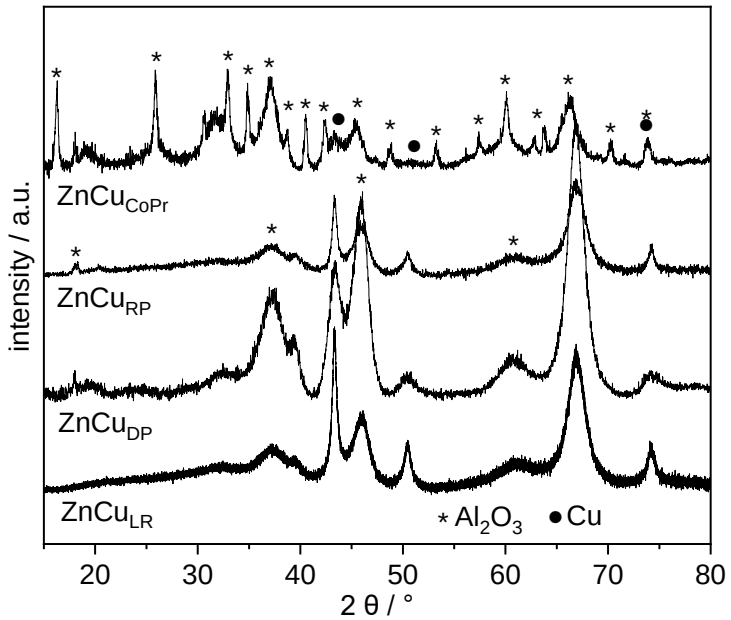

Figure 59: Powder diffractograms of $ZnCu_{DP}$, $ZnCu_{RP}$, $ZnCu_{CoPr}$ and $ZnCu_{LR}$ after Zn grafting. The stars mark γ-Al_2O_3 reflexes[120, 121] and the dots represent metallic Cu[251]. Diffractograms are recorded in an angle range between 5° and 90° in steps of 0.008°.

Investigations concerning the grafted Zn species

To determine if ethyl groups are remaining after the Zn deposition using $ZnEt_2$ or all groups are released as ethane, the C to Zn ratio is determined by elemental analysis. The sample is burned in air. The formed CO_2 is analyzed via gas chromatography. The C to Zn ratio is approximately 2 (2.1). Hence, one ethyl group remains at the Zn. For further characterization, the ethane to Zn ratio is determined. Water is added to the sample so that ethyl groups are converted to ethane. The gas phase is analyzed via gas chromatography again. The ethane to Zn ratio is about 0.85. Approximately one molecule ethane is formed for one Zn atom. To get more information about the grafted species the sample is heated up to 500 °C (5 K/min) in He atmosphere. The gas stream is analyzed using a mass spectrometer. The temperature programmed decomposition (TPD) profile is shown in Figure 60.

Mainly ethylene and water are released during the temperature treatment. Ethylene is a product formed by the decomposition of the ethyl groups. Water most likely desorbs from the Al_2O_3 support. It is also possible that protons that are formed during the ethyl decomposition react with hydroxyl groups of the support and water is formed via this reaction pathway. Besides ethylene, methyl groups as well as methane are produced. These products originate from the decomposition of ethyl groups, too. Similar decomposition products for ethyl groups were found by *Zaera* when he studied the thermal decomposition of ethyl iodide on Pt(111) and by

Dumont et al. during investigations of pyrolysis of $ZnEt_2$.[260, 261] The combination of all obtained results leads to the conclusion that during Zn grafting around one ethyl is released as ethane and one ethyl group remains at the Zn.

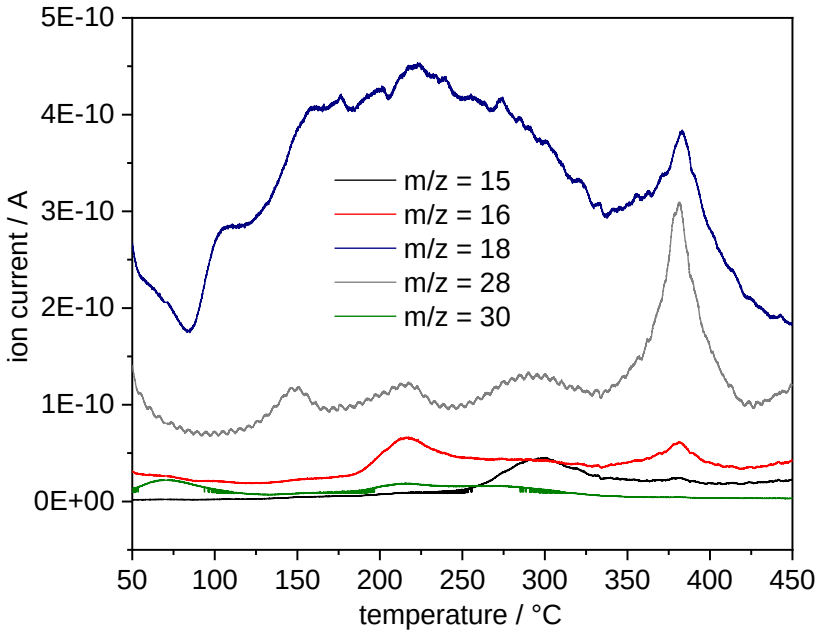

Figure 60: Temperature programmed decomposition (TPD) profile monitored via mass spectroscopy. The sample ($ZnCu_{DP}$) is heated up to 500°C in He (20 mL/min) with a heat ramp of 5 K/min. m/z values: 15 → methyl, 16 → methane, 18 → water, 28 → ethylene/N_2, 30 → ethane.

Scanning transmission electron microscopy – electron energy loss spectroscopy (STEM-EELS) elemental mapping

STEM-EELS elemental mapping is carried out to determine where Zn is deposited during the Zn grafting procedure.

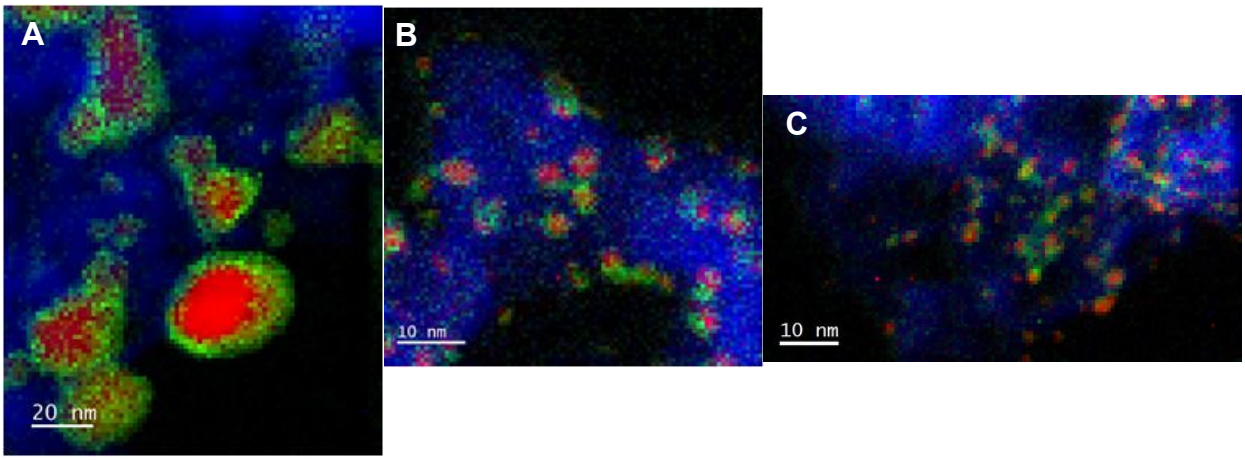

Figure 61: HAADF images of $ZnCu_{RP}$ (A), Cu_{CoPr} (B) and Cu_{DP} (C) and the corresponding EELS elemental maps showing the distribution of Zn (green), Cu (red) and Al (blue).

The HAADF images and the corresponding EELS elemental maps are shown in Figure 61. Zn (green spots) is almost exclusively deposited onto the Cu nanoparticles (red spots). Zn is not distributed on the blue areas (corresponds to Al of the Al_2O_3 support).
It is especially well illustrated for $ZnCu_{RP}$ (Figure 61A) which contains the largest nanoparticles. In addition, with the help of the EELS elemental map the small nanoparticles of $ZnCu_{DP}$ are better visible than just with TEM (see Figure 56). HAADF images of Cu_{LR} are not recorded.

X-Ray photoelectron spectroscopy (XPS)

The oxidation states of Cu and Zn are investigated using X-ray photoelectron spectroscopy (XPS). Cu_{RP} and $ZnCu_{RP}$ is measured as it is and after H_2 treatment at 275 °C. The Cu2p, Zn2p as well as the $CuL_3M_{4,5}M_{4,5}$ Auger electron spectra are shown in Figure 62.

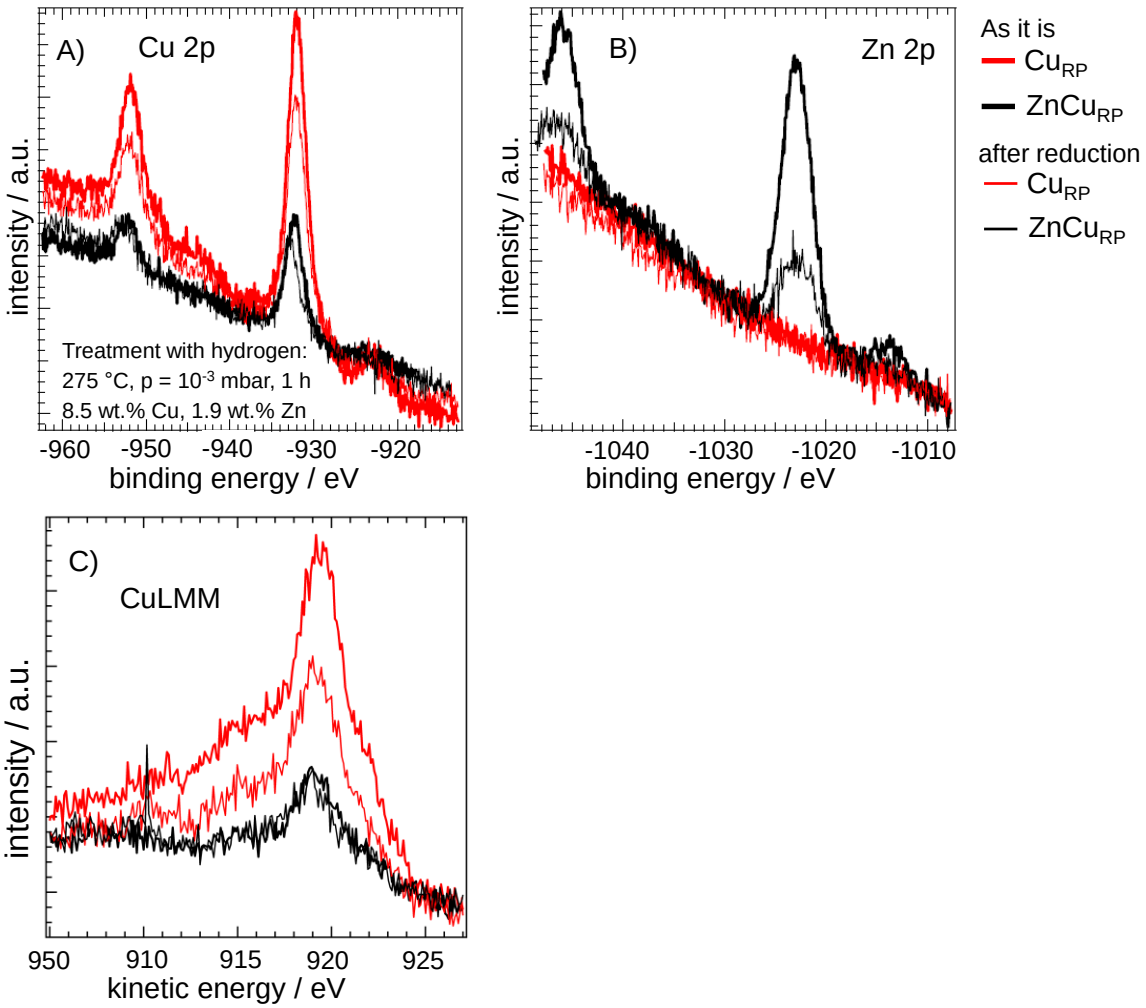

Figure 62: XPS spectra of Cu_{RP} (red lines) and $ZnCu_{RP}$ (black lines) without treatment (thick lines) and after H_2 treatment (thin lines). A: Cu2p; B: Zn2p, C: $CuL_3M_{4,5}M_{4,5}$.

The $Cu2p_{3/2}$ peak of both samples is at BE 932 eV and indicates that Cu(0) is present before and after Zn grafting (see Figure 62A). The absence of the satellite peak at 943.7 eV confirms

the absence of Cu(II)ions.[262] The $CuL_3M_{4,5}M_{4,5}$ Auger electron spectrum underlines the presence of Cu(0) (see Figure 62C). After Zn grafting the intensity decreases dramatically (see black line in Figure 62A). It gives a strong evidence that Zn is deposited onto the Cu nanoparticles that confirm the results obtained by STEM-EELS.

During H_2 treatment the intensity of the signal of pure Cu_{RP} declines caused by sintering of the Cu nanoparticles. However, this sintering effect is less distinct. The $Zn2p_{3/2}$ peak, shown in Figure 62B is located at BE 1023 eV, indicating its oxidation state of 2+ meaning Zn is deposited as Zn(II) onto the Cu nanoparticles.[262] After hydrogen treatment, the signal intensity drops a lot (see thin black line in Figure 62B) accompanied with a reduction of Zn(II) to Zn(0). The decreasing Zn2p intensity is caused by the incorporation of Zn into the Cu surface and consequently a surface alloy is formed. If the migration of Zn into the Cu lattice proceeds α-brass arises.

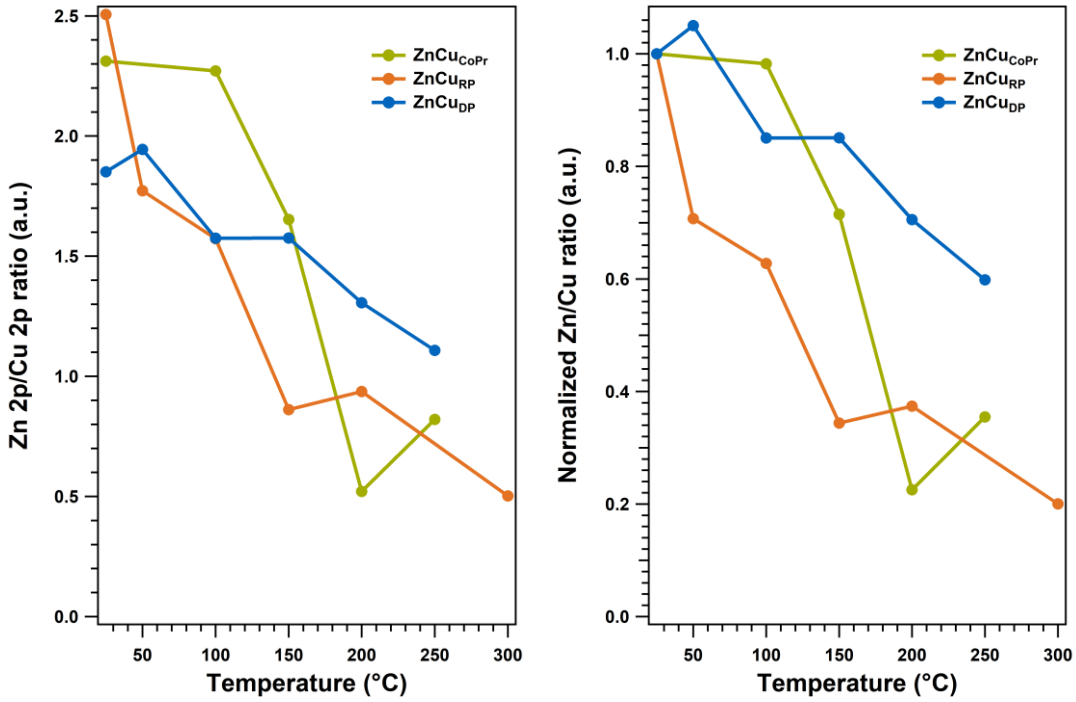

Figure 63: Zn2p/Cu2p ratio and normalized Zn/Cu ratio of $ZnCu_{RP}$, $ZnCu_{CoPr}$ and $ZnCu_{DP}$ obtained by the integration of the Zn2p and Cu2p peaks measured via XPS. The corresponding XPS spectra a depicted in Figure 64. The treatment is conducted in H_2 ($p = 10^{-3}$ mbar) up to 300°C.

In addition, in-situ XPS spectra are recorded of $ZnCu_{RP}$, $ZnCu_{CoPr}$ and $ZnCu_{DP}$ during temperature treatment up to 300°C under H_2 atmosphere. In Figure 63 Zn2p/Cu2p ratio and the normalized Zn/Cu ratio are shown. The corresponding Cu2p and Zn2p spectra as well as the $CuL_3M_{4,5}M_{4,5}$ Auger electron sepctra are depicted in Figure 64. Before the treatment in H_2 atmosphere Cu is present mostly present as Cu(0) and Zn exclusively as Zn(II) in $ZnCu_{DP}$ and $ZnCu_{CoPr}$ like it is in $ZnCu_{RP}$. According to the Auger electron spectra (see Figure 64) some

Cu(I) is also present ($ZnCu_{RP}$ < $ZnCu_{DP}$ < $ZnCu_{CoPr}$) but with increasing temperature it is reduced to Cu(0).

The Zn/Cu ratio decreases for all samples with increasing temperature because of migration of Zn into the lattice of Cu forming a Zn/Cu surface alloy and later α-brass. Interestingly, the temperature at which this process starts, and the formation rate differ a lot for the different samples. Large nanoparticles support the migration (see $ZnCu_{RP}$ in Figure 63) because even immediately after starting with the temperature treatment the Zn/Cu ratio declines. $ZnCu_{DP}$ and $ZnCu_{CoPr}$ have comparable Cu particle sizes whereas the $ZnCu_{CoPr}$ contain slightly larger Cu nanoparticles. The Zn migration begins after 50°C for $ZnCu_{DP}$. Zn/Cu surface alloy formation starts only at about 100°C for $ZnCu_{CoPR}$. However, the Zn2p/Cu2p ratio decrease is more distinct in $ZnCu_{CoPr}$. The Zn migration into the Cu nanoparticles is slowest for $ZnCu_{DP}$ which supports that the small Cu nanoparticles impede Zn incorporation.

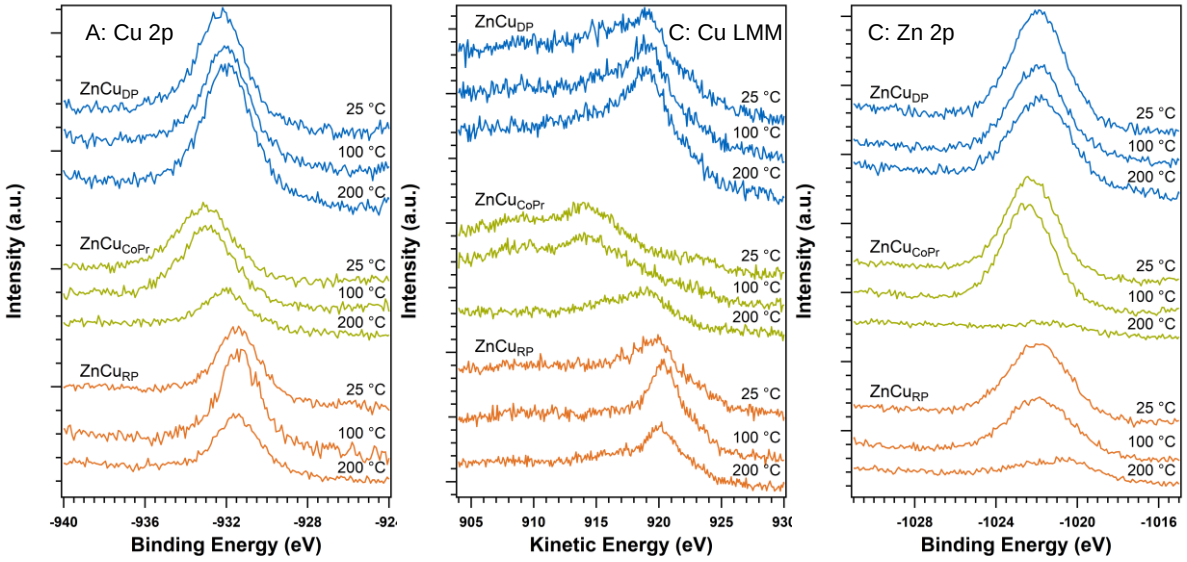

Figure 64: Cu2p and Zn2p spectra as well as the Cu $L_3M_{4,5}M_{4,5}$ Auger electron spectra of $ZnCu_{DP}$, $ZnCu_{RP}$ and $ZnCu_{CoPr}$ during temperature treatment up to 300°C under H_2 atmosphere.

Fourier transformed – infrared spectroscopy (FT-IR)

FT-IR spectroscopy is conducted to get more information about the surface species and adsorption properties of a Zn doped and undoped sample. The studies are carried out using Cu_{DP} and $ZnCu_{DP}$ due to the high Cu dispersion resulting in higher intensities of the signals. In Figure 65 the FT-IR spectra of the Zn doped and undoped catalysts are shown.

Both FT-IR spectra consist of IR bands of water, which is adsorbed on the Al_2O_3 support (1400 to 1800 cm^{-1}). In addition, weak IR bands of CO_2 are visible despite the IR chamber is purged with N_2 overnight.

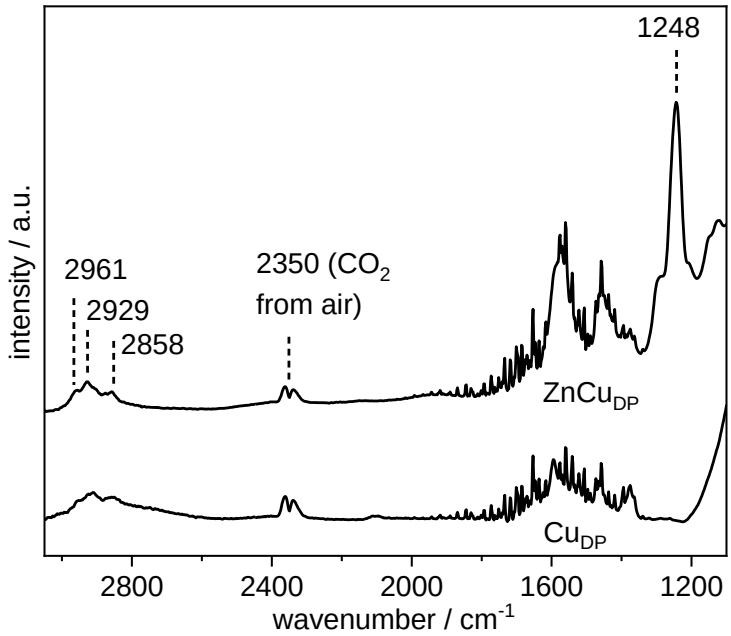

Figure 65: FT-IR spectra of Cu_{DP} and $ZnCu_{DP}$. FT-IR spectra are recorded under inert conditions (He) and room temperature. The pellets are prepared in the glovebox.

Compared to the FT-IR spectrum of Cu_{DP} the FT-IR spectrum of $ZnCu_{DP}$ contains a narrow band at 1248 cm^{-1}. This band corresponds to the CH-deformation vibrations of the ethyl groups that remain after the Zn grafting. Free $\delta_{as/s}$ CH-deformation vibrations arise at 1425 and 1375 cm^{-1}. The asymmetric shape of the signal is characteristic for this type of vibration.[263] A shift to lower wavenumbers of around 130 cm^{-1} can be observed which is most likely caused by binding of the ethyl groups to Zn. In ethyl zinc isopropoxide the deformation vibration of C-H of the secondary C appears at 1159 cm^{-1}.[264] *Boiadjev et al.* obtained similar results after the exposure of dehydroxylated Al_2O_3 at room temperature to a saturated vapor of dimethyl zinc.[265] The bands at around 2900 cm^{-1} corresponds as well to hydrocarbons (ν-CH_2-bond stretching) like ethyl groups but also heptane that is used as solvent.[266] These bands are much more pronounced for $ZnCu_{DP}$ compared to Cu_{DP}. It underlines that after Zn grafting some ethyl groups remain.

Figure 66 the FT-IR spectra of Cu_{DP} (Figure 66A) and $ZnCu_{DP}$-200°C (pre-treated at 200°C in H_2 for 1h, Figure 66B) are shown during the adsorption, desorption of CO. CO is a suitable probe molecule to get information about adsorption and desorption properties of the Cu surface. After adding CO, an IR band appears at 2100 cm^{-1} with a shoulder at 2115 cm^{-1} for both samples. No additional bands arise in the spectrum of $ZnCu_{DP}$-200°C which means that CO adsorb on Cu in both cases despite Zn/Cu surface alloy formation during pretreatment of $ZnCu_{DP}$-200°C. However, no IR-bands belonging to Zn-Cu alloy are visible which would arise at around 1970-1980 cm^{-1} according to *Liu et al.*.[267] The Zn concentration could be too low to observe the alloying effect. Bands of adsorbed CO on ZnO should appear at around 2170-2180 cm^{-1}.[268]

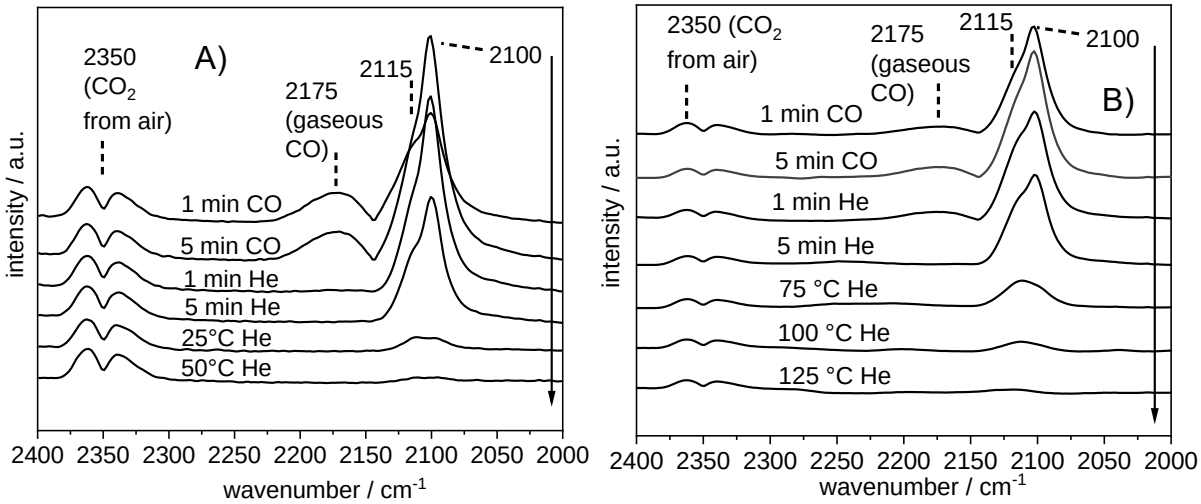

Figure 66: IR spectra in the range of 2000-2400 cm^{-1} of Cu_{DP} (A) and $ZnCu_{DP}$-200°C (B). The IR cell is purged with CO for 5 min and afterwards purged with He. Then it is heated to 250°C (5 K/min) to desorb remaining CO. The pellets are prepared in the glovebox. The flow rate of the gases is 20 mL/min. $ZnCu_{DP}$-200°C is pretreated at 200°C in H_2 for 1h.

The IR band at 2100 cm^{-1} most likely corresponds to linearly adsorbed CO on Cu(110) which fits well with the results obtained by H_2-TPD whereas the band at 2115 cm^{-1} is assigned to Cu(211) or even higher index planes.[258, 268-272] IR bands for CO adsorbed on Cu(100) or Cu(111) would appear at lower wavenumbers.[273, 274]

For CO desorption the samples are heated to 250°C. The desorption of CO is complete at around 50°C for Cu_{DP}. In contrast to that it takes 125 °C to desorb CO completely from the surface of $ZnCu_{DP}$-200°C. The CO desorption behavior is also compared to $ZnCu_{DP}$-40 (pretreated at 40°C in H_2 for 1) and $ZnCu_{DP}$ (without pretreatment). The spectra are shown in Figure 67.

It can clearly be figured out that the CO desorption temperature increase with the addition of Zn and with increasing pretreatment temperature. As we know from XPS, at 200°C pretreatment in H_2 Zn migrates into the Cu lattice forming Zn/Cu surface alloy with strong Zn/Cu interactions. It indicates that these strong interactions favor the adsorption of CO (higher intensities) and CO is stronger adsorbed (higher desorption temperature).

Zn interacts with the CO to stabilize it on the surface. It is also known in methanol synthesis that the adsorption of oxygen-bound intermediates is enhanced by Zn forming partial oxidized $Zn^{\delta+}$.[15] Furthermore, the IR bands shift to higher wavenumbers with increasing temperature indicating a stronger adsorption at higher Cu surface index planes.

After the adsorption of CO, the samples are purged with He to remove gaseous and physisorbed CO. The IR bands for gaseous CO disappear immediately (IR-band at 2175 cm^{-1}).

In addition to that, spectra are recorded of Cu_{DP} and $ZnCu_{DP}$ during heating in pure H_2 to 300°C (Figure 68) to get information about structural changes during reductive pretreatment. Significant changes in the FT-IR spectra cannot be observed, only the desorption of the remaining ethyl groups in the spectra of $ZnCu_{DP}$ (band at 1248 cm^{-1} disappears).

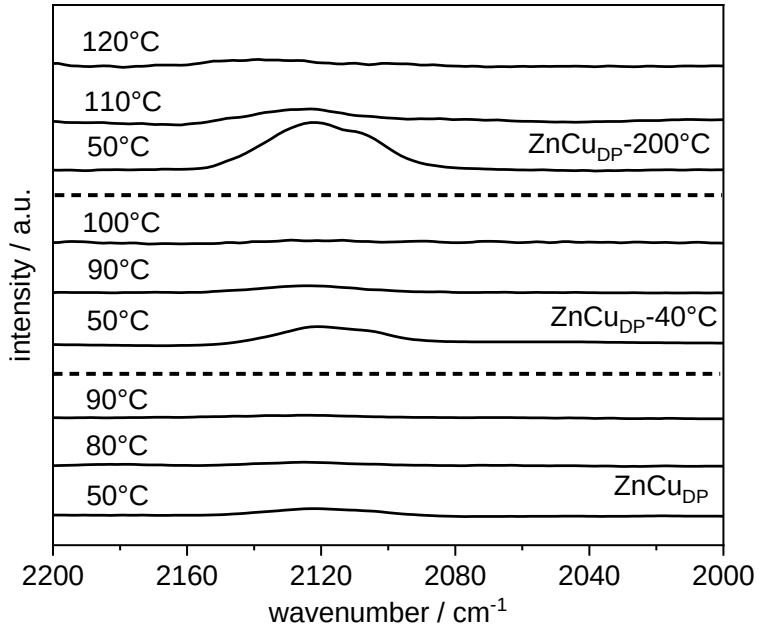

Figure 67: IR spectra in the range of 2000-2200 cm^{-1} of $ZnCu_{DP}$, $ZnCu_{DP}$-40°C and $ZnCu_{Dp}$-200°C. The IR cell is purged with CO for 5 min and afterwards purged with He. Then it is heated to 250°C (5 K/min) to desorb remaining CO. The pellets are prepared in the glovebox. The flow rate of the gases is 20 mL/min. $ZnCu_{DP}$-200°C and $ZnCu_{DP}$-40°C are pretreated at 40 or rather 200°C in H_2 for 1h.

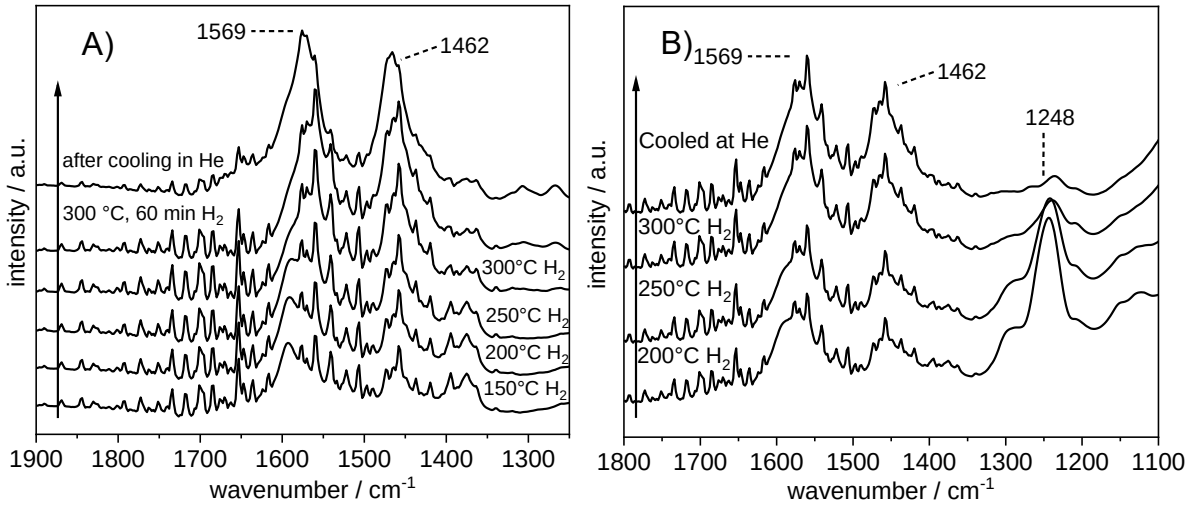

Figure 68: IR-Spectra in the range of 1300-1700 cm^{-1} of Cu_{DP} (A) and $ZnCu_{DP}$ (B) under reductive treatment with H_2. The sample is heated in H_2 gas flow up to 300°C (5 K/min) and held for one hour before it is cooled in He gas flow. The pellets are prepared in the glovebox. The flow rate of the gases is 20 mL/min.

3.4.1.3 Catalytic reaction of CO_2 and H_2 to MeOH

The catalytic reaction of CO_2 and H_2 to MeOH is carried out at 28 bar and temperatures between 200 and 325 °C with a feed gas of H_2:CO_2 3:1. A detailed description and a drawing of the setup are depicted in the experimental part (section 7.2). The catalysts are used either without pretreatment or with reductive pretreatment at different temperatures. The different catalysts as well as the different pretreatments are summarized in Table 14.

Table 14: Abbreviations of the different catalysts (x = DP, CoPr), the description of the catalysts, if the catalysts are pretreated in H_2 (H_2-PT[a]: + = with pretreatment, - = without pretreatment) and at which temperature the catalysts are pretreated (T[b] in °C). H_2-pretreatment conditions: $\dot{V}$ = 20 mL/min, t = 1 h, rate = 1 K/min.

Abbreviation	H_2-PT[a]	T[b]	Description
pureCu_x	+	120	Cu/Al_2O_3 after deposition procedure without Zn
$ZnCu_x$	-	-	$Zn/Cu/Al_2O_3$ after deposition with Zn
$ZnCu_x$-40°C	+	40	$Zn/Cu/Al_2O_3$ after deposition with Zn
$ZnCu_x$-120°C	+	120	$Zn/Cu/Al_2O_3$ after deposition with Zn
$ZnCu_x$-200°C	+	200	$Zn/Cu/Al_2O_3$ after deposition with Zn

The pretreatment temperature adjusts the Zn/Cu ratio at the surface of the catalysts (see XPS, 0). A mild reduction at 40°C leads to the removal of surface oxygen. At 200°C pretreatment temperature the Zn/Cu ratio at the surface is lowest for all samples, because Zn migrates into the Cu lattice, forming Zn/Cu surface alloy.

After Zn deposition as well as after the different reductive pretreatments, the Cu surface area is determined by N_2O-RFC. The values are summarized in Table 15. The Cu surface area drops from 10.1 m^2/g before the Zn deposition to 7.1 m^2/g for $ZnCu_{DP}$ and from 8.5 m^2/g to 7.0 m^2/g for $ZnCu_{CoPr}$. The Zn deposition reduces the accessible Cu surface area by blocking Cu sites. It is known that in industrial-like $Cu/ZnO/Al_2O_3$ catalysts a Zn/ZnO overlayer is formed during the reductive pretreatment and that possibly only 30 % of the initial Cu surface area is available for the catalytic reaction.[132, 191]

The influence of reductive treatment at 40°C, 120°C and 200°C of $ZnCu_{DP}$ and $ZnCu_{CoPr}$ on the Cu surface area is low. Only a slight increase can be observed. It indicates that Zn migrates into the Cu particles and possibly some of the blocked Cu sites are released. Furthermore, it is discussed in literature that Zn^0 which is formed during the reductive pretreatment could contribute to the surface area determination via N_2O because of the oxidation of Zn^0 to ZnO.[131] In particular for $ZnCu_{CoPr}$-200°C (8.5 m_2/g) the surface area increase is most distinct because the Zn migration into the Cu particles is furthest advanced (see Figure 63).

Table 15: Cu crystallite sizes ($^{cat}Size_{crys}$ in nm) after the catalytic reaction calculated with the Scherrer equation. The reflexes at 43 2θ and 50 2θ serve for the determination of the crystallite sizes (see Figure 74). Cu metal surface area of the catalysts after different reductive pretreatments ($^{PT}Cu\text{-}SA_{N2O\text{-}RFC}$ in m^2/g) and of the catalysts after the catalytic reaction ($^{cat}Cu\text{-}SA_{N2O\text{-}RFC}$) determined by N_2O-RFC. The N_2O-RFC is carried out in 1 % N_2O in He at ambient conditions. Before the measurement of the Cu surface area after different reductive pretreatments the catalysts are reduced in pure H_2 at different temperatures (heating rate = 1 K/min) for 1 h. Before the measurement of the Cu surface area after the catalytic reaction the catalysts are purged in He to get rid of residual adsorbates. The catalysts are tested at different reaction temperatures (200, 225, 250, 275, 300, 325 °C) at 28 bar. The overall reaction time is 14 h 50 min. The H_2:CO_2 ratio is 3:1, the GHSV 8000 h^{-1}.

Sample	$^{PT}Cu\text{-}SA_{N2O\text{-}RFC}$	$^{cat}Cu\text{-}SA_{N2O\text{-}RFC}$	$^{cat}Size_{crys}$
$pureCu_{DP}$	10.1	1.4	-
$ZnCu_{DP}$	7.1	1.4	-
$ZnCu_{DP}$-40°C	7.9	1.4	-
$ZnCu_{DP}$-120°C	7.1	1.8	-
$ZnCu_{DP}$-200°C	7.3	1.0	-
$pureCu_{CoPr}$	8.5	4.5	-
$ZnCu_{CoPr}$	7.0	3.0	-
$ZnCu_{CoPr}$-40°C	7.2	-	-
$ZnCu_{CoPr}$-120°C	7.4	-	-
$ZnCu_{CoPr}$-200°C	8.5	3.3	-
$pureCu_{LR}$	6.0		
$ZnCu_{LR}$-120°C	-	-	30.0 ±1.2
$ZnCu_{RP}$-120°C	-	-	27.7 ±3.8

The CO_2 conversion of the different pretreated catalysts at different temperatures is shown in Figure 69. To get information about the role of Zn the catalytic results are compared to Cu/Al_2O_3 ($pureCu_x$) which passed through the Zn deposition procedure but without the addition of $ZnEt_2$.

The CO_2 conversions of the different catalysts increase from 3 % at 200°C to around 23 % at 325°C apart from the catalysts prepared by reductive precipitation.

The CO_2 conversions of the different catalysts prepared by deposition precipitation with urea (DP) are similar especially up to 250°C. The slightest increase of the CO_2 conversion is observed for $ZnCu_{DP}$-200°C after 250°C reaction temperature. This sample has the highest Zn/Cu surface alloy formation and consequently the lowest Zn/Cu ratio at surface after the reductive pretreatment.

The co-precipitated catalysts (CoPr) exhibit also similar CO_2 conversion at the different reaction temperatures. The CO_2 conversions are increased somewhat compared to the catalysts prepared by deposition precipitation with urea (DP) especially at temperatures below 275°C.

The CO_2 conversions of the catalysts prepared by deposition precipitation via ligand removal are also in the same range. For these catalysts it is most distinct that the Zn deposition leads to an increase of the CO_2 conversion.

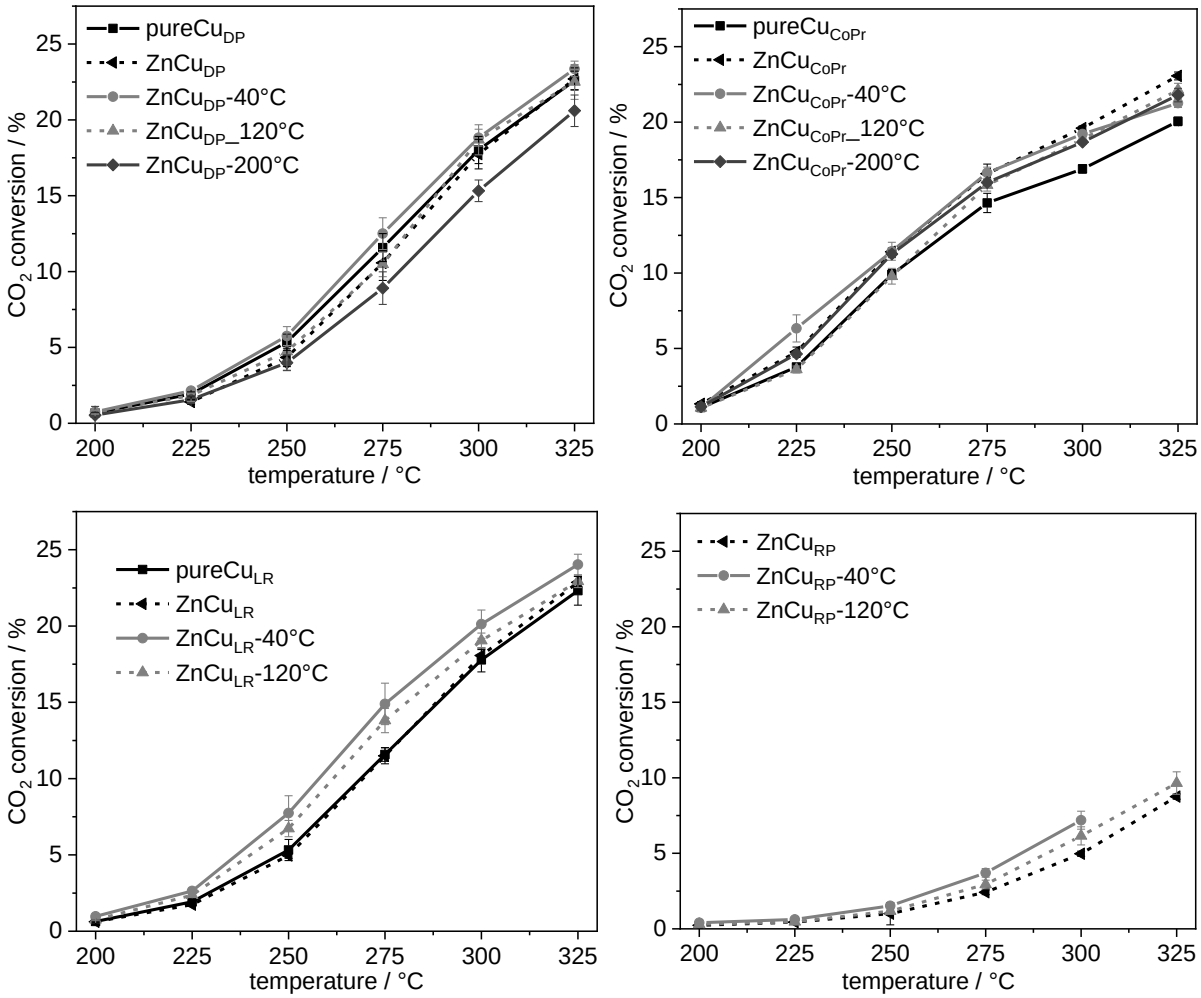

Figure 69: CO_2 conversion at different reaction temperatures (200, 225, 250, 275, 300, 325 °C) at 28 bar for xCu$_y$-z,(x = pure, Zn; y = DP, CoPr, LR, RP; z = 40°C, 120°C, 200°C). pureCu$_{DP}$ and pureCu$_{CoPr}$ pass through the deposition procedure just without the addition of $ZnEt_2$. The H_2:CO_2 ratio is 3:1. The GHSV is 8000 h^{-1}. The catalysts are pretreated in H_2:He 1:1 either at 40°C, 120°C or 200°C for 1 h or are used without pretreatment. The number next to the catalyst labels represents the pretreatment temperature. The overall reaction time is 14 h 50 min.

The low conversion of the catalysts prepared by reductive precipitation is mostly likely caused by the low dispersion or rather the low Cu surface area (around 1 m^2/g).

In summary, the exclusively Zn deposition onto the Cu nanoparticles only slightly influence the CO_2 conversion at least regarding a Zn loading of around 2 wt.%. It leads, if any, to a small increase of the CO_2 conversion. It becomes particularly clear comparing the pure Cu nanoparticles to the Zn/Cu particles.

The catalysts convert CO_2 either to CO or MeOH and some traces of C1 compounds (see Figure 70). Products with higher carbon numbers could not be detected.

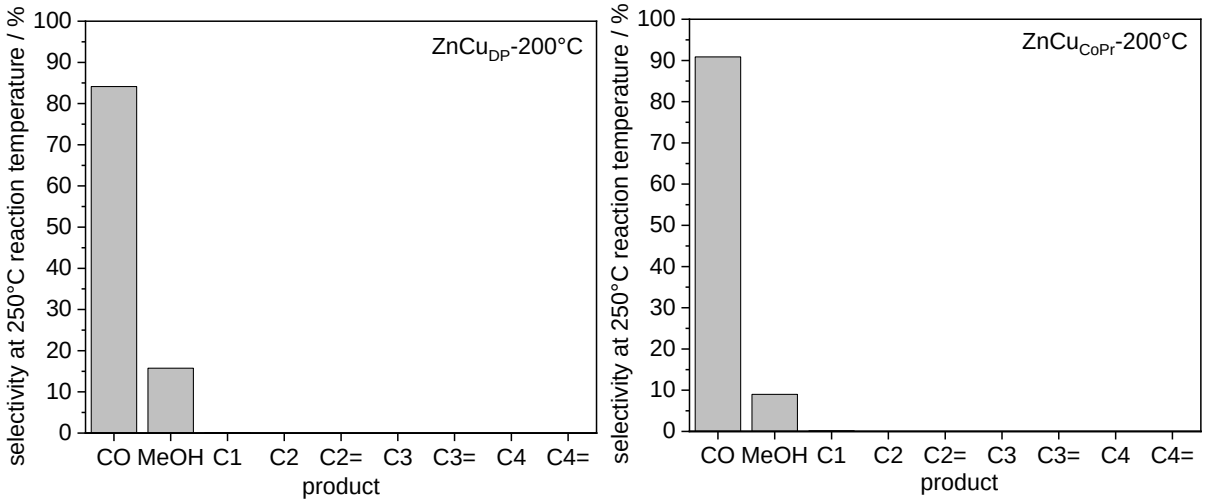

Figure 70: Selectivity at 250°C reaction temperatures at 28 bar for $ZnCu_{DP}$-200°C and $ZnCu_{CoPr}$-200°C The H_2:CO_2 ratio is 3:1. The GHSV is 8000 h^{-1}. The catalysts are tested with pretreatment in H_2:He 1:1 at 200°C for 1 h. The number next to the catalyst labels represents the pretreatment temperature. The overall reaction time is 14 h 50 min

However, compared to the CO_2 conversions the MeOH selectivity differs a lot for the different pretreated catalysts (see Figure 71).

The MeOH selectivity increases (10 to 40 %) with increasing pretreatment temperature for the catalysts prepared by DP. pureCu_{DP} as well as $ZnCu_{DP}$ without pretreatment show the lowest MeOH selectivity. The Zn/Cu interactions are weaker for $ZnCu_{DP}$ compared to the catalysts that are pretreated in H_2 before the catalytic reaction. Rising pretreatment temperature increases the formation of Zn/Cu surface alloy which was observed by XPS (see 0). It indicates that catalysts that exhibit Cu/Zn surface alloy after the reductive pretreatment are more selective to methanol. Despite *Nakamura et al.* state that Zn/Cu surface alloy can act as active species, it is more likely according to *Kattel et al.*, *Laudenschleger et al.* and *Behrens et al.* that Zn is partially oxidized to $Zn^{\delta+}$ or even to ZnO especially in CO_2 rich feeds.[15, 129, 135, 192] Hence the more distinct Zn/Cu alloy does not directly enhance the selectivity. But Zn is highly dispersed after the formation of Zn/Cu surface alloy. It means that under reactions conditions Zn from the preformed Cu/Zn surface alloy is partially oxidized and highly dispersed $Zn^{\delta+}$/ZnO is formed which acts in combination with Cu as active sites. That Zn/Cu surface alloy is a precursor for the formation of highly dispersed Cu/$Zn^{\delta+}$ sites was also proposed by *Kattel et al.* and *Zabilskiy et al*.[135, 197]

The course of the MeOH selectivity of the catalysts prepared by CoPr clarifies this relation. The in-situ XPS measurements showed that only after 100°C pretreatment in H_2 Zn/Cu surface alloy is formed indicated by the decreasing Zn/Cu ratio. It means that $ZnCu_{CoPr}$, $ZnCu_{CoPr}$-40°C and even $ZnCu_{CoPr}$-120°C have more or less the same composition of Zn/Cu at the surface at the beginning of the catalytic reaction. Hence, the MeOH selectivity is nearly the same for all

samples. The slight increase of the MeOH selectivity for $ZnCu_{CoPr}$-120°C suggests that Zn/Cu surface alloy is slightly more advanced. The Zn/Cu alloy formation is very pronounced after reductive pretreatment at 200°C indicated by the low Zn/Cu ratio obtained by XPS measurements. Consequently, the MeOH selectivity of $ZnCu_{CoPr}$-200° is nearly two times higher than that of the other catalysts which supports the importance of a preformed Zn/Cu surface alloy for highly dispersed $Cu/Zn^{\delta+}$ sites. However, the selectivity is half of the selectivity of the comparable $ZnCu_{DP}$-200°C catalyst. The normalized Zn/Cu ratio for $ZnCu_{DP}$-200°C is around 0.7 and for $ZnCu_{CoPr}$-200°C around 0.25. Hence, the Zn/Cu alloy formation is much more distinct for $ZnCu_{CoPr}$-200°C. It indicates that a well-advanced formation of Zn/Cu alloy (formation of α-brass or bulk alloy) could inhibit the promotional effect of a Zn/Cu surface alloy.[275]

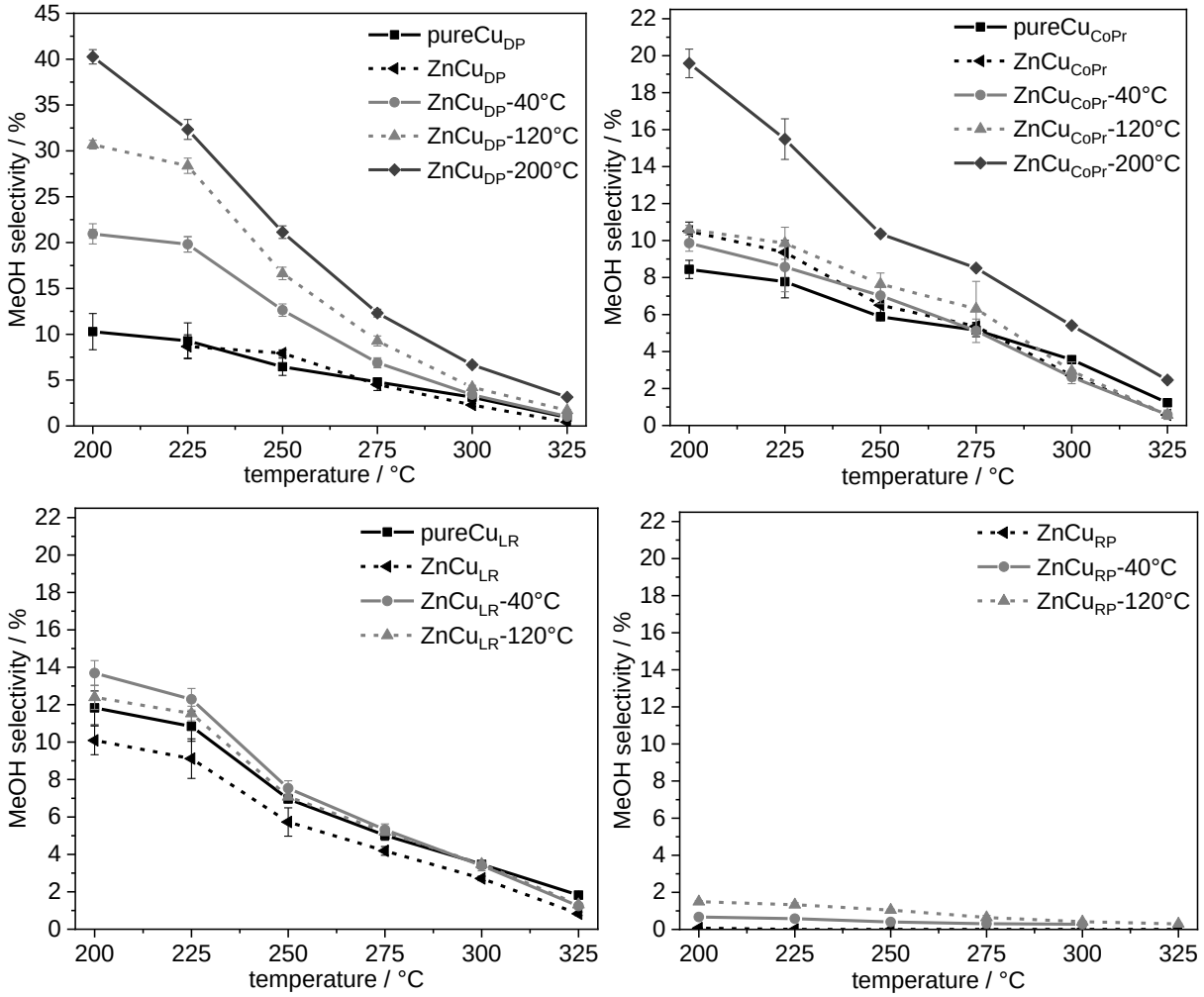

Figure 71: MeOH selectivity at different reaction temperatures (200, 225, 250, 275, 300, 325 °C) at 28 bar for xCu_y-z,(x = pure, Zn; y = DP, CoPr, LR, RP; z = 40°C, 120°C, 200°C). $pureCu_{DP}$ and $pureCu_{CoPr}$ pass through the deposition procedure just without the addition of $ZnEt_2$. The H_2:CO_2 ratio is 3:1. The GHSV is 8000 h^{-1}. The catalysts are pretreated in H_2:He 1:1 either at 40°C, 120°C or 200°C for 1 h or are used without pretreatment. The number next to the catalyst labels represents the pretreatment temperature. The overall reaction time is 14 h 50 min.

The MeOH selectivity of the catalysts prepared by LR is very similar. In this case a reductive pretreatment at 40°C leads to the most selective catalysts but the differences are very low. The Cu nanoparticles prepared by LR are a larger which is indicated by XRD and a smaller Cu surface area. Larger Cu nanoparticles enhance the formation of Zn/Cu alloy. It explains the decrease of MeOH selectivity after 120°C pretreatment by formation of more distinct Zn/Cu alloy.

In addition, the low selectivity of the reductive precipitated catalysts indicates that very large nanoparticles with low Cu dispersion inhibit MeOH formation.

In summary, the addition of Zn leads to an increase in MeOH selectivity indicating that Zn directly located at the Cu surface is essential for high selective MeOH synthesis catalysts, that was previously shown by single crystal experiments.[164] Furthermore, Zn/Cu surface alloy which is formed after reductive pretreatment enhances the dispersion of Zn and consequently the dispersion of $Cu/Zn^{\delta+}$ sites. The addition of Zn only slightly influences CO_2 conversion despite increase of MeOH selectivity. It hints that only Cu sites acts as the active species for the RWGS reaction.[172] The addition of Zn directs the conversion of CO_2 towards the MeOH pathway maybe because of the stabilization of oxygen containing intermediates like formate, which was indicated by *Behrens et al*.[15] In addition, IR experiments with CO showed that CO adsorbs stronger to the surface after the deposition of Zn (see section 0). Claims concerning structure sensitivity of RWGS or MeOH synthesis cannot be made due to the more or less polycrystalline Cu surfaces of the prepared Cu nanoparticles.

To get information about changes of the Zn/Cu nanoparticles during the reaction the Cu surface area of certain catalysts is determined by N_2O-RFC after reaction. The exact values of the obtained Cu surface areas must be interpreted with caution because strong binding adsorbates as well as the Zn/ZnO overlayer can strongly influence the measurement. In addition, TEM images are recorded and STEM-EELS elemental mapping as well as XRD are carried out.

The TEM images as well as the particle size distribution of the catalysts after reaction are shown in Figure 72. The Cu particle sizes of $ZnCu_{DP}$ increase from 2.0 to 7.0 (±1.5) nm and of $ZnCu_{RP}$ from 38.0 (±16) nm to 73 (±39) nm whereas the Cu particles of $ZnCu_{CoPr}$ just grow from 3.7 to 6.5 (±1.1) nm, which indicates the more distinct sintering of the particles prepared by DP. The Cu surface area (see Table 15) decrease from 7.1 to around 1.5 m^2/g for $ZnCu_{DP}$ catalysts whereas the Cu surface area decrease for $ZnCu_{CoPr}$ catalysts is lower (7.0 to around 3.5 m^2/g). Both values confirm the observations by TEM that the Cu nanoparticles prepared by co-precipitation do not agglomerate as much as Cu nanoparticles prepared by DP. The difference is most likely caused by stronger interactions between the Al_2O_3 support and the Cu nanoparticles gained by co-precipitation.[231] In addition, the increase of the Cu crystallite sizes

of $ZnCu_{RP}$-120°C and $ZnCu_{LR}$-120°C (see Table 15) compared to the crystallite size before the catalytic reaction (12 nm for $ZnCu_{LR}$, 18 nm for $ZnCu_{RP}$) obtained by Scherrer equation confirms the agglomeration of the particles during the catalytic reaction.[100-104]

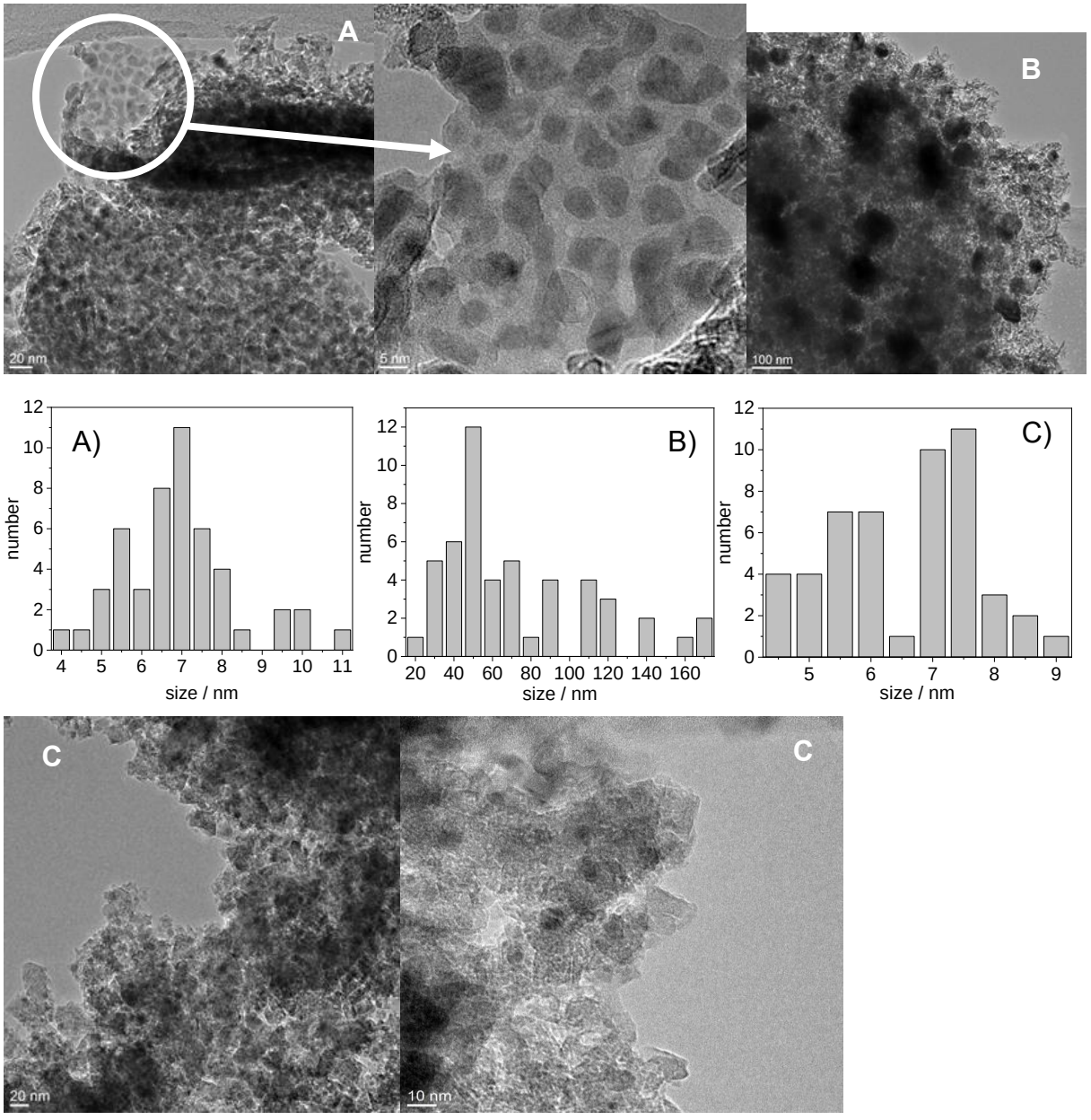

Figure 72: TEM-images and particle size distribution of $ZnCu_{DP}$ (A), $ZnCu_{RP}$ (B) and $ZnCu_{CoPr}$ (C) after the catalytic reaction. The catalytic reaction is carried out at different reaction temperatures (200, 225, 250, 275, 300, 325 °C) at 28 bar. The H_2:CO_2 ratio is 3:1, the GHSV 8000 h^{-1}. The catalysts are pretreated in H_2:He 1:1 at 40°C for 1h. The overall reaction time is 14 h 50 min. For particle size distribution, 50 particles are counted for each sample.

The HAADF images and the corresponding EELS elemental maps of the catalysts after the catalytic reaction are shown in Figure 73. After the catalytic reaction Zn is still located on the Cu nanoparticles and Zn migration onto the Al_2O_3 support does not take place. Part of the green spots are transformed into orange spots which represent Zn/Cu alloy especially for the

reductive precipitated sample which confirms the results even at low temperature pretreatment Zn/Cu alloy is formed at large Cu nanoparticles. In the case of $ZnCu_{DP}$-120°C (Figure 73B) it seems that Zn is highly distributed on the Cu surface and some green and orange areas are visible. It indicates that Zn is partially oxidized but also partially alloyed. $ZnCu_{CoPr}$-120°C exhibits besides some orange areas mainly green areas suggesting that less Zn/Cu alloy is formed. It agrees with the different MeOH selectivity for both catalysts as explained above.

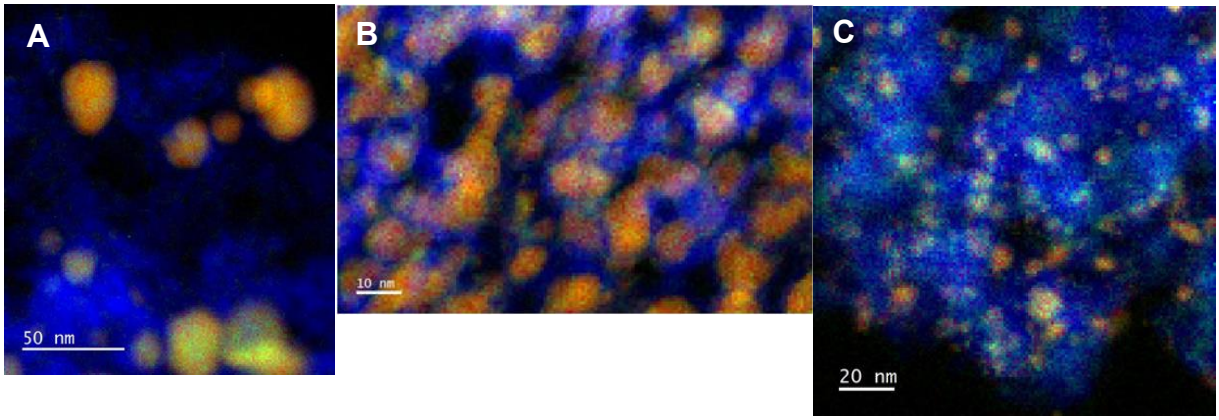

Figure 73: HAADF images of $ZnCu_{RP}$-120°C (A), $ZnCu_{DP}$-120°C (B) and $ZnCu_{CoPr}$-120°C (C) and the corresponding EELS elemental maps showing the distribution of Zn (green), Cu (red), Al (blue), CuZn (orange) after the catalytic reaction. The catalytic reaction is carried out at different reaction temperatures (200, 225, 250, 275, 300, 325 °C) at 28 bar. The H_2:CO_2 ratio is 3:1, the GHSV 8000 h^{-1}. The catalysts are pretreated in H_2:He 1:1 at 200°C for 1h. The overall reaction time is 14 h 50 min.

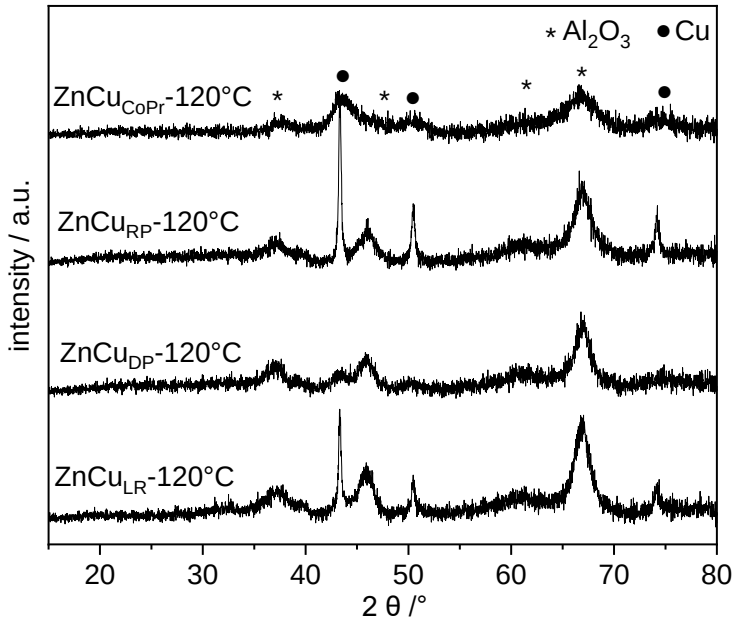

Figure 74: Powder diffractograms of $ZnCu_{DP}$-120°C, $ZnCu_{RP}$-120°C, $ZnCu_{CoPr}$-120°C and $ZnCu_{LR}$-120°C after catalysis. The stars mark γ-Al_2O_3 reflexes[120, 121] and the dots represent metallic Cu[251]. Diffractograms are recorded in an angle range between 5° and 90° in steps of 0.008°. The catalysts are tested at different reaction temperatures (200, 225, 250, 275, 300, 325 °C) at 28 bar. The overall reaction time is 14 h 50 min. The H_2:CO_2 ratio is 3:1, the GHSV 8000 h^{-1}.

The powder diffractograms of the catalysts after the catalytic reaction are shown in Figure 74. Compared to the powder diffractograms after Zn deposition (see Figure 59) the intensity of the reflexes decreases especially for the Al_2O_3 support. The multiple reflexes for the Al_2O_3 support before the reaction of the co-precipitated sample disappear and broad reflexes like for the commercial Al_2O_3 support arise. But even the reflexes for the commercial Al_2O_3 support are less distinct. Interestingly, also the intensity of the Cu reflexes decreases. Despite sintering of the Cu nanoparticles of $ZnCu_{DP}$ during the catalytic reaction the intensity of the Cu reflexes decrease. It indicates that extensive structural changes of the morphology of the catalyst take place even in the Al_2O_3 support. In addition, no reflexes concerning Zn/Cu bulk alloy can be observed. It confirms the suggestion that the alloy formation only takes place at the outer layers of the Cu nanoparticles and that only Zn/Cu surface alloy or diluted α-brass is formed.

3.4.2 Influence of the Cu and Zn loading on the CO_2 hydrogenation to methanol

To investigate if the Zn deposition method is also reliable using different Zn amounts and higher Cu loadings and how the different loadings influence the CO_2 hydrogenation to methanol several $Zn/Cu/Al_2O_3$ catalysts are synthesized. The Cu loading is adjusted to 10 or 25 wt.%. An additional catalyst with 50 wt.% Cu is synthesized via co-precipitation. The Zn loadings vary between 0.25, 1, 2 and 3 wt.% for the catalysts with 10wt.% Cu loading and between 2.5 and 5 wt.% for the catalysts with 25 wt.% Cu loading. A Zn loading of 7.5 wt.% is selected for the catalysts with 50 wt.% Cu loading.

3.4.2.1 Synthesis of the different Cu and Zn loaded catalysts

The labels of the catalysts and their desired Cu and Zn loadings are summarized in Table 16. The synthesis of the different Al_2O_3 supported nanoparticles (see 3.4.1.1) as well as the Zn deposition procedure (see 3.4.1.2) is described in the chapter before.

The Cu and Zn loadings are determined by elemental analysis via ICP-OES and are summarized in Table 17. The measured Cu loadings agree well with the desired value especially for the catalysts prepared by co-precipitation (CoPr) and by deposition precipitation with urea (DP). The Cu loadings for the catalysts prepared by deposition precipitation via ligand removal (LR) deviate widely from the desired value for the high Cu loading of 25 wt.% ($Zn2.5Cu25_{-LR}$, $Zn5Cu25_{-LR}$). In this case, Cu is not deposited exclusively onto the Al_2O_3 support because some Cu is precipitated separately. During sieving of the samples, the Cu particles which are separately precipitated are too small and they are dropped out. Hence, a lower Cu loading is achieved.

The Zn loadings in general are in good agreement but they are partially slightly lower compared to the desired values especially for the catalysts with 5 wt.% Zn loadings.

Table 16: Abbreviations of the different ZnxCuy-z catalysts (x = Zn[b], y = Cu[a], z = preparation method of the Al_2O_3 supported Cu nanoparticles), the declaration of the catalyst labels and the desired Cu (Cu[a)] and Zn (Zn[b]) loadings in wt.%.

Abbreviation	Cu[a]	Zn[b]	Description
$Cu10_{-DP}$	10	-	deposition precip. with urea without Zn
$Zn1Cu10_{-DP}$	10	1	deposition precip. with urea with Zn
$Zn2Cu10_{-DP}$	10	2	deposition precip. with urea with Zn
$Zn3Cu10_{-DP}$	10	3	deposition precip. with urea with Zn
$Cu25_{-DP}$	25	-	deposition precip. with urea without Zn
$Zn2.5Cu25_{-DP}$	25	2.5	deposition precip. with urea with Zn
$Zn5Cu25_{-DP}$	25	5	deposition precip. with urea with Zn
$Cu10_{-CoPr}$	10	-	co-precipitation without Zn
$Zn0.25Cu10_{-CoPr}$	10	0.25	co-precipitation with Zn
$Zn1Cu10_{-CoPr}$	10	1	co-precipitation with Zn
$Zn2Cu10_{-CoPr}$	10	2	co-precipitation with Zn
$Cu25_{-CoPr}$	25	-	co-precipitation without Zn
$Zn2.5Cu25_{-CoPr}$	25	2.5	co-precipitation with Zn
$Zn5Cu25_{-CoPr}$	25	5	co-precipitation with Zn
$Cu50_{-CoPr}$	50	-	co-precipitation without Zn
$Zn7.5Cu50_{-CoPr}$	50	7.5	co-precipitation with Zn
$Cu10_{-LR}$	10	-	deposition precip. via ligand removal without Zn
$Zn0.25Cu10_{-LR}$	10	0.25	deposition precip. via ligand removal with Zn
$Zn1Cu10_{-LR}$	10	1	deposition precip. via ligand removal with Zn
$Zn2Cu10_{-LR}$	10	2	deposition precip. via ligand removal with Zn
$Cu25_{-LR}$	25	-	deposition precip. via ligand removal without Zn
$Zn2.5Cu25_{-LR}$	25	2.5	deposition precip. via ligand removal with Zn
$Zn5Cu25_{-LR}$	25	5	deposition precip. via ligand removal with Zn
$Cu10_{-RP}$	10	-	reductive precip. without Zn
$Zn0.25Cu10_{-RP}$	10	0.25	reductive precip. with Zn
$Zn1Cu10_{-RP}$	10	1	reductive precip. with Zn
$Zn2Cu10_{-RP}$	10	2	reductive precip. with Zn
$Cu25_{-RP}$	25	-	reductive precip. without Zn
$Zn2.5Cu25_{-RP}$	25	2.5	reductive precip. with Zn
$Zn5Cu25_{-RP}$	25	5	reductive precip. with Zn

Table 17: Cu (Cu^a) and Zn (Zn^b) loadings in wt.% determined by ICP-OES as well as the Cu/Zn ratio. The error is determined to be around 5% including the preparation and the ICP-OES measurement itself. In addition, the ratio of Zn atoms per Cu atom at the surface (Zn/Cu_{surf}) of the different catalysts is calculated. For the calculation of Zn/Cu_{surf} the Cu surface areas of the pre-catalysts are used that are summarized in Table 18 and a Cu atom density of $1{,}47 \cdot 10^{19}$ atoms per m^2.[191]

Sample	Cu^a	Zn^b	Cu/Zn	Zn/Cu_{surf}
$Zn1Cu10_{-DP}$	9.6	0.95	10.1	0.6
$Zn2Cu10_{-DP}$	9.8	1.8	5.4	1.1
$Zn3Cu10_{-DP}$	9.8	2.7	3.6	1.7
$Zn2.5Cu25_{-DP}$	26.8	2.4	11.2	1.3
$Zn5Cu25_{-DP}$	25.2	4.3	5.9	2.3
$Zn0.25Cu10_{-CoPr}$	10.1	0.31	32.6	0.3
$Zn1Cu10_{-CoPr}$	10.0	0.90	11.1	0.7
$Zn2Cu10_{-CoPr}$	9.8	1.8	5.4	1.3
$Zn2.5Cu25_{-CoPr}$	24.1	2.3	10.5	0.6
$Zn5Cu25_{-CoPr}$	25.1	4.6	5.5	1.2
$Zn7.5Cu50_{-CoPr}$	50	7.5	6.7	1.8
$Zn0.25Cu10_{-LR}$	9.5	0.35	27.1	0.4
$Zn1Cu10_{-LR}$	9.7	0.83	11.7	0.9
$Zn2Cu10_{-LR}$	10.0	2.0	5.0	2.1
$Zn2.5Cu25_{-LR}$	13.7	2.5	5.5	1.8
$Zn5Cu25_{-LR}$	12.5	4.7	2.7	3.4
$Zn0.25Cu10_{-RP}$	9.0	0.29	31.0	1.6
$Zn1Cu10_{-RP}$	9.1	0.92	9.9	5.9
$Zn2Cu10_{-RP}$	9.1	1.8	5.1	11.3
$Zn2.5Cu25_{-RP}$	21.0	2.2	9.5	69.0
$Zn5Cu25_{-RP}$	27.1	3.1	8.7	97.0

Powder diffractograms are measured from the pre-catalysts (Al_2O_3 supported Cu nanoparticles after calcination without Zn) with high Cu loadings. The powder diffractograms are shown in Figure 75. The powder diffraction of the pre-catalysts with 10 wt.% Cu loading are depicted in Figure 52 and are discussed in section 0.

Only CuO and Al_2O_3 reflexes are observable. It indicates that during calcination the precipitates mainly $Cu(OH)_2$ and $Al(OH)_3$ are transformed into the respective oxides. The reflexes of CuO are very broad for $Cu25_{-CoPr}$ and become narrower for higher Cu loadings ($Cu50_{-CoPr}$). It hints that the CuO nanoparticles are smaller with 25 wt. % loading. In addition, the Al_2O_3 support is less crystalline compared to the sample with just 10 wt.% Cu loading. The CuO reflexes of

$Cu_{25\text{-}DP}$ are much broader compared to $Cu25_{\text{-}LR}$. According to XRD, the order of the CuO nanoparticle sizes are as follows: $Cu25_{\text{-}LR}$ > $Cu25_{\text{-}DP}$ > $Cu25_{\text{-}CoPr}$. $Cu25_{\text{-}RP}$ is not measured because metallic Cu nanoparticles are directly formed during reductive precipitation and the calcination step is not necessary.

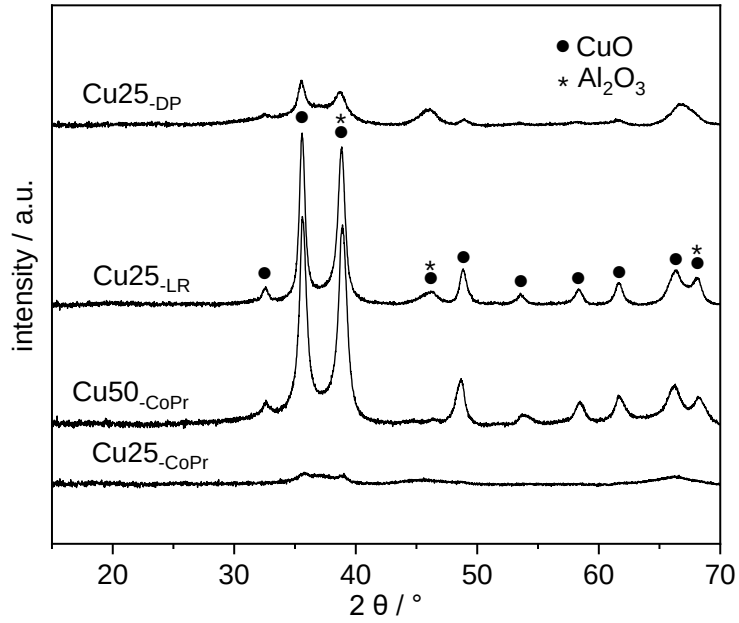

Figure 75: Powder diffractograms of $Cu25_{\text{-}DP}$, $Cu25_{\text{-}LR}$, $Cu25_{\text{-}CoPr}$ and $Cu50_{\text{-}CoPr}$ after calcination at 450°C for 4 h (2.5 K/min). The stars mark γ-Al_2O_3-reflexes[120, 121] and the triangles represent CuO[106]. Diffractograms are recorded in an angle range between 5° and 70° in steps of 0.013°.

In addition, the BET surface area, the pore size and the pore radius are determined of all pre-catalysts. The results are summarized in Table 18. In general, the BET surface areas decrease with increasing Cu loading. For the catalysts prepared by DP and LR a commercial Al_2O_3 support is used. Hence, Cu is precipitated onto the support. A higher Cu loading leads to plugging of the pores of the support. Consequently, the BET surface area drops. In the case of the co-precipitated pre-catalysts in which the Al_2O_3 support is formed simultaneously during the precipitation and subsequent calcination it is different. The higher Cu content inhibits the formation of highly porous Al_2O_3 which results in lower BET surface area. Nevertheless, a BET surface area of 123 m^2/g is achieved for the pre-catalysts with 50 wt.% Cu.

Like for the pre-catalysts with 10 wt.% Cu (see section 0), H_2-TPR is carried out of the 25 wt.% and 50 wt.% Cu loaded pre-catalyst to get information about the morphology of the different Cu nanoparticles. The H_2-TPR profiles are depicted in Figure 76. The TPR-profiles for the catalysts with 25 wt.% Cu loading prepared DP and LR are shifted to lower temperatures indicating that CuO nanoparticles interact less with the Al_2O_3 support which is most likely caused by larger Cu nanoparticles compared to the catalysts with 10 wt.% Cu loading.

Table 18: BET surface area (SA_{BET} in m^2/g), pore volume (V_{pore} in mL/g_{cat}) and pore radius (r_{pore} in nm) of the pre-catalysts. Cu crystallite sizes ($Size_{crys}$ in nm) after Zn deposition calculated with the Scherrer equation. The reflexes at 43 2θ and 50 2θ serve for the determination of the crystallite sizes (see Figure 59 and Figure 77). Cu metal surface area of the pre-catalysts ($Cu\text{-}SA_{N2O\text{-}RFC}$ in m^2/g) and of the catalysts after Zn deposition and subsequent reductive treatment at 120°C ($^{120°C}Cu\text{-}SA_{N2O\text{-}RFC}$) determined by N_2O-RFC. The N_2O-RFC is carried out in 1 % N_2O in He at ambient conditions. Before the measurement, the pre-catalysts are reduced in pure H_2 at 300°C (1 K/min) for 1 h. $Cu10_{\text{-}RP}$ and $Cu25_{\text{-}RP}$ are pretreated in pure H_2 at 40°C (1 K/min) for 1 h. The catalysts after Zn deposition are pretreated in pure H_2 at 120°C (1K/min) for 1h.

Sample	S_{BET}	V_{pore}	r_{pore}	$Size_{crys}$	$Cu\text{-}SA_{N2O\text{-}RFC}$	$^{120°C}Cu\text{-}SA_{N2O\text{-}RFC}$
$Cu10_{\text{-}DP}$	208	0.54	3.74	-	10.5	-
$Cu25_{\text{-}DP}$	148	0.44	4.54	-	11.6	-
$Zn2Cu10_{\text{-}DP}$	-	-	-	5.0 ±3.0	7.1	7.1
$Zn2.5Cu25_{\text{-}DP}$	-	-	-	10.4 ±1.0	-	7.2
$Zn5Cu25_{\text{-}DP}$	-	-	-	11.9 ±0.7	-	-
$Cu10_{\text{-}CoPr}$	185	0.51	3.74	-	8.5	-
$Cu25_{\text{-}CoPr}$	156	0.32	3.17	-	24.5	-
$Cu50_{\text{-}CoPr}$	123	0.22	3.18	-	26.0	-
$Zn2Cu10_{\text{-}CoPr}$	-	-	-	-	7.0	7.4
$Zn2.5Cu25_{\text{-}CoPr}$	-	-	-	-	-	17.5
$Zn5Cu25_{\text{-}CoPr}$	-	-	-	-	-	-
$Zn7.5Cu50_{\text{-}CoPr}$	-	-	-	6.5 ±0.6	-	-
$Cu10_{\text{-}LR}$	192	0.57	3.76	-	6.0	-
$Cu25_{\text{-}LR}$	133	0.45	4.54	-	8.8	-
$Zn2Cu10_{\text{-}LR}$	-	-	-	12.0 ±4.0	-	-
$Zn2.5Cu25_{\text{-}LR}$	-	-	-	13.7 ±1.2	-	5.4
$Zn5Cu25_{\text{-}LR}$	-	-	-	12.1 ±1.5	-	-
$Cu10_{\text{-}RP}$	-	-	-	-	1.0	-
$Cu25_{\text{-}RP}$	-	-	-	-	0.2	-
$Zn2Cu10_{\text{-}RP}$	-	-	-	18.0 ±2.0	-	-
$Zn2.5Cu25_{\text{-}RP}$	-	-	-	18.9 ±1.5	-	-
$Zn5Cu25_{\text{-}RP}$	-	-	-	20.8 ±2.1	-	-

This effect is much more pronounced for the co-precipitated catalysts with 25 wt.% Cu. The TPR profile is massively shifted to lower temperatures. But only one signal appears like in the TPR profile of the 10 wt.% Cu loaded pre-catalyst. The lower temperature (168 °C for $Cu25_{\text{-}CoPr}$ compared to 293 °C for $Cu10_{\text{-}coPr}$) indicate that with higher Cu loading the CuO nanoparticles are less incorporated into the Al_2O_3 support and hence the metal support interactions are less

distinct. The TPR signal for the 50 wt.% Cu loaded pre-catalyst appears at slightly higher temperatures which means that this sample contains more bulk CuO. It confirms the results obtained by XRD because the reflexes for CuO of $Cu50_{\text{-CoPr}}$ are by far more distinct which demonstrates that the CuO particles are quite larger compared to $Cu25_{\text{-CoPr}}$.

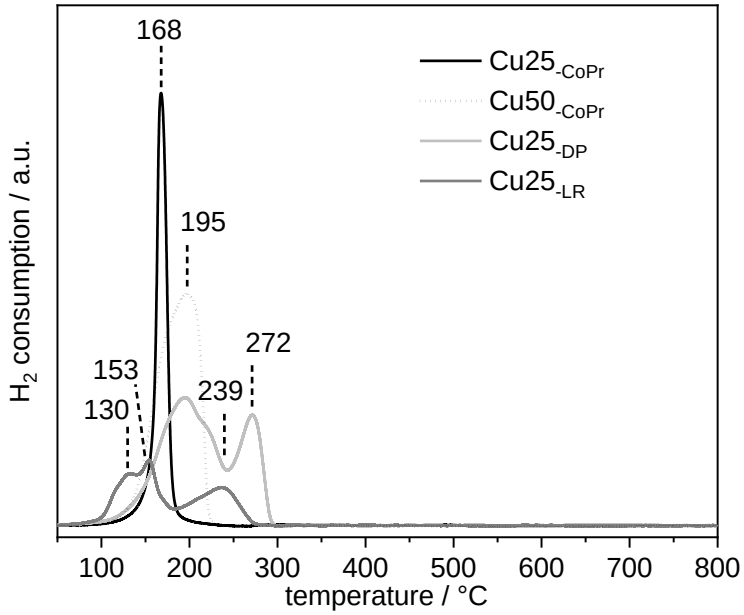

Figure 76: TPR profiles of $Cu25_{\text{-CoPr}}$, $Cu50_{\text{-CoPr}}$, $Cu25_{\text{-DP}}$ and $Cu25_{\text{-LR}}$ after calcination in air at 450°C (2.5 K/min) for 4h. The TPR profiles are carried out in a temperature range of 50°C to 800°C (5 K/min) in 2.5 % H_2 in He.

Before the Zn deposition, the pre-catalysts are reduced in H_2 to form Al_2O_3 supported metallic Cu nanoparticles. In Figure 77 the powder diffractograms of the catalysts with 25 wt.% and 50 wt.% Cu are shown after Zn grafting. Powder diffractograms of the catalysts with 10 wt.% Cu loading and 2 wt.% Zn are shown in Figure 59 and discussed in section 0.

Only Cu and Al_2O_3 reflexes can be observed. ZnO is not formed. It indicates that even with high Zn loadings Zn is deposited in thin layers onto the Cu nanoparticles. The catalysts originating of the same pre-catalysts show very similar patterns. Hence, the deposition of larger Zn amounts does not influence the Cu dispersion. The Cu crystallite sizes are determined using the Scherrer equation and the reflexes at 43 2θ and 50 2θ.[100-104] The values are summarized in Table 18. The crystallite sizes increase from around 5 ±3.0 nm (this value is not reliable, see discussion section 0, Cu nanoparticle size by TEM = 2.0 ±0.5 nm) to around 11 nm for the catalysts with 25 wt.% Cu loading prepared by DP. It indicates that a higher Cu amount does not lead automatically to a higher Cu dispersion for this precipitation method. The Cu crystallite size of the catalysts prepared by LR stays constant. But in this case the Cu loading differs only slightly because the 25 wt.% Cu loading could not be achieved as discussed before. The Cu crystallite sizes of the catalysts prepared by RP slightly increase with higher Cu loadings. Because of the very broad Cu reflexes of the catalysts with 25 wt.% Cu loading prepared by co-

precipitation only the Cu crystallite size of the 50 wt.% Cu loaded catalysts could be calculated (6.5 ±0.6 nm).

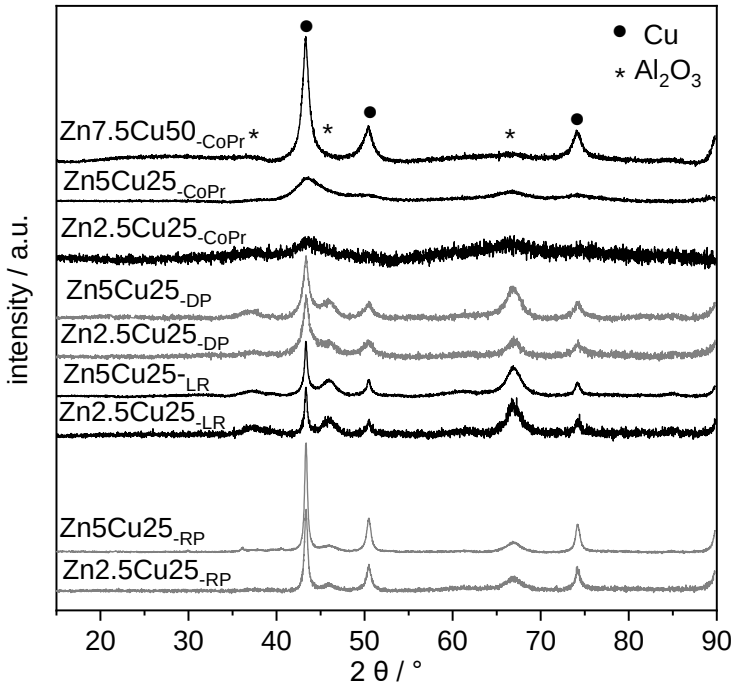

Figure 77: Powder diffractograms of the catalysts with 25 wt.% and 50 wt.% Cu after Zn deposition. The stars mark γ-Al_2O_3 reflexes[120, 121] and the dots represent metallic Cu[251]. Diffractograms are recorded in an angle range between 5° and 90° in steps of 0.008°.

In addition, the Cu surface area is determined via N_2O-RFC of the pre-catalysts as well as of the catalysts with 25 wt.% Cu loading after Zn deposition and reductive pretreatment at 120°C. All catalysts are pretreated at this temperature before the catalytic reaction for better comparability. The Cu surface areas are summarized in Table 18. The Cu surface area of the pre-catalysts prepared by DP ($Cu10_{-DP}$ and $Cu25_{-DP}$) only slightly increases from 10.5 to 11.6 m^2/g. The same course can be observed for the catalysts prepared by LR ($Cu10_{-LR}$ = 6.0 and $Cu25_{-LR}$ = 8.8) The values for the catalysts prepared by reductive precipitation are not reliable because the Cu surface area are around 1 or even below 1 m^2/g. In contrast to the precipitation methods in which the Cu is precipitated onto the Al_2O_3 support and the Cu surface area does not increase substantially with higher Cu loadings the Cu surface areas of the co-precipitated catalysts increase massively from 8.5 m^2/g for $Cu10_{-CoPR}$ to 24.5 m^2/g for $Cu25_{-CoPr}$ and to 26.0 m^2/g for $Cu50_{-CoPr}$. Especially from 10 to 25 wt.% Cu loading the Cu surface area increase is almost linearly to the increase of the Cu amount. An even higher Cu loading leads only to a slight rise. It agrees with the obtained powder diffractograms in which $Cu50_{-Copr}$ and the respective ZnCu catalysts show narrower reflexes compared to 25 wt.% catalyst. In summary, a Cu loading of 25 wt. % for the catalysts prepared by different deposition precipitation methods (DP, LR, RP) leads to larger Cu nanoparticles and only slight increases of the Cu surface area. This is in

good agreement with the results obtained by XRD. In addition, pre-catalysts prepared by co-precipitation have higher Cu surface areas with increasing Cu loading. However, a Cu loading of 50 wt.% Cu leads not to a substantial rise of the Cu surface area.
The Cu surface areas after Zn deposition and subsequent reductive pretreatment decrease because Zn is blocking Cu sites as discussed in section 3.4.1.3. The Cu surface area of 17.5 m^2/g for the co-precipitated catalysts ($Zn2.5Cu25_{\text{-CoPr}}$) is by far the highest.

3.4.2.2 CO_2 hydrogenation to methanol with different Cu and Zn loaded catalysts
The catalytic reaction of CO_2 and H_2 to MeOH is carried out at 28 bar and temperatures between 200 and 325 °C with a feed gas of H_2:CO_2 3:1. A detailed description and a drawing of the setup are depicted in the experimental part (section 7.2). The catalysts are used after reductive pretreatment at 120°C in H_2 for 1 h.
The CO_2 conversions of the catalysts are shown in Figure 78. In general, a higher Cu loading of 25 wt.% or even 50 wt.% in the case of $Zn7.5Cu50_{\text{-CoPr}}$ increases the CO_2 conversion especially at temperatures up to 275°C. The conversion increase of the co-precipitated catalysts with Cu loadings of 25 wt.% or 50 wt.% is up to three times higher at 225°C compared to the catalysts with 10 wt.% Cu loading. As we know from N_2O-RFC, the Cu surface area of the higher loaded catalysts is by far higher than that of the 10 wt.% Cu loaded catalysts. Hence, a higher Cu surface area leads to a large increase of the CO_2 conversion. The increase of the Cu surface for the catalysts prepared by LR and DP is not as much distinct with higher Cu loading. However, the CO_2 conversions also increase a lot. The CO_2 conversion of the catalysts prepared by RP remains very low due to the low Cu dispersion.
The Zn loading also influences the CO_2 conversion. Because the different Cu particles sizes have an influence on the Zn/Cu surface alloy formation and the catalysts are pretreated at 120°C in H_2 the extent of Zn/Cu surface alloy formation is very distinguished for the different catalysts. It means that the Zn/Cu surface alloy formation for the catalysts prepared by DP with higher Cu loading is expected to be more distinct due to the larger Cu nanoparticles compared to the catalysts with only 10 wt.% Cu. $Zn3Cu10_{\text{-DP}}$ for example converts less CO_2 compared to the other catalysts with the same Cu loading. The higher Zn loading of 3 wt.% compared to the lower loadings of 1 and 2 wt.% possibly leads to blocking of Cu sites and hence the CO_2 conversion is lowered.
The Zn/Cu surface alloy formation in the co-precipitated catalysts is less distinct for the catalysts with 10 and 25 wt.% Cu loading because N_2O-RFC and XRD confirmed that these catalysts consist of Cu nanoparticles with a similar size. Alloy formation of the 10 wt.% Cu loaded sample with 2 wt.% Zn loading begins only after 100°C. In contrast to that, it is expected that

the Zn/Cu surface alloy formation is more distinct for Zn7.5Cu50-CoPr because of the larger Cu nanoparticles.

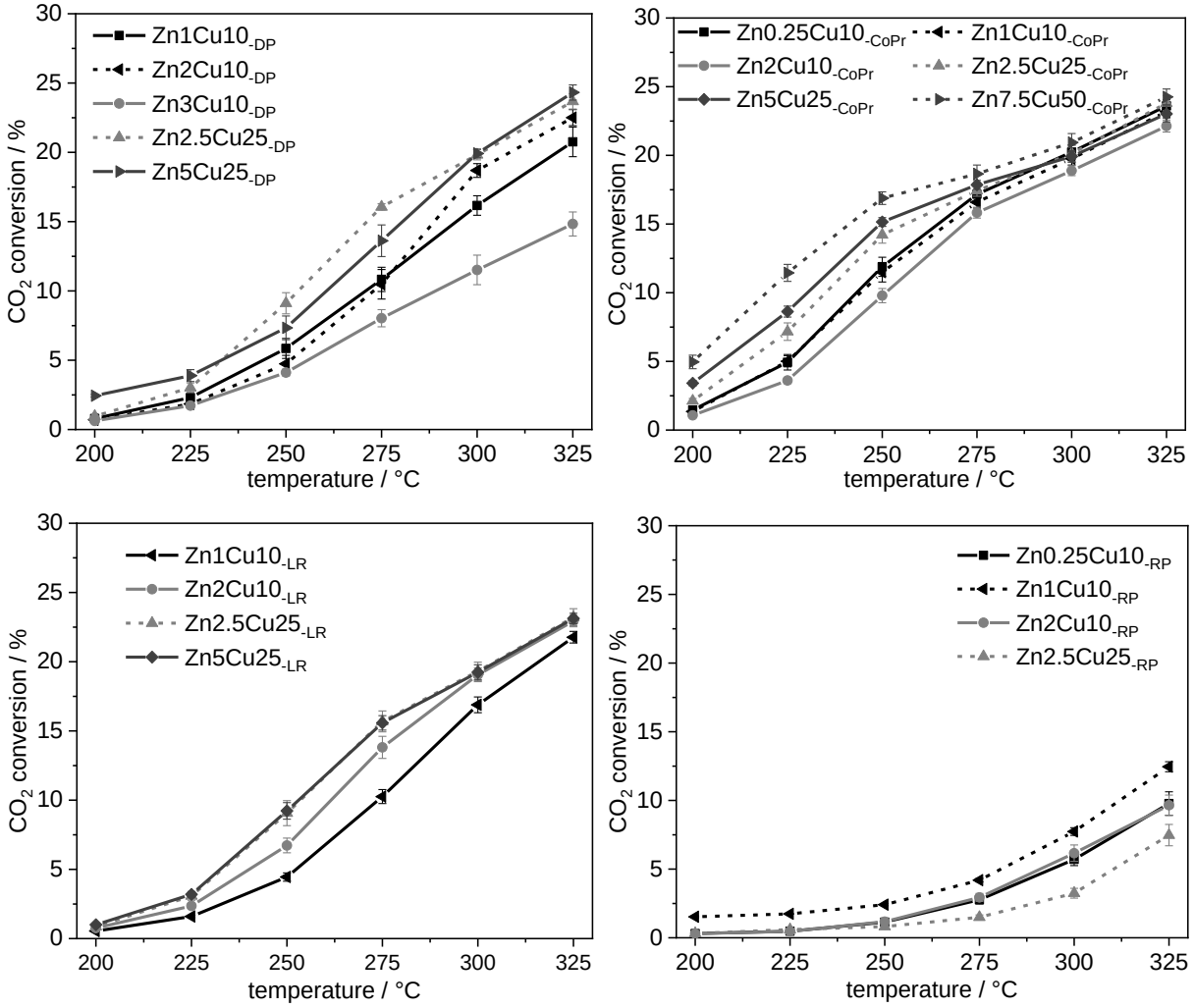

Figure 78: CO_2 conversion at different reaction temperatures (200, 225, 250, 275, 300, 325 °C) at 28 bar for the different Cu and Zn loaded catalysts ZnxCuy-$_z$ (x= Zn loading in wt.%, y = Cu loading in wt.%, z = precipitation method). The H_2:CO_2 ratio is 3:1. The GHSV is 8000 h^{-1}. The catalysts are pretreated in H_2:He 1:1 at 120°C for 1 h. The overall reaction time is 14 h 50 min.

The ratios of the Zn atoms to the Cu surface atoms (Zn/Cu_{surf}) are calculated using the Cu surface areas of the pre-catalyst and the Zn loadings. The values are summarized in Table 17. The MeOH selectivity of the different catalysts is depicted in Figure 79. The explanation for the different MeOH selectivity is complex and is discussed in detail. Hence, only the different MeOH selectivity of the catalysts prepared by DP and CoPr is presented. The MeOH selectivity of the other catalysts is shown in the appendix (Figure 114)

For the catalysts prepared by DP with 10 wt.% Cu loading the MeOH selectivity follows the order Zn2Cu10-$_{DP}$ > Zn1Cu10-$_{DP}$ ≈ Zn3Cu10-$_{DP}$. The Zn/Cu surface alloy formation at 120 °C pretreatment for all the catalysts behaves similarly because of the same pre-catalyst. Therefore, the different MeOH selectivity can be referred to the different Zn/Cu_{surf} ratios. 3 wt. % Zn

(Zn/Cu_{surf} = 1.7) seems to inhibit MeOH formation most likely to the overloading of the Cu surface whereas 1 wt.% Zn loading (Zn/Cu_{surf} = 0.6) is too low to form highly dispersed $Zn^{\delta+}$ sites. The effect of overloading the Cu surface by Zn is even more pronounced for the samples with higher Cu loadings. Because the Cu surface area does not increase drastically with higher Cu amounts the addition of 5 wt.% Zn means that the Zn/Cu_{surf} increase to 2.3. The larger Cu nanoparticles namely enhance the Zn/Cu alloy formation during the reductive pretreatment at 120°C and hence a higher Zn/Cu_{surf} value could be compensated by the more distinct Zn/Cu surface alloy formation but this effect cannot be observed. Possibly the Zn/Cu alloy formation is even increased but the extensive alloying is not beneficial for the formation of highly dispersed $Cu/Zn^{\delta+}$ sites.[275]

The different MeOH selectivity of co-precipitated catalysts also indicates the importance of the Zn loading regarding the Zn/Cu surface alloy formation. The MeOH selectivity for the catalysts with 10 wt.% Cu follows the order $Zn0.25Cu10_{-CoPr}$ > $Zn1Cu10_{-CoPr}$ > $Zn2Cu10_{-CoPr}$. After 120°C pretreatment the Zn/Cu surface alloy formation is low as discussed before. Hence, higher Zn loading leads to a higher Zn concentration on the Cu surface because less Zn can migrate into the Cu surface at these pretreatment conditions. In this case 0.25 wt.% Zn that means a low Zn/Cu_{surf} of just 0.3 is enough or at least more beneficial to form the promoting Zn/Cu surface alloy and consequently highly dispersed $Cu/Zn^{\delta+}$ sites during the catalytic reaction. In general, a higher Cu surface area leads to higher MeOH selectivity but the low selectivity of $Zn2.5Cu25_{-CoPr}$ shows that this suggestion is insufficient.

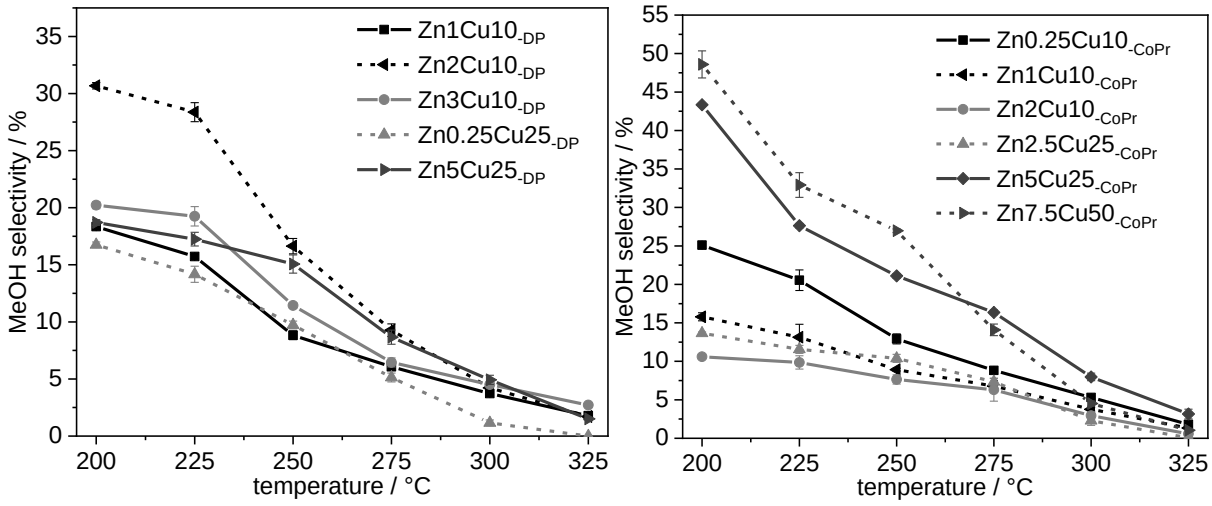

Figure 79: MeOH selectivity at different reaction temperatures (200, 225, 250, 275, 300, 325 °C) at 28 bar for the different Cu and Zn loaded catalysts ZnxCuy-z (x= Zn loading in wt.%, y = Cu loading in wt.%, z = precipitation method). The H_2:CO_2 ratio is 3:1. The GHSV is 8000 h^{-1}. The catalysts are pretreated in H_2:He 1:1 at 120°C for 1 h. The overall reaction time is 14 h 50 min.

The Zn/Cu_{surf} of $Zn5Cu25_{-CoPr}$ is 1.2 and consequently twice as high as the value of $Zn2.5Cu25_{-CoPr}$. It shows that not only a high Cu dispersion is needed for high methanol selectivity. It

agrees with the explanation of the different MeOH selectivity of the catalysts prepared by DP that the Zn amount which is deposited onto the Cu nanoparticles plays an important role.
It also indicates that it is not only important that simply Zn/Cu surface alloy be formed for highly dispersed $Cu/Zn^{\delta+}$ sites. In addition, the amount of Zn is crucial which is deposited onto the Cu surface before Zn/Cu surface alloy formation.[129, 131] Too high Zn amounts leads to blocking of the Cu sites or to extensive Zn/Cu alloy formation which is not beneficial for the formation of highly dispersed $Cu/Zn^{\delta+}$ sites. Too low Zn amounts can lead to the absence of Zn/Cu surface alloy and hence the lack of highly dispersed $Cu/Zn^{\delta+}$ sites.
In Figure 80 the interpolated temperature for 5 % CO_2 conversion for all catalysts and the respective MeOH selectivity are shown. The red symbols and red scripture represent the catalysts without Zn. The conversions and selectivity are interpolated with a polynomial function. The catalysts labels are summarized in Table 40 in section 1.1. It clearly figures out that Zn is enhancing the MeOH selectivity but also slightly reduces the temperature for 5 % conversion. In general, a higher Cu surface area leads to higher MeOH selectivity because most of the data points concerning the catalysts prepared by DP and CoPr which have the highest Cu surface areas lie above the points concerning to the catalysts with lower Cu surface areas (catalysts prepared by LR and RP).

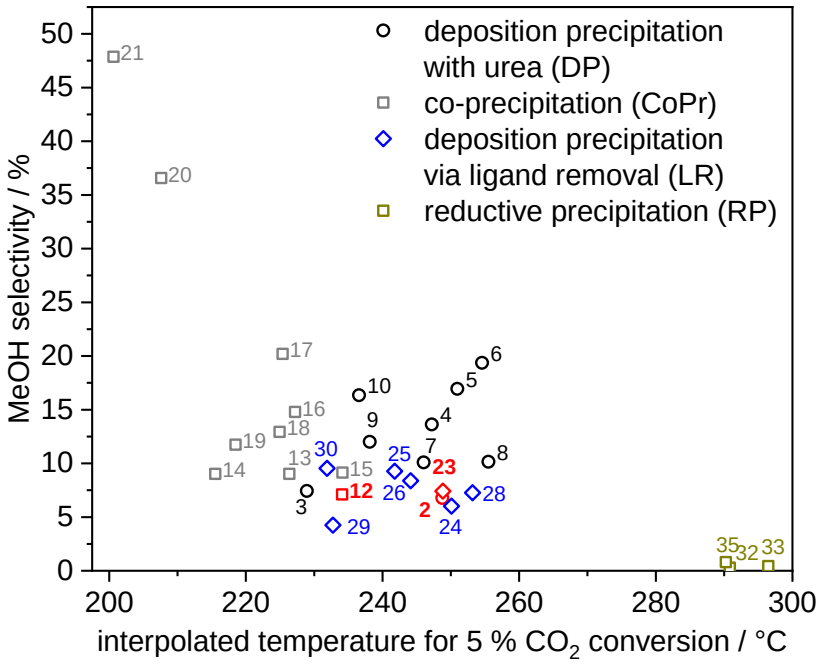

Figure 80: Interpolated temperature for 5 % CO_2 conversion for all catalysts and the respective MeOH selectivity. The red symbols and red scripture represent the catalysts without Zn. The catalysts labels are summarized in Table 40 in the appendix in section 1.1.

To get information of structural changes of the catalysts during the catalytic reaction powder diffractograms are measured exemplarily of the catalysts $Zn5Cu25_{-DP}$, $Zn5Cu25_{-LR}$,

Zn5Cu25$_{-RP}$, Zn5Cu25$_{-CoPr}$ and Zn7.5Cu50$_{-CoPr}$. The powder diffractograms are shown in Figure 81 and the respective Cu crystallite sizes are summarized in Table 19.

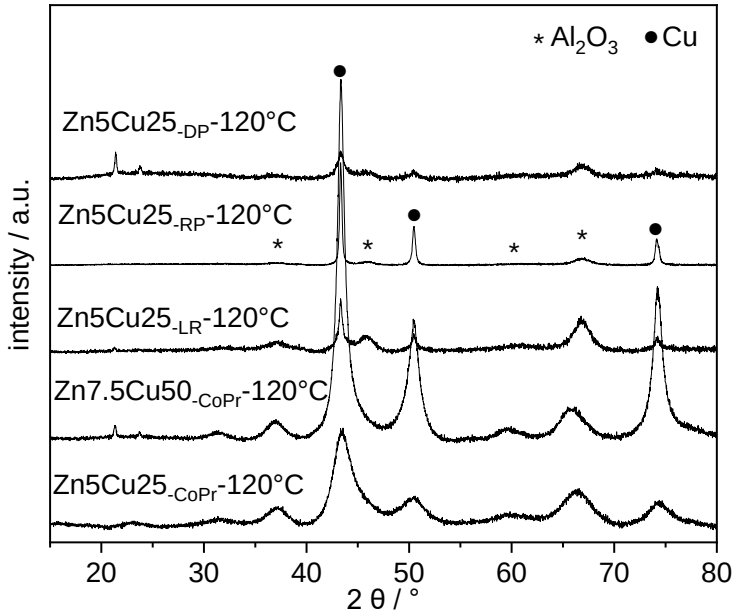

Figure 81: Powder diffractograms of Zn5Cu25$_{-DP}$, Zn5Cu25$_{-LR}$, Zn5Cu25$_{-RP}$, Zn5Cu25$_{-CoPr}$ and Zn7.5Cu50$_{-CoPr}$ after catalysis. The stars mark γ-Al_2O_3 reflexes[120, 121] and the dots represent metallic Cu[251]. Diffractograms are recorded in an angle range between 5° and 90° in steps of 0.008°. The catalysts are tested at different reaction temperatures (200, 225, 250, 275, 300, 325 °C) at 28 bar. The overall reaction time is 14 h 50 min. The H_2:CO_2 ratio is 3:1, the GHSV 8000 h^{-1}. The catalysts are pretreated in H_2:He 1:1 at 120°C for 1 h.

Table 19: Cu crystallite sizes ($^{cat}Size_{crys}$ in nm) after the catalytic reaction calculated with the Debye-Scherrer equation. The reflexes at 43 2θ and 50 2θ serve for the determination of the crystallite sizes (see Figure 74). Cu metal surface area of the catalysts after the catalytic reaction ($^{cat}Cu\text{-}SA_{N2O\text{-}RFC}$) determined by N_2O-RFC. The N_2O-RFC is carried out in 1 % N_2O in He at ambient conditions. Before the measurement of the Cu surface area after the catalytic reaction the catalysts are purged in He to get rid of residual adsorbates. The catalysts are tested at different reaction temperatures (200, 225, 250, 275, 300, 325 °C) at 28 bar. The overall reaction time is 14 h 50 min. The H_2:CO_2 ratio is 3:1, the GHSV 8000 h^{-1}.

Sample	$^{cat}Cu\text{-}SA_{N2O\text{-}RFC}$	$^{cat}Size_{crys}$
Zn2.5Cu25$_{-DP}$-120°C	4.0	-
Zn5Cu25$_{-DP}$-120°C	-	14.5 ±1.7
Zn2.5Cu25$_{-LR}$-120°C	2.2	-
Zn5Cu25$_{-LR}$-120°C	-	20.3 ±1.4
Zn2.5Cu25$_{-RP}$-120°C	-	-
Zn5Cu25$_{-RP}$-120°C	-	32.1 ±3.8
Zn2.5Cu25$_{-CoPr}$-120°C	5.4	-
Zn5Cu25$_{-CoPr}$-120°C	-	3.9 ±0.5
Zn7.5Cu50$_{-CoPr}$-120°C	-	10.0 ±1.4

Similar to the powder diffractograms of the catalysts with 10 wt.% Cu loading after catalysis (see Figure 74) only reflexes of Cu and Al_2O_3 are observable. The reflexes of the Al_2O_3 support are less distinct and hence the overlap of the Cu reflexes is lower. The crystallite sizes increase which confirms that the Cu nanoparticles agglomerate during the catalytic reaction.
Besides XRD, the Cu surface areas of the spent catalysts ($Zn5Cu25_{-DP}$, $Zn5Cu25_{-LR}$, $Zn5Cu25_{-CoPr}$) are determined by N_2O-RFC. The Cu surface areas decrease a lot compared to the Cu surface areas before the catalytic reaction, which agrees with the increasing Cu crystallite sizes. The drop of the Cu surface area of $Zn5Cu25_{-CoPr}$ is higher compared to catalyst with 10 wt.% Cu (see Table 15). Hence, the stabilizing effect of the Al_2O_3 support is less distinct with higher Cu loadings because Cu/Al_2O_3 interactions are weakened which was also obtained by H_2-TPR measurements.

3.4.3 Catalysts containing highly dispersed ZnO synthesized by $ZnEt_2$ grafting

Zn was deposited directly onto the Cu nanoparticles which were supported on Al_2O_3 for all the catalysts applied in the last chapters. Therefore, in another approach diethyl zinc is grafted onto the Al_2O_3 support, calcined in air to form highly dispersed ZnO and afterwards Cu is deposited via deposition precipitation with urea (DP). It has the advantage that ZnO is present to stabilize the Cu dispersion.[201, 202] In addition, according to *Lunkenbein et al.* it is expected that Zn migrates onto the Cu nanoparticles during the reductive pretreatment.[132] This step is bypassed by the direct deposition of diethyl zinc onto the Cu nanoparticles.

3.4.3.1 Synthesis of the catalysts

The synthesis of the catalysts is divided in two parts: the grafting of diethyl zinc on the Al_2O_3 support and the subsequent deposition of Cu via DP. Two catalysts are synthesized with different Cu to Zn ratios (10:1 ($ZnCu_{ref1}$) and 2:1 ($ZnCu_{ref2}$)). The results are compared to $ZnCu_{DP}$ which was already used for the investigations in the last two chapters with around 2 wt.% Zn and 10 wt.% Cu loading.

Grafting of diethyl zinc

During the first synthesis step diethyl zinc is grafted onto dehydroxylated Al_2O_3. Afterwards an IR spectrum is measured to prove if diethyl zinc was successfully grafted. The IR spectra of the pure dehydroxylated Al_2O_3 support as well as after the grafting step are shown in Figure 82. The assignment of the different signals was already discussed in section 0. The most significant signal occurs at 2961 cm^{-1} which represents *v*-CH_2-bond stretching. The signals around 2900 cm^{-1} appear also in the spectrum of pure Al_2O_3 but less in intensity. The series of signals below 1650 cm^{-1} (1641, 1531, 1461 cm^{-1}) are assigned to any organic compound and cannot

be allocated easily. The signals at 1248 cm^{-1} belong to $\delta_{as/s}$-CH-deformation of the grafted diethyl zinc because both signals are absent in the spectrum of pure Al_2O_3. *Boiadjiev et al.* observed similar results for the exposure of hydroxylated alumina at room temperature to a saturated vapor of dimethyl zinc which was discussed in section 0.[265] They described the surface species as O-Zn-CH_3 groups. During the exposure, they observed methane formation as well as a decrease of the OH-band after it. The primary reaction was indicated as the conversion of dimethyl zinc and a surface OH-group to O-Zn-CH_3 species and methane. Therefore, it seems reasonable to suppose a formation of O-Zn-CH_2-CH_3 species on the Al_2O_3 surface in the case of diethyl zinc. In addition, the signals at 3581, 3683 and 3729 cm^{-1} which belong to the OH-groups of the dehydroxylated Al_2O_3 decrease in intensity. It hints that the OH-groups are consumed during the grafting step which indicates the formation of a O-Zn-CH_2-CH_3 species on the surface.

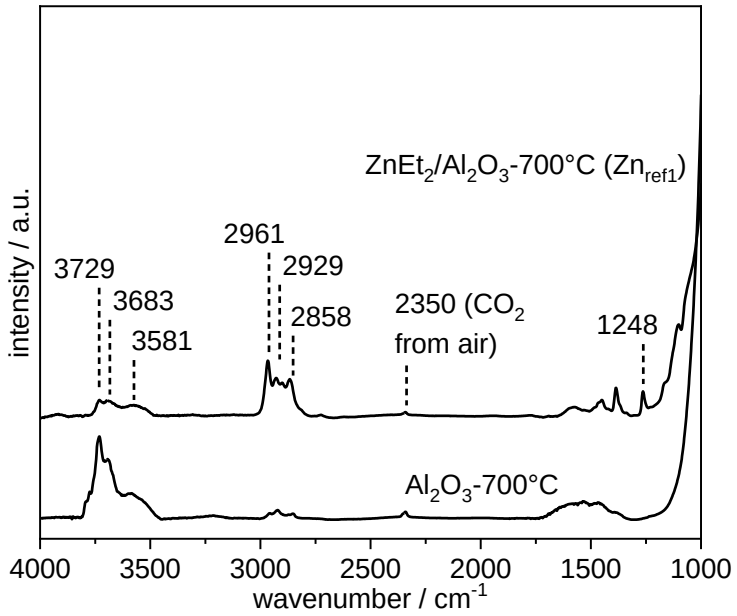

Figure 82: IR spectrum of the Al_2O_3 support (black line) before the grafting with ZnEt2. The Al_2O_3 support is calcined at 500°C (5K/min, 8h) and dehydroxylated at 700°C at 10^{-6} bar to create isolated hydroxyl groups. IR spectrum of the Al_2O_3 support after grafting with $ZnEt_2$ at room temperature (grey line).

The grafting procedure is performed at room temperature as well as at 40°C under hydrogen atmosphere. It turned out that the grafting of diethyl zinc is possible under both conditions. It means that under the same reaction conditions diethyl zinc can be grafted on Al_2O_3 like it was done on Cu. Therefore, the selectivity of the deposition on the Cu nanoparticles originates from the thermodynamic stabilities of the different surface species generated during the grafting. The Cu-Zn interactions seem to be more dominant which could be the reason why the zinc groups prefer Cu sites over Al_2O_3.

The grafting procedure is carried out with different Zn loadings. The BET surface area of the commercial Al_2O_3 is about 220 m^2/g. and the OH density of aluminum oxide treated at 700°C

amounts 0.6 nm^{-1}.[276] The amount of the OH groups of the used amount of Al_2O_3 support is 0.11 mmol resulting in a maximum Zn loading of 1.44 % if all hydroxyl groups are occupied with Zn. However, loadings of 0.7 ($ZnCu_{ref1}$) and 4.2 wt.% ($ZnCu_{ref2}$) are achieved and determined by elemental analysis via ICP-OES. That means that besides grafting of diethyl zinc also agglomerates can be formed, or diethyl zinc can be deposited in several layers onto the Al_2O_3 support.

After Zn grafting the samples are calcined at 250°C in air to decompose the O-Zn-CH_2-CH_3 species into highly dispersed ZnO. The powder diffractograms are shown in Figure 83.

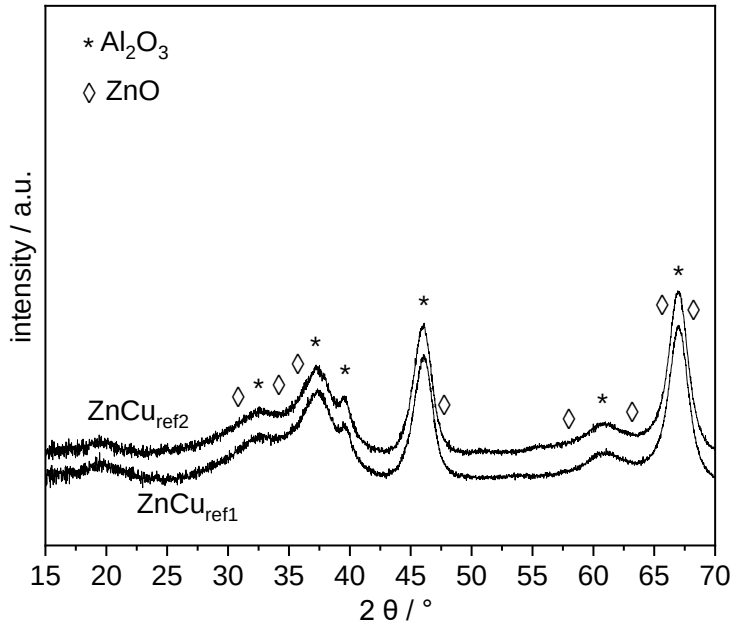

Figure 83: Powder diffractograms of $ZnCu_{ref1}$ and $ZnCu_{ref2}$ after Zn grafting and subsequent calcination at 250°C for 4 h (2.5 K/min). The stars mark γ-Al_2O_3-reflexes[120, 121] and the diamonds represent ZnO[277]. Diffractograms are recorded in an angle range between 5° and 70° in steps of 0.013°.

Only reflexes of the Al_2O_3 support are observable. It is not surprising that the powder diffractograms do not contain reflexes of ZnO because the reflexes of Al_2O_3 are very dominant and ZnO is highly dispersed with low loadings.

Deposition of Cu onto the ZnO/Al_2O_3 support

During the second synthesis step Cu is deposited onto the ZnO/Al_2O_3 support via deposition precipitation with urea (DP). The precipitation method is described in more detail in section 3.4.1.1 and the catalysts ($ZnCu_{ref1}$ and $ZnCu_{ref2}$) are compared to the catalysts $ZnCu_{DP}$ in which Zn was grafted directly onto the Cu nanoparticles.

After the deposition of Cu, the Cu and Zn loading is determined by elemental analysis via ICP OES (see Table 20). The Cu loadings are 6.8 and 9.6 wt.% and the Zn loadings are 0.7 and 4.2 for $ZnCu_{ref1}$ and $ZnCu_{ref2}$. The desired ratios of Cu/Zn with 10/1 and 2/1 are almost achieved.

In addition, powder diffractograms of the catalysts are measured after calcination and compared to Cu_{DP} (CuO on Al_2O_3) which is the precursor or rather the pre-catalyst of $ZnCu_{DP}$. The powder diffractograms are depicted in Figure 84.

Table 20: Cu (Cu^a) and Zn (Zn^b) loadings in wt.% determined by ICP-OES. The error is determined to be around 5% including the preparation and the ICP-OES measurement itself.

Sample	Cu^a	Zn^b
$ZnCu_{DP}$	6.9	0.7
$ZnCu_{rer1}$	9.6	4.2
$ZnCu_{ref2}$	9.8	1.8

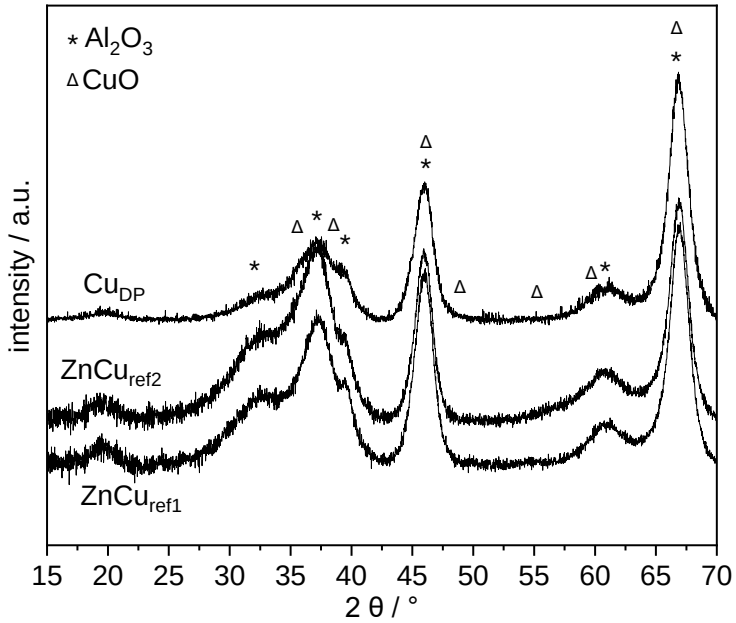

Figure 84: Powder diffractograms of Cu_{DP}, $ZnCu_{ref1}$ and $ZnCu_{ref2}$ after deposition of Cu and subsequent calcination at 450°C for 4 h (2.5 K/min). The stars mark γ-Al_2O_3-reflexes[120, 121]. The triangles represent CuO-reflexes[106]. Diffractograms are recorded in an angle range between 5° and 70° in steps of 0.013°.

Like in the powder diffractograms after Zn grafting, only reflexes assigned to Al_2O_3 are observable. CuO reflexes are implied at most in the region between 35 and 40 2θ and 60 2θ. The powder diffractograms of $ZnCu_{ref1}$ and $ZnCu_{ref2}$ fit well with the powder diffractogram of Cu_{DP} indicating a similar structure and nature of the deposited CuO particles.

Table 21: BET surface area (SA_{BET} in m^2/g), pore volume (V_{pore} in mL/g_{cat}) and pore radius (r_{pore} in nm) of $ZnCu_{ref1}$, $ZnCu_{ref2}$, the pure Al_2O_3 support and Cu_{DP}.

Sample	SA_{BET}	V_{pore}	r_{pore}
Cu_{DP}	208	0.54	3.74
$ZnCu_{ref1}$	167	0.52	4.58
$ZnCu_{ref2}$	156	0.52	4.56
Al_2O_3	220	0.58	3.74

In addition, the BET surface area as well as the pore volume and the pore radius are determined. The values are summarized in Table 21. The BET surface area of the reference catalysts is lower than the BET surface area of the pure Al_2O_3 and Cu_{DP}. On top of the CuO the ZnO plug the pores of the Al_2O_3 support which further decrease the BET surface area compared to the pure Al_2O_3 support and to CuO on Al_2O_3 (Cu_{DP}).

Furthermore, H_2-TPR is measured to investigate the different support/Cu interactions. The H_2-TPR profiles are shown in Figure 85.

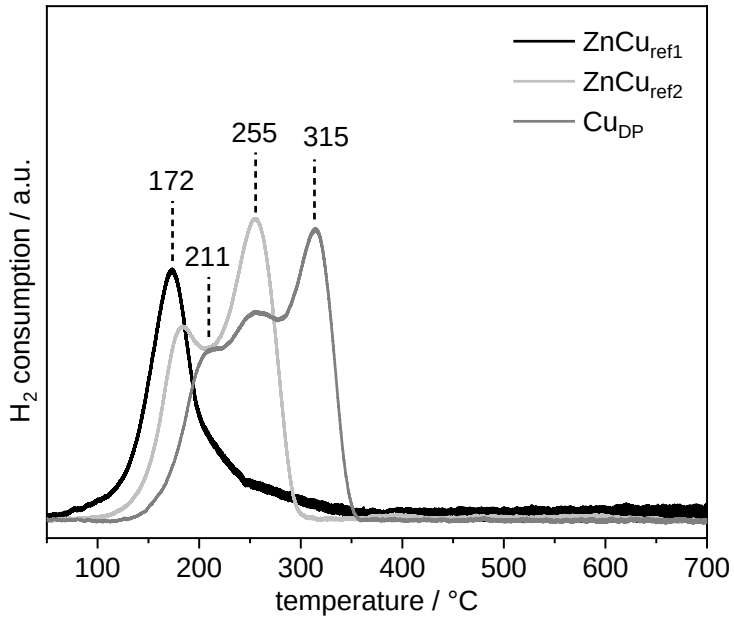

Figure 85: H_2-TPR profiles of $ZnCu_{ref1}$, $ZnCu_{ref2}$ and Cu_{DP} after calcination in air at 450°C (2.5 K/min) for 4h. The TPR profiles are carried out in a temperature range of 50°C to 800°C (5 K/min) in 2.5 % H_2 in He.

In general, three signals can be observed for Cu_{DP}, two for $ZnCu_{ref2}$ and one for $ZnCu_{ref1}$. The different signals of Cu_{DP} are discussed in detail in section 0. In addition, the signals of $ZnCu_{ref2}$ and $ZnCu_{ref1}$ are shifted to lower temperatures which suggest that the ZnO underlay which is located between the Al_2O_3 support and the Cu particles decreases the support/Cu interactions.[252, 253] The difference between $ZnCu_{ref1}$ and $ZnCu_{ref2}$ is most likely caused by the lower Cu loading of $ZnCu_{ref1}$ which leads to a smaller particle distribution that is represented by only one signal at low temperature in the TPR-profile.

The Cu surface area is determined by N_2O-RFC. The values are compared to pure Cu_{DP} and to $ZnCu_{DP}$ (Cu_{DP} as precursor after Zn deposition, see section 3.4.1.2) and are summarized in Table 22.

The Cu surface areas decrease with the addition of Zn. The decrease of $ZnCu_{DP}$ is caused by the deposition of Zn onto the Cu nanoparticles as discussed in section 3.4.1.3.

Table 22: Cu metal surface area of $ZnCu_{ref1}$, $ZnCu_{ref2}$, Cu_{DP} and $ZnCu_{DP}$ determined by N_2O-RFC (Cu-$SA_{N2O\text{-}RFC}$ in m^2/g). The N_2O-RFC is carried out in 1 % N_2O in He at ambient conditions. Before the measurement $ZnCu_{ref1}$, $ZnCu_{ref2}$ and Cu_{DP} are reduced in pure H_2 at 300°C (1 K/min) for 1 h. $ZnCu_{DP}$ is not pretreated before the measurement.

Sample	Cu-$SA_{N2O\text{-}RFC}$
Cu_{DP}	10.1
$ZnCu_{ref1}$	6.1
$ZnCu_{ref2}$	7.0
$ZnCu_{DP}$	7.1

Since the Cu nanoparticles of $ZnCu_{ref1}$ and $ZnCu_{ref2}$ are prepared by the same method as the particles of Cu_{DP}, the Cu metal surface area should be similar. But they differ up to 4 m^2/g.
The decrease of the Cu surface of $ZnCu_{ref1}$ and $ZnCu_{ref2}$ compared to Cu_{DP} is most likely caused by an $Zn^{\delta+}$/ZnO overlayer which deposits on the Cu nanoparticles during the reduction according to *Lunkenbein et al.*.[132, 199] Interestingly, it seems that with the deposition of Zn directly onto the Cu nanoparticles this overlayer growth can be simulated because the Cu surface area of $ZnCu_{DP}$ is nearly the same.
The lower value of $ZnCu_{ref1}$ compared to $ZnCu_{ref2}$ originates from the lower Cu loading but the difference is not as much distinct as it would be expected due to the large differences of the Cu loadings. It indicates that $ZnCu_{ref1}$ most likely contains smaller Cu nanoparticles which was also observed by H_2-TPR.

3.4.3.2 CO_2 hydrogenation to methanol

The CO2 hydrogenation reaction is carried out at 28 bar and temperatures between 200 and 325 °C with a feed gas of H_2:CO_2 3:1. A detailed description and a drawing of the setup are depicted in the experimental part (section 7.2). The catalysts $ZnCu_{ref1}$ and $ZnCu_{ref2}$ are reductively pretreated in H_2 at 300°C for 1 h. The catalysts are compared to pure Cu on Al_2O_3 ($pureCu_{DP}$), to $ZnCu_{DP}$ (Zn is directly deposited onto the Cu) without pretreatment and to $ZnCu_{DP}$-200°C that is pretreated at 200°C in H_2.
The CO_2 conversion as well as the MeOH selectivity are shown in Figure 86. The CO_2 conversion of $ZnCu_{ref1}$ and $ZnCu_{ref2}$ are higher than of the other catalysts up to 275°C reaction temperature. The different CO_2 conversions of Cu_{DP}, $ZnCu_{DP}$ and $ZnCu_{DP}$-200°C are discussed in detail in section 3.4.1.3. It is expected that a $Zn^{\delta+}$/ZnO layer on top of the Cu nanoparticles is formed during the reductive pretreatment of $ZnCu_{ref1}$ and $ZnCu_{ref2}$. In the case of $ZnCu_{DP}$ just Zn is deposited onto the Cu nanoparticles. $ZnCu_{DP}$-200°C is the same catalysts than $ZnCu_{DP}$ with the difference that due to the reductive pretreatment at 200°C in H_2 highly dispersed Zn/Cu surface alloy developed which is then transformed to highly dispersed Cu/$Zn^{\delta+}$ sites during the

catalytic reaction. However, it seems that the preformed $Zn^{\delta+}$/ZnO layer is favorable for higher CO_2 conversion which could be caused by facilitated CO_2 activation in the presence of ZnO.[278]

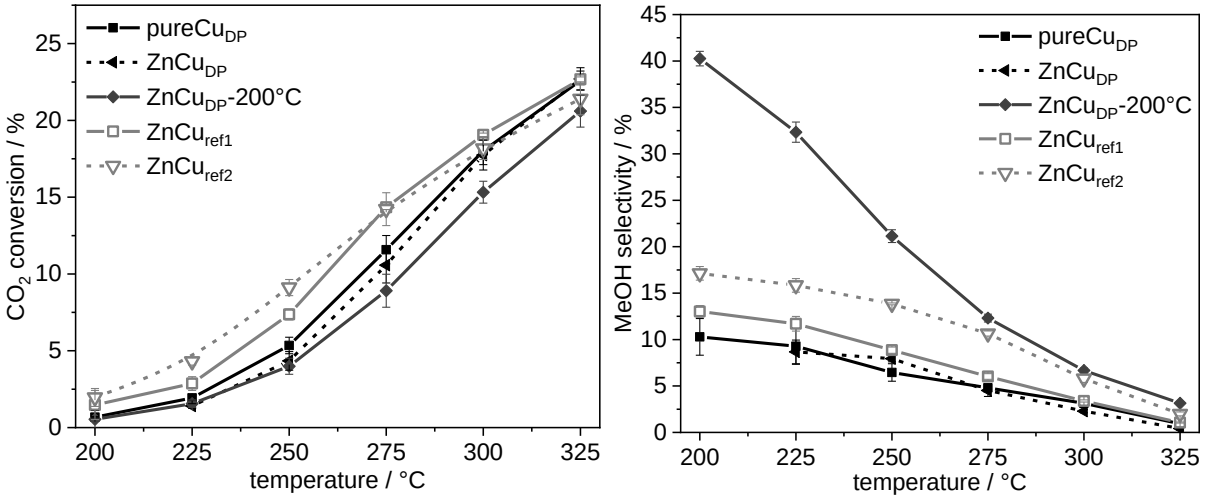

Figure 86: CO_2 conversion and MeOH selectivity at different reaction temperatures (200, 225, 250, 275, 300, 325 °C) at 28 bar for pureCu_{DP}, $ZnCu_{DP}$, $ZnCu_{DP}$-200°C, $ZnCu_{ref1}$ and $ZnCu_{ref2}$. The H_2:CO_2 ratio is 3:1. The GHSV is 8000 h^{-1}. The catalysts are pretreated in H_2:He 1:1 at 300°C or 200°C for 1 h. The overall reaction time is 14 h 50 min.

In general, the MeOH selectivity of the Zn containing catalysts is higher compared to the catalyst with pure Cu on Al_2O_3 (Cu_{DP}). However, the selectivity of $ZnCu_{DP}$-200°C is by far the highest with 40% at 200°C. It indicates that the preformed Zn/Cu surface alloy leads to $Cu/Zn^{\delta+}$ sites that are more dispersed or more selective than that formed during the reduction of a CuO/ZnO/Al_2O_3 catalyst ($ZnCu_{ref1}$ and $ZnCu_{ref2}$). It underlines the importance of a Zn/Cu surface alloy for the formation of highly dispersed $Cu/Zn^{\delta+}$ sites and hence for high methanol selectivity which was discussed in detail in section 3.4.1.3.

Table 23: Cu metal surface area of $ZnCu_{ref1}$, $ZnCu_{ref2}$, $ZnCu_{DP}$ and $ZnCu_{DP}$-200°C after catalysis determined by N_2O-RFC ($^{cat}Cu\text{-}SA_{N2O\text{-}RFC}$ in m^2/g). The N_2O-RFC is carried out in 1 % N_2O in He at ambient conditions. The catalysts are tested at different reaction temperatures (200, 225, 250, 275, 300, 325 °C) at 28 bar. The overall reaction time is 14 h 50 min. The H_2:CO_2 ratio is 3:1, the GHSV 8000 h^{-1}.

Sample	$^{cat}Cu\text{-}SA_{N2O\text{-}RFC}$
$ZnCu_{ref1}$	3.4
$ZnCu_{ref2}$	3.8
$ZnCu_{DP}$	1.4
$ZnCu_{DP}$-200°C	1.0

In addition, the Cu surface areas are measured after catalysis to investigate if ZnO has an influence on the Cu surface area and consequently on the Cu dispersion. The values are summarized in Table 23.

The Cu surface areas of $ZnCu_{ref1}$ and $ZnCu_{ref2}$ decrease by far less than the Cu surface areas of $ZnCu_{DP}$ and $ZnCu_{DP}$-200°C. The only difference is that in $ZnCu_{ref1}$ and $ZnCu_{ref2}$ Zn is not deposited onto the Cu nanoparticles, but it is located between the Cu nanoparticles. That could be the reason why the Cu nanoparticles do not sinter as much as the Cu nanoparticles in $ZnCu_{DP}$ and $ZnCu_{DP}$-200°C. The ZnO particles between the Cu nanoparticles act as spacer and prevent sintering which was also observed by *Behrens et al*.[141] It means that Zn is not only beneficial for the formation of the active sites. It also acts as structural promotor to stabilize the Cu dispersion and consequently a high Cu surface area.[166, 203, 206, 208]

3.5 Conclusions

A new synthesis route for $Cu/Zn/Al_2O_3$ catalysts via grafting of $ZnEt_2$ on Al_2O_3 supported Cu nanoparticles is developed to generate strong Cu-Zn interactions that are important for the catalytic reaction of CO_2 to MeOH. $ZnEt_2$ turned out to be an ideal grafting agent because of the easy cleavage of the ethyl groups reacting with H_2. The advantage of the synthesis route is the exclusive deposition of Zn(II) on metallic Cu nanoparticles. The Al_2O_3 support is not involved compared to conventional co-precipitation or incipient wetness impregnation in which ZnO and CuO are distributed within the whole catalyst. It allows to study the role of Zn in direct vicinity of Cu and to exclude the influence of Zn, which is located between the Cu particles and the Al_2O_3 support.

Zn/Cu surface alloy formation is observed even below 100°C. By reductive pre-treatment of the catalysts, it is possible to adjust the Zn/Cu ratio at the surface and hence the extent of Zn/Cu surface alloy formation. It turned out that the formation of Cu/Zn surface alloy after reductive pretreatment leads to the formation of highly dispersed $Cu/Zn^{\delta+}$ sites during the catalytic reaction. A very pronounced alloy formation or even bulk alloy is not as beneficial as Zn/Cu surface alloy. In addition, the Zn coverage is important depending on the Cu particle size and consequently the level of Zn/Cu alloy formation. Too low or high Zn amounts enhance only slightly the selectivity to methanol. In general, the presence of Zn at the Cu surface increases the selectivity to methanol by far.

For comparison, catalysts were prepared where Zn or rather ZnO is first and exclusively deposited on Al_2O_3. Cu is precipitated afterwards onto the support. It turned out that these catalysts are more resistant towards sintering than the catalysts where Zn is exclusively deposited onto the Cu nanoparticles. It means that the Zn atoms located on the Cu nanoparticles does not prevent sintering and ZnO must be located between the Cu nanoparticles to decrease Cu particle agglomeration. In addition, the selectivity to methanol is increased with this catalyst but the increase is lower than for the catalysts where Zn is deposited directly onto the Cu nanoparticles. It underlines the importance of the formation of Zn/Cu surface alloy as precursor for catalysts with high methanol selectivity.

4

MeOH Synthesis – Development of Copper/Zirconia Based Catalysts for MeOH Synthesis

4.1 Introduction

Due to the rising concentration of CO_2 in the atmosphere and the role of CO_2 as greenhouse gas, methanol synthesis from pure CO_2 feeds is of great interest.[6, 125-128] The challenges of activation and converting CO_2 have already been discussed in section 3.2.1. Usually, $Cu/ZnO/Al_2O_3$ catalysts are applied in the industrial methanol synthesis process using typical syngas feeds ($CO/CO_2/H_2$).

Due to the low selectivity to methanol and the preference to CO formation via the RWGS reaction using $Cu/ZnO/Al_2O_3$ with CO_2 rich gas feeds alternative catalyst systems must be designed.[129, 151, 279]

In particular In_2O_3, ZrO_2, TiO_2, CeO_2 or Ga_2O_3 oxide-based systems seems to be very promising.[279-289] Especially ZrO_2 based catalysts show high CO_2 conversion and methanol selectivity at lower pressures.[286, 289] Because the reaction setup (parallel testing unit with 12 reactors) used for this work can only be applied at a maximum pressure of 10 bar, ZrO_2 based catalysts are the preferred systems. The role of ZrO_2 in methanol synthesis as well as the different promotors that are added to the ZrO_2 based catalysts are presented in the next section.

For this work, different Cu/ZrO_2 catalysts are synthesized by variation of several parameters during the co-precipitation procedure and are applied in CO_2 hydrogenation to methanol using a parallel testing unit (PTU). In addition, promotor screening is carried out and the influence of different reaction parameters is studied. Selected catalysts are characterized and analyzed by XRD, H_2-TPD and N_2O-RFC.

4.2 Theoretical background

In the following, the role of ZrO_2 in Cu/ZrO_2 catalysts is presented as well as the influence of promotors on the catalytic activity of Cu/ZrO_2 based catalysts.

4.2.1 Cu/ZrO_2 catalysts

Fujitani et al. compared different catalyst supports for the hydrogenation of CO_2 to methanol at 250°C and 50 bar. The promoting effect of ZrO_2 is on the same level as Al_2O_3. Ga_2O_3. ZnO is most beneficial.[290]

Koeppel et al. prepared Cu/ZrO_2 catalysts with different methods and compared the catalytic activity. It turned out that precipitation methods gain the highest activity and methanol selectivity by formation of a large interfacial surface area of the two components CuO and ZrO_2. Especially co-precipitation is most promising due to the development of microcrystalline Cu particles, which are stabilized by amorphous ZrO_2. A linear relationship between surface area and catalytic activity was found within the same preparation method but not comparing the different prepared catalysts which hints that the interfacial area between the two compounds is important.[285] The precipitation as well the ageing temperature also influence the structure of precipitated Cu/ZrO_2 based catalysts.[291] *Ro et al.* also stated that the interfacial surface area of Cu and ZrO_2 enhances methanol formation.[292]

Liu et al. also investigated the influence of the preparation method on the catalytic activity. ZrO_2 aerogel prepared by supercritical fluid drying and subsequent deposition precipitation of Cu leads to the catalysts with highest methanol formation rates. The higher formation rate is caused by the higher Cu surface area, small particle size distribution and small Cu nanoparticles.[293]

Temperature-programmed reduction and temperature-programmed desorption experiments of Cu/ZrO_2 catalysts showed that Cu loadings below 10 wt.% and calcination below 650°C leads to the highest dispersion of Cu. ZrO_2 is useful for gaining a high Cu surface area.[294]

Furthermore, *Pokrovski et al.* studied the adsorption of CO and CO_2 on tetragonal and monoclinic ZrO_2. Monoclinic ZrO_2 has a much higher adsorption capacity than tetragonal ZrO_2. They explain the differences by the higher concentration and basicity of the OH-groups, the stronger Lewis acidity of Zr^{4+} cations and the stronger Lewis basicity of the O^{2-} ions.[295]

Wang et al. confirms that the monoclinic ZrO_2 phase is more beneficial and they indicate that this phase leads to higher catalytic activity.[296, 297] *Frei et al.* also suggest that the monoclinic ZrO_2 phase leads to an larger increase of the catalytic activity due to oxygen vacancies which facilitate the adsorption of the reactants CO or rather CO_2.[283]

Tada et al. investigated the active site of Cu/ZrO_2 catalysts by using Cu/ZrO_2 catalysts with different morphologies. It turned out, that the interfacial sites between Cu and α-ZrO_2 act as

active sites and they can only be formed by the reduction of an amorphous $Cu_aZr_{1-a}O_b$ precursor. The specific precursor also leads to a high dispersion of Cu. They also stated that methanol decomposition influences the methanol selectivity. Hence, α-ZrO_2 leads to high methanol selectivity due to the low adsorption energy of methanol.[287-289]

Larmier et al. studied the CO_2 hydrogenation to methanol with catalysts prepared by grafting of $[Cu(O^tBu)]_4$ on the hydroxyl groups of ZrO_2. They also did DFT calculations to get information about the reaction mechanism. Like for the reaction mechanism on $Cu/ZnO/Al_2O_3$ catalysts the formate species plays a key role as reaction intermediate. They also stated that the interface of Cu and ZrO_2 is imminent for high active Cu/ZrO_2 methanol catalysts like the other authors proposed.[284] The methanol formation via the formate pathway was also suggested from *Ma et al.* by studying inverse ZrO_2/Cu catalysts.[298]

Kattel et al. did DFT calculations to determine what would be the most promoting effect of ZrO_2 in Cu/ZrO_2 catalysts in a catalyst by design approach. The combination of reduced Zr^{3+} and Cu sites would most likely increases the interaction with $*CO_2$, *CO, *HCO and $*H_2CO$. It would mean that methanol formation follows the pathway RWGS and subsequent CO hydrogenation which is quite different to the reaction mechanism presented in section 3.2.2. Formate (*HCOO) would even lead to poisoning of the catalyst and inhibiting the formate reaction pathway.[299]

Liu et al. also did DFT calculation to find out what could be a highly active catalyst. They indicate that $(ZrO_2)_3$/Cu(110) would be a promising catalyst.[300]

Besides using ZrO_2 as support material, the role of Zr as promotor was investigated in several studies.[301-304]

Fisher et al. indicate that the addition of Zr to Cu/SiO_2 catalysts does not significantly influences the RWGS. However, the methanol synthesis rate increases. They suggest that Zr facilitates the adsorption of CO or rather CO_2 which can be easier hydrogenated with H_2 adsorbed on the Cu surface.[305] Similar results are obtained by *Arena et al.* investigating $Cu/ZnO/ZrO_2$ catalysts.[306]

Suh et al. stated that Zr can also act as stabilizer for Cu^+ and that the ratio between Cu^0/Cu^+ is essential for high methanol formation rates. As discussed in section 3.2.3, several authors propose that Cu^+ plays an important role in the methanol formation mechanism.[307]

In addition, the Cu dispersion can be enhanced by the addition of Zr. *Yang et al.* found out by studying Zr promoted Cu/ZnO catalysts that without Zr Cu is well-crystallized and consequently less active in methanol synthesis. The addition of Zr leads to highly dispersed Cu nanoparticles which increase the catalytic activity.[308] The same relation was found by *Zhang et al.* investigating Zr doped Cu/γ-Al_2O_3 catalysts.[309]

4.2.2 Promotion of Cu/ZrO_2 catalysts

The addition of promoters to Cu/ZrO_2 based catalysts further enhances their catalytic activity. Many studies report about promotion of the $Cu/ZnO/ZrO_2$ system.

Sloczinsky et al. investigated the influence of B, Ga, In, Gd, Y, Mg and Mn on the catalytic activity of a $Cu/ZnO/ZrO_2$ catalyst. They found that Ga_2O_3 and Y_2O_3 drastically enhance the methanol yield. In_2O_3 decreases the overall catalytic activity of the catalyst. At higher temperatures Ga_2O_3 and Gd_2O_3 are beneficial for higher methanol selectivity.[310, 311]

Guo et al. studied the promotional effect of La for Cu/ZrO_2 catalysts. They found out, that to some extent the Cu surface area increases with the La loading. The most promoting effect has a La loading of 5 wt.%. In addition, they stated that with increasing La loading the number of basic sites rises and hence the selectivity to methanol.[312]

Besides La, also Ag was investigated as promotor for Cu/ZrO_2 catalysts. The addition of Ag enhances the MeOH selectivity compared to Ag/ZrO_2 and Cu/ZrO_2 which hints the presence of special active sites which originate from a Cu/Ag alloy.[286]

Phongamwong et al. added SiO_2 to a ternary $CuO/ZnO/ZrO_2$ catalyst. SiO_2 creates higher long-term stability of the catalysts by acting as spacer. It further enhances the Cu metal surface area as well as the basicity of the ternary catalyst.[313]

Hengne et al. studied the effect of Sn on Ni/ZrO_2 or $Ni/In//ZrO_2$ catalysts. Sn decreases the selectivity to methane and increases the selectivity to methanol.[314]

Wang et al. investigated mixed oxide catalysts $CuO/ZnO/ZrO_2/M_xO_y$ (M = W, Cr, Mo). WoO_3 as well as MoO_3 increase the selectivity to methanol and the methanol yield. Cr_2O_3 slightly decreases both.[315]

Weiwei et al. reported about Cu/Ce/Zr catalysts. The components form a solid solution which enhances the Cu surface area, the Cu dispersion and hence the surface concentration of the formate species. Both contribute to high catalytic activity and high methanol selectivity.[316]

4.3 Motivation

Cu/ZrO_2 based catalyst are efficient in methanol synthesis from CO_2 even at pressures as low as 10 or 20 bar as mentioned in the introduction. Therefore, these catalysts are ideal for reaction setups that can only be operated in this pressure range. In this case a parallel testing unit with 12 parallel reactors is used for the investigations which was previously constructed for CO_2 methanation and hence only pressures up to 10 bar can be applied.

Therefore, a Cu/ZrO_2 catalyst is synthesized by variation of different preparation parameters to achieve high methanol selectivity and high CO_2 conversion at these conditions. Based on this Cu/ZrO_2 catalyst, a promotor screening is carried out to investigate the influence of different metals on the CO_2 conversion as well as on the methanol selectivity. The different promotors are added either during the co-precipitation procedure or by impregnation of the precipitate after the co-precipitation.

In addition, the influence of reaction parameters (total gas flow, pressure, H_2/CO_2 ratio, temperature) is investigated using a standard Cu/ZrO_2 catalyst. The data are evaluated by a design of experiment approach. These measurements are carried out in a single testing unit used for the catalytic measurements in section 3.

4.4 Results and discussion

First, the synthesis of several Cu/ZrO_2 catalysts and their catalytic performance in methanol synthesis from CO_2 are described. Afterwards, the influence of the different promotors on the catalytic performance is shown. In addition, the effect of pressure, temperature, total gas flow and CO_2/H_2 ratio on the catalytic performance is discussed.

4.4.1 Synthesis, characterization and catalytic performance of Cu/ZrO_2 catalysts

Different Cu/ZrO_2 catalysts are synthesized by variation of the co-precipitation, ageing and calcination parameters. Some of the catalysts are analyzed by XRD, elemental analysis via ICP-OES, H_2-TPR and N_2O-RFC (determination of the Cu surface are). In addition, all catalysts are applied in methanol synthesis from CO_2 using a parallel testing unit. The catalyst with the best catalytic performance is further used for promotor screening by addition of various metals.

4.4.1.1 Synthesis of Cu/ZrO_2 catalysts

The Cu/ZrO_2 catalysts are synthesized by co-precipitation according to a modified procedure of *Tada et al.*.[286] Zirconyl nitrate ($ZrO(NO_3)_2 \cdot 3H_2O$) and Cu nitrate ($Cu(NO_3)_2 \cdot 3H_2O$) act reactants. A titration curve is measured to determine the pH value at which both components precipitate simultaneously (see Figure Figure 87).

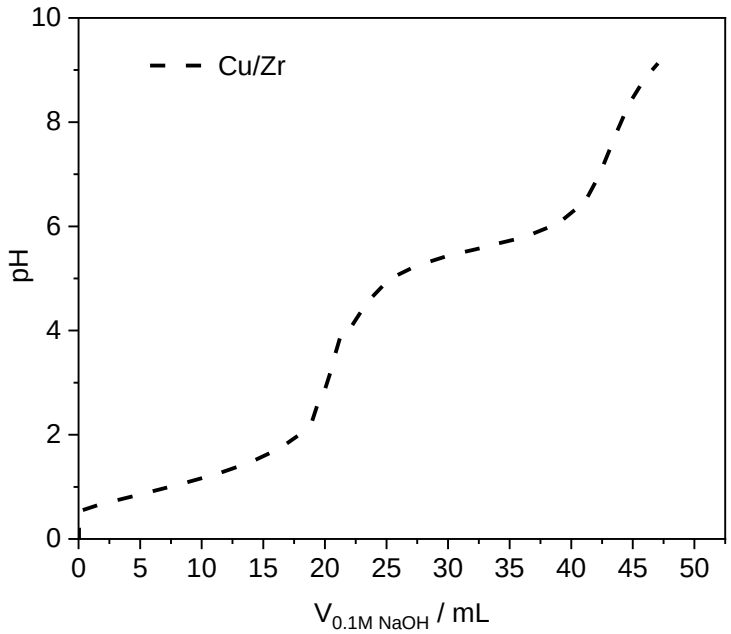

Figure 87: Titration curve of a 0.1 M solution containing zirconyl nitrate and Cu nitrate. The titration is carried out at room temperature using a 0.1 M solution of NaOH.

The last step of the titration curve is located at around pH = 6. Above this pH value both components precipitate completely. Hence, a pH = 6.5 and a pH = 8.0 is selected for the synthesis of the different Cu/ZrO_2 catalysts.

In addition, different other synthesis parameters are varied, for example the precipitation temperature, the composition of the precipitation agent, ageing time or calcination temperature. All varied parameters are summarized in Table 24.

Table 24: Variation of the synthesis parameters for the synthesis of different Cu/ZrO_2 catalysts.

Parameter	Variation 1	Variation 2	Variation 3
Cu-loading in wt.%	25	40	55
Erlenmeyer-flask	standard	with barriers	
Precip. agent Na_2CO_3 : NaOH	1:1	1:2	1:4
Precip. temperature	25 °C	50 °C	75 °C
Precip. pH-value	6.5	8	
Ageing temperature	25 °C	50 °C	75 °C
Ageing time	0 h	2 h	4 h
Drying temperature	80 °C	120 °C	
Calcination temperature	350 °C	425 °C	500 °C
Calcination time	2 h	4 h	6 h
Calcination heating rate	2.5 K/min	5 K/min	

First, 100 mL deionized water is added in an Erlenmeyer-flask to achieve a uniform precipitation even at the beginning of the procedure. The Zr/Cu nitrate solution is added dropwise and by addition of the precipitation agent using a titrator the desired pH value is adjusted. After the precipitation, the catalysts are aged, washed, dried and calcined at different conditions (see Table 24). The precise procedure is described in the experimental part (section 7.3).

The full combination of all parameters would result in 34992 experiments. Therefore, 24 randomly selected combinations are determined and synthesized. The synthesis parameters as well as the catalysts labels (Cat1 to Cat24) are summarized in Table 32 and Table 33 in the experimental part (section 7.3).

4.4.1.2 Catalytic hydrogenation of CO_2 to methanol

The catalytic performance of the different Cu/ZrO_2 catalysts is measured using a parallel testing unit and a single testing unit.

Parallel testing unit

For catalytic measurements with the parallel testing unit, each of the 12 reactors is filled with 800 mg catalyst. The catalysts are reduced in H_2 at 300°C for 2 h subsequently. After that the catalytic reaction is carried out at four different reaction temperatures (275°C, 250°C, 225°C, 200°C), at 10 bar and with H_2/CO_2 ratio of 3/1 (total gas flow = 40 mL/min). The reduction as

well as the reaction procedure is described in detail in the experimental part (section 7.3). In addition, a flow chart of the setup is presented in this section.

The main goal of the measurements is to find the catalyst with the best catalytic performance whose synthesis parameters can be used for promotor screening. The target figures for the catalytic performance are the CO_2 conversion as well as the MeOH selectivity. Because the presentation of all CO_2 conversions and MeOH selectivity curves would be very confusing the MeOH selectivity at the temperature of 5 % CO_2 conversion is selected as decisive parameter. Thus, all catalysts are represented as one datapoint. The temperature of 5 % CO_2 conversion as well as the MeOH selectivity at this temperature is interpolated using polynomial fits. The exact calculations are described in the experimental part (section 7.3). In Figure 88 the MeOH selectivity at the temperature of 5 % CO_2 conversion are shown.

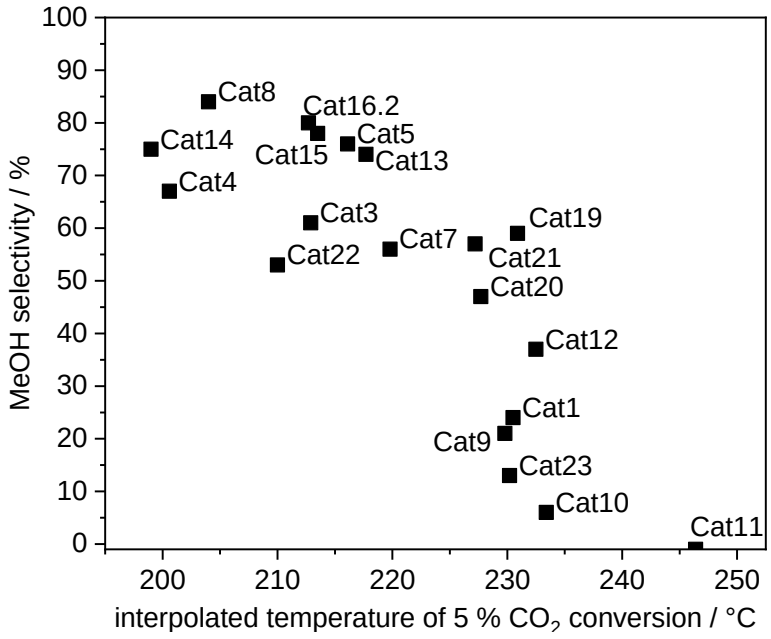

Figure 88: Interpolated temperature of 5 % CO_2 conversion for all catalysts and the respective MeOH selectivity. The catalytic reaction is carried out at 4 different reaction temperatures (275°C, 250°C, 225°C, 200°C), at 10 bar and with H_2/CO_2 ratio of 3/1 (total gas flow = 40 mL/min). The catalysts are pre-reduced in H_2 at 300°C for 2 h.

Cat4, Cat5, Cat8, Cat13, Cat14, Cat15 and Cat16.2 show the best catalytic performances with highest MeOH selectivity at lowest temperature for 5 % CO_2 conversion. Comparing the different synthesis parameters 5 of the 7 catalysts have Cu loadings of 55 wt.% (the other 2 40 wt.%). In addition, the precipitation agent with a Na_2CO_3/NaOH = 1/4 seems to be most beneficial because 5 of the 7 catalyst are synthesized with this agent (the other 2 with Na_2CO_3/NaOH = 1/2). Furthermore, ageing at mild conditions (at 25°C) or even no ageing and calcination for only 2 h is most appropriate. The pH-value, calcination temperature and the other parameters apparently influence less the catalytic performance of the catalysts.

Due to the highest MeOH selectivity Cat8 is selected for the further investigations and the promotor screening.

Single testing unit

In addition to the catalytic measurements with the parallel testing unit three catalysts (Cat1, Cat8 and Cat13) are investigated using a single testing unit to check if the same trend of the catalytic performances can be obtained. It is important to note, that for the single testing unit only 150 mg catalyst and a total gas flow of 20 mL/min are applied. Therefore, the exact values cannot be compared. In this case, the catalytic reaction is carried out at five different temperatures (200°C, 225°C, 250°C, 275°C, 300°C) at 10 bar. The reduction (at 300°C in H_2 for 2 h) and the reaction procedure as well as a flow chart of the single testing unit are described in the experimental part (section 7.2).

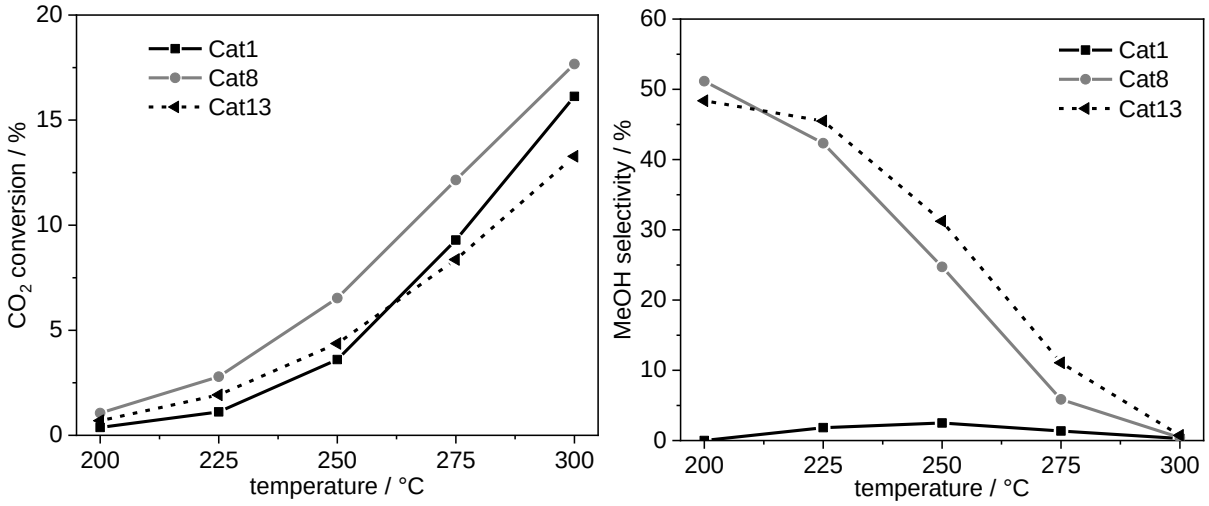

Figure 89: CO_2 conversion and MeOH selectivity at different reaction temperatures (200, 225, 250, 275, 300°C) at 10 bar for Cat1, Cat8, Cat13. The H_2:CO_2 ratio is 3:1. The GHSV is 8000 h^{-1}. The catalysts are pretreated in H_2 at 300°C for 2 h.

The CO_2 conversion as well the MeOH selectivity is depicted in Figure 89. With increasing temperature, the CO_2 conversions rise and the MeOH selectivity drops due to the higher production of CO via the RWGS reaction. Cat8 has the highest CO_2 conversion and with Cat13 the highest MeOH selectivity. Cat1 which is selected as an example for poorly catalytic performance exhibits by far the lowest MeOH selectivity. The results strengthen the founding obtained with the parallel testing unit and verify that the parallel testing unit gives reliable and reproducible results.

The measurements confirm that high CO_2 conversion as well as high MeOH selectivity can be obtained using Cat8, which is selected for further investigations and the promotor screening.

4.4.1.3 Characterization of Cu/ZrO_2 catalysts

To get information about the composition, the morphology and the surface area few of the Cu/ZrO_2 catalysts especially Cat8 are characterized using XRD, BJH/BET method, elemental analysis via ICP-OES, H_2-TPR and N_2O-RFC (determination of Cu surface area).

The powder diffractograms of selected Cu/ZrO_2 catalysts are measured after calcination at 350°C, 425°C or 500 °C and are shown in Figure 90.

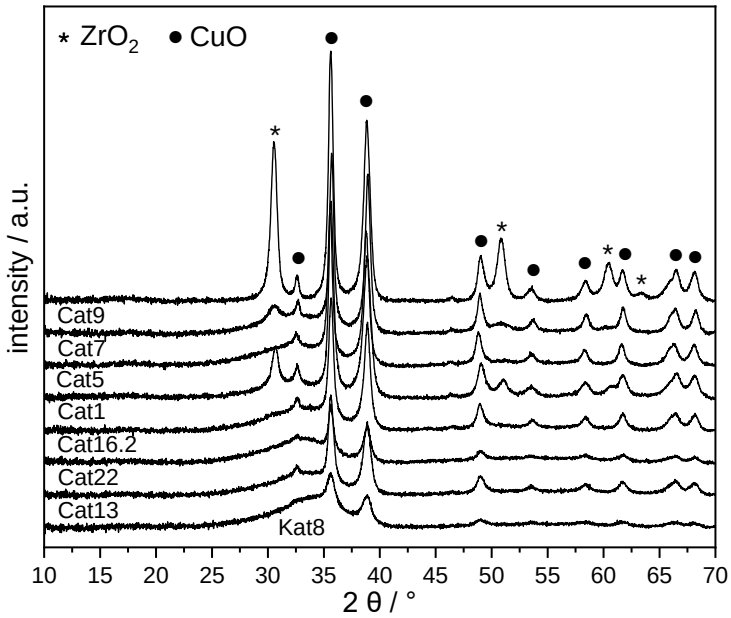

Figure 90: Powder diffractograms of selected Cu/ZrO_2 catalysts after calcination at 350°C, 425°C or 500°C in air. The dots represent CuO[106] and the stars ZrO_2[317]. Diffractograms are recorded in an angle range between 5° and 70° in steps of 0.013°.

CuO is observable in all powder diffractograms (main reflexes at 35 and 38 2θ). Reflexes concerning ZrO_2 (mainly at 30 2θ) only appear if the catalyst is highly crystalline (especially Cat9). In addition, the crystallinity of CuO differs a lot. Interestingly, all catalysts which exhibit ZrO_2 reflexes (Cat1, Cat7, Cat9) are calcined at 500°C. These catalysts and Cat5 (calcined at 500°C) cause also narrow reflexes of CuO. It indicates that calcination at 500°C leads to distinct separation of CuO and ZrO_2 and large crystallites.

Cat8, Cat13 and Cat 16.2 that outperformed most of the other catalysts in the catalytic reaction consist mainly of amorphous morphology indicated by the absence of ZrO_2 reflexes and CuO reflexes with low intensity. In addition, the CuO crystallite size is determined using the Scherrer equation and the reflexes at 35 and 38 2θ.[100-104] The crystallite sizes are summarized in Table 25. The average CuO crystallite size is similar for all catalysts and is between 13.2 (Cat13) and 18.7 nm (Cat7). Higher calcination temperature (500°C) generally leads to slightly increased crystallite size (Cat1, Cat5, Cat7, Cat9). The average CuO crystallite size of Cat8 is only 7.6 nm, which is much lower than for the other catalysts.

Table 25: Crystallite sizes ($Size_{crys}$) in nm for different Cu/ZrO_2 catalysts after calcination at 350°C, 425°C or 500°C. The reflexes at 35 and 38 2θ (see Figure 90) and the Scherrer equation is used for calculation.

catalyst	$Size_{crys}$	catalyst	$Size_{crys}$
Cat 1	14.5 ±2.9	Cat 9	15.8 ±2.4
Cat 5	16.8 ±1.2	Cat 13	13.2 ±1.6
Cat 7	18.7 ±1.1	Cat 16.2	15.6 ±1.1
Cat 8	7.6 ±0.7	Cat 22	13.0 ±1.6

Furthermore, the BET surface area as well as the pore volume and the pore radius of Cat1, Cat8 and Cat13 are determined by the BET/BJH method. The values are summarized in Table 26.

Table 26: BET surface area (SA_{BET} in m^2/g), pore volume (V_{pore} in mL/g_{cat}) and pore radius (r_{pore} in nm) of Cat1, Cat8, Cat13 after calcination at 500°C (Cat1) or at 350°C (Cat8, Cat13) in air. Cu loading (Cu^a) in wt.% is determined by ICP-OES. The error is determined to be around 5% including the preparation and the ICP-OES measurement itself. Metallic Cu surface ($Cu\text{-}SA_{N2O\text{-}RFC}$) in m^2/g area is determined by N_2O-RFC. Before the measurement, the catalyst is reduced at 300°C in H_2 for 2 h. The N_2O-RFC is carried out in 1 % N_2O in He at ambient conditions.

catalyst	SA_{BET}	V_{pore}	r_{pore}	Cu^a	$Cu\text{-}SA_{N2O\text{-}RFC}$
Cat 1	24	0.09	1.70	55.3	
Cat 8	108	0.46	1.69	56.0	6.3 ±0.4
Cat 13	109	0.29	1.69	55.1	

Cat1, which is less active in methanol synthesis, exhibit the smallest BET surface area. Calcination at 500°C most likely leads to the decomposition of the porous structure because the BET surface is only one fourth of the BET surface of the catalytically highly active catalysts Cat8 (108 m^2/g) and Cat13 (109 m^2/g). They are calcined at 350°C.

The Cu loadings of these catalysts are determined by elemental analysis via ICP-OES and are also depicted in Table 26. The desired Cu loading of 55 wt.% could be achieved which underlines the reliability and reproducibility of the co-precipitation procedure.

The metallic Cu surface area of Cat8 is determined by N_2O-RFC. A Cu surface of 6.3 ±0.4 m^2/g is obtained. *Koeppel et al.* reported a Cu surface area of 5.1 m^2/g for a co-precipitated Cu/ZrO_2 catalyst with 50 wt.% Cu loading.[285]

For investigation of the reduction properties of the CuO/ZrO_2 catalysts and especially of Cat8, H_2-TPR is carried out. The H_2-TPR profile is shown in Figure 91.

Only one large TPR signal at 162°C with a shoulder at 125°C is obtained. *Zhou et al.* indicate a similar value (182°C) for 5 wt.% Cu loaded Cu/ZrO_2 catalyst.[294] The shoulder of the signal at 125°C could relate to the reduction of Cu(II) to Cu(I) or the reduction of a different CuO species. The narrow signal hints a small particle size distribution. In addition, *Dow et al.* claim that low reduction temperatures are assigned to amorphous and highly dispersed CuO oxide

species. They investigated different supported CuO species regarding their reduction properties.[253]

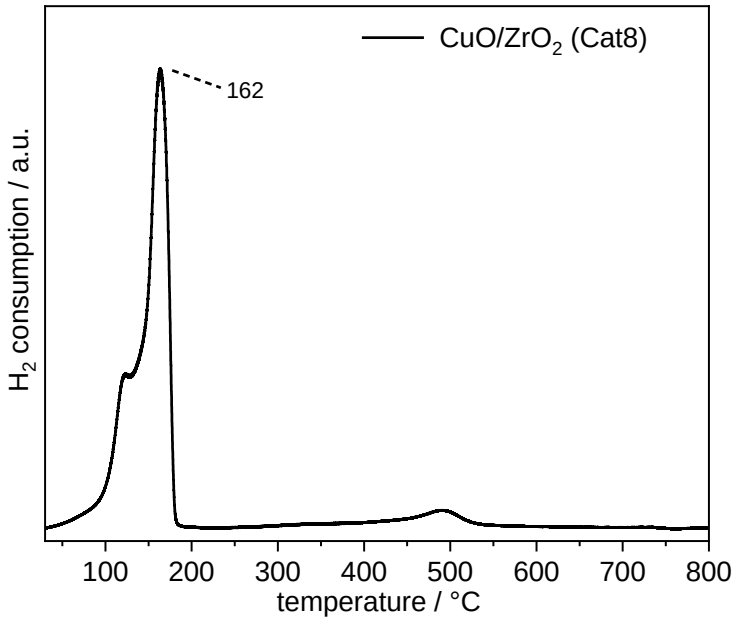

Figure 91: H_2-TPR profiles of CuO/ZrO_2 (Cat8) after calcination in air at 350°C (5 K/min) for 2 h. The TPR profile is carried out in a temperature range of 50°C to 800°C (5 K/min) in 2.5 % H_2 in He.

In summary, Cat8 exhibits the best catalytic activity (highest MeOH selectivity at lowest temperature for 5 % CO_2 conversion). In addition, the morphology of the catalyst as well as the properties of the CuO particles are very promising. Therefore, the co-preparation procedure of this catalyst is used as base for promotor screening and further investigations.

4.4.2 Promotor screening based on Cu/ZrO_2 catalysts for methanol synthesis from CO_2

The promoting metals are mainly chosen because of their application in other catalytic reactions either as catalytic active species itself or as promotor. Two different procedures are carried out. Zn, Al, Ag, Mn, Fe, Ce, In, Ni, Bi, Cd, Cr, Sm and Ga are added as nitrate to the Cu/zirconyl nitrate solution during the co-precipitation. Catalysts with 10 and 20 wt.% of promoting metal are synthesized inspired by *Tada et al.* (Ag loading of 5 wt.% and 10 wt.%, but lower Cu loadings).[286] Li, Na, K, Rb, Cs, Mg, Ca, Sr, Ba and B are introduced by impregnation of the Cu/ZrO_2 precipitate during the last washing step. In this case, catalysts with 5 and 15 wt.% of the promoting metals are synthesized. The Cu loading of 55 wt.% stays constant. The synthesis parameters are mainly used from the synthesis of Cat8 (see section before 4.4.1) and are described in the experimental part (section 7.3). The pH-values for the co-precipitation of the different catalysts are determined by titration curves (see Figure 112 in section 7.3) and are summarized in Table 34 in section 7.3.

4.4.2.1 Synthesis of different promoted Cu/ZrO_2 catalysts

Synthesis of different promoted (Zn, Al, Ag, Mn, Fe, Ce, In, Ni, Bi, Cd, Cr, Sm, Ga) Cu/ZrO_2 catalysts by co-precipitation

The appropriate nitrate of the promoting metal is added to the aqueous Cu/zirconyl nitrate solution which is added dropwise into an Erlenmeyer flask. The precipitation starts with the addition of the precipitation agent (Na_2CO_3/NaOH 1/4). A titrator adjusts the desired pH-value. The precipitation temperature is 25°C. After precipitation, the precipitate is directly washed with water, dried (80°C) and calcined at 400°C.

Synthesis of different promoted (Li, Na, K, Rb, Cs, Mg, Ca, Sr, Ba, B) Cu/ZrO_2 catalysts by impregnation of the precipitate

For the synthesis of alkali, alkaline earth metal and B promoted Cu/ZrO_2 catalysts co-precipitation is unsuitable because these metals precipitate only at high pH-values. However, at high pH-values Cu would precipitate as CuO. Therefore, an alternative procedure is carried out. First, a large amount of 55 wt.% Cu loaded Cu/ZrO_2 catalyst is co-precipitated and washed. The precipitate is divided in several portions, which are impregnated by the corresponding promoting metal solution. The amount of water, which is used for the impregnation step, is determined by measuring the water absorption of the Cu/Zr precipitate. This procedure has the advantage to conventional incipient wetness impregnation methods that the promoting metals are spread across the precipitate and subsequent drying and calcination leads to stronger interaction between the promoting metal, CuO and ZrO_2.

4.4.2.2 Characterization of selected catalysts

Some of the catalysts are characterized by XRD to determine the influence of the different promoting metals on the catalyst structure. Only co-precipitated catalysts are measured. The catalysts are abbreviated as follows: CuxYz (x = Cu loading in wt.%, Y = promoting metal, z = loading of the promoting metal in wt.%). The powder diffractograms are shown in Figure 92 and Figure 93.

Reflexes concerning CuO especially at 35 and 38 2θ appear for all promoted catalysts whereas reflexes of ZrO_2 (mainly at 30 2θ) are detected only partially (Cu55Ag20, Cu55Ag10). However, the intensity as well as the width of the CuO reflexes differs. The CuO reflexes in the powder diffractograms of the catalysts with the same promoting metals but different loadings have similar intensities, and the catalysts exhibit similar crystallinity. The addition of Al and Zn leads to a less distinct crystallinity whereas the addition of Ag promotes the opposite. Furthermore, the addition of Bi, Mn, Cd and Ni apparently influence the crystallinity by creating a less crystalline structure of the catalysts like Zn and Al (Figure 93).

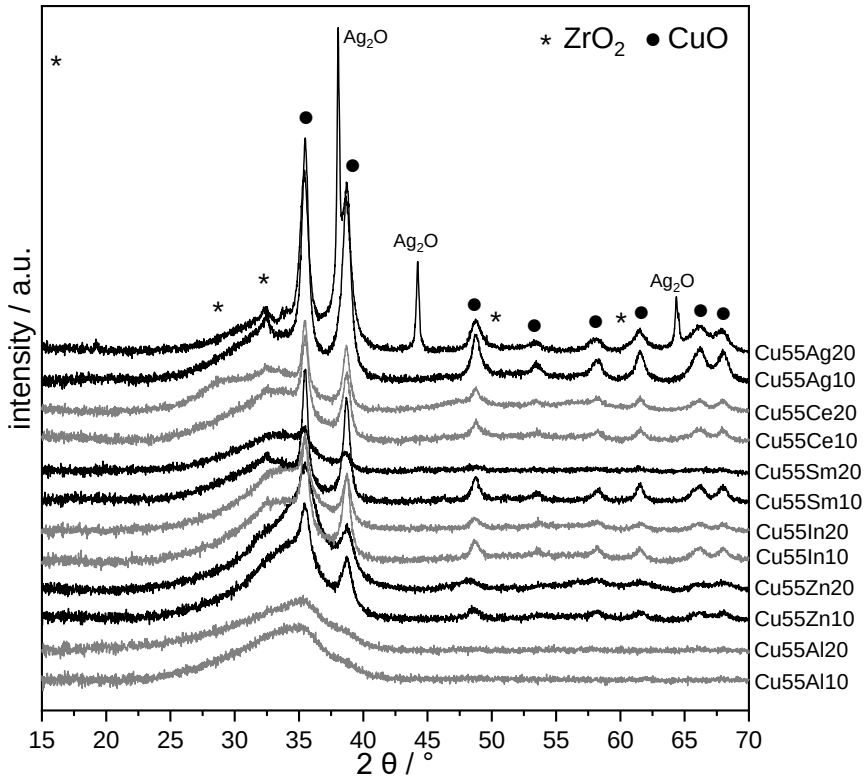

Figure 92: Powder diffractograms of selected Cu/ZrO_2 catalysts CuxYz (x = Cu loading in wt.%, Y = promoting metal, z = loading of the promoting metal in wt.%) after calcination at 400°C in air. The dots represent CuO[106] and the stars ZrO_2[317]. Diffractograms are recorded in an angle range between 5° and 70° in steps of 0.013°.

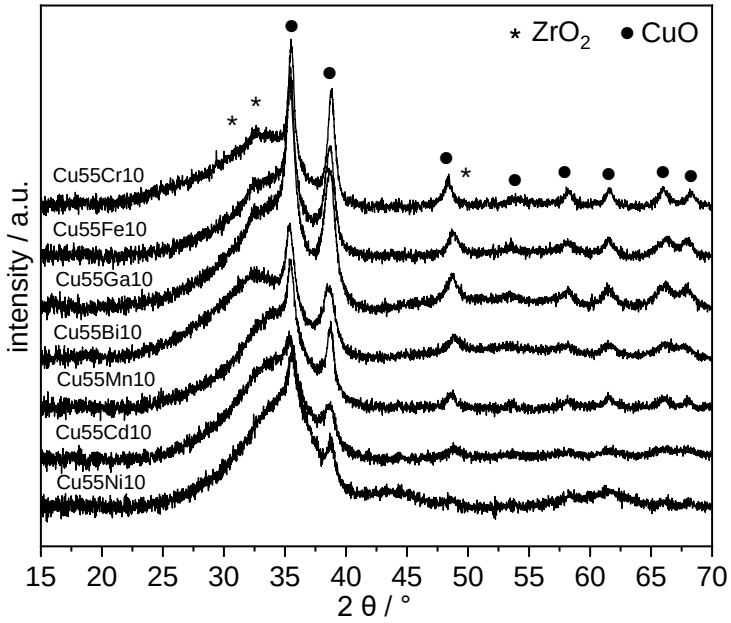

Figure 93: Powder diffractograms of selected Cu/ZrO_2 catalysts CuxYz (x = Cu loading in wt.%, Y = promoting metal, z = loading of the promoting metal in wt.%) after calcination at 400°C in air. The dots represent CuO[106] and the stars ZrO_2[317]. Diffractograms are recorded in an angle range between 5° and 70° in steps of 0.013°.

Reflexes of the promoted metals appear only for Ag_2O, which is most likely caused by separation of CuO and Ag_2O and the formation of large Ag_2O particles. The absence of the reflexes

concerning the other promoting metals underlines the homogeneity of the prepared catalysts. The CuO particle size of selected catalysts is determined using the Scherrer equation and the CuO reflexes at 35 2θ and 38 2θ.[100-104] The values are summarized in Table 27.

Table 27: Crystallite sizes ($Size_{crys}$) in nm for different promoted Cu/ZrO_2 catalysts CuxYz (x = Cu loading in wt.%, Y = promoting metal, z = loading of the promoting metal in wt.%) after calcination at 400°C in air. The reflexes at 35 and 38 2θ (see Figure 92 and Figure 93) and the Scherrer equation are used for calculation.

catalyst	$Size_{crys}$
Cu55Zn10	-
Cu55Zn20	-
Cu55Al10	-
Cu55Al20	-
Cu55Ag10	12.8
Cu55Ag20	11.0
Cu55Mn10	10.9
Cu55Fe10	9.0 ±0.4
Cu55Ce10	11.1 ±0.8
Cu55Ce20	14.1 ±0.4

catalyst	$Size_{crys}$
Cu55In10	11.3 ±2.0
Cu55In20	11.0
Cu55Ni10	-
Cu55Bi10	6.6
Cu55Cd10	-
Cu55Cr10	12.4 ±0.3
Cu55Sm10	15.5 ±0.2
Cu55Sm20	-
Cu55Ga10	7.2 ±0.4

The crystallite sizes are similar for all the catalysts (between 9.0 and 15.5 nm). Especially the CuO crystallite sizes of Cu55Bi10 and Cu55Ga10 are smaller with values of 6.6 and 7.2 nm respectively. The CuO crystallite sizes of the Al and Zn as well as Ni and Cd promoted catalysts that exhibit very broad and less intensive CuO reflexes could not be determined.

Besides investigating the structure of the different promoted catalysts, also the Cu loading and the loadings of the promoting metal are determined by elemental analysis via ICP-OES. The results are summarized in Table 28.

The catalysts in which the promoting metal is added directly during co-precipitation match well the desired Cu loading of 55 wt.% and the desired value of the promoting metal of 10 and 20 wt.%. Only the values for Cu55Fe20, Cu55Al20 and Cu55In10 differ slightly which is most likely caused by errors during the sample preparation. The results confirm the reliability as well as the reproducibility of the co-precipitation procedure.

The Cu loadings of the samples in which the promoting metals are impregnated during the last washing step vary a bit more and are generally lowered. It is caused by the addition of the promoting metals, which leads to an overall lower Cu loading. In addition, the loadings of the promoting metals also differ widely. That is not surprising because the exact amount of metal precursor, which is absorbed by the precipitate, could not be determined. In this case, the elemental analysis only serves as a control to check whether the impregnation was successful and if different loadings are obtained. The disadvantage of this procedure is accepted due to

the advantage of more distinct interactions between the promoting metal and the other components.

Table 28: Cu loading (Cu[a]) and loading of the promoting metal (Y[b]) in wt.% determined by ICP-OES. The error is determined to be around 5% including the preparation and the ICP-OES measurement itself.

catalyst	Cu[a]	Y[b]	catalyst	Cu[a]	Y[b]
Cu55Zn10	51.1	10.0	Cu55Sm10	53.1	9.8
Cu55Zn20	51.5	19.9	Cu55Sm20	54.7	18.2
Cu55Al10	53.0	10.5	Cu55Ga10	51.3	8.1
Cu55Al20	49.7	19.6	Cu55Ga20	57.1	20.1
Cu55Ag10	57.2	10.1	Cu55Mg5	45.9	2.4
Cu55Ag20	58.0	19.1	Cu55Mg15	50.9	13.7
Cu55Mn10	55.2	8.2	Cu55Ba5	48.6	3.6
Cu55Mn20	55.3	20.8	Cu55Ba15	51.1	13.4
Cu55Fe10	55.1	5.8	Cu55Ca5	50.5	3.8
Cu55Fe20	51.2	19.9	Cu55Ca15	48.1	12.6
Cu55In10	53.5	6.1	Cu55K5	49.1	5.5
Cu55In20	53.7	21.4	Cu55K15	42.4	14.3
Cu55Ni10	55.3	10.3	Cu55Sr5	54.5	5.9
Cu55Ni20	54.0	20.1	Cu55Sr15	46.9	18.6
Cu55Bi10	53.0	11.2	Cu55Na5	48.3	11.7
Cu55Bi20	50.4	19.7	Cu55Na15	48.9	23.9
Cu55Cd10	55.6	9.3	Cu55B5	47.4	9.9
Cu55Cd20	56.1	19.7	Cu55B15	47.5	17.8
Cu55Cr10	52.3	10.5	Cu55Rb5	53.3	9.4
Cu55Cr20	52.5	19.9	Cu55Rb15	51.4	19.0
			Cu55Li5	41.4	7.2

4.4.2.3 Catalytic performances of the promoted Cu/ZrO_2 catalysts

The catalytic performance of the different Cu/ZrO_2 catalysts is measured using a parallel testing unit and a single testing unit.

Parallel testing unit

Like for the catalytic measurements in the last section (0) the parallel testing unit is used and each of the 12 reactors is filled with 800 mg catalyst. The catalysts are reduced in H_2 at 400°C for 2 h subsequently. After that the catalytic reaction is carried out at four different reaction temperatures (275°C, 250°C, 225°C, 200°C), at 10 bar and with H_2/CO_2 ratio of 3/1 (total gas flow = 40 mL/min). The reduction as well as the reaction procedure is described in detail in the experimental part (section 7.3). In addition, a flow chart of the setup is presented in this section.

The data are equally evaluated as it was done in 0. The target figures for the catalytic performance are the CO_2 conversion as well as the MeOH selectivity. Because the presentation of all CO_2 conversions and MeOH selectivity curves would be very confusing the MeOH selectivity at the temperature of 5 % CO_2 conversion is selected as decisive parameter. Thus, the different catalysts are represented by one data point. The temperature of 5 % CO2 conversion as well as the MeOH selectivity at this temperature is interpolated using polynomial fits. The exact calculations are described in the experimental part (section 7.3). In Figure 94 and Figure 96 the MeOH selectivity at the temperature of 5 % CO_2 conversion are depicted.

The catalysts in which the promoting metals are added during the co-precipitation procedure are summarized in Figure 94. It figures out that the promoting metals strongly influence the MeOH selectivity as well as the CO_2 conversion. The catalysts with high CO_2 conversion and simultaneously high MeOH selectivity are located top left of the diagram. Zn, Ga, Sm as well as Ag, Cd and slightly Fe and Al increase the MeOH selectivity compared to the standard Cu/ZrO_2 system. In and Ni decrease the MeOH selectivity and enhance the temperature of 5 % CO_2 conversion. For most of the promotor metals, the 10 wt.% loaded catalysts exhibit higher catalytic performances.

The promotional effect of Ag was already discussed by *Tada et al.* by forming special active sites due to Ag/Cu alloy formation.[286] The low CO_2 conversion is most likely caused by the separation of Ag_2O and CuO and the high crystallinity of the catalyst, which was observed by XRD. In addition, $Cu/ZnO/ZrO_2$ composites are well known catalysts for methanol synthesis. The role of Zn is discussed in detail in 3.2.3. Ga based catalysts are also very promising for the catalytic hydrogenation of CO_2 to methanol as it was mentioned in the introduction. The addition of Ga helps to suppress the RWGS reaction which explain the slightly higher temperature for 5 % CO_2 conversion compared to the pure Cu/ZrO_2 system.[281] Sm is known as electronical promotor in Ni based catalysts for hydrogenation reactions which could be similar in this case.[318] Interestingly, In does not enhance the MeOH selectivity despite the important role of In_2O_3 in recently developed catalysts. Maybe, the reaction pressure of 10 bar is too low for In as beneficial promotor.[279, 283, 314] With Ni and Fe as promotor also methane and ethane is produced which is not surprising because Ni and Fe are parts for CO_2 methanation catalysts.[319]

Due to the low conversions of $Cu_{55}Cd_{20}$ and of the catalysts containing Bi the CO_2 conversions and MeOH selectivity are shown separately in Figure 95. The CO_2 conversions of all catalysts are very low compared to the standard Cu/ZrO_2 catalyst. Interestingly, the MeOH selectivity of the catalysts is increased. Also, Cu55Cd10 which is depicted in Figure 94 has the same effect. The promoting metals that are added during the washing step of the precipitate are summarized in Figure 96.

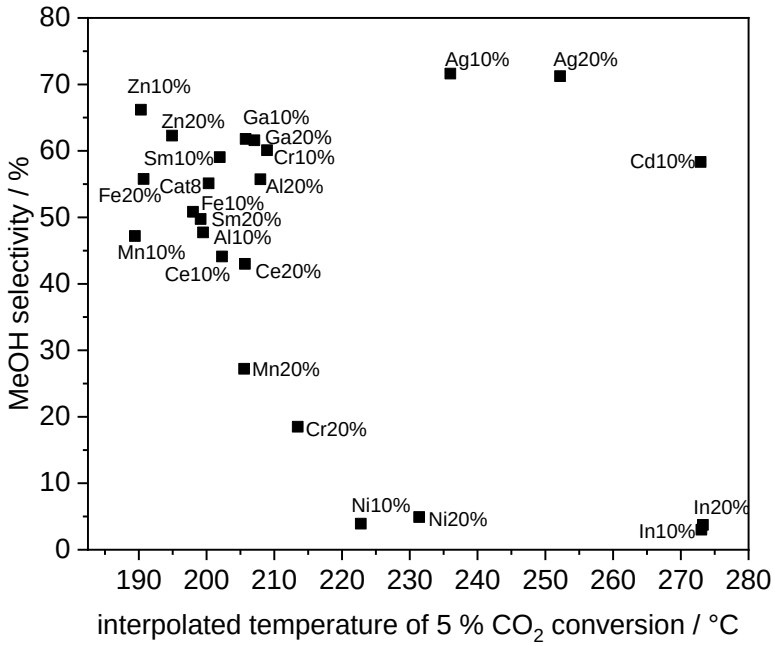

Figure 94: Interpolated temperature for 5 % CO_2 conversion for different promoted Cu(55wt.%)/ZrO_2 catalysts (Yz: Y = promoting metal, z = Loading in wt.%) and the respective MeOH selectivity. The catalytic reaction is carried out at 4 different reaction temperatures (275°C, 250°C, 225°C, 200°C), at 10 bar and with H_2/CO_2 ratio of 3/1 (total gas flow = 40 mL/min). The catalysts are pre-reduced in H_2 at 400°C for 2 h.

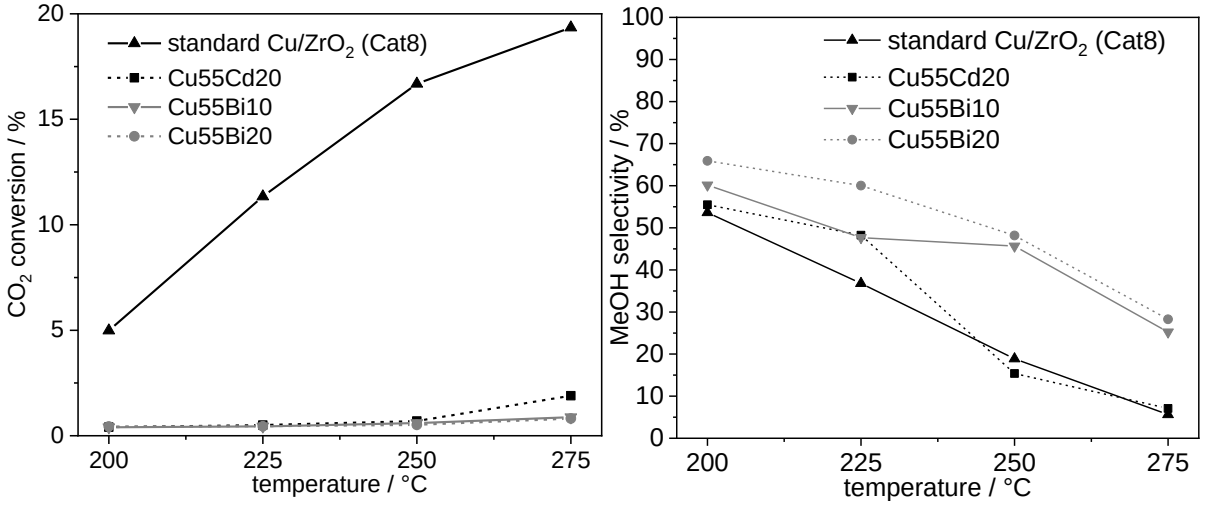

Figure 95: CO_2 conversion and MeOH selectivity at different reaction temperatures (200, 225, 250, 275°C) at 10 bar for Cu55Cd20, Cu55Bi10, Cu55Bi20 and the standard Cu/ZrO_2 catalyst. The H_2:CO_2 ratio is 3:1 with a total gas flow of 40 mL/min. The catalysts are pretreated in H_2 at 400°C for 2 h.

The alkaline earth metals Ba, Ca and Mg with 5 wt.% loading enhance the MeOH selectivity compared to the standard Cu/ZrO_2 catalyst. All other promotors especially the alkaline metals strongly decrease the MeOH selectivity. The poor catalytic performances of Na and K are possibly caused by formation of CuO even at drying. Hence, most likely low dispersed CuO is formed which inhibits higher CO_2 conversions.

Zhong et al. studied the role of earth alkaline oxides in CuO/ZrO_2 catalysts. The earth alkaline metals enhance the Cu surface area and the strength of the basic sites at the surface. In addition, they decrease the reduction temperature of CuO.[320]

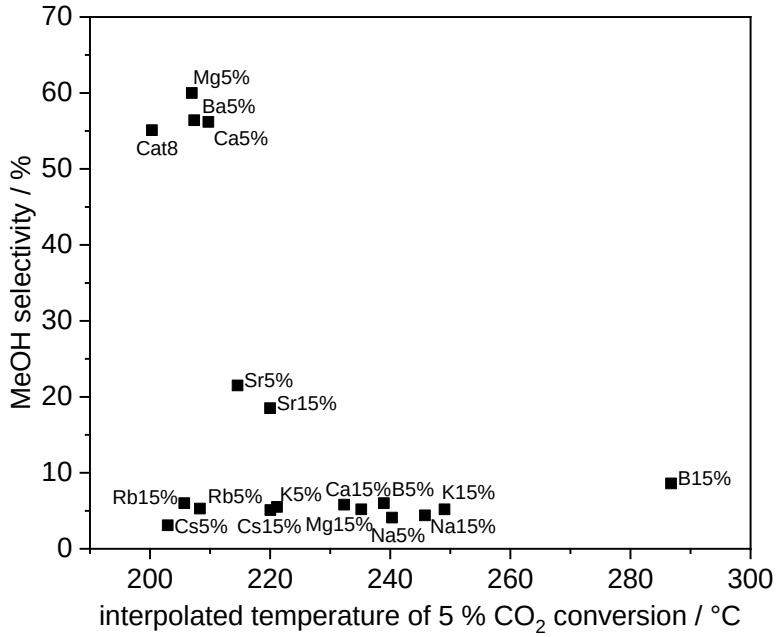

Figure 96: Interpolated temperature for 5 % CO_2 conversion for different promoted Cu(55wt.%)/ZrO_2 catalysts (Yz: Y = promoting metal, z = Loading in wt.%) and the respective MeOH selectivity. The catalytic reaction is carried out at 4 different reaction temperatures (275°C, 250°C, 225°C, 200°C), at 10 bar and with H_2/CO_2 ratio of 3/1 (total gas flow = 40 mL/min). The catalysts are pre-reduced in H_2 at 400°C for 2 h.

Single testing unit

In addition to the catalytic measurements with the parallel testing unit some of the promoted Cu/ZrO_2 catalysts are measured using a single testing unit like it was done for the pure Cu/ZrO_2 catalysts (see section 0). In contrast to the parallel testing unit, the catalytic measurements are carried out with only 150 mg catalyst and a total gas volume of 20 mL/min. Therefore, the exact values cannot be compared. In this case, the catalytic reaction is carried out at five different temperatures (200°C, 225°C, 250°C, 275°C, 300°C) at 10 bar. The reduction (at 400°C in H_2 for 2 h) and the reaction procedure as well as a flow chart of the single testing unit are described in the experimental part (section 7.3).

The CO_2 conversion as well as the MeOH selectivity of Cu55Zn10, Cu55Ce10, Cu55Cd10, Cu55Ag10 and the standard Cu/ZrO_2 catalyst (Cat8) are shown in Figure 97.

Zn and Ce enhance the CO_2 conversion compared to the standard Cu/ZrO_2 catalyst, which confirm the results obtained by the parallel testing unit. Especially at low temperature, the addition of Zn is beneficial. At 225°C the Zn promoted catalyst shows a CO_2 conversion of 9.37 % which is more than three times higher than for the standard Cu/ZrO_2 catalyst. However, both promoting metals decrease the MeOH selectivity. The promoting effect of Cd and Ag is exactly

the opposite. They decrease the CO_2 conversion and enhance the MeOH selectivity especially at high temperatures. Both agree with the results obtained with the parallel testing unit.

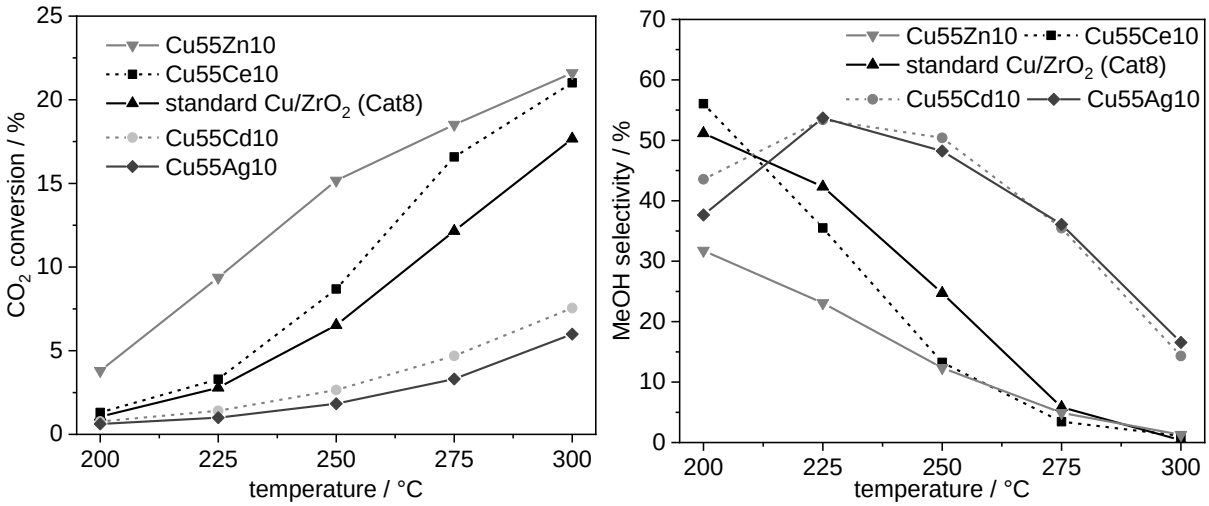

Figure 97: CO_2 conversion and MeOH selectivity at different reaction temperatures (200, 225, 250, 275, 300°C) at 10 bar for Cu55Zn10, Cu55Ce10, Cu55Cd10, Cu55Ag10 and the standard Cu/ZrO_2 catalyst (Cat8). The H_2:CO_2 ratio is 3:1. The GHSV is 8000 h^{-1}. The catalysts are pretreated in H_2 at 400°C for 2 h.

In summary, the results of the catalytic measurements on both the parallel testing unit as well as the single testing unit are similar. It strengthens the reliability and the reproducibility of the results for methanol synthesis based on CO_2 obtained by the parallel testing unit, which was the main goal of these investigations. For promotor screening and especially high throughput screening, the parallel testing unit is the ideal setup to measure many catalysts in short time.
In addition, several promotors are found to be very beneficial for Cu/ZrO_2 catalysts. Some of them like Al, Ce or Zn enhance the CO_2 conversion whereas other promotors like Ag, Bi, Ga and Cd increase the MeOH selectivity. In addition, earth alkaline metals show exceptionally promoting properties.

4.4.3 Influence of different reaction parameters on the conversion and selectivity of the hydrogenation of CO_2 to methanol using a Cu/ZrO_2 catalyst

In this section, the influence of variation of different parameters on the catalytic performance is investigated using the standard Cu/ZrO_2 (Cat8) catalyst (see section 4.4.1).
For the measurements, the feed composition $\dot{V}(H_2):\dot{V}(CO_2)$, the total gas flow ($\dot{V}_{ges}$), the pressure and the temperature are varied.
The variation of the parameters is summarized in Table 29. In addition, the catalytic performance is measured once during stepwise heating and once during stepwise cooling (hysteresis).

Table 29: Variation of the parameters for the catalytic measurements using a $Cu/_{ZrO2}$ catalyst: feed composition $\dot{V}(H_2):\dot{V}(CO_2)$, total gas flow ($\dot{V}_{ges}$) in mL/min, pressure in bar, temperature in °C.

	$\dot{V}(H_2)$: $\dot{V}(CO_2)$	$\dot{V}_{ges}$	pressure	temperature
variation 1	3:1	20	10	200
variation 2	4:1	30	20	225
variation 3	-	-	28	250
variation 4	-	-	-	275

4.4.3.1 Catalytic experiments for quantifying the effect of different reaction parameters

The catalytic measurements are carried out with a single testing unit using 150 mg standard Cu/ZrO2 (Cat8) catalyst. The reduction procedure is equal for all experiments and is carried out at 300°C in H_2 for 1 h. After the reductive pretreatment the catalytic reaction starts. Therefore, four different temperatures (200, 225, 250 and 275°C) are adjusted and the catalytic performance is measured at increasing temperature and at decreasing temperature (hysteresis measurement). This procedure helps to determine the deactivation of the catalysts under these reaction conditions by comparing the catalytic performance of the catalyst at both conditions. In addition, the influence of the four possible combinations of the feed composition $\dot{V}(H_2):\dot{V}(CO_2)$ and the total gas flow ($\dot{V}_{ges}$) are measured at each temperature. The variation of the total gas flow ($\dot{V}_{ges}$) simulates a change of the contact time and hence a change of the GHSV (gas hourly space velocity). A higher GHSV leads to shorter contact time of the gas molecules with the catalyst surface. In general, low GHSV is beneficial for MeOH synthesis. The exact reduction and reaction procedure is described in the experimental part (section 7.3). Like for the catalytic measurements in section 4.4.1 and 4.4.2 the target figures for the catalytic performance are the CO_2 conversion as well as the MeOH selectivity. Because the variation of all parameters leads to many diagrams, which would be very confusing the MeOH selectivity at the temperature of 5 % CO_2 conversion is selected as decisive parameter. Thus, the catalytic performance at different reaction parameters is represented by one data point. The temperature of 5 % CO2 conversion ($T(X_{CO2}=0.05)$) as well as the MeOH selectivity at this temperature ($S(T(X_{CO2}=0.05))$) is interpolated using polynomial fits and are shown in Figure 98. The exact calculations are described in the experimental part (section 7.3).

The labels of the datapoints consists of the feed composition $\dot{V}(H_2):\dot{V}(CO_2)$ and the total gas flow ($\dot{V}_{ges}$) ($\dot{V}(H_2)/\dot{V}(CO_2)$-$\dot{V}_{ges}$). It figures out that varying the pressure divides the data points in three clusters. Increasing pressure leads to higher conversion which means a lower $T(X_{CO2}=0.05)$ and to higher MeOH selectivity ($S(T(X_{CO2}=0.05))$) which is typical for methanol synthesis catalysts. High pressures shift the chemical equilibrium towards the product according to Le Chatelier's principle considering the reaction equations (see Figure 48). Hence, at

higher pressures methanol synthesis is preferred due to the decrease of the number of molecules. At low temperatures, the RWGS reaction is mostly suppressed because of the higher activation energy, which leads to higher MeOH selectivity. In addition, a feed composition of $\dot{V}(H_2)/\dot{V}(CO_2)$ 4/1 is beneficial for MeOH selectivity at all varied reaction conditions.

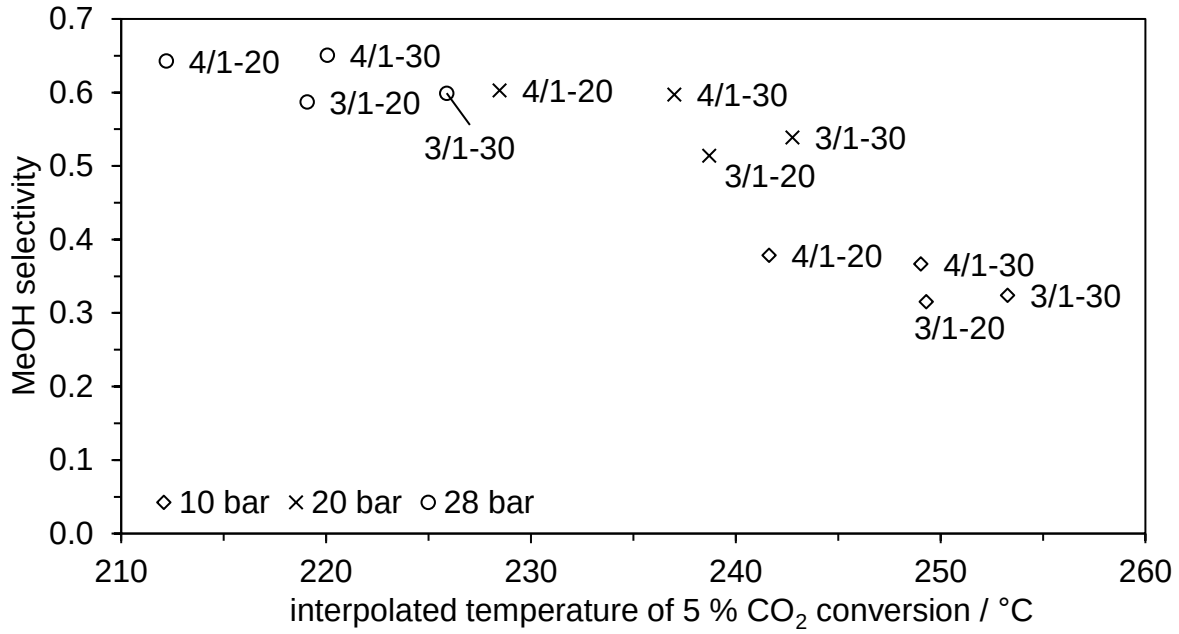

Figure 98: Interpolated temperature of 5 % CO_2 conversion and the respective MeOH selectivity for different reaction conditions using standard Cu/ZrO_2 catalyst (Cat8). The catalytic reaction is carried out at 4 different reaction temperatures (200°C, 225°C, 250°C, 275°C), at 10 bar, 20 and 28 bar and with H_2/CO_2 ratio of 3/1 or 4/1 (total gas flow = 20 or 30 mL/min). The catalysts are pre-reduced in H_2 at 300°C for 2 h.

4.4.3.2 Evaluating of the results using Design of Experiments (DoE)

The experiments that are carried out at 10, 20 and 28 bar are divided in three statistical experimental designs. With the variation of the different parameters, a full factorial 2^3 experimental design is obtained. The experimental design is summarized in Table 30.

Table 30: Full factorial 2^3 experimental design for the statistical evaluation of the experiments.

factor	parameter	unit	- level	+ level
A	$\dot{V}(H_2) : \dot{V}(CO_2)$	-	3:1	4:1
B	$\dot{V}_{Gesamt}$	mL/min	20	30
C	hysteresis-branch	-	T↑	T↓

The evaluation of the effect sizes and the sum of the squares indicate that only the three main effects (feed composition $\dot{V}(H_2):\dot{V}(CO_2)$, total gas flow ($\dot{V}_{ges}$), hysteresis) are important as undependable effects (see Figure 99). The calculations are described in the experimental part in section 7.3.

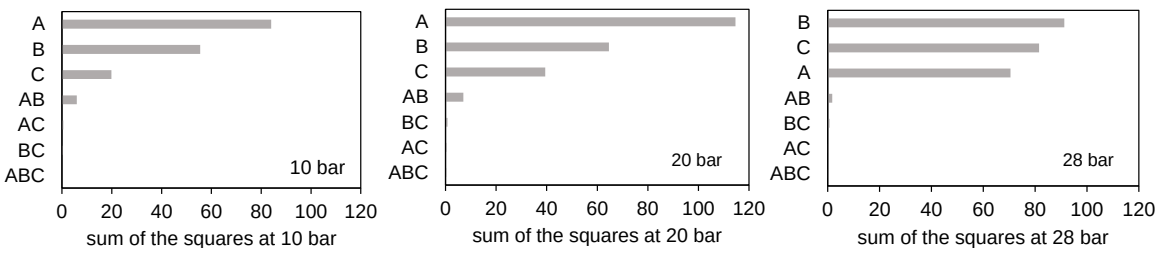

Figure 99: Sum of the squares at pressures of 10, 20 and 28 bar.

The interaction effects (AB, AC, BC and ABC) are not significant and are related to experimental deviations. Therefore, only the influence of the pressure and the temperature on the main effects (A, B and C) is discussed in the following. A positive effect is related to an increase of the temperature of 5 % CO_2 conversion ($T(X_{CO2}=0.05)$ and hence to a decrease of the catalytic activity. In addition, higher MeOH selectivity $S(T(X_{CO2}=0.05))$ at $T(X_{CO2}=0.05)$ is also associated to a positive effect. For all other responses a direct correlation does not exist between the parameters and the sign of the effect.

Pressure dependency of the main effects (A, B and C)

First, the pressure dependency of the main effects (A, B and C) on the temperature and MeOH selectivity at 5 % CO_2 conversion $S(T(X_{CO2}=0.05))$ are evaluated.

A higher concentration of H_2, meaning $\dot{V}(H_2)/\dot{V}(CO_2)$ = 4/1, leads to an decrease of the temperature of 5 % CO_2 conversion ($T(X_{CO2}=0.05)$) (see Figure 100). This effect is observable for all pressure variations and increase generally. The positive effect of the GHSV on $T(X_{CO2}=0.05)$ indicates that the CO_2 conversions decrease with increasing GHSV. It agrees with literature that a small GHSV leads to higher contact time and hence to enhanced catalytic performance.

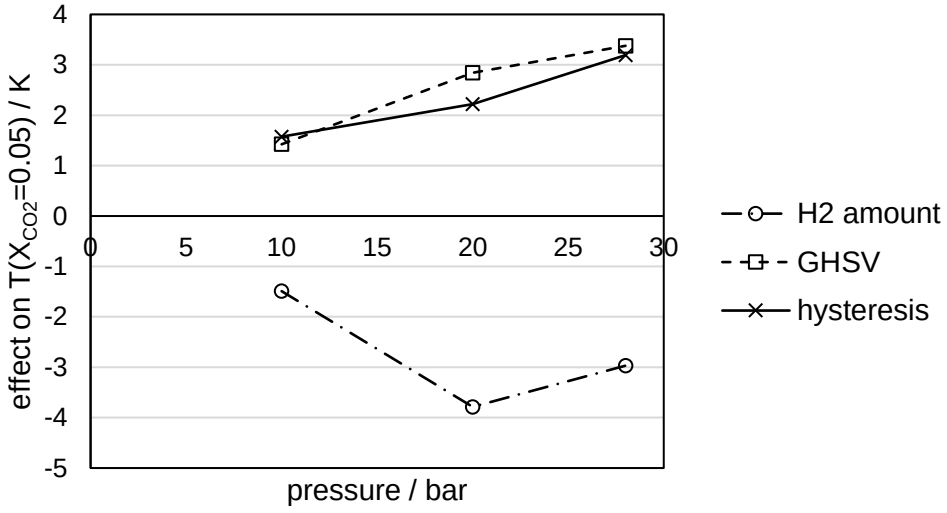

Figure 100: Pressure dependency of the main effects on the temperature at 5 % CO_2 conversion $T(X_{CO2}=0.05)$ in K.

The activity of the catalyst decreases slightly regarding the measurements at decreasing temperature (hysteresis) which is induced by light deactivation of the catalyst.

The MeOH selectivity S(T(X_{CO2}=0.05)) also correlates positively with an increasing concentration of H_2 which means that the MeOH selectivity is increased with the feed composition $\dot{V}(H_2)/\dot{V}(CO_2)$ = 4/1 (see Figure 101) especially up to 20 bar. The GHSV as well as the hysteresis only slightly influence the MeOH selectivity.

In summary, higher pressures shift the chemical equilibrium towards the products (see Figure 48). The MeOH selectivity only increases slightly at higher pressures, which nevertheless means that the MeOH yield increases with increased pressure. Hence, the interplay between high CO_2 conversion at a maximum MeOH selectivity is important for high MeOH yields.

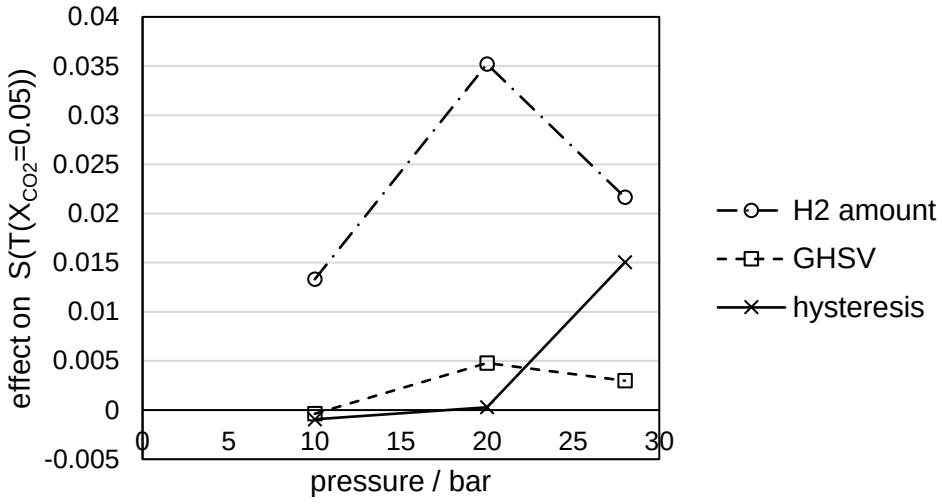

Figure 101: Pressure dependency of the main effects on the MeOH selectivity at the temperature at 5 % CO_2 conversion T(X_{CO2}=0.05) in K.

Pressure and temperature dependency of the main effects

The discussion before was related to the interpolated temperatures for 5 % CO_2 conversion and the corresponding MeOH selectivity. In this section, the effects of the parameters on the actual CO_2 conversion and MeOH selectivity are discussed.

Effect of the feed composition $\dot{V}(H_2)$:$\dot{V}(CO_2)$

With increasing $\dot{V}(H_2)$:$\dot{V}(CO_2)$ the CO_2 conversion increase for all temperatures. It is more pronounced at higher pressures, which is shown in Figure 102.

In addition, $\dot{V}(H_2)$:$\dot{V}(CO_2)$ also influences positively the MeOH selectivity. However, no linear correlation between $\dot{V}(H_2)$:$\dot{V}(CO_2)$ and the temperature or the pressure could be found (see Figure 103).

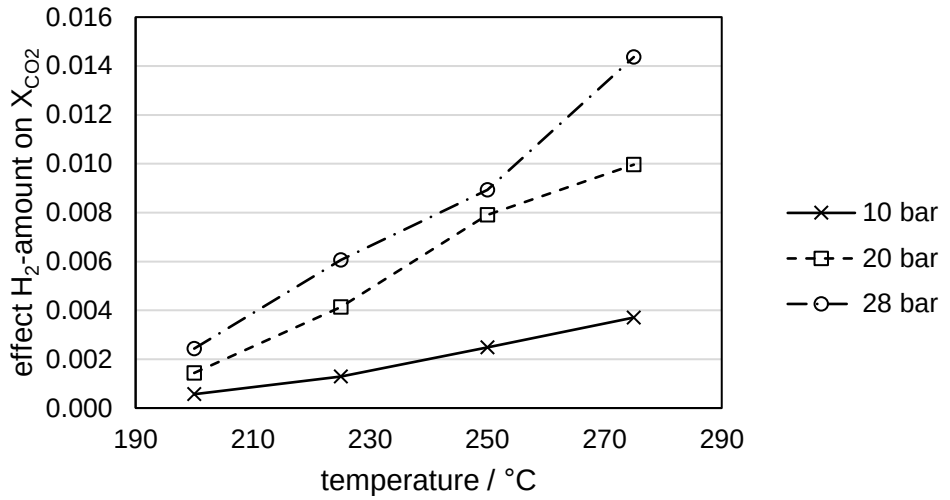

Figure 102: Pressure and temperature dependency of the H_2 amount on the CO_2 conversion.

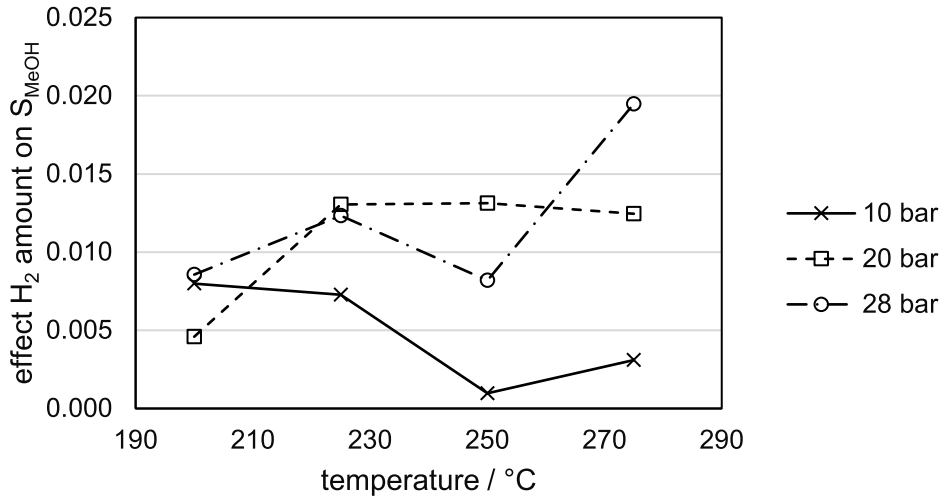

Figure 103: Pressure and temperature dependency of the H_2 amount on the MeOH selectivity.

Effect of the GHSV (variation of $\dot{V}_{ges}$)

Decreasing the GHSV leads to an increase of the CO_2 conversion, because of increasing the contact time between the gas molecules and the catalyst surface.

This effect is also more pronounced at higher pressures, which is depicted in Figure 104.

A lower GHSV namely leads to an increase of the CO_2 conversion but to a slightly decrease of the MeOH selectivity (see Figure 105).

However, higher pressures are necessary to increase appropriately the MeOH selectivity.

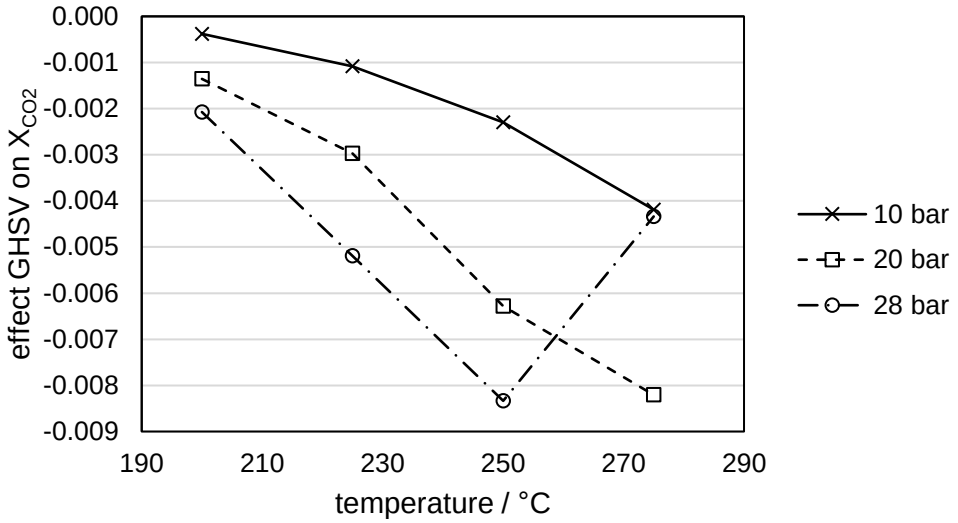

Figure 104: Pressure and temperature dependency of the GHSV on the CO_2 conversion.

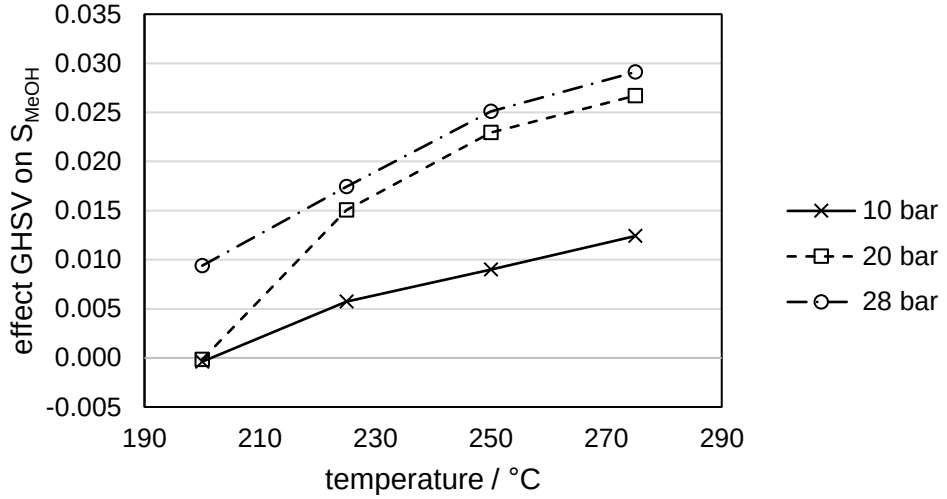

Figure 105: Pressure and temperature dependency of the GHSV on the MeOH selectivity.

Effect of hysteresis (measuring at increasing/decreasing temperature)

The effects induced by the hysteresis measurements are only weakly pronounced. It means that the catalysts only slightly deactivate during the measurement.

The CO_2 conversion decreases slightly comparing the catalytic activity during stepwise heating up from 200 to 275° and during stepwise cooling down the same direction. It is indicated by the negative effect shown in Figure 106.

In contrast to that, the MeOH selectivity even increases slightly. However, the effect is only less pronounced (see Figure 107).

In summary, a feed gas composition of $\dot{V}(H_2)/\dot{V}(CO_2) = 4/1$ is beneficial for high CO_2 conversion as well as high MeOH selectivity. In addition, a lower GHSV enhances the CO_2 conversion and

only slightly decreases the MeOH selectivity. Deactivation of the Cu/ZrO_2 during these measurements (total reaction time = 45 h) are negligible.

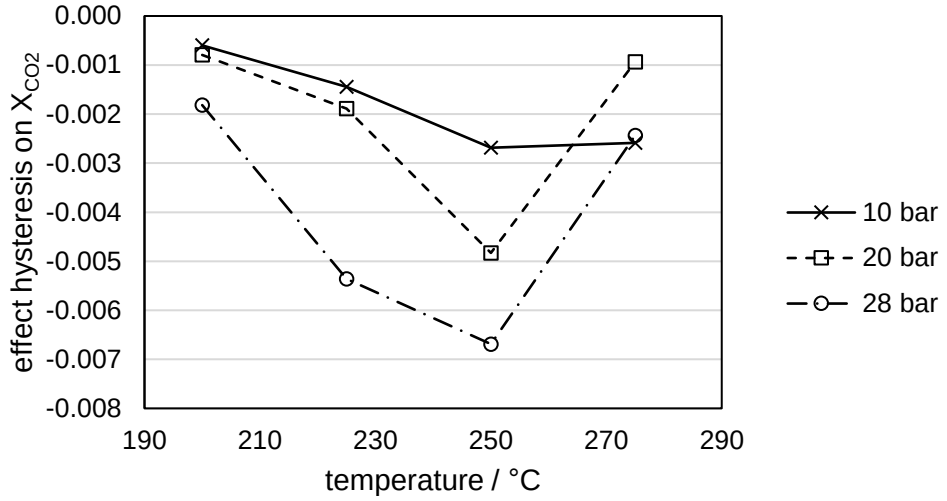

Figure 106: Pressure and temperature dependency of the hysteresis on the CO_2 conversion.

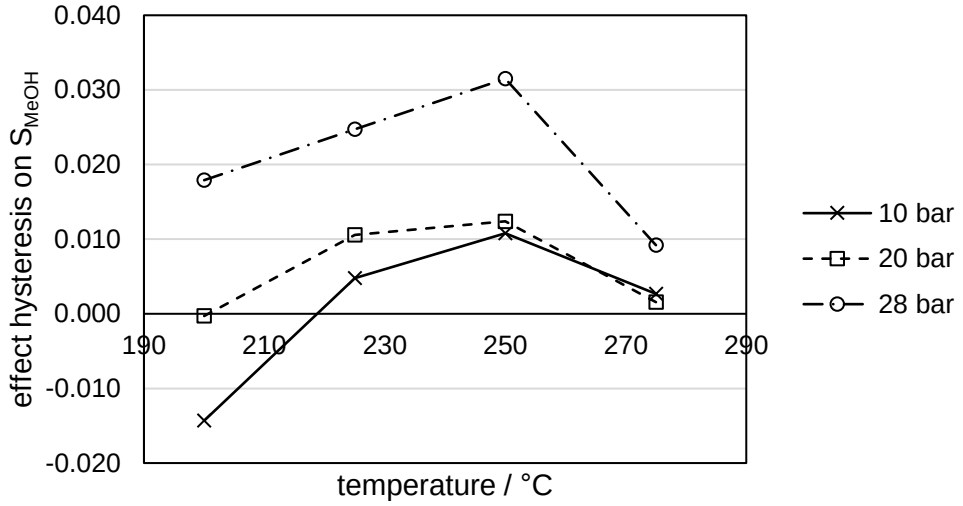

Figure 107: Pressure and temperature dependency of the hysteresis on the MeOH selectivity.

4.5 Conclusions

By variation of different preparation parameters of the co-precipitation of different Cu/ZrO_2 catalysts an optimized procedure for the synthesis of Cu/ZrO_2 systems was developed. The different catalysts are tested in CO_2 hydrogenation to methanol at 10 bar which was prescribed by the testing setup (parallel testing unit, PTU). The most active (high CO_2 conversion and high MeOH selectivity) catalysts are prepared using a precipitation agent of $NaOH/Na_2CO_3$ 4/1, precipitation temperature of 25 or 50°C, only mild ageing (25 °C for 2 h) or without ageing, drying at 80°C and calcination at 350°C for 2 h (rate = 5 K/min).

Based on this preparation method, differently promoted Cu/ZrO_2 catalysts are synthesized either by co-precipitation or by impregnation of pure Cu/Zr precipitate. It turned out that especially Zn, Al, Ce, Ga and to some extent the earth alkaline metals enhance the CO_2 conversion by far and even partially the MeOH selectivity compared to the pure Cu/ZrO_2 catalyst. Cd and Ag increase the MeOH selectivity but decrease the CO_2 conversion a lot.

All catalysts were tested with the parallel testing unit (PTU). Hence, the parallel testing was put in operation successfully for methanol synthesis from CO_2 at 10 bar. The catalytic results are reliable and reproducible. It was verified by measuring some of the catalysts with a single testing unit. Despite measuring at different GHSV the order of the different active catalysts does not change. It underlines the credibility of the results obtained by the PTU.

A parameter study was done by variation of the GHSV (varying the total gas flow) and the H_2/CO_2 ratio depending on the pressure and temperature. It turned out that a feed gas composition of H_2/CO_2 4/1 is beneficial for high CO_2 conversions as well as high methanol selectivity. Small GHSV leads to an increase of the CO_2 conversion but to a slight decrease of the methanol selectivity. The deactivation of the catalysts is negligible for the reaction time (45 h).

5

Summary

The investigations of the Cu catalyzed ethynylation as well as the CO_2 hydrogenation to methanol provided many interesting results, which are summarized in the following section.

Chapter 2 - Reppe Chemistry – Ethynylation of Formaldehyde to 1,4-Butynediol

Copper(I) acetylide, Cu_2C_2, was characterized and its formation was investigated during the activation of $CuO/Bi_2O_3/SiO_2$ catalysts as well as the ethynylation of formaldehyde for the first time. New insights regarding the Cu_2C_2 formation and the catalytic reaction itself could be generated. It could be confirmed by catalytic experiments using pure Cu_2C_2 as well as $CuO/Bi_2O_3/SiO_2$ catalysts that copper(I) acetylide, Cu_2C_2, is the active species in the ethynylation reaction of formaldehyde to 1,4-butyndiol. In addition, the reduction of Cu(II) to Cu(I) that is necessary for Cu_2C_2 formation is induced by acetylene not by formaldehyde in contrast to literature.

Identification and characterization of copper(I) acetylide, Cu_2C_2, succeeded by Raman spectroscopy and X-Ray diffraction. Additionally, a clear relationship between Cu_2C_2 formation and the catalytic activity of catalysts with different Cu loadings and different temperature treatments is proven based on the results obtained by Raman spectroscopy and X-Ray diffraction. The formation of small and amorphous Cu_2C_2 particles during the activation of CuO based catalysts leads to high 1,4-butynediol formation rates in the ethynylation reaction. Furthermore, Cu_2C_2 formation most likely takes place in liquid phase via dissolution/re-precipitation processes. The amount of formed Cu_2C_2 could be quantified by TGA. CuO of the $CuO/Bi_2O_3/SiO_2$ is almost completely converted to Cu_2C_2 during 5 h activation.

The lacking initializing period as well as the same 1,4-butynediol formation rate by using the same catalyst twice indicates that the ethynylation reaction itself takes place at the surface of precipitated Cu_2C_2.

Chapter 3 - MeOH synthesis – Synthesis of Methanol Catalysts via Diethyl Zinc Grafting on Alumina Supported Cu Nanoparticles

A new synthesis route for $Cu/Zn/Al_2O_3$ catalysts via grafting of $ZnEt_2$ on Al_2O_3 supported Cu nanoparticles was developed to gain strong Cu-Zn interactions that are important for the catalytic reaction of CO_2 to MeOH. The advantage of the synthesis route is the targeted deposition of Zn(II) on metallic Cu nanoparticles while the Al_2O_3 support is not involved compared to conventional preparation procedures in which ZnO and CuO are distributed within the whole catalyst. It allows to study the role of Zn in direct vicinity of Cu and to exclude the influence of Zn, which is located between the Cu particles and the Al_2O_3 support. By reductive pre-treatment of the catalysts, it is possible to adjust the Zn/Cu ratio at the surface and hence the extent of Zn/Cu surface alloy formation. It turned out that the formation of Cu/Zn surface alloy after re-

ductive pretreatment leads to the formation of highly dispersed Cu/$Zn^{\delta+}$ sites during the catalytic reaction. In addition, the Zn coverage is crucial depending on the Cu particle size and consequently on the level of Zn/Cu surface alloy formation.
For comparison, catalysts are prepared where Zn or rather ZnO is first deposited on Al_2O_3. Cu is precipitated afterwards onto the support. It turned out that these catalysts are more resistant towards sintering of the Cu nanoparticles than the catalysts in which Zn is targeted deposited onto the Cu nanoparticles. ZnO which is located between the Cu nanoparticles protects them against sintering.

Chapter 4 - MeOH synthesis – Development of Cu/Zirconia Based Catalysts for MeOH Synthesis
By variation of different preparation parameters of the co-precipitation of different Cu/ZrO_2 catalysts an optimized procedure for the synthesis of Cu/ZrO_2 systems was developed. A precipitation agent of NaOH/Na_2CO_3 4/1, precipitation temperature of 25 or 50°C, only mild ageing (25 °C for 2 h) or without ageing, drying at 80°C, calcination at 350°C for 2 h (rate = 5 K/min) is beneficial for the catalytic activity im methanol synthesis, which means high CO_2 conversion and high MeOH selectivity.
Based on this preparation method, different promoted Cu/ZrO_2 catalysts are synthesized either by co-precipitation or by impregnation of the Cu/Zr precipitate. Zn, Al, Ce, Ga and to some extent the earth alkaline metals increase the CO_2 conversion by far and even partially the MeOH selectivity rises compared to the pure Cu/ZrO_2 catalyst. In contrast to that, Cd and Ag increase the MeOH selectivity but decrease the CO_2 conversion a lot.
All catalysts were tested with the parallel testing unit (PTU). Hence, the parallel testing was put in operation successfully for methanol synthesis from CO_2 at 10 bar. The catalytic results are reliable and reproducible.
With the help of a parameter study by variation of the GHSV (varying the total gas flow) and the H_2/CO_2 ratio depending on the pressure and temperature, it turned out that a feed gas composition of H_2/CO_2 4/1 is beneficial for high CO_2 conversions as well as high methanol selectivity. Small GHSV leads to an increase of the CO_2 conversion but to a slight decrease of the methanol selectivity.

6

Zusammenfassung

Untersuchungen der kupferkatalysierten Ethinylierung sowie der CO_2 Hydrierung zu Methanol führten zu neuen Erkenntnissen und Schlussfolgerungen. Diese werden im Folgenden kurz zusammengefasst.

Kapitel 2 - Reppe Chemie – Ethinylierung von Formaldehyd zu 1,4-Butindiol

Kupfer(I)acetylid, Cu_2C_2, wurde charakterisiert und dessen Bildung während der Aktivierung von $CuO/Bi_2O_3/SiO_2$ Katalysatoren sowie der Ethinylierung von Formaldehyd zu 1,4-Butindiol zum ersten Mal untersucht. Neue Einblicke hinsichtlich der Cu_2C_2 Bildung und der katalytischen Reaktion konnten gewonnen werden.

Durch Katalysereaktionen mit reinem Kupfer(I)acetylid, Cu_2C_2, sowie $CuO/Bi_2O_3/SiO_2$ Katalysatoren konnte bestätigt werden, dass Kupfer(I)acetylid, Cu_2C_2, die aktive Spezies in der Ethinylierung von Formaldehyd zu 1,4-Butindiol ist. Acetylen, nicht Formaldehyd, wirkt dabei als Reduktionmittel, um Cu(II) zu Cu(I) zu reduzieren. Die Identifikation und Charakterisierung von Kupfer(I)acetylid, Cu_2C_2, gelang mittels Raman Spektroskopie sowie Röntgendiffraktometrie. Zusätzlich dazu konnte ein klarer Zusammenhang zwischen der Bildung von Cu_2C_2 und der katalytischen Aktivität von Katalysatoren mit verschiedenen Kupferbeladungen und Katalysatoren, die unterschiedlich calciniert wurden, hergestellt werden. Die Bildung von kleinen, amorphen Cu_2C_2 Partikeln während der Aktivierung von kupferbasierten Katalysatoren führt zu hohen 1,4-Butindiol Bildungsraten. Cu_2C_2 wird in Lösung durch Auflösungs- und Abscheidungsprozesse gebildet. Das gebildete Cu_2C_2 wurde mittels TG-MS quantifiziert. CuO wird praktisch vollständig nach 5 h Aktivierung zu Cu_2C_2 umgesetzt.

Die fehlende Initialisierungsperiode sowie die gleiche 1,4-Butindiol Bildungsrate beim zweimaligen Verwenden des gleichen Katalysators zeigt, dass die Ethinylierungsreaktion auf der Oberfläche von abgeschiedenem Cu_2C_2 stattfindet.

Kapitel 3 - MeOH Synthese – Synthese von Methanolkatalysatoren mittels Grafting von Diethylzink auf Aluminiumoxid geträgerte Kupfer-Nanopartikel

Ein neuer Syntheseweg zur Herstellung von $Cu/Zn/Al_2O_3$-Katalysatoren mittels Grafting von Diethylzink auf Al_2O_3 geträgerte Kupfernanopartikel wurde entwickelt, um starke Cu-Zn Wechselwirkungen zu generieren, die sehr wichtig für die katalytische Reaktion von CO_2 zu Methanol sind. Der Vorteil des Synthesewegs ist die exklusive Abscheidung von Zn(II) auf metallische Kupfernanopartikel. Der Al_2O_3-Träger wird bei diesem Syntheseweg nicht mit einbezogen. Somit befindet sich kein Zink auf oder im Träger im Gegensatz zu konventionellen Herstellungsmethoden von $Cu/ZnO/Al_2O_3$ Katalysatoren.

Dies erlaubt die Untersuchung der Rolle von Zink in direkter Nachbarschaft zu Kupfer, wobei der Einfluss von Zink, welches sich auf dem Al_2O_3-Träger befindet, ausgeschlossen wird. Durch reduktive Vorbehandlung mit H_2 ist es möglich das Zn/Cu Verhältnis an der Oberfläche

einzustellen und folglich die Bildung der Zn/Cu-Oberflächenlegierung. Es stellte sich heraus, dass die Bildung einer Zn/Cu-Oberflächenlegierung nach der reduktiven Vorbehandlung zu fein verteilten Cu/ $Zn^{\delta+}$ Zentren während der Reaktion führt. Außerdem spielt die Zinkbedeckung in Abhängigkeit von der Partikelgröße eine große Rolle und beeinflusst somit das Ausmaß der Zn/Cu Oberflächenlegierungsbildung.
Zum Vergleich wurden Katalysatoren präpariert, bei denen Zn beziehungsweise ZnO zuerst und ausschließlich auf den Al_2O_3-Träger abgeschieden wurde und danach Kupfer mittels Fällung aufgebracht wurde. Es stellte sich heraus, dass diese Katalystoren im Vergleich zu den Katalysatoren, bei denen Zn exklusiv auf die Kupfernanopartikel abgeschieden wurde, stärker gegen Sintern der Kupfernanopartikel geschützt sind. Das bedeutet, dass ZnO, das sich unter oder zwischen den Kupfernanopartikeln befindet, das Sintern behindert.

Kapitel 4 - MeOH Synthese – Entwicklung von Kupfer/Zirkonoxid basierten Katalysatoren für die Methanolsynthese

Durch Variation unterschiedlicher Präparationsparameter der Co-Fällung von verschiedenen Cu/ZrO_2 Katalysatoren wurde eine optimierte Synthesevorschrift zur Herstelleung Cu/ZrO_2 basierter Systeme entwickelt. Ein Fällungsreagenz von $NaOH/Na_2CO_3$ 4/1, eine Fällungstemperatur von 25 oder 50°C, mildes oder kein Altern (25 °C für 2 h), Trocknung bei 80°C, Calcinierung bei 350°C für 2 h (Heizrate = 5 K/min) steigert die katalytische Aktivität in der Methanolsynthese, was mit hohem CO_2-Umsatz und hoher MeOH-Selektivität einhergeht.
Auf Basis dieser Synthesevorschrift wurden verschiedene promotierte Cu/ZrO_2-Katalysatoren entweder durch Co-Fällung oder durch Imprägnierung des Cu/Zr-Präzipitats hergestellt. Zn, Al, Ce, Ga und teilweise die Erdalkalimetalle erhöhen den CO_2-Umsatz und MeOH-Selektivität verglichen zum reinen Cu/ZrO_2-System. Im Gegensatz dazu erhöhen Cd und Ag zwar die MeOH-Selektivtät aber erniedrigen in hohem Ausmaß den CO_2-Umsatz.
Alle Katalysatoren wurden in einer Paralleltestanlage (PTU) mit 12 Reaktoren getestet. Folglich wurde die Paralleltestanlage erfolgreich für die Methanolsynthese aus CO_2 bei 10 bar in Betrieb genommen. Die Katalyseergebnisse sind zuverlässig und reproduzierbar.
Mit Hilfe einer Parameterstudie durch Variation der GHSV (durch verändern des Gesamtvolemstroms) und des H_2/CO_2-Verhältnisses in Abhängigkeit von Druck und Temperatur stellte sich heraus, dass eine Feedzusammensetzung von H_2/CO_2 = 4/1 vorteilhaft für einen hohen CO_2-Umsatz sowie eine hohe Methanol-Selektivität ist. Eine kleine GHSV führt ebenfalls zu höherem CO_2-Umsatz jedoch zu etwas niedrigerer Methanol-Selektivität.

7

Experimental

7.1 Experimental to chapter 2 – Reppe Chemistry - Ethynylation of Formaldehyde with Acetylene to 1,4-Butynediol

Caution: Because Cu acetylide compounds are to some extend unstable against heat and impacts, proper safety precautions should be taken when handling the materials. Especially dry samples are able to explode under the influence of impact or heat. Wearing protective equipment is recommended for the handling of any explosive materials. All Cu acetylides samples or activated catalysts used in this work are disarmed by **carefully** addition of nitric acid.

Synthesis of the catalysts

All chemicals were used without further purification.

Chemical	Supplier	Purification grade
$Cu(NO_3)_2 \cdot 3H_2O$	VWR Chemicals	GPR Rectapure
Na_2SiO_3	Alfa Aesar	technical
Bi_2O_3	Sigma Aldrich	99%
NaOH	Grüssing GmbH	99%
NaH_2PO_4	ChemSolute	≥ 99%
Paraformaldehyde	Alfa Aesar	97%
MeOH	VWR Chemicals	GPR Rectapure
CuCl	Alfa Aesar	97%
NH_3 solution (25%)	Merck	-
H_3PO_4 (85%)	VWR Chemicals	Normapure
Acetonitrile	VWR Chemicals	Chromapure
1,3-propanediol	Alfa Aesar	99%
Acetylene	Westfalen	2.6
Nitrogen	Westfalen	5.0
$Al(NO_3)_3 \cdot 9H_2O$	Merck	≥ 95%
Na_2CO_3	VWR Chemicals	Normapur
$Cu(CH_3COO)_2$	Alfa Aesar	99 %
Conc. HNO_3	VWR Chemicals	Normapure
Propargyl alchohol	Sigma Aldrich	99%

Preparation of pure and silica supported Cu_2C_2[71]

In a glovebox 2.50 g copper(I) chloride is weighed in a Schlenk tube and 50 mL of a 25 wt.% ammonia solution are added. The Schlenk tube is purged with nitrogen via a septum for 8 min before switching to acetylene. Immediately a red to brown solid precipitates. After 2 h reaction time, the Schlenk tube is purged with nitrogen again to remove the remaining acetylene. The

precipitate is washed with water and methanol. The only difference between the preparation of pure copper(I) acetylide to supported one is the addition of silica to the 50 mL ammonia solution. **Be careful because copper(I) acetylide is highly explosive at dry condition!**

Preparation of copper-bismuth-silica catalyst

The different Cu and Bi loaded catalysts were synthesized by a common co-precipitation procedure.[99] The weight percentage of bismuth is kept in a constant ratio to the weight percentage of copper of 1:8.75. Bi_2O_3 is dissolved in 2 mL of concentrated HNO_3 and added to a solution of $Cu(NO_3)_2 \cdot 3\ H_2O$ in water. In a second beaker, a 2 M solution of Na_2SiO_3 in water is prepared. For the coprecipitation process, 150 mL of distilled water are filled into an 800 mL beaker containing a stirring bar, a pH electrode and a thermometer and placed onto a magnetic hot plate stirrer. After heating to 60 °C, the stirring speed is set to 400 rpm and the precipitation process started. The 2 M solution of Na_2SiO_3 and the solution containing both Bi_2O_3 and $Cu(NO_3)_2 \cdot 3\ H_2O$ are simultaneously added dropwise over a time frame of 20 min using two peristaltic pumps operating at a constant volumetric flow rate. During this process the pH of the reaction mixture is kept at a constant value of 7 by titration with 2 M HNO_3. The titration is controlled by a 906 Titrando titrator by *Metrohm*. After both precursor solutions are fully added to the reaction mixture, the titration is stopped, the stirring speed is adjusted to 300 rpm and the reaction mixture aged for 60 min. The resulting precipitate is filtered off under vacuum, washed with distilled water until the electrical conductivity of the filtrate is below 4 mS m^{-1}, dried at 80 °C overnight and calcined at 450 °C, 600 or 700°C for 4 h with a heating rate of 2.5 K min^{-1}. The obtained catalyst is then sieved to give particles of a diameter d with 100 µm < d ≤ 300 µm.

Preparation of copper-bismuth-alumina catalysts

For the measurement series investigating the influence of the calcination temperature on the catalytic activity of alumina supported catalysts, catalysts all containing 35 wt. % copper and 4 wt. % bismuth but calcined at different temperatures are prepared.

The different $CuO/Bi_2O_3/Al_2O_3$ catalysts were synthesized by variation of a common co-precipitation procedure.[250, 321]

Bi_2O_3 is dissolved in 2 mL of concentrated HNO_3 and added to a solution of $Cu(NO_3)_2 \cdot 3\ H_2O$ and $Al(NO_3)_3 \cdot 9\ H_2O$ in water giving a 2 M solution. The co-precipitation process is performed analogously to the co-precipitation process of the silica supported catalysts but with only one precursor solution, 2 M aqueous Na_2CO_3 as precipitation agent and at 50 °C. The resulting suspension is aged analogously, the precipitate filtered off, washed until the electrical conductivity is below 4 mS m^{-1} and dried at 80 °C overnight. The catalysts were calcined at 450°C,

600°C and 700°C for 4 h with a heating rate of 2.5 K min^{-1}. After calcination, the catalyst is sieved to give particles of a diameter *d* with 100 µm < *d* ≤ 300 µm.

Ethynylation of formaldehyde to 1,4-butynediol

For a standard catalytic test 50.34 g paraformaldehyde, 10.90 g methanol and 50.34 g water are weighed in a three-necked flask, attached to the reactor setup (see Figure 108) and heated to 100 °C under reflux. NaOH (1.40 g) and $NaH_2PO_4 \cdot H_2O$ (4.84 g) are added as a buffer and the suspension is stirred at 100 °C until a clear solution is obtained. After addition of 5.00 g catalyst and 1,3-propanediol (5.00 g) acting as an internal standard, the stirring speed is set to maximum and the reaction mixture purged with nitrogen for 60 min. The gas stream is then switched to acetylene to start the reaction and the reaction setup flushed with acetylene for 8 min. The pressure relieve valve is then closed, the acetylene pressure set to 1.2 bar and the reaction mixture stirred until the end of the reaction at 100 °C. At the end of the reaction, the reaction setup is cooled down and purged with nitrogen for 10 min to remove residual acetylene and reaction gases. Samples of 0.5 mL of reaction mixture are collected during the nitrogen purge phase and the reaction period using a syringe. They are used to determine the composition of the reaction mixture via GC analysis. A blank test was carried out without any catalyst to show that no products are formed under the selected activation/reaction conditions (see Figure 109B).

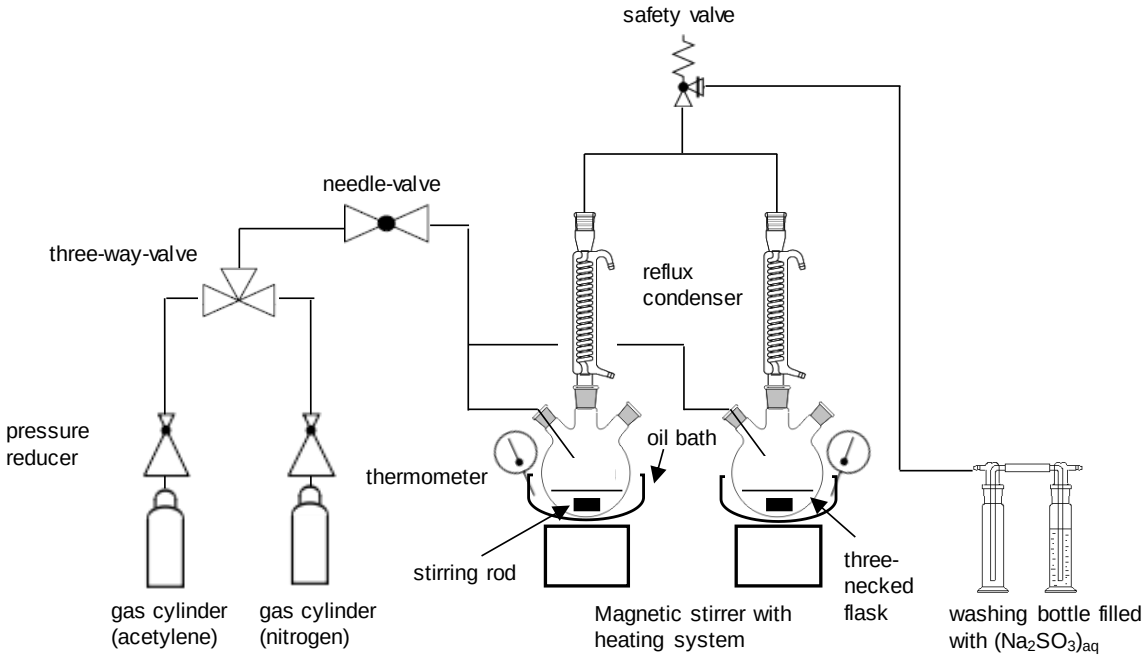

Figure 108: Reaction setup for the ethynylation of formaldehyde with acetylene.

Product analysis via gas chromatography

Samples of 0.5 mL of reaction mixture are transferred into a test tube. 1.5 mL acetonitrile is added to end the reaction process and precipitate buffer salts. The suspension is mixed thoroughly and filtered over activated aluminum oxide (*PURALOX SCCa150/200* from *SASOL Germany GmbH*). The filtrate is collected in GC vials and analyzed quantitatively by gas chromatography. Gas chromatograms are recorded on an *Agilent G1530A* machine fitted with a TCD detector. A *HP-PLOT-Q* (stationary phase: solid polystyrene/divinylbenzene, length: 30 m, inner diameter: 0.32 mm, film thickness: 0.2 µm) GC column is used to separate the different components and 1,3-propanediol is used as internal standard for calibration.

For the calculation of the 1,4-butynediol and propargyl alcohol yield the molar amount of the product is calculated:

$$n_i(t) = \frac{n_{int.st.} \frac{A_{i,t}}{A_{int.st}}}{m_{i,GC}}$$

$n_i(t)$ = molar amount at reaction time t for component i

$n_{int.st.}$ = molar amount of the internal standard (1,3-propanediol)

$A_{i,t}$ = area of component i obtained from the GC after reaction time t

$A_{int.st.}$ = area of the internal standard obtained from the GC after reaction time t

$m_{i,GC}$ = slope of the calibration curve for component i obtained from the GC

Then, the product yield is obtained as follows:

$$Y_i = \frac{n_i(t)}{n_{i,max}}$$

Y_i = yield of component i

$n_i(t)$ = molar amount at reaction time t for component i

$n_{i,max}$ = maximum molar amount of component i, which can be produced (calculated from the formaldehyde concentration)

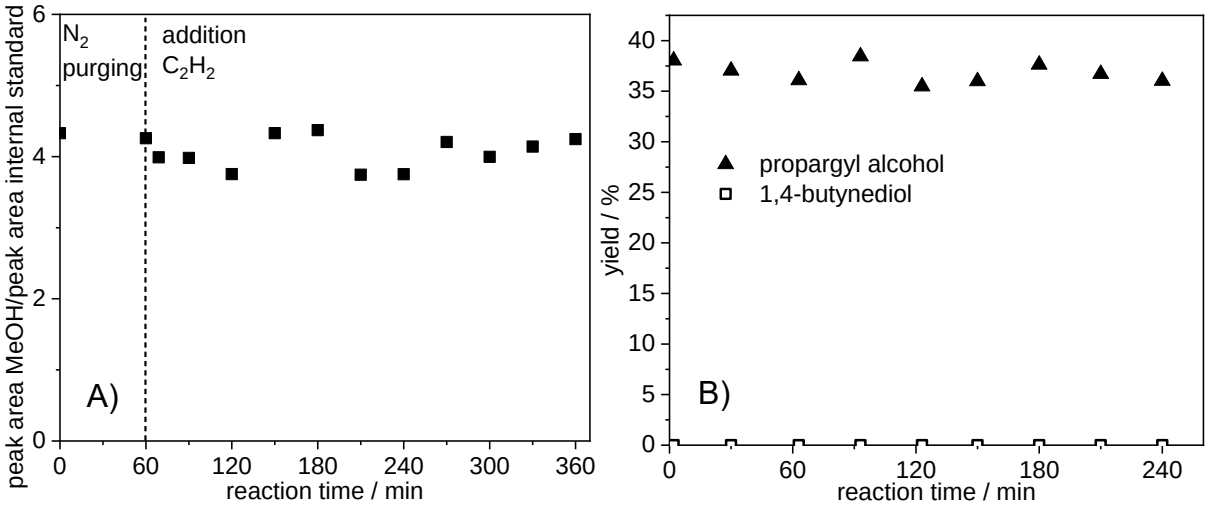

Figure 109: (A) Ratio of peak area MeOH to peak area internal standard obtained from GC. (B) Blank test to verify that without catalyst no reaction occurs.

Characterization and analysis methods

Sample preparation for Raman spectroscopy, X-Ray diffraction and TGA

Samples of 3.5 mL of reaction mixture are collected during the purging and the reaction period. The samples were filtrated. The solids were washed with water and methanol and dried under vacuum.

Analysis via X-Ray diffraction

The powdered catalyst sample is placed onto a flatbed support, inserted into the X-ray machine and measured with an *Empyrean* diffractometer from *PANalytical* (K_α(Cu), λ=1 5419, Ni as K_β(Cu)-filter) in reflection mode. Diffractograms are recorded in an angle range between 5° and 70° in steps of 0.008°. They are analyzed using the *HighScore Plus* software from *PANalytical*. The crystallite sizes were calculated with the Scherrer equation[100-104]:

$$L = \frac{K\,\lambda}{\Delta(2\theta)\,cos\theta}$$

Δ(2θ) = the quantity of the line broadening at half the maximum intensity (FWHM) in radians

K = shape factor (0.9 to 1)

λ = wavelength of the X-Ray source

θ = Bragg angle

L = mean size of the ordered crystalline domains

Analysis via Raman spectroscopy

Raman spectra are recorded on an *InVia* Raman Microscope from *Renishaw* with a *Newton EMCCD Camera* (Spectroscopy EMCCD, width: 25.6 mm, 1600 pixel, 3 MHz) from *Andor*. For the measurements, a frequency-doubled Nd:YAG laser (λ=532 nm) and an objective with 50x

magnification (*Leica N PLAN EPI* 50x/0.75) are used. The standard laser intensity was 0.015 mW and the standard scanning time 5 sec with 10 repetitions.

Quantification of copper(I) acetylide via TGA

The TGA was carried out using a *STARe System* TGA DSC^{3+},TGA 2 from *Mettler Toledo GmbH* and the software *STAReSoftware* version 14.000 from *Mettler Toledo GmbH*. The samples were heated from 25°C to 1000°C in synthetic air with a heating rate of 10 Kmin^{-1}. The gas phase analysis done by MS was measured using a *ThermoStar*^{TM} from *Pfeiffer Vacuum* and the software *QUADERA*® version 4.62 from *INFICON Holding AG*.

Sample preparation for copper leaching measurements

To investigate copper leaching processes, the concentration of copper(II) ions dissolved in the reaction mixture is measured *in situ* during the reaction using an ion-selective electrode and by elemental analysis via ICP-OES. First method requires using a four-necked round flask in the reactor setup instead of the three-necked flask described in the section before. A copper(II)-selective electrode by *Metrohm* is inserted through the additional opening and an Ag/AgCl(aq) (3 M KCl) reference electrode through the opening otherwise used for sample extraction. For the copper content determination by ICP-OES samples were taken with a syringe and the organic compounds were removed by heating at 90°C for 10 hours. The residue was dissolved with 2 mL concentrated phosphoric acid and diluted with water. 10 mL of the solution was used for the ICP-OES analysis.

Analysis of copper content via ICP-OES

The copper content was determined using an ICP-OES 700 from *Agilent*. A multiple element standard from *Merck* was used for external calibration.

Sample preparation for EPR spectroscopy

0.08 mL of the reaction suspension are filled in a capillary with a syringe. The capillaries were put into EPR tubes. The EPR tubes were purged with argon and closed.

Analysis via EPR spectroscopy

EPR spectra were recorded using a *JEOL JES-RE 2X* spectrometer on x-band frequency at -120°C. The spectra were measured at a microwave frequency of 9.20 GHz, 5 mW, a modulation amplitude of 0.4 mT and a sweep-time of 4 min. The sweep-width is 230.430 mT at a constant time of 0.1 s and a modulation frequency of 100 kHz. The microwave frequency is

determined by *Advantest R5372* instrument and the temperature by a *JEOL ES DVT2* thermometer which is equipped with a calibrated thermocouple. The g- and A-values are calibrated as a standard via Mn(II) (nuclear spin I = 5/2) in a magnesium(II) oxide matrix (g = 1.981).

7.2 Experimental to chapter 3 – MeOH Synthesis - Synthesis of Methanol Catalysts via Diethy Zinc Grafting on Alumina Supported Copper Nanoparticles

Synthesis of the catalysts

All chemicals were used without further purification.

Chemical	Supplier	Purification grade
$Cu(NO_3)_2 \cdot 3H_2O$	VWR Chemicals	GPR Rectapure
$Al(NO_3)_3 \cdot 9H_2O$	Merck	≥ 95%
NaOH	Grüssing GmbH	99%
$Cu(CH_3COO)_2$	Alfa Aesar	99 %
Hydrazine monohydrate	Merck	≥99%
2-Ethoxyethanol	VWR Chemicals	99%
γ-Al_2O_3	SASOL (PURALOX®)	≥99%
Urea	VWR chemicals	95%
NH_3 solution (25%)	Merck	for analysis
H_3PO_4 (85%)	VWR Chemicals	Normapure
$ZnEt_2$	Sigma Aldrich	1M in heptane
Heptane	Signa Aldrich	Anhydrous ≥99%
Pentane	Sigma Aldrich	Anhydrous ≥99%
EtOH	Merck	(1% MTK) for analysis
CO_2	Westfalen	4.5
H_2	Westfalen	5.0
He	Westfalen	5.0
N_2O	Westfalen	(1% in He 6.0)
CO	Westfalen	(10% in He 4.7)
Hexamethyldisilazane	Alfa Aesar	98 %

Preparation of Al_2O_3 supported Cu nanoparticles by reductive precipitation (Cu_{RP})

The different loaded Al_2O_3 supported Cu nanoparticles were synthesized by variation of a common procedure.[246, 249] The reaction flask is heated with hexamethyldisilazane (HMDS) for inerting the flask prior to the experiment. HMDS is heated to the boiling point so it creeps up the glass walls. Then, the vessel is evacuated to evaporate the remaining HMDS. Copper(II)acetate trihydrate (amount depends on the Cu loading) is dissolved in 20 mL deionized water and mixed with 100 mL ethoxyethanol. The supporting material (Al_2O_3, sieved 100-300 µm)

(amount depends on the Cu loading) is added to form a suspension. Then hydrazine (monohydrate 1.5 mL) is added to form the orange copper-hydrazine complex. The suspension is heated to 55°C under reflux and held for 2h. The red-black product is cooled and washed with 2x 50mL dry ethanol via whatman-filtration technique. The product is dried under vacuum and stored in an inert atmosphere.

Preparation of Al_2O_3 supported Cu nanoparticles by deposition precipitation with urea (Cu_{DP})

The different loaded Al_2O_3 supported Cu nanoparticles were synthesized by variation of a common procedure.[246, 247] Copper(II)nitrate trihydrate (amount depends on the Cu loading) is dissolved in 200 mL deionized water. Supporting material (Al_2O_3, sieved 100-300µm) and urea (both amounts depends on the Cu loading) is added. The suspension is heated to 90°C under reflux for continuously decomposition of urea. Reaction was kept for 2 days and precipitation is finished as soon as the blue solution has turned colorless. The precipitate was filtered and washed with 3x 50 mL water and dried overnight at 80°C. The dry precursor was calcined at 450°C for 4h (2,5 K/min).

Preparation of Al_2O_3 supported Cu nanoparticles by co-precipitation (Cu_{CoPr})

The different loaded Al_2O_3 supported Cu nanoparticles were synthesized by variation of a common co-precipitation procedure.[250, 321] A metal nitrate solution of $Cu(NO_3)_2$ trihydrate and $Al(NO_3)_3$ nonahydrate (both amounts depends on the Cu loading) dissolved in 95 mL deionized water is prepared. For precipitation, 500 mL deionized water is heated to 50°C and stirred rapidly at 400 rpm. The nitrate solution was constantly added with a flow rate of 5 mL/min using a peristaltic pump. The pH was kept at 7 (see titration curve Figure 110) using an automated titration device. A 2 M NaOH solution serves as precipitation agent. After precipitation, the solution is aged at 50°C for 1h. The aged product is filtered and washed with deionized water until the residue does not exceed a conductivity of 4 mS m^{-1} (removal of Na^+). The precursor is dried overnight at 80°C and further calcined for 4h at 450°C (2.5 K/min).

Preparation of Al_2O_3 supported Cu nanoparticles by deposition precipitation via ligand removal (Cu_{LR})

The different loaded Al_2O_3 supported Cu nanoparticles were synthesized by variation of a common procedure.[246, 248] Copper(II)nitrate trihydrate (amount depends on the Cu loading) is dissolved in 100 mL deionized water in an Erlenmeyer flask. Supporting material (Al_2O_3, sieved 100-300µm) and aqueous ammonia (10%) is added. The suspension is stirred. Reaction was kept for 2 to 3 days and precipitation is finished as soon as the blue solution has turned colorless and a light blue precipitate formed. The precipitate was filtered and washed with 3x 50 mL water and dried overnight at 80°C. The dry precursor was calcined at 450°C for 4h (2,5 K/min).

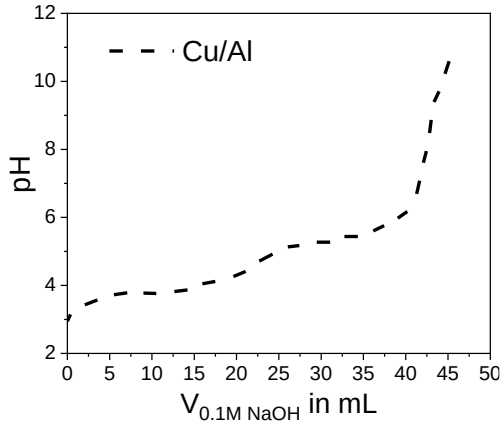

Figure 110: Titration curve of a 0.1 M solutions containing Al nitrate and Cu. The titration was carried out at room temperature using a 0.1 M solution of NaOH.

Grafting with $ZnEt_2$ ($ZnCu_{DP}$, $ZnCu_{CoPr}$, $ZnCu_{LR}$, $ZnCu_{RP}$)

Before Zn grafting, the calcined precursors are reduced at 300 °C at 20mL/min in pure H_2 flow for 1h with a heating ramp of 1 K/min.

Then, 500 mg of reduced precursor is added into a three-neck Schlenk-flask and a pressure relief valve is mounted. The flask is purged with H_2 for 5 min before the addition of dry and degassed heptane (20 mL). H_2 was bubbled through the suspension. After 5 minutes purging $ZnEt_2$ (amount depends on the Cu loading) in heptane solution (1 M) is added. The reaction is kept for 3 h under constant H_2 flow. As soon as the reaction is finished the solvent is decanted with a syringe and the residue is washed two times with 10 mL dry and degassed pentane. The catalyst is dried overnight under vacuum before it is stored in an inert atmosphere. The samples $pureCu_{DP}$, $pureCu_{LR}$, $pureCu_{CoPr}$ were prepared by the same procedure just without the addition of $ZnEt_2$.

Preparation of $ZnCu_{ref1}$, $ZnCu_{ref2}$

First Al_2O_3 was calcined at 500°C (5K/min, 8h) in air to get rid of surface impurities and water. After that it was dehydroxylated at 700°C at 10^{-6} bar to create isolated hydroxyl groups. For the grafting step, a $ZnEt_2$ heptane solution (1M) was added and it is slowly stirred for 3 h in Ar atmosphere. The solid was washed two times with 10 mL dry and degassed pentane before it was transferred into the glovebox. To transform it into highly dispersed ZnO it was calcined at 250°C (2.5 K/min, 5h) afterwards. Then Cu was precipitated onto the ZnO/Al_2O_3 support via deposition precipitation with urea which was described before.

CO_2 hydrogenation to methanol

The reaction setup is shown in Figure 111. The catalyst (150 mg) is placed in an U-shaped reactor. Before the catalytic reaction the catalysts are pretreated at 40°C, 120°C or 200°C (heating rate: 1 K/min) in 50% H_2/He (20 mL/min) for 45 min or are used without pretreatment. The catalytic reaction is carried out at 28 bar and at 6 temperature steps: 200°C, 225°C, 250°C, 275°C, 300°C, 325°C. The heating rate between the steps is 2.5 K/min and the holding time is 2 h for each step. The CO_2/H_2 ratio is 1/3 with a GHSV of 8000 h^{-1}. The product feed composition is determined by online gas chromatography with a *Perkin Elmer Clarus 590 GC* equipped with thermal conductivity detector (TCD). The catalyst is removed inside the glovebox for further characterization. An empty reactor was measured under the same catalytic conditions to exclude effects caused by the reactor itself.

The data are evaluated using following equations:

First, the volume fraction $\varphi_i(t)$ is calculated for each gas after reaction time t with help of the calibration parameters.

$$\varphi_i(t) = \frac{A_i - u_{i,GC}}{m_{i,GC}}$$

$\varphi_i(t)$ = volume fraction at reaction time t for component i

A_i = area obtained from the GC for a component i

$u_{i,GC}$ = y-intercept of the calibration curve for component i obtained from the GC

$m_{i,GC}$ = slope of the calibration curve for component i obtained from the GC

With the volume fraction $\varphi_i(t)$ and with the knowledge that CO_2 is only converted to CO or MeOH the mass balance can be calculated regarding the carbon containing components. Hence, the CO_2 mole fraction $\varphi_{CO_2}(t=0)$ before the reaction can be calculated.

$$\varphi_{CO_2}(t=0) = \varphi_{CO_2}(t) + \varphi_{CO}(t) + \varphi_{MeOH}(t)$$

$\varphi_{CO_2}(t=0)$ = CO_2 mole fraction before the reaction

$\varphi_{CO_2}(t)$ = CO_2 mole fraction at reaction time t

$\varphi_{CO}(t)$ = CO mole fraction at reaction time t

$\varphi_{MeOH}(t)$ = MeOH mole fraction at reaction time t

With the CO_2 mole fraction before the reaction the CO_2 conversion X_{CO_2} can be determined.

$$X_{CO_2} = \frac{\varphi_{CO_2}(t=0) - \varphi_{CO_2}(t)}{\varphi_{CO_2}(t=0)}$$

X_{CO_2} = CO_2 conversion

$\varphi_{CO_2}(t=0)$ = CO_2 mole fraction before the reaction

$\varphi_{CO_2}(t)$ = CO_2 mole fraction at reaction time t

The yield of component i can be calculated as follows:

$$Y_i = \frac{\varphi_i(t)}{\varphi_{CO_2}(t=0)}$$

Y_i = yield of component i
$\varphi_i(t)$ = volume fraction at reaction time t for component i
$\varphi_{CO_2}(t=0)$ = CO_2 mole fraction before the reaction

The selectivity of component i can be calculated as follows:

$$S_i = \frac{Y_i}{X_{CO_2}}$$

S_i = selectivity of component i
Y_i = yield of component i
X_{CO_2} = CO_2 conversion

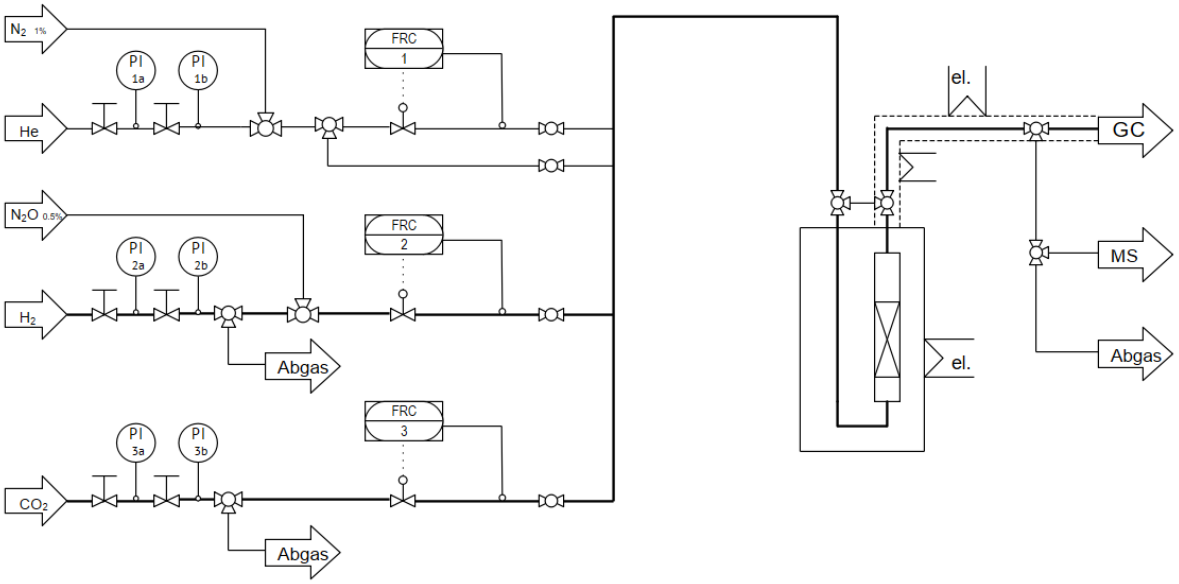

Figure 111: Flow chart of the single testing unit (STU).

Interpolation of the temperature of 5 % CO_2 conversion and the corresponding selectivity

First, the temperature of 5 % CO_2 conversion is calculated by interpolation of the different CO_2 conversion curves. With a polynomial fit (polynomial fit of 4th degree) the trend line can be obtained with the following equation:

$$U(T) = aT^4 + bT^3 + cT^2 + dT + e$$

Then, the temperature of 5 % CO_2 conversion $T(U = 0.05)$ can be calculated with the following equation:

$$aT^4 + bT^3 + cT^2 + dT + e - 0.05 = 0$$

The methanol selectivity at this temperature can be interpolated with a polynomial fit of 3rd degree. By insertion of $T(U = 0.05)$, the corresponding methanol selectivity $S(T(U = 0.05))$ is calculated as follows:

$$S\big(T(U)\big) = aT(U = 0.05)^3 + bT(U = 0.05)^2 + cT(U = 0.05) + d$$

Characterization and analysis methods

Elemental analysis

ICP-OES measurements for determination of Cu and Zn content are conducted on an Agilent 700 ICP-OES. Around 40 mg sample are dissolved in 2 mL of concentrated phosphoric acid and stirred overnight at 90°C. The samples were diluted with distilled water and concentrated to obtain a maximum Al concentration of 40 ppm. A commercial standard (1000 ppm Merck ICP multi-element standard solution IV) is used for external calibration from 1.0 to 50.0 ppm. All values contain errors from pipettes used for dilution. Therefore, an error of 1% is estimated. In addition, an error of 5% is estimated regarding the preparation procedure.

Determination of the C content

5 mg of the sample is burned in synthetic air. Carbon containing ligands are decomposed and carbon reacts to carbon dioxide. The formed carbon dioxide is quantified via gas chromatography.

Determination of ethane to Zn ratio

65 mg of the sample is added in a Schlenk tube with a defined volume and 1 mL water is added. After 30 min reaction a defined volume of the gas phase was collected with a syringe. The ethane content in the syringe was determined by gas chromatography.

X-Ray diffraction

The samples after calcination are placed onto a flatbed support, inserted into the X-ray machine and measured with an *Empyrean* diffractometer from *PANalytical* (K_α(Cu), λ=1 5419, Ni as K_β(Cu)-filter) in reflection mode. Diffractograms are recorded in an angle range between 5° and 70° in steps of 0.013°. For the air sensitive samples (after reduction and Zn grafting) the diffractograms are recorded in an angle between 5° and 90° in steps of 0.008°. In this case the samples are filled into capillaries to exclude air contact. The diffractograms are analyzed using the *HighScore Plus* software from *PANalytical*.

The crystallite sizes were calculated with the Scherrer equation[100-104]:

$$L = \frac{K\,\lambda}{\Delta(2\theta)\,cos\theta}$$

$\Delta(2\theta)$ = the quantity of the line broadening at half the maximum intensity (FWHM) in radians
K = shape factor (0.9 to 1)
λ = wavelength of the X-Ray source
θ = Bragg angle
L = mean size of the ordered crystalline domains

BET surface area

Full N_2 isotherm measurements are conducted on a *Quantachrome NovaTouch*. N_2 physisorption isotherms are conducted at -196 °C. Before the measurement the samples were degassed (10 K/min, 120 °C, 3 h, 42 mbar). 100 mg sample are used and 39 points (adsorption and desorption) over the full partial pressure range were measured.

Temperature programmed reduction (TPR)

The calcined sample is placed in an U-shaped glass reactor. The sample is heated to 800 °C (5 K/min) in 50 mL/min 2.5 % H_2/He. The H_2 consumption is monitored using a thermal conductivity detector (TCD). The measurement is carried out in an *Autochem*.

Monitoring the grafting procedure with $ZnEt_2$

For monitoring the grafting procedure, the capillary of mass spectrometer is connected with the flask in which the grafting procedure is carried out. Due to the continuous H_2 gas flow the gas phase of the reaction flask is piped to the mass spectrometer (ThermoSTAR, *Pfeiffer Vacuum*).

Temperature programmed decomposition (TPD)

For the TPD experiment, 400 mg of the catalyst is added in an U-shaped reactor. The reactor is mounted in an oven and is heated to 500°C (5K/min) in 20 mL/min He flow. The exhaust gas stream is analyzed with a mass spectrometer (ThermoSTAR, *Pfeiffer Vacuum*).

X-ray photoemission spectroscopy (XPS)

X-ray photoelectron spectra were recorded on a Leybold-Heraeus LHS 10 spectrometer using a non-monochromatized Mg Kα source (1253.6 eV). The powder samples were pressed into cavities and measured as pellets. Preparation of the sample as well as the transfer into the XPS spectrometer was carried out under Ar atmosphere. All spectra were acquired in an ultra-high vacuum chamber at a pressure below $5 \cdot 10^{-8}$ mbar. The analyzer was operated at a constant pass energy of 100 eV leading to an energy resolution with a full width at half-maximum (FWHM) of ~1.1 eV. The energy scale was corrected for sample charging by using the

O 1s main signal (531.0 eV). The reductive pretreatment was carried out at 10^{-3} mbar H_2 heating to 300°C.

In-situ adsorption/desorption experiments using a modified IR spectrometer

In-situ IR-Spectroscopy was performed on a *Biorad FTS-575C FTIR* spectrometer with a resolution of 4 cm^{-1} and 32 scans. Samples were measured in a self-designed cell with the possibility to heat in defined ranges to 300°C and add gases into the cell chamber. The cell is equipped with ZnSe windows. Gas flow was controlled by mass flow controllers and temperature was controlled by a thermocouple connected to a *Eurotherm* temperature controller. The IR cell can be assembled in a glovebox to inertly prepare a pellet of the sample before mounting in the IR-spectrometer.

CO adsorption/desorption: CO is added to the gas stream (5% in He) and a spectrum is collected each minute up to five minutes. Subsequently the sample was heated in He gas stream to 250°C and every 25°C a spectrum is collected before it is cooled down.

H_2 adsorption/desorption: pure H_2 is applied and the sample was heated to 300°C. Every 25°C a spectrum is collected. After 1 hour at the maximum temperature another spectrum is collected before it is cooled down.

Determination of the Cu surface area by N_2O-RFC

Before the Cu surface area determination, the samples are reduced at 300 °C for 1 h (1 K/min) in pure H_2. The N_2O copper surface area is determined at 1 bar pressure and 308 K. At this temperature, no significant bulk oxidation of copper takes place. A mixture of 1% N_2O/He is used. The gas composition is analyzed using a mass spectrometer. After the measurement, the mass spectrometer is calibrated with a gas mixture of 1% N_2/He for the determination of the formed N_2.

The amount of copper surface atoms is calculated from the catalyst mass, flow rate and N_2 area obtained by mass spectrometry. In order to determine the Cu surface area, a mean copper surface atom density of 1.47 10^{19} atoms per m^2 is used. The latter one is the arithmetic mean value of the low index planes Cu(111), Cu(110), and Cu(100). As subsurface oxidation cannot be completely avoided the intersection between the disappearing N_2 signal and rising N_2O signal at the breakthrough point is used as a limit for the integration of the N_2 signal. The stoichiometric reaction is shown below.

$$2\ Cu_s + N_2O \longrightarrow Cu_s{-}O{-}Cu_s + N_2$$

Determination of the Cu surface area by H_2-TPD

Before the Cu surface area determination, the samples are reduced at 300 °C for 1 h (1 K/min) in pure H_2. The reduced sample is cooled down to 235 K in He and pressurized with 24 bar hydrogen for 30 minutes. Full hydrogen coverage of copper is achieved according to literature at these conditions. The catalyst is rapidly cooled down to 77 K, depressurized to atmospheric pressure and flushed at least 30 min with helium until the baseline in the mass spectrometer shows a constant value. Subsequently, the catalyst bed is heated up at atmospheric pressure in helium flow with a linear heat ramp of 6 K/min to 523 K. The desorption of H_2 during heating is monitored by a mass spectrometer. The amount of adsorbed hydrogen is calculated using the H_2 desorption peak area. Raw data are corrected by baseline subtraction. Cu surface area calculation is carried out analog to the determination by N_2O-RFC.

Transmission electron microscopy (TEM)

It is carried out probe-corrected on a Titan TEM from Thermo-Fishser Scientific and operated at the accelerating voltage of 300 kV. First, a bunch of images are acquired (both at low and high mags) to the morphology and crystal structure of nanoparticles. X-ray energy dispersive (EDS) and selected area electron diffraction (SAED) datasets are also acquired to determine the average elemental composition and the crystal structure of materials, respectively.

Scanning transmission electron microscopy – electron energy loss spectroscopy (STEM-EELS) elemental mapping

For determining the elemental distribution in materials, the microscope is set in the scanning TEM (STEM) mode and used both annular dark-field (ADF) and high-angle annular dark-field (HAADF) detectors to make STEM images. In the case of HAADF detector, the image-contrast is dominated by atomic number (Z). It is then followed by setting the Gatan-Image Filter (GIF Quantum 966) into the electron energy-loss spectroscopy (EELS) mode. In this way, STEM-EELS spectrum image (SI) data sets are acquired for each sample. EELS conditions are set in such a way that CuL23 and ZnL23 energy-loss edges are acquired to generate the Cu and Zn maps, respectively. The entire datasets are acquired and post-processed in Gatan Microscopy Suite (GMS of version 3.2).

7.3 Experimental to chapter 4 – MeOH Syntesis - Development of Copper/Zirconia Based Catalysts for MeOH Synthesis

Synthesis of the catalysts

All chemicals were used without further purification.

Chemical	Supplier	Purification grade
$Cu(NO_3)_2 \cdot 3H_2O$	VWR Chemicals	GPR Rectapure
$Al(NO_3)_3 \cdot 9H_2O$	Merck	≥ 95%
NaOH	Grüssing GmbH	99%
Na_2CO_3	VWR Chemicals	Normapur
Bi_2O_3	Sigma Aldrich	99%
$AgNO_3$	Merck	for analysis
$Mn(NO_3)_2 \cdot 4H_2O$	Merck	for analysis
$Fe(NO_3)_3 \cdot 9H_2O$	Amresco	for analysis
$Ce(NO_3)_3 \cdot 6H_2O$	Fluka	>99%
H_3PO_4 (85%)	VWR Chemicals	Normapure
$Zn(NO_3)_2 \cdot 6H_2O$	Alfea Aesar	98.5%
$In(NO_3)_3 \cdot xH_2O$	Sigma Aldrich	99.9%
$Ni(NO_3)_2 \cdot 6H_2O$	VWR Chemicals	GPR Rectapur
$Cd(NO_3)_2 \cdot 4H_2O$	Sigma Aldrich	98%
$Cr(NO_3)_3 \cdot 9H_2O$	Alfea Aesar	>98.5 %
$Sm(NO_3)_3 \cdot 6H_2O$	Alfea Aesar	99.9%
$Ga(NO_3)_3 \cdot xH_2O$	Sigma Aldrich	99.9%
$Mg(NO_3)_2 \cdot 6H_2O$	VWR Chemicals	Normapur
$Ba(NO_3)_2$	Alfea Aesar	99.95%
$Sr(NO_3)_2$	Sigma Aldrich	99%
$Ca(NO_3)_2 \cdot 4H_2O$	Merck	99%
K_2CO_3	Grüssing GmbH	99.5%
H_3BO_3	Merck	99%
Cs_2CO_3	Merck	extra pure
Li_2CO_3	Merck	extra pure
CHO_2Rb	Sigma Aldrich	98%
CO_2	Westfalen	4.5
H_2	Westfalen	5.0
He	Westfalen	5.0
N_2O	Westfalen	(1% in He 6.0)

Chemical	Supplier	Purification grade
$ZrO(NO_3)_2$	Arcos Organics	99.5 %
Conc. HNO_3	VWR Chemicals	Normapure

Preparation of different Cu/ZrO_2 catalysts

First, a 1M stock solution was prepared containing 120.8 g $Cu(NO_3)_2 \cdot 3H_2O$ and 171.13 g $ZrO(NO_3)_2$. The dissolution of $ZrO(NO_3)_2$ was facilitated by the addition of HNO_3. The exact molarity of the solution was determined by gravimetric analysis. In addition, different precipitation agents were prepared. The values are summarized in Table 31.

Table 31: Preparation of the different precipitation agents.

ratio Na_2CO_3 : NaOH	c(NaOH) in mol/L	$c(Na_2CO_3)$ in mol/L	c(NaOH) in g/L	$c(Na_2CO_3)$ in g/L
1 : 1	1.25	1.25	50.00	132.49
1 : 2	0.83	1.66	66.64	88.29
1 : 4	2.00	0.50	79.99	52.99

For the co-precipitation, 100 mL deionized H_2O was added to an Erlenmeyer flask. The nitrate solution is pumped with a peristaltic pump into the flask within 20 min and it is stirred at 400 rpm. The pH value is controlled by a 906 Titrando titrator by *Metrohm* which adds continuously the precipitation agent. After the co-precipitation, the precipitate is aged, washed with deionized water until the residue does not exceed a conductivity of 4 mS m^{-1} (removal of Na^+), dried and calcined. The different synthesis parameters of the Cu/ZrO_2 catalysts are summarized in Table 32 and Table 33. The catalysts were sieved before the catalysis and only the fraction between 100 and 300 µm was used.

Table 32: Precipitation parameters of the 24 randomly selected Cu/ZrO_2 catalysts.

Catalyst	Cu-loading in wt.%	$V_{Cu\text{-}nitrate}$ in mL	$V_{zirkonyl\ nitrate}$ in mL	Prec. agent	$T_{Precipit.}$ in °C	Flask	pH-value
Cat 1	55	21.640	9.460	1:1	75	barriers	8
Cat 2	25	9.835	15.770	1:4	75	standard	8
Cat 3	40	15.735	12.615	1:2	50	standard	6.5
Cat 4	55	21.640	9.460	1:2	25	standard	8
Cat 5	55	21.640	9.460	1:4	25	standard	8

Cat 6	40	15.735	12.615	1:2	75	barriers	8
Cat 7	55	21.640	9.460	1:2	25	barriers	8
Cat 8	55	21.640	9.460	1:4	25	standard	8
Cat 9	55	21.640	9.460	1:2	50	barriers	8
Cat 10	25	9.835	15.770	1:4	75	barriers	6.5
Cat 11	40	15.735	12.615	1:1	25	standard	6.5
Cat 12	25	9.835	15.770	1:4	25	barriers	8
Cat 13	55	21.640	9.460	1:4	50	standard	6.5
Cat 14	40	15.735	12.615	1:4	50	standard	6.5
Cat 15	40	15.735	12.615	1:4	75	standard	8
Cat 16	55	21.640	9.460	NH_3	25	barriers	6.5
Cat 16.2	55	21.640	9.460	1:2	25	barriers	6.5
Cat 17	55	21.640	9.460	1:1	75	standard	8
Cat 18	25	9.835	15.770	1:1	50	standard	8
Cat 19	25	9.835	15.770	1:1	50	standard	6.5
Cat 20	40	15.735	12.615	1:1	50	barriers	6.5
Cat 21	55	21.640	9.460	1:1	75	standard	8
Cat 22	40	15.735	12.615	1:1	50	standard	8
Cat 23	40	15.735	12.615	1:2	50	standard	6.5
Cat 24	25	9.835	15.770	1:2	75	barriers	8

Table 33: Ageing, drying and calcination parameters of the 24 randomly selected Cu/ZrO_2 catalysts.

catalyst	T_{ageing} in °C	T_{ageing} in h	T_{drying} in °C	$T_{calcination}$ in °C	$T_{calcinatio}$ in h	$Rate_{heating}$ in K/min
Cat 1	75	4	120	500	6	2.5
Cat 2	50	4	80	350	2	5
Cat 3	75	0	120	350	6	2.5
Cat 4	25	4	80	350	6	5
Cat 5	25	0	80	500	2	5
Cat 6	75	4	80	425	2	5
Cat 7	75	0	120	500	4	2.5
Cat 8	25	2	80	350	2	5
Cat 9	75	4	80	500	6	2.5
Cat 10	50	4	80	350	6	5
Cat 11	75	4	80	350	2	5

Cat 12	75	2	80	500	2	2.5
Cat 13	75	0	80	350	6	5
Cat 14	25	0	120	425	2	2.5
Cat 15	25	0	120	500	2	5
Cat 16	50	0	120	500	2	2.5
Cat 16.2	50	0	120	500	2	2.5
Cat 17	50	0	120	425	2	5
Cat 18	75	4	120	350	4	2.5
Cat 19	25	0	80	425	6	2.5
Cat 20	75	0	120	425	4	2.5
Cat 21	25	2	80	425	2	5
Cat 22	50	0	120	350	6	5
Cat 23	25	4	120	500	6	5
Cat 24	50	0	80	425	6	2.5

Synthesis of different promoted Cu/ZrO_2 catalysts

Synthesis by co-precipitation

For co-precipitation only metal nitrates were used as precursor materials. Titration curves were measured to determine the pH value for the precipitation procedures. The titration curves are shown in Figure 112. The titration curves are measured with 0.1M nitrate solutions at room temperature using a 906 Titrando titrator by *Metrohm* by adding a 0.1M NaOH solution.

Like for the synthesis of different Cu/ZrO_2 catalysts, a 1.0M stock solution containing Cu nitrate (120.8 g) and zirconyl nitrate (171.1 g) was prepared. The metal nitrate of the promoting metal was added. The precipitation parameters are similar to that of Cat8. A Na_2CO_3 : NaOH 1:4 solution was used as precipitation agent. First, 100 mL deionized H_2O was added to an Erlenmeyer flask (without barriers). The nitrate solution is pumped with a peristaltic pump into the flask within 20 min and it is stirred at 400 rpm. The pH value is controlled by a 906 Titrando titrator by *Metrohm* which adds continuously the precipitation agent and the precipitation takes place at 25 °C. After the co-precipitation, the precipitate was directly washed with deionized water until the residue does not exceed a conductivity of 4 mS m^{-1} (removal of Na^+), dried at 80°C overnight and calcined at 400°C (5 K/min) for 2 h. The different loadings, the amounts of the different nitrates, the different volumes as well as the pH values are summarized in Table 34. The following nitrates are used as precursors: $Al(NO_3)_3 \cdot 9H_2O$, $Zn(NO_3)_2 \cdot 6H_2O$, $Ag(NO_3)$, $Mn(NO_3)_2 \cdot 4H_2O$, $Fe(NO_3)_3 \cdot 9H_2O$, $Ce(NO_3)_3 \cdot 6H_2O$, $In(NO_3)_3 \cdot xH_2O$, $Ni(NO_3)_2 \cdot 6H_2O$, $Cd(NO_3)_2 \cdot 4H_2O$, $Cr(NO_3)_3 \cdot 9H_2O$, $Sm(NO_3)_3 \cdot 6H_2O$, $Ga(NO_3)_3 \cdot xH_2O$, $Bi(NO_3)_3$ (Bi_2O_3 dissolved in HNO_3).

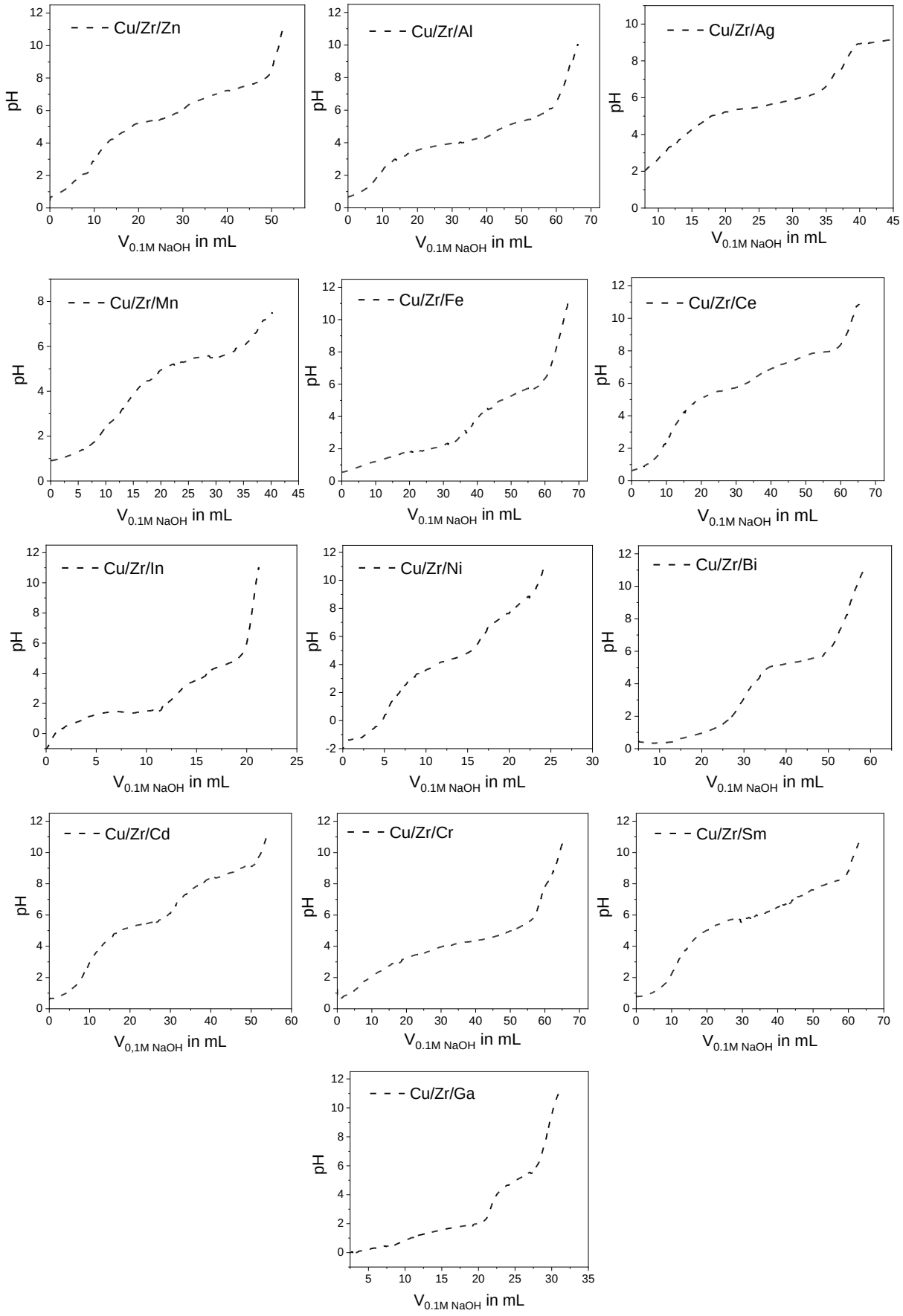

Figure 112: Titration curves of a 0.1 M solutions containing zirconyl nitrate, Cu nitrate and the corresponding promotor precursor. The titration was carried out at room temperature using a 0.1 M solution of NaOH.

The catalysts were sieved before the catalysis and only the fraction between 100 and 300 µm was used.

Table 34: Different promotor metals which are added to the Cu/ZrO_2 system during the co-precipitation procedure. 10 and 20 wt.% of the promoting metal was added. The amount of the promoting nitrate precursor ($m_{nitrate}$), the total volume of water (V_{H2O}), the volume of the zirconyl solution ($V_{Zr\text{-}sol}$), the volume of the Cu solution ($V_{Cu\text{-}sol}$) as well as the pH-value obtained by the titration curves (Figure 112).

promoting metal	loading in wt.%	$m_{nitrate}$ in g	V_{H2O} in mL	$V_{Zr\text{-}sol}$ in mL	$V_{Cu\text{-}sol}$ in mL	pH-value
Zn	10	1.3650	4.590	8.520	25.965	8
Zn	20	2.7299	9.175	6.085	25.965	8
Al	10	4.1712	11.120	8.520	25.965	7
Al	20	8.3424	22.240	6.085	25.965	7
Ag	10	0.4725	2.780	8.520	25.965	6.5
Ag	20	0.9449	5.560	6.085	25.965	6.5
Mn	10	1.3706	5.460	8.520	25.965	6
Mn	20	2.7413	10.920	6.085	25.965	6
Fe	10	2.1698	5.370	8.520	25.965	6.5
Fe	20	4.3397	10.745	6.085	25.965	6.5
Ce	10	0.9297	2.140	8.520	25.965	8.5
Ce	20	1.8593	4.280	6.085	25.965	8.5
In	10	1.0214	2.615	8.520	25.965	6.5
In	20	2.0428	5.225	6.085	25.965	6.5
Ni	10	1.4864	5.110	8.520	25.965	8.5
Ni	20	2.9728	10.225	6.085	25.965	8.5
Bi	10	0.6689	1.435	8.520	25.965	6.5
Bi	20	1.3378	2.870	6.085	25.965	6.5
Cd	10	0.8233	2.670	8.520	25.965	9
Cd	20	1.6465	5.340	6.085	25.965	9
Cr	10	2.3087	5.770	8.520	25.965	8
Cr	20	4.6175	11.540	6.085	25.965	8
Sm	10	0.8868	1.995	8.520	25.965	8.5
Sm	20	1.7736	3.990	6.085	25.965	8.5
Ga	10	1.1004	4.305	8.520	25.965	6
Ga	20	2.2008	8.605	6.085	25.965	6

Synthesis by impregnation of the Cu/Zr precipitate

For the impregnation of the Cu/Zr precipitate the promotor is added to the catalysts during the last washing step. Therefore, a standard Cu/Zr precursor was co-precipitated using a similar procedure than that of Cat8. Like for the synthesis of different Cu/ZrO_2 catalysts, a 1.0M stock solution containing Cu nitrate (120.8 g) and zirconyl nitrate (171.1 g) was prepared. A Na_2CO_3:NaOH 1:4 solution was used as precipitation agent. First, 100 mL deionized H_2O was added to an Erlenmeyer flask (without barriers). The nitrate solution is pumped with a peristaltic pump into the flask within 120 min and it is stirred at 400 rpm. The pH value (pH =8) is controlled by a 906 Titrando titrator by *Metrohm* which adds continuously the precipitation agent. The precipitation takes place at 25 °C. After the co-precipitation, the precipitate was directly washed with deionized water until the residue does not exceed a conductivity of 4 mS m^{-1} (removal of Na^+).

Table 35: Different promotor metals which are added to the Cu/ZrO_2 system during the washing by impregnation. 5 and 15 wt.% of the promoting metal was added. The amount of the promoting precursor ($m_{precursor}$) and the amount of precipitate (m_{prec}).

promoting metal	loading in wt.%	$m_{precursor}$ in g	m_{prec} in g
Mg	5	4.7097	14.79
Mg	15	14.1290	14.79
Ba	5	0.8496	14.79
Ba	15	2.5487	14.79
Ca	5	2.6305	14.79
Ca	15	7.8914	14.79
K	5	1.5780	14.79
K	15	4.7341	14.79
Sr	5	1.0783	14.79
Sr	15	3.2348	14.79
Na	5	2.0582	15.33
Na	15	6.1745	15.33
B	5	2.5532	15.33
B	15	7.6596	15.33
Cs	5	1.0944	15.33
Cs	15	3.2833	15.33
Rb	5	0.6816	15.33
Rb	15	2.0448	15.33
Li	5	4.7524	15.33

The precipitate is divided into several portions. In pre-experiments a catalyst mass of 5:1 compared to before and after drying was determined. Hence, around 80% of the precipitate correspond to water. Based on this value the amounts of the promotor precursors could be calculated which are impregnated during one washing step. The volume for the impregnation is 50 mL. For the impregnation/washing step one part of the Cu/Zr precipitate and 50 mL of the promoting metal solution was added into an Erlenmeyer flask. Then the precipitate is filtrated. After that the precipitate is dried at 80 °C overnight and subsequently calcined at 400°C (5 K/min) for 2 h. The different amount of promoting metal precursors, the amount of Cu/Zr precipitate as well as the different Cu loadings are summarized in Table 35.
The following metal precursors were used: $Mg(NO_3)_2 \cdot 6H_2O$, $Ba(NO_3)_2$, $Ca(NO_3)_2 \cdot 4H_2O$, K_2CO_3, $Sr(NO_3)_2$, Na_2CO_3, H_3BO_3, Cs_2CO_3, CHO_2Rb, Li_2CO_3.
The catalysts were sieved before the catalysis and only the fraction between 100 and 300 µm was used.

CO_2 hydrogenation to methanol

Parallel testing unit (PTU)

First the 12 reactors were filled with quartz wool and 200 mg white corundum and 800 mg catalysts were added before quartz wool was put on the catalysts bed again. Then the reactors were installed into the PTU and the reductive pretreatment was started. The reduction takes place at 2 bar and at 300°C for the pure Cu/ZrO_2 catalysts and at 400°C for the different promoted Cu/ZrO_2 catalysts. The heating rate is 2.5 K/min. The total gas flow is 40 mL/min (25% H_2 in N_2). The reduction parameters after achieving the reduction temperature are summarized in Table 36.

Table 36: Reduction parameter after achieving the reduction temperature.

time in min	temperature in °C	$\dot{V}(N_2)$ in mL/min	$\dot{V}(H_2)$ in mL/min
60	300/400	20	20
30	300/400	10	30
30	300/400	0	40

The catalytic reaction was started after cooling down to 275 °C. The catalytic reaction was carried out at 10 bar, a total gas flow of 40 mL/min (25% CO_2 in H_2). The temperature program was measured in decreasing order (275°C, 250°C, 225°C, 200°C). Each temperature was measured for 8 h. The product analysis was done with a *Siemens Maximum Edition I* process

gas chromatograph. The GC works at 110°C and isothermal conditions. One analysis takes 5 min. The PTU setup is shown in Figure 113.

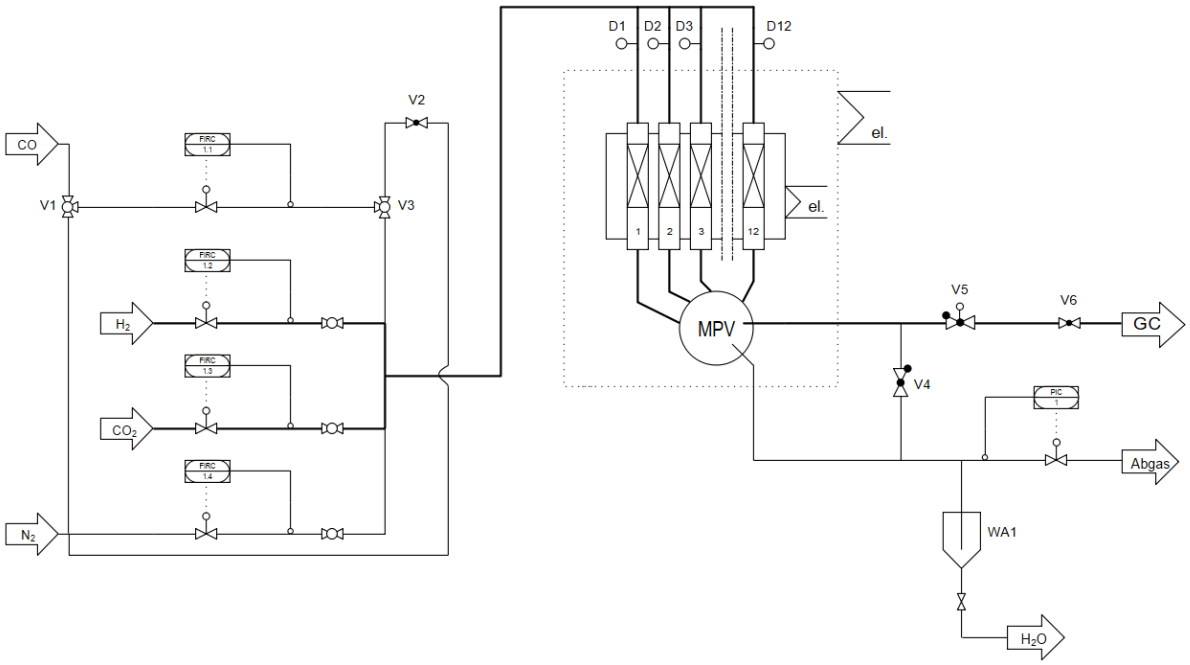

Figure 113: Flow chart of the parallel testing unit (PTU).

Single testing unit (STU)

The reaction setup is shown in Figure 111. The catalyst (150 mg) is placed in an U-shaped reactor. Before the catalytic reaction the catalysts are pretreated at 300°C for pure Cu/ZrO2 catalysts or at 400°C for promoted Cu/ZrO_2 catalysts (heating rate: 2.5 K/min) in H_2 with a total gas flow of 40 mL/min. The reduction procedure after achieving the reduction temperature of 300°C or 400°C is summarized in Table 37. The catalytic reaction is carried out at 10 bar and at 6 temperature steps measured in increasing order: 175°C, 200°C, 225°C, 250°C, 275°C, 300°C. The heating rate between the steps is 2.5 K/min and the holding time is 2 h for each step. The CO_2/H_2 ratio is 1/3 with a GHSV of 8000 h^{-1}.

Table 37: Reduction parameter after achieving the reduction temperature.

Time in min	Temperature in °C	$\dot{V}$(He) in mL/min	$\dot{V}(H_2)$ in mL/min	He-MFC in %	H_2-MFC in %
60	300	32	8	23,5	2,1
30	300	20	20	13,7	12,2
30	300	0	40	0	29,0

The product feed composition is determined by online gas chromatography with a *Perkin Elmer Clarus 590 GC* equipped with thermal conductivity detector (TCD). An empty reactor was measured under the same catalytic conditions to exclude effects caused by the reactor itself. The calculation of the CO_2 conversions, the yields and selectivity are shown in section 0. The interpolation of the temperature of 5 % CO_2 conversion and the corresponding methanol selectivity is described in section 0 as well.

Parameter study using a Cu/ZrO_2 catalyst and the single testing unit (STU)

The preparation of the reactor as well as the reduction procedure is described in section 0. After that the catalytic reaction starts. The temperature program of the hysteresis measurements is summarized in Table 38.

Table 38: Temperature program of the hysteresis measurements.

heating rate in K/min	1	-	1	-	1	-	1	-
time in min	10	320	25	320	25	320	25	320
temperature in °C	200	200	225	225	250	250	275	275

heating rate in K/min	-	-	1	-	1	-	1	-
time in min	25	320	25	320	25	320	25	320
temperature in °C	275	275	250	250	225	225	200	200

Within the 320 min hold time, the total gas flow, as well as the H_2:CO_2 ratio was varied as it is summarized in Table 39.

Table 39: Parameter variation within the 320 min hold time of each temperature step.

ratio H_2:CO_2	$\dot{V}_{Gesamt}$ in mL/min	$\dot{V}(H_2)$ in mL/min	$\dot{V}(CO_2)$ in mL/min	H_2-MFC in %	CO_2-MFC in %
3:1	20	15	5	8.4	26.1
3:1	30	22.5	7.5	14.25	32.54
4:1	20	16	4	8,8	18
4:1	30	24	6	15.5	26.3

The calculation of the CO_2 conversions, the yields and selectivity are shown in section 0. The interpolation of the temperature of 5 % CO_2 conversion and the corresponding methanol selectivity is described in section 0 as well.

Evaluation applying Design of Experiment (DoE)

Calculation of the effects (E):

$$E = \frac{< A, r >}{n}$$

$< A, r >$ = Sum of the products obtained from the variable matrix and the result matrix
n = number of experiments (8)

Calculation of the sum of the squares (Q(E)):

$$Q(E) = n\,E^2$$

n = number of experiments
E = effect

Characterization of the different Cu/ZrO_2 catalysts
All characterization methods are described in section 7.2.

8

Literature

[1] N. Wiberg, A. F. Holleman, *Lehrbuch der Anorganischen Chemie, Vol. 102*, de Gruyter & Co, Berlin, **2007**.

[2] Z. Chen, T. J. Meyer, *Angewandte Chemie International Edition* **2013**, *52*, 700-703.

[3] F. C. Buciuman, F. Patcas, T. Hahn, *Chemical Engineering and Processing: Process Intensification* **1999**, *38*, 563-569.

[4] S. Paria, O. Reiser, *ChemCatChem* **2014**, *6*, 2477-2483.

[5] G. Evano, N. Blanchard, M. Toumi, *Chemical Reviews* **2008**, *108*, 3054-3131.

[6] X. Jiang, X. Nie, X. Guo, C. Song, J. G. Chen, *Chemical Reviews* **2020**, *120*, 7984-8034.

[7] K. C. Waugh, *Catalysis Letters* **2012**, *142*, 1153-1166.

[8] W. Reppe, *Justus Liebigs Annalen der Chemie* **1955**, *596*, 6-11.

[9] W. Reppe, *Justus Liebigs Annalen der Chemie* **1955**, *596*, 25-38.

[10] W. Reppe, *Justus Liebigs Annalen der Chemie* **1955**, *596*, 1-4.

[11] R. J. Madon, P. Nagel, K. Lee, D. S. Thakur, WO 2017035133A1, **2017**

[12] R. Madon, P. Nagel, S. Hedrick, D. Thakur, US 9006129B2, **2015**

[13] R. Madon, P. Nagel, S. Hedrick, D. Thakur, US 9308522B2, **2016**

[14] F. Studt, M. Behrens, E. L. Kunkes, N. Thomas, S. Zander, A. Tarasov, J. Schumann, E. Frei, J. B. Varley, F. Abild-Pedersen, J. K. Nørskov, R. Schlögl, *ChemCatChem* **2015**, *7*, 1105-1111.

[15] M. Behrens, F. Studt, I. Kasatkin, S. Kühl, M. Hävecker, F. Abild-Pedersen, S. Zander, F. Girgsdies, P. Kurr, B.-L. Kniep, M. Tovar, R. W. Fischer, J. K. Nørskov, R. Schlögl, *Science* **2012**, *336*, 893-897.

[16] P. Pässler, W. Hefner, K. Buckl, H. Meinass, A. Meiswinkel, H.-J. Wernicke, G. Ebersberg, R. Müller, J. Bässler, H. Behringer, D. Mayer, in *Ullmann's Encyclopedia of Industrial Chemistry*, Wiley-VCH Verlag GmbH & Co. KGaA, **2000**.

[17] P. e. a. Pässler, *Ullmann's Encyclopedia of Industrial Chemistry*, Wiley-VCH Verlag GmbH & Co. KGaA, Weinheim, **2012**.

[18] B. P. Company, in *Statistical Review of World Energy, Vol. 68th ed*, British Petroleum Company, London, **2019**.

[19] H. Schobert, *Chemical Reviews* **2014**, *114*, 1743-1760.

[20] I.-T. Trotuş, T. Zimmermann, F. Schüth, *Chem. Rev.* **2014**, *114*, 1761-1782.

[21] E. V. Hort, P. Taylor, in *Kirk-Othmer Encyclopedia of Chemical Technology*, John Wiley & Sons, Inc., **2000**.

[22] W. Reppe, *Justus Liebigs Annalen der Chemie* **1955**, *596*, 12-25.

[23] W. Reppe, *Justus Liebigs Annalen der Chemie* **1955**, *596*, 38-79.

[24] W. Reppe, *Justus Liebigs Annalen der Chemie* **1955**, *596*, 80-158.

[25] W. Reppe, *Justus Liebigs Annalen der Chemie* **1955**, *596*, 158-224.

[26] W. Reppe, *Justus Liebigs Annalen der Chemie* **1953**, *582*, 1-37.

[27] E. H. W. Reppe, *Chemie Ingenieur Technik* **1950**, *22*, 273-283.

[28] W. Reppe, *Chemie Ingenieur Technik* **1950**, *22*, 437-442.

[29] W. Reppe, *Chemie Ingenieur Technik* **1950**, *22*, 527-539.

[30] W. Reppe, *Chemie Ingenieur Technik* **1950**, *22*, 361-373.

[31] W. Reppe, *Justus Liebigs Annalen der Chemie* **1956**, *601*, 81-138.

[32] M. Irgang, V. Menger, P. Stops, F. Graf, US 5714644, **1991**

[33] H. Gräfje, W. Körnig, H.-M. Weitz, W. Reiß, G. Steffan, H. Diehl, H. Bosche, K. Schneider, H. Kieczka, in *Ullmann's Encyclopedia of Industrial Chemistry*, Wiley-VCH Verlag GmbH & Co. KGaA, **2000**.

[34] A. M. Stock, US 4149004, **1979**

[35] O. F. Hecht, US 2768215, **1956**

[36] H. Eugene, US 3920756, **1975**

[37] W. Reiss, H. I. Joschek, R. Schnur, S. Winderl, J. Dehler, H. Hoffmann, US 4093688, **1978**

[38] W. Reiss, S. Winderl, W. Schroeder, H. Hoffmann, US 4067914, **1978**

[39] F. Codignola, G. Vergini, P. Gronchi, P. Centola, US 4288641, **1981**

[40] B. S. Shinde, A. M. Sathe, WO 2010119448A1, **2010**

[41] A. Böttcher, J. Henkelmann, T. Preiss, M. Brunner, US 6350714B1, **2002**

[42] A. M. Stock, J. D. Verbsky, US 4294997, **1981**

[43] P. L. Ellinger, US 2939844, **1960**

[44] L. T. Edward, W. J. Frederic, US 2439765, **1948**

[45] S. Koritala, US 4174300, **1979**

[46] F. J. Broecker, W. Reiss, K. Baer, S. Winderl, W. Schroeder, H. Hoffmann, US 3954669, **1976**

[47] J. M. Fremont, US 4143231, **1979**

[48] J. M. Fremont, US 4107082, **1978**

[49] J. M. Fremont, US 4110249, **1978**

[50] J. M. Fremont, US 4584418, **1986**

[51] J. M. Fremont, US 4127734, **1978**

[52] H. J. Wölk, DE 102009010158A1, **2010**

[53] R. J. Baptista, A. S. Travis, *History and Technology* **2006**, *22*, 187-224.

[54] W. Reppe, A. Steinhofer, H. Spaenig, K. Locker, DE 740514C, **1943**

[55] W. Reppe, E. Keyssner, DE 725326C, **1942**

[56] A. Steinhofer, H. Spaenig, K. Locker, W. Reppe, US 2300969, **1942**

[57] F. Wiessner, US 5444169, **1995**

[58] E. V. Hort, US 4002694, **1977**

[59] D. J. Zak, US 4085151, **1978**

[60] J. L. Prater, R. L. Hedworth, US 4117248, **1978**

[61] M. Clyde, F. Frederick, F. D. Leask, US 2712560, **1955**

[62] J. R. Kirchner, US 3650985, **1972**

[63] J. R. Kirchner, US 3560576, **1971**

[64] F. E. Hecht, M. E. Chiddix, US 3294849, **1966**

[65] T. Haas, B. Jaeger, R. Weber, S. F. Mitchell, C. F. King, *Applied Catalysis A: General* **2005**, *280*, 83-88.

[66] J. Gao, G. Yang, H. Li, M. Dong, Z. Wang, Z. Li, *Processes* **2019**, *7*, 198.

[67] R. Matyáš, J. Pachman, in *Primary Explosives*, Springer Berlin Heidelberg, Berlin, Heidelberg, **2013**, pp. 303-324.

[68] G. P. Moss, P. A. S. Smith, D. Tavernier, *Pure and Applied Chemistry* **1995**, *67*, 1307.

[69] A. M. Sladkov, L. Y. Ukhin, *Russian Chemical Reviews* **1968**, *37*, 748-763.

[70] G. Hübner, G. Rauhut, H. Stoll, E. Roduner, *The Journal of Physical Chemistry B* **2003**, *107*, 8568-8573.

[71] V. F. Brameld, M. T. Clark, A. P. Seyfang, *Journal of the Society of Chemical Industry* **1947**, *66*, 346-353.

[72] D. Blake, G. Calvin, G. Coates, *Proceedings of the Chemical Society of London* **1959**, 396-397.

[73] U. Létinois-Halbes, P. Pale, S. Berger, *The Journal of Organic Chemistry* **2005**, *70*, 9185-9190.

[74] H. Lang, A. Jakob, B. Milde, *Organometallics* **2012**, *31*, 7661-7693.

[75] I. A. Garbuzova, I. R. Gol'ding, A. N. Schegolikhin, *Journal of Raman Spectroscopy* **1995**, *26*, 391-395.

[76] S. S. Y. Chui, M. F. Y. Ng, C.-M. Che, *Chemistry – A European Journal* **2005**, *11*, 1739-1749.

[77] F. Cataldo, *Journal of Raman Spectroscopy* **2008**, *39*, 169-176.

[78] F. Cataldo, *Polymer International* **1999**, *48*, 15-22.

[79] K. Judai, J. Nishijo, N. Nishi, *Advanced Materials* **2006**, *18*, 2842-2846.

[80] U. Ruschewitz, R. Pöttgen, *Zeitschrift für anorganische und allgemeine Chemie* **1999**, *625*, 1599-1603.

[81] F. Cataldo, *European Journal of Solid State and Inorganic Chemistry* **1998**, *35*, 281-291.

[82] G. Reuss, W. Disteldorf, A. O. Gamer, A. Hilt, in *Ullmann's Encyclopedia of Industrial Chemistry*, Wiley-VCH Verlag GmbH & Co. KGaA, **2000**.

[83] H. R. Gerberich, G. C. Seaman, in *Kirk-Othmer Encyclopedia of Chemical Technology*, John Wiley & Sons, Inc., **2000**.

[84] R. Kiyama, J. Osugi, K. Suzuki, *The Review of Physical Chemistry of Japan* **1952**, *22*, 13.

[85] R. Kiyama, J. Osugi, K. Suzuki, *The Review of Physical Chemistry of Japan* **1952**, *22*, 7.

[86] R. Kiyama, J. Osugi, K. Suzuki, Y. Kometani, *The Review of Physical Chemistry of Japan* **1953**, *23*, 9.

[87] K. Suzuki, *The Review of Physical Chemistry of Japan* **1953**, *23*, 10.

[88] K. Suzuki, *The Review of Physical Chemistry of Japan* **1954**, *23*, 7.

[89] S. S. Kale, R. V. Chaudhari, P. A. Ramachandran, *Industrial & Engineering Chemistry Product Research and Development* **1981**, *20*, 309-315.

[90] S. P. Gupte, P. B. Jadkar, R. V. Chaudhari, *Reaction Kinetics and Catalysis Letters* **1984**, *24*, 173-177.

[91] F.-W. Chang, J.-M. Chen, J.-C. Guo, *Chemical Engineering Science* **1992**, *47*, 3793-3800.

[92] J.-J. Chu, K.-T. Li, I. Wang, *Applied Catalysis A: General* **1993**, *97*, 123-132.

[93] H. Li, L. Ban, Z. Wang, P. Meng, Y. Zhang, R. Wu, Y. Zhao, *Nanomaterials* **2019**, *9*, 842.

[94] Z. Wang, L. Ban, P. Meng, H. Li, Y. Zhao, *Nanomaterials* **2019**, *9*, 1038.

[95] Z. Wang, L. Ban, P. Meng, H. Li, Y. Zhao, *Nanomaterials* **2019**, *9*, 1137.

[96] Z. Wang, Z. Niu, Q. Hao, L. Ban, H. Li, Y. Zhao, Z. Jiang, *Catalysts* **2019**, *9*, 35.

[97] G. Yang, Y. Xu, X. Su, Y. Xie, C. Yang, Z. Dong, J. Wang, *Ceramics International* **2014**, *40*, 3969-3973.

[98] G. Yang, Y. Yu, M. U. Tahir, S. Ahmad, X. Su, Y. Xie, J. Wang, *Reaction Kinetics, Mechanisms and Catalysis* **2019**, *127*, 425-436.

[99] E. Geravand, Z. Shariatinia, F. Yaripour, S. Sahebdelfar, *Chemical Engineering Research and Design* **2015**, *96*, 63-77.

[100] P. Scherrer, *Göttinger Nachrichten Math. Phys.* **1918**, *2*, 98.

[101] P. Scherrer, *Bestimmung der inneren Struktur und der Größe von Kolloidteilchen mittels Röntgenstrahlen. In: Kolloidchemie Ein Lehrbuch*, Springer, Berlin/Heidelberg, Germany, **1912**.

[102] B. D. Hall, D. Zanchet, D. Ugarte, *J. Appl. Crystallogr.* **2000**, *33*, 1335.

[103] M. A. R. Miranda, J. M. Sasaki, *Acta Crystallogr., Sect. A: Found. Adv.* **2018**, *74*, 54.

[104] J. I. Langford, A. J. C. Wilson, *J. Appl. Crystallogr.* **1978**, *11*, 102.

[105] Y. Zhan, X. Zhou, B. Fu, Y. Chen, *Journal of Hazardous Materials* **2011**, *187*, 348-354.

[106] V. Massarotti, D. Capsoni, M. Bini, A. Altomare, A. G. G. Moliterni, in *Zeitschrift für Kristallographie - Crystalline Materials, Vol. 213*, **1998**, p. 259.

[107] B. Peacor Donald, in *Zeitschrift für Kristallographie - Crystalline Materials, Vol. 138*, **1973**, p. 274.

[108] D. P. Lapham, J. L. Lapham, *International Journal of Pharmaceutics* **2019**, *568*, 118522.

[109] R. Bardestani, G. S. Patience, S. Kaliaguine, *The Canadian Journal of Chemical Engineering* **2019**, *97*, 2781-2791.

[110] A. Badalyan, P. Pendleton, *Langmuir* **2003**, *19*, 7919-7928.

[111] B. Lafuente, R. T. Downs, H. Yang, N. Stone, in *Highlights in Mineralogical Crystallography*, 2015 ed., W. De Gruyter, Berlin, **2015**, pp. 1-33.

[112] M. N. Ess, H. Bladt, W. Mühlbauer, S. I. Seher, C. Zöllner, S. Lorenz, D. Brüggemann, U. Nieken, N. P. Ivleva, R. Niessner, *Combust. Flame* **2016**, *163*, 157.

[113] V. T. Aleksanyan, I. A. Garbuzova, I. R. Gol'ding, A. M. Sladkov, *Spectrochimica Acta Part A: Molecular Spectroscopy* **1975**, *31*, 517-524.

[114] R. Nast, W. Pfab, *Zeitschrift für anorganische und allgemeine Chemie* **1957**, *292*, 287-292.

[115] R. Klement, E. Ködderman-Gros, *Zeitschrift für anorganische Chemie* **1947**, *254*, 201-216.

[116] F. Cataldo, C. S. Casari, *Journal of Inorganic and Organometallic Polymers and Materials* **2007**, *17*, 641-651.

[117] K. Judai, S. Numao, J. Nishijo, N. Nishi, *J. Mol. Catal. A: Chem.* **2011**, *347*, 28.

[118] B. Kozlevcar, *Croatica Chemica Acta* **2008**, *81*, 369-379.

[119] H. Lumbeck, J. Voitländer, *Journal of Catalysis* **1969**, *13*, 117-122.

[120] K. Shirasuka, H. Yanagida, G. Yamaguchi, Y. Kyokaishi, *Journal of the Ceramic Assocation* **1976**, *84*, 610-613.

[121] P. A. Foster, *Journal of The Electrochemical Society* **1959**, *106*, 971.

[122] R. A. Van Nordstrand, W. P. Hettinger, C. D. Keith, *Nature* **1956**, *177*, 713-714.

[123] R. F. Cooley, J. S. Reed, *Journal of the American Ceramic Society* **1972**, *55*, 395-398.

[124] N. Matubayasi, S. Morooka, M. Nakahara, H. Takahashi, *Journal of Molecular Liquids* **2007**, *134*, 58-63.

[125] S. G. Jadhav, P. D. Vaidya, B. M. Bhanage, J. B. Joshi, *Chemical Engineering Research and Design* **2014**, *92*, 2557-2567.

[126] D. Sheldon, *Johnson Matthey Technol. Rev.* **2017**, *61*.

[127] G. A. Olah, *Angewandte Chemie International Edition* **2013**, *52*, 104-107.

[128] M. D. Porosoff, B. Yan, J. G. Chen, *Energy & Environmental Science* **2016**, *9*, 62-73.

[129] J. Nakamura, Y. Choi, T. Fujitani, *Topics in Catalysis* **2003**, *22*, 277-285.

[130] L. C. Grabow, M. Mavrikakis, *ACS Catalysis* **2011**, *1*, 365-384.

[131] S. Kuld, C. Conradsen, P. G. Moses, I. Chorkendorff, J. Sehested, *Angewandte Chemie International Edition* **2014**, *53*, 5941-5945.

[132] T. Lunkenbein, J. Schumann, M. Behrens, R. Schlögl, M. G. Willinger, *Angewandte Chemie International Edition* **2015**, *54*, 4544-4548.

[133] I. Kasatkin, P. Kurr, B. Kniep, A. Trunschke, R. Schlögl, *Angewandte Chemie International Edition* **2007**, *46*, 7324-7327.

[134] S. Kuld, M. Thorhauge, H. Falsig, C. F. Elkjær, S. Helveg, I. Chorkendorff, J. Sehested, *Science* **2016**, *352*, 969-974.

[135] S. Kattel, P. J. Ramírez, J. G. Chen, J. A. Rodriguez, P. Liu, *Science* **2017**, *355*, 1296-1299.

[136] R. van den Berg, G. Prieto, G. Korpershoek, L. I. van der Wal, A. J. van Bunningen, S. Lægsgaard-Jørgensen, P. E. de Jongh, K. P. de Jong, *Nature Communications* **2016**, *7*, 13057.

[137] M. Behrens, *Angewandte Chemie International Edition* **2016**, *55*, 14906-14908.

[138] O. Martin, C. Mondelli, A. Cervellino, D. Ferri, D. Curulla-Ferré, J. Pérez-Ramírez, *Angewandte Chemie International Edition* **2016**, *55*, 11031-11036.

[139] L. Martínez-Suárez, N. Siemer, J. Frenzel, D. Marx, *ACS Catalysis* **2015**, *5*, 4201-4218.

[140] C. Baltes, S. Vukojević, F. Schüth, *Journal of Catalysis* **2008**, *258*, 334-344.

[141] M. Behrens, A. Furche, I. Kasatkin, A. Trunschke, W. Busser, M. Muhler, B. Kniep, R. Fischer, R. Schlögl, *ChemCatChem* **2010**, *2*, 816-818.

[142] M. S. Spencer, *Catalysis Letters* **1998**, *50*, 37-40.

[143] J. Ott, V. Gronemann, F. Pontzen, E. Fiedler, G. Grossmann, B. Kersebohm, G. Weiss, C. Witte, in *Ullmann's Encyclopedia of Industrial Chemistry*, **2012**, p. 27.

[144] I. Nakamura, H. Nakano, T. Fujitani, T. Uchijima, J. Nakamura, *Surface Science* **1998**, *402-404*, 92-95.

[145] H. Nishimura, T. Yatsu, T. Fujitani, T. Uchijima, J. Nakamura, *Journal of Molecular Catalysis A: Chemical* **2000**, *155*, 3-11.

[146] T. Fujitani, Y. Choi, M. Sano, Y. Kushida, J. Nakamura, *The Journal of Physical Chemistry B* **2000**, *104*, 1235-1240.

[147] T. Yatsu, H. Nishimura, T. Fujitani, J. Nakamura, *Journal of Catalysis* **2000**, *191*, 423-429.

[148] K. M. V. Bussche, G. F. Froment, *Applied Catalysis A: General* **1994**, *112*, 37-55.

[149] A. Ludviksson, R. Zhang, C. T. Campbell, K. Griffiths, *Surface Science* **1994**, *313*, 64-82.

[150] Y. Yang, J. Evans, J. A. Rodriguez, M. G. White, P. Liu, *Physical Chemistry Chemical Physics* **2010**, *12*, 9909-9917.

[151] E. L. Kunkes, F. Studt, F. Abild-Pedersen, R. Schlögl, M. Behrens, *Journal of Catalysis* **2015**, *328*, 43-48.

[152] M. E. Fakley, J. R. Jennings, M. S. Spencer, *Journal of Catalysis* **1989**, *118*, 483-486.

[153] S. Fujita, M. Usui, H. Ito, N. Takezawa, *Journal of Catalysis* **1995**, *157*, 403-413.

[154] Y. Morikawa, K. Iwata, K. Terakura, *Applied Surface Science* **2001**, *169-170*, 11-15.

[155] J. Nakamura, I. Nakamura, T. Uchijima, T. Watanabe, T. Fujitani, *Studies in Surface Science and Catalysis* **1996**, *101*, 1389-1399.

[156] W. J. van Rensburg, M. A. Petersen, M. S. Datt, J.-A. van den Berg, P. van Helden, *Catalysis Letters* **2015**, *145*, 559-568.

[157] Y. Yang, C. A. Mims, D. H. Mei, C. H. F. Peden, C. T. Campbell, *Journal of Catalysis* **2013**, *298*, 10-17.

[158] G. C. Chinchen, P. J. Denny, D. G. Parker, M. S. Spencer, D. A. Whan, *Applied Catalysis* **1987**, *30*, 333-338.

[159] K. C. Waugh, *Catalysis Today* **1992**, *15*, 51-75.

[160] M. Muhler, E. Törnqvist, L. P. Nielsen, B. S. Clausen, H. Topsøe, *Catalysis Letters* **1994**, *25*, 1-10.

[161] J. Yoshihara, C. T. Campbell, *Journal of Catalysis* **1996**, *161*, 776-782.

[162] P. B. Rasmussen, M. Kazuta, I. Chorkendorff, *Surface Science* **1994**, *318*, 267-280.

[163] Y. Kanai, T. Watanabe, T. Fujitani, M. Saito, J. Nakamura, T. Uchijima, *Catalysis Letters* **1994**, *27*, 67-78.

[164] I. Nakamura, T. Fujitani, T. Uchijima, J. Nakamura, *Journal of Vacuum Science & Technology A* **1996**, *14*, 1464-1468.

[165] J. Yoshihara, S. C. Parker, A. Schafer, C. T. Campbell, *Catalysis Letters* **1995**, *31*, 313-324.

[166] P. B. Rasmussen, P. M. Holmblad, T. Askgaard, C. V. Ovesen, P. Stoltze, J. K. Nørskov, I. Chorkendorff, *Catalysis Letters* **1994**, *26*, 373-381.

[167] J. Szanyi, D. W. Goodman, *Catalysis Letters* **1991**, *10*, 383-390.

[168] S. G. Neophytides, A. J. Marchi, G. F. Froment, *Applied Catalysis A: General* **1992**, *86*, 45-64.

[169] J. Nakamura, I. Nakamura, T. Uchijima, Y. Kanai, T. Watanabe, M. Saito, T. Fujitani, *Journal of Catalysis* **1996**, *160*, 65-75.

[170] C. T. Campbell, K. A. Daube, J. M. White, *Surface Science* **1987**, *182*, 458-476.

[171] I. Nakamura, T. Fujitani, T. Uchijima, J. Nakamura, *Surface Science* **1998**, *400*, 387-400.

[172] T. Fujitani, I. Nakamura, T. Uchijima, J. Nakamura, *Surface Science* **1997**, *383*, 285-298.

[173] T. Fujitani, I. Nakamura, S. Ueno, T. Uchijima, J. Nakamura, *Applied Surface Science* **1997**, *121-122*, 583-586.

[174] Y. Choi, K. Futagami, T. Fujitani, J. Nakamura, *Applied Catalysis A: General* **2001**, *208*, 163-167.

[175] G. J. Millar, C. H. Rochester, K. C. Waugh, *Journal of the Chemical Society, Faraday Transactions* **1992**, *88*, 1033-1039.

[176] G. J. Millar, C. H. Rochester, S. Bailey, K. C. Waugh, *Journal of the Chemical Society, Faraday Transactions* **1992**, *88*, 2085-2093.

[177] J. E. Bailie, C. H. Rochester, G. J. Millar, *Catalysis Letters* **1995**, *31*, 333-340.

[178] J. D. Grunwaldt, A. M. Molenbroek, N. Y. Topsøe, H. Topsøe, B. S. Clausen, *Journal of Catalysis* **2000**, *194*, 452-460.

[179] E. K. Poels, D. S. Brands, *Applied Catalysis A: General* **2000**, *191*, 83-96.

[180] M. M. Viitanen, W. P. A. Jansen, R. G. van Welzenis, H. H. Brongersma, D. S. Brands, E. K. Poels, A. Bliek, *The Journal of Physical Chemistry B* **1999**, *103*, 6025-6029.

[181] E. D. Batyrev, J. C. van den Heuvel, J. Beckers, W. P. A. Jansen, H. L. Castricum, *Journal of Catalysis* **2005**, *229*, 136-143.

[182] M. Sano, T. Adaniya, T. Fujitani, J. Nakamura, *The Journal of Physical Chemistry B* **2002**, *106*, 7627-7633.

[183] T. Fujitani, J. Nakamura, *Catalysis Letters* **1998**, *56*, 119-124.

[184] Y. Kanai, T. Watanabe, T. Fujitani, T. Uchijima, J. Nakamura, *Catalysis Letters* **1996**, *38*, 157-163.

[185] T. Van Herwijnen, W. A. De Jong, *Journal of Catalysis* **1974**, *34*, 209-214.

[186] M. S. Spencer, *Topics in Catalysis* **1999**, *8*, 259.

[187] M. S. Spencer, *Surface Science* **1987**, *192*, 329.

[188] M. S. Spencer, *Surface Science* **1987**, *192*, 323-328.

[189] M. S. Spencer, *Surface Science* **1987**, *192*, 336-343.

[190] M. S. Spencer, *Catalysis Letters* **1999**, *60*, 45.

[191] M. B. Fichtl, J. Schumann, I. Kasatkin, N. Jacobsen, M. Behrens, R. Schlögl, M. Muhler, O. Hinrichsen, *Angewandte Chemie International Edition* **2014**, *53*, 7043-7047.

[192] D. Laudenschleger, H. Ruland, M. Muhler, *Nature Communications* **2020**, *11*, 3898.

[193] S. Zander, E. L. Kunkes, M. E. Schuster, J. Schumann, G. Weinberg, D. Teschner, N. Jacobsen, R. Schlögl, M. Behrens, *Angewandte Chemie International Edition* **2013**, *52*, 6536-6540.

[194] R. Naumann d'Alnoncourt, X. Xia, J. Strunk, E. Löffler, O. Hinrichsen, M. Muhler, *Physical Chemistry Chemical Physics* **2006**, *8*, 1525-1538.

[195] R. Naumann d'Alnoncourt, M. Kurtz, H. Wilmer, E. Löffler, V. Hagen, J. Shen, M. Muhler, *Journal of Catalysis* **2003**, *220*, 249-253.

[196] T. S. Askgaard, J. K. Norskov, C. V. Ovesen, P. Stoltze, *Journal of Catalysis* **1995**, *156*, 229-242.

[197] M. Zabilskiy, V. L. Sushkevich, D. Palagin, M. A. Newton, F. Krumeich, J. A. van Bokhoven, *Nature Communications* **2020**, *11*, 2409.

[198] V. Schott, H. Oberhofer, A. Birkner, M. Xu, Y. Wang, M. Muhler, K. Reuter, C. Wöll, *Angewandte Chemie International Edition* **2013**, *52*, 11925-11929.

[199] T. Lunkenbein, F. Girgsdies, T. Kandemir, N. Thomas, M. Behrens, R. Schlögl, E. Frei, *Angewandte Chemie International Edition* **2016**, *55*, 12708-12712.

[200] W. P. A. Jansen, J. Beckers, J. C. v. d. Heuvel, A. W. Denier v. d. Gon, A. Bliek, H. H. Brongersma, *Journal of Catalysis* **2002**, *210*, 229-236.

[201] T. Fujitani, J. Nakamura, *Applied Catalysis A: General* **2000**, *191*, 111-129.

[202] M. M. Günter, T. Ressler, B. Bems, C. Büscher, T. Genger, O. Hinrichsen, M. Muhler, R. Schlögl, *Catalysis Letters* **2001**, *71*, 37-44.

[203] C. V. Ovesen, B. S. Clausen, J. Schiøtz, P. Stoltze, H. Topsøe, J. K. Nørskov, *Journal of Catalysis* **1997**, *168*, 133-142.

[204] K. C. Waugh, *Catalysis Letters* **1999**, *58*, 163-165.

[205] K. Tohji, Y. Udagawa, T. Mizushima, A. Ueno, *The Journal of Physical Chemistry* **1985**, *89*, 5671-5676.

[206] W. X. Pan, R. Cao, D. L. Roberts, G. L. Griffin, *Journal of Catalysis* **1988**, *114*, 440-446.

[207] W. R. A. M. Robinson, J. C. Mol, *Applied Catalysis* **1990**, *60*, 73-86.

[208] R. Burch, S. E. Golunski, M. S. Spencer, *Journal of the Chemical Society, Faraday Transactions* **1990**, *86*, 2683-2691.

[209] O. Martin, J. Pérez-Ramírez, *Catalysis Science & Technology* **2013**, *3*, 3343-3352.

[210] M. Behrens, *Journal of Catalysis* **2009**, *267*, 24-29.

[211] P. L. Hansen, J. B. Wagner, S. Helveg, J. R. Rostrup-Nielsen, B. S. Clausen, H. Topsøe, *Science* **2002**, *295*, 2053-2055.

[212] P. C. K. Vesborg, I. Chorkendorff, I. Knudsen, O. Balmes, J. Nerlov, A. M. Molenbroek, B. S. Clausen, S. Helveg, *Journal of Catalysis* **2009**, *262*, 65-72.

[213] H. Wilmer, T. Genger, O. Hinrichsen, *Journal of Catalysis* **2003**, *215*, 188-198.

[214] R. A. Hadden, B. Sakakini, J. Tabatabaei, K. C. Waugh, *Catalysis Letters* **1997**, *44*, 145-151.

[215] F. Liao, Y. Huang, J. Ge, W. Zheng, K. Tedsree, P. Collier, X. Hong, S. C. Tsang, *Angewandte Chemie International Edition* **2011**, *50*, 2162-2165.

[216] R. Burch, R. J. Chappell, S. E. Golunski, *Journal of the Chemical Society, Faraday Transactions 1: Physical Chemistry in Condensed Phases* **1989**, *85*, 3569-3578.

[217] R. Zhang, A. Ludviksson, C. T. Campbell, *Catalysis Letters* **1994**, *25*, 277-292.

[218] J. C. Frost, *Nature* **1988**, *334*, 577-580.

[219] K. C. Waugh, *Catalysis Letters* **1990**, *7*, 345-349.

[220] K. Klier, V. Chatikavanij, R. G. Herman, G. W. Simmons, *Journal of Catalysis* **1982**, *74*, 343-360.

[221] G. R. Sheffer, T. S. King, *Journal of Catalysis* **1989**, *116*, 488-497.

[222] G. R. Sheffer, T. S. King, *Journal of Catalysis* **1989**, *115*, 376-387.

[223] L. E. Y. Nonneman, V. Ponec, *Catalysis Letters* **1990**, *7*, 213-217.

[224] V. Ponec, *Surface Science* **1992**, *272*, 111-117.

[225] G. C. Chinchen, K. C. Waugh, D. A. Whan, *Applied Catalysis* **1986**, *25*, 101-107.

[226] J. Nakamura, T. Uchijima, Y. Kanai, T. Fujitani, *Catalysis Today* **1996**, *28*, 223-230.

[227] G. C. Chinchen, M. S. Spencer, K. C. Waugh, D. A. Whan, *Journal of the Chemical Society, Faraday Transactions 1: Physical Chemistry in Condensed Phases* **1987**, *83*, 2193-2212.

[228] P.-J. Chu, B. C. Gerstein, G. R. Sheffer, T. S. King, *Journal of Catalysis* **1989**, *115*, 194-204.

[229] M. B. Fichtl, D. Schlereth, N. Jacobsen, I. Kasatkin, J. Schumann, M. Behrens, R. Schlögl, O. Hinrichsen, *Applied Catalysis A: General* **2015**, *502*, 262-270.

[230] M. V. Twigg, M. S. Spencer, *Topics in Catalysis* **2003**, *22*, 191-203.

[231] M. Kurtz, H. Wilmer, T. Genger, O. Hinrichsen, M. Muhler, *Catalysis Letters* **2003**, *86*, 77-80.

[232] D. B. Rasmussen, T. V. W. Janssens, B. Temel, T. Bligaard, B. Hinnemann, S. Helveg, J. Sehested, *Journal of Catalysis* **2012**, *293*, 205-214.

[233] M. Agnelli, J. P. Candy, J. M. Basset, J. P. Bournonville, O. A. Ferretti, *Journal of Catalysis* **1990**, *121*, 236-247.

[234] D. Baudouin, J.-P. Candy, U. Rodemerck, F. Krumeich, L. Veyre, P. B. Webb, C. Thieuleux, C. Copéret, *Catalysis Today* **2014**, *235*, 237-244.

[235] J. P. Candy, O. A. Ferretti, G. Mabilon, J. P. Bournonville, A. El Mansour, J. M. Basset, G. Martino, *Journal of Catalysis* **1988**, *112*, 210-220.

[236] F. Humblot, J. P. Candy, F. Le Peltier, B. Didillon, J. M. Basset, *Journal of Catalysis* **1998**, *179*, 459-468.

[237] F. Humblot, F. Lepeltier, J. P. Candy, J. Corker, O. Clause, F. Bayard, J. M. Basset, *Journal of the American Chemical Society* **1998**, *120*, 137-146.

[238] P. Rouge, A. Garron, S. Norsic, C. Larabi, N. Merle, L. Delevoye, R. M. Gauvin, K. C. Szeto, M. Taoufik, *Molecular Catalysis* **2019**, *471*, 21-26.

[239] G. J. Siri, J. M. Ramallo-López, M. L. Casella, J. L. G. Fierro, F. G. Requejo, O. A. Ferretti, *Applied Catalysis A: General* **2005**, *278*, 239-249.

[240] V. D. Stytsenko, *Applied Catalysis A: General* **1995**, *126*, 1-26.

[241] R. Becker, H. Parala, F. Hipler, O. P. Tkachenko, K. V. Klementiev, W. Grünert, H. Wilmer, O. Hinrichsen, M. Muhler, A. Birkner, C. Wöll, S. Schäfer, R. A. Fischer, *Angewandte Chemie International Edition* **2004**, *43*, 2839-2842.

[242] M. Kurtz, N. Bauer, C. Büscher, H. Wilmer, O. Hinrichsen, R. Becker, S. Rabe, K. Merz, M. Driess, R. A. Fischer, M. Muhler, *Catalysis Letters* **2004**, *92*, 49-52.

[243] J. Hambrock, M. K. Schröter, A. Birkner, C. Wöll, R. A. Fischer, *Chemistry of Materials* **2003**, *15*, 4217-4222.

[244] N. J. Brown, A. García-Trenco, J. Weiner, E. R. White, M. Allinson, Y. Chen, P. P. Wells, E. K. Gibson, K. Hellgardt, M. S. P. Shaffer, C. K. Williams, *ACS Catalysis* **2015**, *5*, 2895-2902.

[245] M. Behrens, B. Kniep, P. Kurr, R. Schlögl, M. Hieke, WO2013072197A1, **2011**

[246] K. P. de Jong, in *Synthesis of Solid Catalysts*, Wiley-VCH Verlag GmbH & Co. KGaA, **2009**, pp. 111-134.

[247] Z. Wang, D. Brouri, S. Casale, L. Delannoy, C. Louis, *Journal of Catalysis* **2016**, *340*, 95-106.

[248] X. Wang, M. Chen, X. Chen, R. Lin, H. Zhu, C. Huang, W. Yang, Y. Tan, S. Wang, Z. Du, Y. Ding, *Journal of Catalysis* **2020**, *383*, 254-263.

[249] H. H. Huang, F. Q. Yan, Y. M. Kek, C. H. Chew, G. Q. Xu, W. Ji, P. S. Oh, S. H. Tang, *Langmuir* **1997**, *13*, 172-175.

[250] M. Lok, in *Synthesis of Solid Catalysts*, Wiley-VCH Verlag GmbH & Co. KGaA, **2009**, pp. 135-151.

[251] S. Rao, T. R. Anantharaman, *Current Science* **1963**, *32*, 262.

[252] S. J. Gentry, P. T. Walsh, *Journal of the Chemical Society, Faraday Transactions 1: Physical Chemistry in Condensed Phases* **1982**, *78*, 1515-1523.

[253] W.-P. Dow, Y.-P. Wang, T.-J. Huang, *Applied Catalysis A: General* **2000**, *190*, 25-34.

[254] G. C. Chinchen, C. M. Hay, H. D. Vandervell, K. C. Waugh, *Journal of Catalysis* **1987**, *103*, 79-86.

[255] O. Hinrichsen, T. Genger, M. Muhler, *Chemical Engineering & Technology* **2000**, *23*, 956-959.

[256] T. Genger, O. Hinrichsen, M. Muhler, *Catalysis Letters* **1999**, *59*, 137-141.

[257] G. Anger, A. Winkler, K. D. Rendulic, *Surface Science* **1989**, *220*, 1-17.

[258] K. C. Waugh, *Solid State Ionics* **2004**, *168*, 327-342.

[259] M. B. Fichtl, Dissertation thesis, Technische Universität München (Munich), **2014**.

[260] F. Zaera, *Surface Science* **1989**, *219*, 453-466.

[261] H. Dumont, A. Marbeuf, J.-E. Bourée, O. Gorochov, *Journal of Materials Chemistry* **1993**, *3*, 1075-1079.

[262] H. Y. Chen, S. P. Lau, L. Chen, J. Lin, C. H. A. Huan, K. L. Tan, J. S. Pan, *Applied Surface Science* **1999**, *152*, 193-199.

[263] J. Coates, in *Encyclopedia of Analytical Chemistry*, John Wiley & Sons Ltd, Chichester, **2006**.

[264] R. J. Herold, S. L. Aggarwal, V. Neff, *Canadian Journal of Chemistry* **1963**, *41*, 1368-1380.

[265] V. Boiadjiev, W. T. Tysoe, *Chemistry of Materials* **1998**, *10*, 1141-1152.

[266] A. Oleinik, V. Dodonov, G. Lysenko, O. Druzhkov, *Russian Chemical Bulletin* **1994**, *43*, 1577-1579.

[267] Z. Liu, A. Rittermeier, M. Becker, K. Kähler, E. Löffler, M. Muhler, *Langmuir* **2011**, *27*, 4728-4733.

[268] F. Boccuzzi, G. Ghiotti, A. Chiorino, *Surface Science* **1985**, *156*, 933-942.

[269] D. L. Roberts, G. L. Griffin, *Journal of Catalysis* **1988**, *110*, 117-126.

[270] G. J. Millar, C. H. Rochester, S. Bailey, K. C. Waugh, *Journal of the Chemical Society, Faraday Transactions* **1993**, *89*, 1109-1115.

[271] G. J. Millar, C. H. Rochester, K. C. Waugh, *Journal of the Chemical Society, Faraday Transactions* **1991**, *87*, 1467-1472.

[272] A. J. Elliott, R. A. Hadden, J. Tabatabaei, K. C. Waugh, F. W. Zemicael, *Journal of Catalysis* **1995**, *157*, 153-161.

[273] N.-Y. Topsøe, H. Topsøe, *Journal of Molecular Catalysis A: Chemical* **1999**, *141*, 95-105.

[274] J. Pritchard, T. Catterick, R. K. Gupta, *Surface Science* **1975**, *53*, 1-20.

[275] E. Frei, A. Gaur, H. Lichtenberg, L. Zwiener, M. Scherzer, F. Girgsdies, T. Lunkenbein, R. Schlögl, *ChemCatChem* **2020**, *12*, 4029-4033.

[276] F. Rascón, R. Wischert, C. Copéret, *Chemical Science* **2011**, *2*, 1449-1456.

[277] H. MCMurdie, M. Morris, E. Evans, B. Paretzkin, W. Wong-Ng, L. Ettlinger, *Powder Diffraction* **1986**, *1*, 76.

[278] H. Noei, C. Wöll, M. Muhler, Y. Wang, *The Journal of Physical Chemistry C* **2011**, *115*, 908-914.

[279] O. Martin, A. J. Martín, C. Mondelli, S. Mitchell, T. F. Segawa, R. Hauert, C. Drouilly, D. Curulla-Ferré, J. Pérez-Ramírez, *Angewandte Chemie International Edition* **2016**, *55*, 6261-6265.

[280] J. Graciani, K. Mudiyanselage, F. Xu, A. E. Baber, J. Evans, S. D. Senanayake, D. J. Stacchiola, P. Liu, J. Hrbek, J. F. Sanz, J. A. Rodriguez, *Science* **2014**, *345*, 546.

[281] F. Studt, I. Sharafutdinov, F. Abild-Pedersen, C. F. Elkjær, J. S. Hummelshøj, S. Dahl, I. Chorkendorff, J. K. Nørskov, *Nature Chemistry* **2014**, *6*, 320-324.

[282] S. E. Collins, J. J. Delgado, C. Mira, J. J. Calvino, S. Bernal, D. L. Chiavassa, M. A. Baltanás, A. L. Bonivardi, *Journal of Catalysis* **2012**, *292*, 90-98.

[283] M. S. Frei, C. Mondelli, A. Cesarini, F. Krumeich, R. Hauert, J. A. Stewart, D. Curulla Ferré, J. Pérez-Ramírez, *ACS Catalysis* **2020**, *10*, 1133-1145.

[284] K. Larmier, W.-C. Liao, S. Tada, E. Lam, R. Verel, A. Bansode, A. Urakawa, A. Comas-Vives, C. Copéret, *Angewandte Chemie International Edition* **2017**, *56*, 2318-2323.

[285] R. A. Koeppel, A. Baiker, A. Wokaun, *Applied Catalysis A: General* **1992**, *84*, 77-102.

[286] S. Tada, F. Watanabe, K. Kiyota, N. Shimoda, R. Hayashi, M. Takahashi, A. Nariyuki, A. Igarashi, S. Satokawa, *Journal of Catalysis* **2017**, *351*, 107-118.

[287] S. Tada, A. Katagiri, K. Kiyota, T. Honma, H. Kamei, A. Nariyuki, S. Uchida, S. Satokawa, *The Journal of Physical Chemistry C* **2018**, *122*, 5430-5442.

[288] S. Tada, S. Kayamori, T. Honma, H. Kamei, A. Nariyuki, K. Kon, T. Toyao, K.-i. Shimizu, S. Satokawa, *ACS Catalysis* **2018**, *8*, 7809-7819.

[289] S. Tada, K. Oshima, Y. Noda, R. Kikuchi, M. Sohmiya, T. Honma, S. Satokawa, *Industrial & Engineering Chemistry Research* **2019**, *58*, 19434-19445.

[290] T. Fujitani, M. Saito, Y. Kanai, T. Kakumoto, T. Watanabe, J. Nakamura, T. Uchijima, *Catalysis Letters* **1994**, *25*, 271-276.

[291] E. Frei, A. Schaadt, T. Ludwig, H. Hillebrecht, I. Krossing, *ChemCatChem* **2014**, *6*, 1721-1730.

[292] I. Ro, Y. Liu, M. R. Ball, D. H. K. Jackson, J. P. Chada, C. Sener, T. F. Kuech, R. J. Madon, G. W. Huber, J. A. Dumesic, *ACS Catalysis* **2016**, *6*, 7040-7050.

[293] J. Liu, J. Shi, D. He, Q. Zhang, X. Wu, Y. Liang, Q. Zhu, *Applied Catalysis A: General* **2001**, *218*, 113-119.

[294] R.-x. Zhou, T.-m. Yu, X.-y. Jiang, F. Chen, X.-m. Zheng, *Applied Surface Science* **1999**, *148*, 263-270.

[295] K. Pokrovski, K. T. Jung, A. T. Bell, *Langmuir* **2001**, *17*, 4297-4303.

[296] L.-C. Wang, Q. Liu, M. Chen, Y.-M. Liu, Y. Cao, He, K.-N. Fan, *The Journal of Physical Chemistry C* **2007**, *111*, 16549-16557.

[297] X. Guo, D. Mao, G. Lu, S. Wang, G. Wu, *Journal of Catalysis* **2010**, *271*, 178-185.

[298] Y. Ma, J. Wang, K. R. Goodman, A. R. Head, X. Tong, D. J. Stacchiola, M. G. White, *The Journal of Physical Chemistry C* **2020**, *124*, 22158-22172.

[299] S. Kattel, B. Yan, Y. Yang, J. G. Chen, P. Liu, *Journal of the American Chemical Society* **2016**, *138*, 12440-12450.

[300] L. Liu, X. Su, H. Zhang, N. Gao, F. Xue, Y. Ma, Z. Jiang, T. Fang, *Applied Surface Science* **2020**, *528*, 146900.

[301] E. S. Borovinskaya, S. Trebbin, F. Alscher, C. Breitkopf, *Catalysts* **2019**, *9*, 1037.

[302] F. C. F. Marcos, L. Lin, L. E. Betancourt, S. D. Senanayake, J. A. Rodriguez, J. M. Assaf, R. Giudici, E. M. Assaf, *Journal of CO2 Utilization* **2020**, *41*, 101215.

[303] S. Ren, X. Fan, Z. Shang, W. R. Shoemaker, L. Ma, T. Wu, S. Li, N. B. Klinghoffer, M. Yu, X. Liang, *Journal of CO2 Utilization* **2020**, *36*, 82-95.

[304] V. L'hospital, L. Angelo, Y. Zimmermann, K. Parkhomenko, A.-C. Roger, *Catalysis Today* **2020**.

[305] I. A. Fisher, H. C. Woo, A. T. Bell, *Catalysis Letters* **1997**, *44*, 11-17.

[306] F. Arena, G. Italiano, K. Barbera, S. Bordiga, G. Bonura, L. Spadaro, F. Frusteri, *Applied Catalysis A: General* **2008**, *350*, 16-23.

[307] Y.-W. Suh, S.-H. Moon, H.-K. Rhee, *Catalysis Today* **2000**, *63*, 447-452.

[308] C. Yang, Z. Ma, N. Zhao, W. Wei, T. Hu, Y. Sun, *Catalysis Today* **2006**, *115*, 222-227.

[309] Y. Zhang, J. Fei, Y. Yu, X. Zheng, *Energy Conversion and Management* **2006**, *47*, 3360-3367.

[310] J. Słoczyński, R. Grabowski, P. Olszewski, A. Kozłowska, J. Stoch, M. Lachowska, J. Skrzypek, *Applied Catalysis A: General* **2006**, *310*, 127-137.

[311] J. Słoczyński, R. Grabowski, A. Kozłowska, P. Olszewski, M. Lachowska, J. Skrzypek, J. Stoch, *Applied Catalysis A: General* **2003**, *249*, 129-138.

[312] X. Guo, D. Mao, G. Lu, S. Wang, G. Wu, *Journal of Molecular Catalysis A: Chemical* **2011**, *345*, 60-68.

[313] T. Phongamwong, U. Chantaprasertporn, T. Witoon, T. Numpilai, Y. Poo-arporn, W. Limphirat, W. Donphai, P. Dittanet, M. Chareonpanich, J. Limtrakul, *Chemical Engineering Journal* **2017**, *316*, 692-703.

[314] A. M. Hengne, A. K. Samal, L. R. Enakonda, M. Harb, L. E. Gevers, D. H. Anjum, M. N. Hedhili, Y. Saih, K.-W. Huang, J.-M. Basset, *ACS Omega* **2018**, *3*, 3688-3701.

[315] G. Wang, D. Mao, X. Guo, J. Yu, *International Journal of Hydrogen Energy* **2019**, *44*, 4197-4207.

[316] W. Wang, Z. Qu, L. Song, Q. Fu, *Journal of Catalysis* **2020**, *382*, 129-140.

[317] P. Duwez, F. Odell, *Journal of the American Ceramic Society* **1950**, *33*, 274-283.

[318] L. Laitao, L. Songjun, D. Gengfeng, L. Fengyi, *Reaction Kinetics and Catalysis Letters* **2002**, *75*, 289-296.

[319] T. Burger, F. Koschany, O. Thomys, K. Köhler, O. Hinrichsen, *Applied Catalysis A: General* **2018**, *558*, 44-54.

[320] C. Zhong, X. Guo, D. Mao, S. Wang, G. Wu, G. Lu, *RSC Advances* **2015**, *5*, 52958-52965.

[321] J. Schumann, T. Lunkenbein, A. Tarasov, N. Thomas, R. Schlögl, M. Behrens, *ChemCatChem* **2014**, *6*, 2889-2897.

9

Appendix

9.1 Additional data

Table 40: Catalysts labels for Figure 80 of the different Cu and Zn loaded catalysts ZnxCuy-$_z$-a (x= Zn loading in wt.%, y = Cu loading in wt.%, z = precipitation method, a = pretreatment temperature before catalysis). The catalysts were pretreated in H_2:He 1:1 in general at 120°C (except it is particularly specified) for 1 h.

Abbreviation	Catalyst number	Description
pureCu10$_{-DP}$	2	deposition precip. with urea without Zn
Zn1Cu10$_{-DP}$	7	deposition precip. with urea with Zn
Zn2Cu10$_{-DP}$	3	deposition precip. with urea with Zn
Zn2Cu10$_{-DP}$-40°C	4	deposition precip. with urea with Zn
Zn2Cu10$_{-DP}$-120°C	5	deposition precip. with urea with Zn
Zn2Cu10$_{-DP}$-200°C	6	deposition precip. with urea with Zn
Zn3Cu10$_{-DP}$	8	deposition precip. with urea with Zn
Zn2.5Cu25$_{-DP}$	9	deposition precip. with urea with Zn
Zn5Cu25$_{-DP}$	10	deposition precip. with urea with Zn
pureCu10$_{-CoPr}$	12	co-precipitation without Zn
Zn0.25Cu10$_{-CoPr}$	17	co-precipitation with Zn
Zn1Cu10$_{-CoPr}$	18	co-precipitation with Zn
Zn2Cu10$_{-CoPr}$	13	co-precipitation with Zn
Zn2Cu10$_{-CoPr}$-40°C	14	co-precipitation with Zn
Zn2Cu10$_{-CoPr}$-120°C	15	co-precipitation with Zn
Zn2Cu10$_{-coPr}$-200°C	16	co-precipitation with Zn
Zn2.5Cu25$_{-CoPr}$	19	co-precipitation with Zn
Zn5Cu25$_{-CoPr}$	20	co-precipitation with Zn
Zn7.5Cu50$_{-CoPr}$	21	co-precipitation with Zn
pureCu10$_{-LR}$	23	deposition precip. via ligand removal without Zn
Zn1Cu10$_{-LR}$	28	deposition precip. via ligand removal with Zn
Zn2Cu10$_{-LR}$	24	deposition precip. via ligand removal with Zn
Zn2Cu10$_{-LR}$-40°C	25	deposition precip. via ligand removal with Zn
Zn2Cu10$_{-LR}$-120°C	26	deposition precip. via ligand removal with Zn
Zn2.5Cu25$_{-LR}$	29	deposition precip. via ligand removal with Zn
Zn5Cu25$_{-LR}$	30	deposition precip. via ligand removal with Zn
Zn1Cu10$_{-RP}$	35	reductive precip. with Zn
Zn2Cu10$_{-RP}$-40°C	32	reductive precip. with Zn
Zn2Cu10$_{-RP}$-120°C	33	reductive precip. with Zn

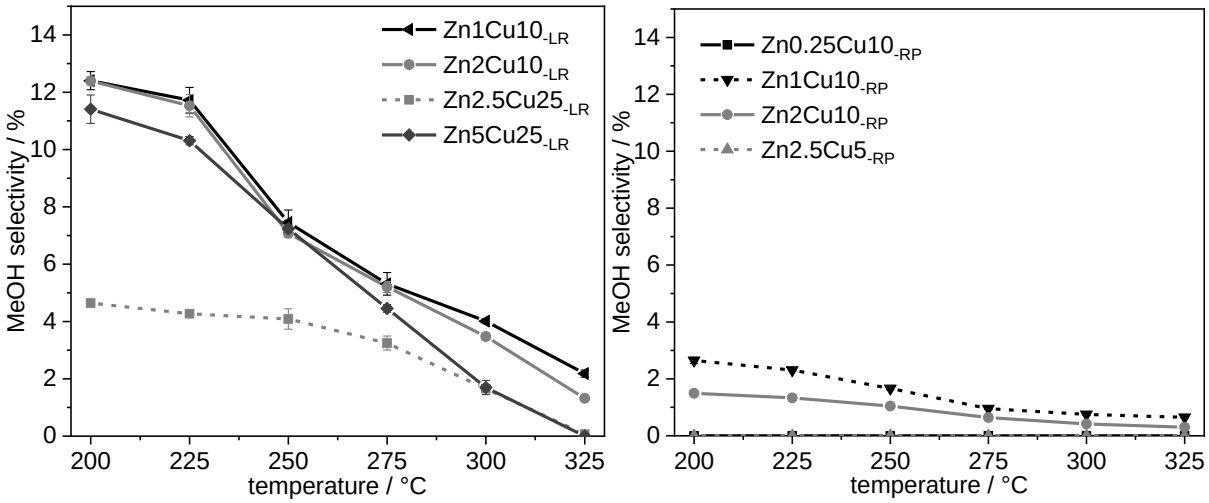

Figure 114: MeOH selectivity at different reaction temperatures (200, 225, 250, 275, 300, 325 °C) at 28 ba rfor the different Cu and Zn loaded catalysts ZnxCuy-$_z$ (x= Zn loading in wt.%, y = Cu loading in wt.%, z = precipitation method). The H_2:CO_2 ratio is 3:1. The GHSV is 8000 h^{-1}. The catalysts were pretreated in H_2:He 1:1 at 120°C for 1 h. The overall reaction time is 14 h 50 min.

9.2 List of Publications

- Walter Reppe Revival – Identification and Genesis of Copper Acetylides Cu_2C_2 as Active Species in Ethynylation Reactions
  Tobias Bruhm, Andrea Abram, Johannes Häusler, Oliver Thomys, Klaus Köhler
  Submitted

- Correlation between the Formation and Properties of the Active Species Cu_2C_2 and the Catalytic Activity of CuO based Ethynylation Catalysts
  Tobias Bruhm, Andrea Abram, Johannes Häusler, Oliver Thomys, Klaus Köhler
  In preparation

- Synthesis of Al_2O_3 Supported bimetallic Zn/Cu Nanoparticles by Surface Organometallic Chemistry as Model Catalysts for Methanol Synthesis from CO_2
  Tobias Bruhm, Manoja K. Samantaray, Walid Al Maksoud, Dalaver. H. Anjum, Tim Kratky, Klaus Köhler, Sebastian Günther, Ulrich Heiz, Jean-Marie Basset
  In preparation

9.3 Conference contributions

- Walter Reppe Revival – the formation of the active species in the ethynylation of formaldehyde to form 1,4-butynediol
  Tobias Bruhm, Oliver Thomys, Andrea Abram, Klaus Köhler
  52. Jahrestreffen Deutscher Katalytiker, Weimar, Germany, 13 – 15 March 2019

- Genesis and Role of Copper Acetylide Cu_2C_2 as Active Species in the Catalytic Ethynylation of Formaldehyde to 1,4-Butynediol
  Tobias Bruhm, Oliver Thomys, Andrea Abram, Klaus Köhler
  53. Jahrestreffen Deutscher Katalytiker, Weimar, Germany, 11 – 13 March 2020

- Genesis of Active Copper Acetylide Cu_2C_2 via a Leaching Mechanism in Catalytic Ethynylation of Formaldehyde to 1,4-Butynediol
  Tobias Bruhm, Oliver Thomys, Andrea Abram, Klaus Köhler
  54. Jahrestreffen Deutscher Katalytiker, Weimar, Germany, 16 – 19 March 2021